Modeling and Control of Gas Turbine Thermoacoustic Pulsations

vorgelegt von
MS Aeronautical Engineering
Valter Bellucci
aus Rome (Italy)

von der Fakultät für Verkehrs- und Maschinensysteme
der Technischen Universität Berlin
zur Erlangung des akademischen Grades

Doktor der Ingenieurwissenschaften
- Dr.-Ing. -

genehmigte Dissertation

Promotionsausschuss:

Vorsitzender: Prof. Dr.-Ing. V. Popov
Berichter: Prof. Dr.-Ing. C.O. Paschereit
Berichter: Prof. A. Dowling

Tag der wissenschaftliche Aussprache: 23. April 2009

Berlin 2009
D83

Acknowledgments

This work was carried out during the time I have been working in the Gas Turbine Combustor Department of ALSTOM (Switzerland) and in the Combustion Research Laboratory of the Paul Scherrer Institut (PSI) in Switzerland.
First of all, I would like to thank Prof. Oliver Paschereit for having given me the opportunity to work in the field of thermoacoustics, his continual suggestions and the supervision of this thesis that he performed at the Experimentelle Strömungsmechanik - Hermann-Föttinger-Institut of the Technischen Universität Berlin.
I also would like to thank Dr. Peter Flohr and Dr. Peter Jansohn who supported and encouraged the realization of this work at ALSTOM and PSI respectively.
Special thanks to Dr. Bruno Schuermans for the stimulating discussions on the various thermoacoustic topics, the support in the transfer matrix measurement campaigns and the development of the thermoacoustic network.
I have also to thank Dr. Dariusz Nowak for the Finite Element acoustic computations, Dr. Francois Meili and Dr. Stefano Bernero for the transfer matrix measurements, Dr. Gislain Singla for the post-processing of flame transfer matrices, Dr. Fernando Biagioli for his inputs on combustion modeling, Dr. Weiqun Geng for the CFD simulations and Giulio Borghesi for the fruitful discussions on the low Mach number asymptotic expansion.
A thank also to Daniele Tabacco, Emily Zhang, Jonathan Reynolds, Curtis Sim, Michael Stobart, Donald Mikalson, Adrienn Szivoz and Brian Cox who gave an important contribution to this work during the time they spent in ALSTOM.
Finally, a great thank to my wife Elisabeth for her support and comprehension during the difficult moments.

Abstract

This work deals with the analysis of thermoacoustic pulsations occurring in gas turbine combustion chambers and with the suppression of such pulsations by means of passive control techniques.

First, perturbation techniques employed to derive thermoacoustic governing equations are illustrated. In a gas turbine combustion system generally the low Mach number hypothesis holds. As a result of our low Mach number perturbation analysis, the single components of the combustion system may be adequately described by different sets of governing equations. In hood and combustor the perturbation field may be approximated by pure acoustic wave propagation (i.e. one can solve for the wave or Helmholtz equation). On the contrary, suitable perturbation equations for burner and flame are the linearized incompressible Navier-Stokes equations. Using the further assumption of negligible dissipative effects in the perturbed burner flow, a thermoacoustic wave equation (including heat release fluctuations as a source term) is derived for modeling the entire combustion system. As a result of the use of this thermoacoustic wave equation in combination with heat release fluctuations dependent of the acoustic field, the Rayleigh criterion is recovered as a necessary condition for combustion instability.

The split of the combustion system into hood, burner, flame and combustor components is the prerequisite for the development of an acoustic network capable to simulate the thermoacoustic behavior of the gas turbine. In the low-frequency range, the perturbation field in burner and flame may be approximated as one-dimensional and then described by a two-port transfer matrix, which relates pressure and velocity perturbations upstream and downstream of the element. The burner transfer matrix has to account for wave propagation and dissipative effects, the latter being related to the transformation of kinetic energy of the perturbation flow into vorticity released at burner walls. Using measurements performed in an atmospheric impedance tube, we show that the transfer matrix of an industrial burner may be modeled by analytical incompressible flow models only in the very low-frequency range, the application of numerical methodologies been necessary for larger frequencies. Analytical flame transfer matrices are also derived by including two physical mechanisms: fuel concentration oscillations generated by velocity fluctuations at the fuel injection location and oscillations of the flame area induced by fluctuations of the flow velocity normal to the flame front. The flame analytical model is validated by means of flame transfer matrices measured atmospherically in a combustion rig operated with both natural gas and oil.

In order to dampen thermoacoustic pulsations, passive control techniques employing Helmholtz resonators and perforated screens are also illustrated. In particular, in this thesis we present an acoustic theory providing the pressure suppression achieved by the application of Helmholtz resonators to a combustion chamber. The theory predicts the maximization of the pressure suppression for a specific

value of the resonator impedance. This indicates that the acoustic response of the resonator must be accurately predicted during the design phase. Thus, we also present a nonlinear acoustic model that shows a very good agreement with measurements performed in an impedance tube on a wide range of damper geometries and bias flow conditions.

Finally, the different acoustic models we have used to characterize hood, burners, flames, combustor and dampers are combined together into an acoustic network applied to the simulation of heavy-duty gas turbines. The network is capable to compute both system eigenvalues (stability map) and pulsation spectra. The reported results show a very good agreement between simulations and pulsation spectra measured in field engines. In particular, the network demonstrates a valid engineering tool to predict the effect of the application of dampers to gas turbine combustors and to support the development of new burners by identifying the design parameters able to perform the thermoacoustic combustor tuning at engine level.

Contents

Nomenclature

Notation

a	radius
A	area
B	total enthalpy
c	speed of sound
C_p	specific heat at constant pressure
C_v	specific heat at constant volume
D	molecular diffusion coefficient
E	total energy
f	frequency
$\mathcal{F}$	downstream wave Riemann invariant
g_j	eigenmode amplitude
G	Green function
$\mathcal{G}$	upstream wave Riemann invariant
$\mathcal{H}$	closed loop tranfer function
He	Helmholtz number
$i = \sqrt{-1}$	complex unity
$\mathbf{I}$	unit tensor
k	wave number
$\mathbf{k}$	vector wave number
k_j	mode wave number
ℓ	end-correction
L	geometric length
L'	effective length
M	Mach number
$\mathbf{n}$	unit vector normal to surface
p	pressure
P	area ratio

Pr	Prandtl number
q	quality factor
$\mathbf{q}$	heat flux
Q	heat release per unit volume and time
Q_A	heat release per unit area and time
Q_M	heat release per unit mass of reactants
r	radial coordinate
r_f	reflection coefficient on damper flange
R	acoustic resistance
$\mathcal{R}$	gas constant
Re	Reynolds number
$s = i\omega + \upsilon$	Laplace variable (complex frequency) in e^{st} notation
s_j	poles of the system
S	entropy
S_f	flame speed
S_p	acoustic pressure flame source
S_u	acoustic velocity flame source
Sd	Stokes number
Sh	shear number
St	Strouhal number
St_{ac}	acoustic Strouhal number
t	time
T	temperature
$\mathbf{T}$	transfer function of acoustic element
T_{ij}	transfer function components of acoustic element
u	flow velocity magnitude or component
$\mathbf{u}$	flow velocity vector
x	axial coordinate
$\mathbf{x}$	space vector
X	acoustic reactance
U_f	flame surface velocity magnitude
$\mathbf{U}_f$	flame surface velocity vector
V	volume
Y	mass fraction
Z	acoustic impedance
Z'	acoustic impedance normalized by $\overline{\rho}\,\overline{c}$

Greek

α	damping coefficient
β	flame angle

γ	specific heat ratio
Γ	one-dimensional propagation constant
δ	Dirac's delta function
δ_f	flame thickness
Δh_F	heat release per unit mass of reactants
ζ	pressure loss coefficient
θ	azimuthal coordinate
κ	thermal conductivity
λ	acoustic wave length
Λ_j	mode normalization factor
μ	viscosity coefficient
ν	kinematic viscosity
ξ_j	modal damping coefficient
$\boldsymbol{\pi}$	vector potential
ρ	density
σ	variance of time-lag distribution
τ	characteristic time
$\boldsymbol{\tau}$	stress tensor
υ	damping factor or growth rate
υ_j	modal damping factor or growth rate
ϕ	scalar potential
Φ	pressure losses
φ	flow variable placeholder
ψ_j	eigenmode
ω	circular frequency in $e^{i\omega t}$ notation
ω_j	eigenfrequency
$\boldsymbol{\Omega}$	vorticity

Subscripts

B	fuel injection zone
E	enclosure connected to damper
f	flame front
fl	damper flange
F	fuel stream
i	irrotational component
n	resonator neck
r	radial vector component
res	resonance condition
R	resonator
O	oxidant stream

V	damper volume
x	axial vector component
Ω	rotational component
1	location upstream the acoustic element
2	location downstream the acoustic element
∞	reference quantity

Superscripts

$\overline{(\cdot)}$	mean flow quantity
$(\cdot)'$	flow variable perturbation in time domain
$\widehat{(\cdot)}$	flow variable perturbation in frequency domain
$\widetilde{(\cdot)}$	nondimensional quantity

Operators

$\overline{D}(\cdot)/Dt$	mean flow Lagrangian derivative $\partial/\partial t + \overline{\mathbf{u}} \cdot \nabla$
$(\cdot)^T$	transpose tensor
$\mathcal{O}(\cdot)$	order of magnitude

Chapter 1

Introduction

1.1 Thermoacoustic Phenomena in Gas Turbine Combustors

Thermoacoustic pulsations are a cause for concern in many combustion applications as diverse as rocket engines, gas turbines, boilers and furnaces. Thermoacoustic pulsations are generally defined as acoustic fluctuations induced by an unsteady heat release process [1]. Hydrodynamic instabilities (turbulence and flow instabilities) may generate "combustion noise", being in this case the heat release fluctuations independent of the acoustic field. Combustion noise is usually responsible for broadband sound emission ("loudspeaker" behavior of the flame). When the excitation frequency matches one of the eigenfrequencies of the combustion system, a pressure pulsation peak is generated in correspondence of the eigenfrequency ("resonance"). Moreover, pressure and entropy waves produced by heat release fluctuations are reflected back at combustor boundaries and may influence the hydrodynamic instabilities as well as activate other mechanisms responsible for heat release fluctuations. When this happens, a feedback cycle between fluctuations of velocity, pressure, entropy and heat release is found and very large pressure pulsation amplitudes may occur ("combustion instability" related to the "amplifier" behavior of the flame).

Thermoacoustic related problems are the increase of pollutant emissions (e.g. NO_x and CO) and the decrease of component lifetime (due to High Cycle Fatigue and overheating) that finally limit the operational range of the combustion system. [1]. In this work we focus on thermoacoustic pulsations generated in low-emission heavy-duty gas turbines, which have a high susceptibility to thermoacoustic pulsations because of the lean premixed combustion regime they operate with (e.g. laminar speed fluctuations induced by assigned equivalence ratio oscillations are much larger in lean premixed conditions than in stoichiometric conditions). Furthermore, in order to reduce NOx formation, the by-pass air entering downstream of the primary combustion zone is minimized in premixed combustion systems, this air having an acoustic damping effect in diffusion flame combustors.

1.2 Modeling of Thermoacoustic Systems

In principle, the reacting Navier-Stokes equations include nonlinear generation and propagation of sound, i.e. they can be used to simulate both resonance and combustion instability. Therefore, the Direct

Numerical Simulation (DNS) of the Navier-Stokes equations provides solutions including acoustic wave propagation. However, the following difficulties arise when developing finite-volume, finite-differences or finite-element numerical schemes for computing gas turbine combustor flows usually characterized by low values of the average Mach number [2], [3].

(i) Very disparate length scales exist in the flow field: thickness of mixing layers, thickness of acoustic and viscous boundary layers, turbulence scales and acoustic wave lengths. To capture all these multi-scale effects, an adequate grid refinement must be used in the computational domain. As a consequence, the computational cost becomes very large also for simple geometries. This is due to the high number of grid points and to the time-step restriction on the finest zones of the mesh. In particular, the simulation of the sound generation process due to vortical regions requires the smallest scales of turbulence to be solved. This means that the number of grid points must be $\geq Re^{9/4}$, being Re the Reynolds number of the flow [4].

(ii) In low Mach number unsteady flows the energy radiated as acoustic waves is usually a very small fraction of the total energy of the flow and the magnitude of acoustic disturbances may be smaller than the computational sound induced by the numerical scheme (this is usually the case when applying Computational Fluid Dynamic (CFD) codes to acoustic problems). In order to minimize both dissipation and dispersion errors occuring in the space discretization, high-order Essentially-Non-Oscillatory (ENO) and Dispersion-Relation-Preserving (DRP) schemes are used [3]. For time-integration, high-order Runge-Kutta techniques are usually employed and high-precision computation is also necessary.

(iii) Non-reflecting boundary conditions must be developed where the domain is truncated (inflow and outflow). In general, the Method of Characteristics (MOC) is employed: in this case the non-reflecting boundaries can be applied in flow regions where the small disturbance hypothesis holds. On solid walls, accurate wall conditions allow not to deteriorate the order of accuracy of the spatial discretization.

(iv) Long time solutions are necessary to obtain adequate spectral resolution.

These difficulties restrict the use of the direct computation to low Reynolds number simple flows (e.g. mixing layers) or to inviscid computations.
Large Eddy Simulation (LES) represents a valid alternative to model turbulent effects by relaxing the grid refinement constrain [5], [6]. When sound generation due to vortical motions has not to be computed, the computational constraint is that the grid must have a sufficient number of grid points to account for the shortest wave length propagating through the domain.
As an alternative to DNS and LES, perturbation techniques may be applied to the Navier-Stokes equations to derive governing equations for small disturbances of the steady mean flow solution [7], [8], [9]. Concerning the numerical difficulties above described, this approach permits the minimization of the round-off error and gives the possibility to use most effective schemes for the steady mean flow (computed by a CFD solver) and the perturbation flow (computed by a Computational Aeroacoustic (CAA) solver). Moreover, in the perturbation equations vorticity, acoustic and entropy fluctuations may be separated [8]. In the linear case, far away from boundaries the three modes are decoupled. If second-order

effects are considered, the interaction terms may be used for modeling the influence of fluctuations on the mean flow and vice-versa [10].

The methodology we use in this work to predict the acoustic field generated in gas turbine combustors is based on the coupling between three-dimensional acoustics, low-order analytical models, CFD and experiments. The combustion system is lumped into several elements (e.g. hood, burners, flames, combustor, cooling channels, etc.) that are combined in a *thermoacoustic network* [11], [12], [13], [14], [15]. This approach has the advantage that different mathematical models may be used for the different network elements. For instance, hoods and combustors with simple geometries may be represented by means of analytical solutions of the wave equation. Multi-burner arrangements are simulated by modeling hood and combustor as Multiple Input Multiple Output (MIMO) elements, described by a function linking pressure and velocity fluctuations at burner locations. A more accurate prediction of single- and multi-burner hood and combustor elements is obtained by using acoustic Finite Element Methods (FEM) to compute the acoustic modes of the chambers, eventually combined with CFD providing the speed of sound of the steady mean flow. Modeling issues related to this approach are the effect of mean flow convection on wave propagation and the absorption of acoustic power at boundaries, the latter affecting the damping and thus the stability of the system. When the geometrical extent of burners and flames is small compared to acoustic wavelengths, only plane wave propagation may be considered (this "compactness" assumption restricts the application of the network approach to the low-frequency regime). Compact burners and compact flames are treated as two-ports elements, where pressure and velocity fluctuations upstream and downstream of the element are coupled linearly via a four-element *transfer matrix*. In particular, the flame transfer matrix describes the interaction process between periodic heat release and acoustic field. Being the heat release process responsible for combustion instabilities, the modeling of the flame transfer matrix is of crucial importance when simulating thermoacoustic phenomena. Thus, flame transfer matrices directly obtained from experiments and implemented in the acoustic network allow for an accurate representation of sound generation and scattering due to the flame. For existing burners, the flame transfer matrix may be measured using loudspeakers for the acoustic forcing and reconstructing the acoustic field by means of the Multi-Microphone Method [16]. Finally, the eigenfrequencies of the acoustic network (written in the frequency domain) determine the linear stability of the combustion system and permit to identify unstable modes. Pulsation spectra may be also obtained in the time domain by introducing nonlinearities to limit the growth of pressure amplitude [14], [17]

To fit measured flame transfer matrices to low-order analytical models gives more physical insight into the mechanism responsible for the combustion instability and thus it is a valid approach to identify measures for pulsation control. Flame transfer matrix models may be obtained by integrating the governing equations across the flame thickness for subsonic combustion [18] or under the hypothesis of low Mach number mean flow [19]. The flame transfer matrix elements are given when the relation between heat release oscillations and acoustic field in front of the flame is known (*transfer function*), such a relation depending on the characteristics of the combustion process (premixed vs. diffusion flame, bluff-body vs. free-vortex flame stabilization, gas vs. liquid fuel, etc.). Combustion instability mechanisms are inherently complex since they are the result of interactions between different physical phenomena (see Fig. 1.1), which at the end lead to a "time-lag" between heat release oscillations and fluctuations of acoustic velocity and/or pressure in front of the flame [20]. For time-lag values within a certain range of variation, the system becomes unstable. Several physical mechanisms responsible

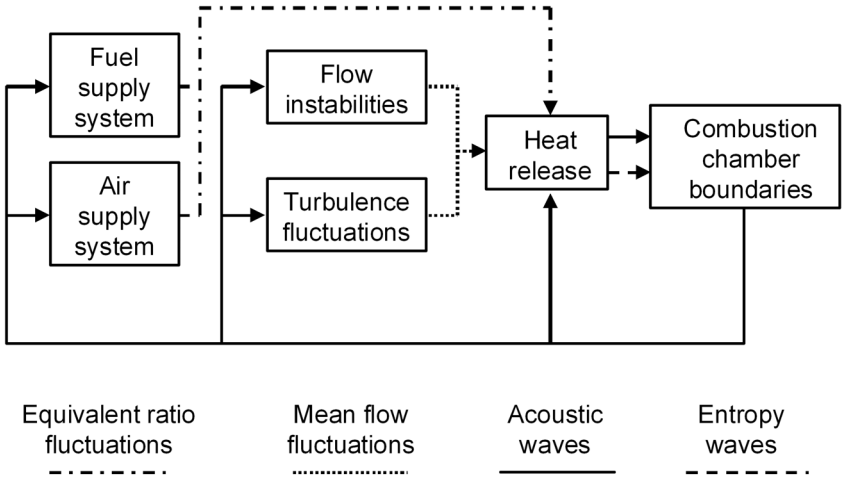

Figure 1.1: Thermoacoustic interactions in combustion systems.

for time-lag effects have been identified [21]. For lean premixed flames, the sensitivity of heat release fluctuations to equivalence ratio oscillations may represent a strong feedback mechanism [16], [18], [22], [23], [24], [25]. In this case, heat release fluctuations are induced by fuel concentration oscillations caused by acoustic fluctuations at the fuel injector location. The time-lag occurring between heat release and fuel concentration oscillations is the convective time that fuel concentration fluctuations need to travel from the injector to the flame. Analytical models have been proposed to account for the flame shape effect on the time-lag distribution in the frequency domain [24], [26]. As an alternative, steady CFD computations may be performed on the combustor to determinate the time-lag distribution [25]. Flame transfer function mechanisms related to flame speed fluctuations and flame area oscillations have been also proposed [24], [26], [27], [28].

1.3 Passive Control of Thermoacoustic Pulsations

In classical acoustics, Helmholtz resonators are coupled to enclosures in order to reduce pressure pulsations. A Helmholtz resonator consists of a volume with a neck through which the fluid inside the resonator communicates with an external medium [29]. In combustion applications, a cooling flow (*bias flow*) must be maintained through the resonator in order to prevent overheating. When a Helmholtz resonator is applied to an enclosure, in correspondence of the neck mouth a boundary with a frequency dependent behavior is realized. The acoustic response of resonator is described by the impedance $Z_n = R_n + iX_n$, i.e. the ratio in the frequency domain between acoustic pressure and acoustic velocity normal to the resonator neck mouth. Helmholtz developed a theory to predict the neck mouth impedance of a cavity

resonator with a cylindrical neck [30]. When the neck is short and narrow with respect to the wavelength (low-frequency range), all the fluid particles in the neck are assumed to fluctuate with the same acoustic speed and the "harmonic oscillator" mechanical analogy may be used. However, not only the fluid in the neck but also part of the fluid in the communicating volumes (outside the damper and inside the resonator cavity) participates in acoustic fluctuations. For long wavelengths, the air at the neck end may be modeled as a zero-mass solid piston fluctuating and then radiating acoustic energy outside of the neck. For a tube terminating in a half-space (infinite flange), when the neck Helmholtz number is small the radiation reactance can be included by replacing the tube length with the "effective" length [29]. This "end-correction" may be applied at both ends of the neck when the infinite flange assumption is used for the resonator cavity and the outside domain. More accurate resonator models have been proposed, e.g. using an internal end-correction depending on the resonator geometry [31] or modeling wave propagation inside the resonator volume [32].

An accurate prediction of visco-thermal acoustic damping and conversion of acoustic energy into shedding of vortices generated at the rims of the neck (the vortices being convected downstream and dissipated into heat by turbulence) is also important for the correct evaluation of the damper resistance R_n. Previous investigations have been oriented to model independently the linear and nonlinear regimes of orifices in the case of low Helmholtz numbers and low Mach numbers. In absence of bias flow, the vortex-shedding dissipative process is nonlinear because it depends on the convection and dissipation of (acoustically produced) vorticity by means of the acoustic field itself. Thus R_n depends on the acoustic pressure in front of the neck, which is a function of the applied resonator impedance. The acoustic resistance may be modeled starting from one-dimensional fluid dynamic models applied to the orifice flow [33], [34], [35], [36], [37], [38]. For sufficiently high acoustic pressure amplitudes, the resistance R_n is found to increase with the acoustic pressure. However, for acoustic Strouhal numbers $\ll 1$ the flow in the neck can be considered quasi-steady and the resistance expressed by means of a constant discharge coefficient. When a bias flow enters the neck, there is a linear contribution to R_n coming from the bias flow convection of vorticity. The linear effect is assumed dominant over the nonlinear effect when the bias flow velocity is sufficiently larger than the acoustic velocity. In this case Z_n depends on frequency, orifice geometry and bias flow velocity independently of acoustic pressure. Several quasi-steady one-dimensional models have been applied to orifices with bias flow [39], [37], [38], [40].

The mechanism responsible for the damping is mathematically analyzed by replacing the enclosure area where the damper is applied with the damper impedance Z_n. To study the characteristics of the neck mouth uncoupled from the enclosure, one can consider a plane wave of frequency ω incident on a wall under anechoic conditions for the reflected wave (in anechoic conditions the acoustic energy of a normally incident plane wave is fully absorbed) [29]. This analysis shows that for a given frequency and pressure amplitude in front of the resonator, the maximum acoustic power absorption is achieved for $X_n = Im(Z_n) \approx 0$, i.e. when the resonator resonance frequency ω_{res} coincides with the pulsation frequency. When the resonator is coupled to the enclosure, sound reflection from the enclosure boundary must be considered. The effect of the damper on the resonance frequency ω_N of the enclosure without resonator has been studied by other authors [41], [42]. The analysis has been performed under the following assumptions: acoustically compact (point-impedance) resonator; harmonic oscillator model for the damper; ω_N in the low frequency range where the average separation between eigenfrequencies is much larger than the average modal bandwidth; sound generation by means of point sources located

inside the enclosure. The acoustic pressure field of the coupled system has been compared to that of the enclosure without the resonator. At the frequency ω_N, amplitude reduction may occur for $\omega_{res} = \omega_N$ because of the sound cancelation performed by the neck mouth (seen as a "pseudo-source") on the acoustic field produced by the sound sources inside the enclosure. When $|Z_n| \ll 1$, the pressure on the neck mouth is small and the pseudo-source velocity is tuned to cancel the pressure produced by the sound sources. The analysis also shows that if the excitation is not confined to ω_N, amplitude maxima may occur for frequencies close to ω_N. In the frequency range including the new maxima and for a given damping coefficient of the enclosure, the sound reduction may be maximized by appropriately tuning the resonator resistance. Note that the resonator damping which gives the maximum reduction in pressure amplitude does not coincide with the damping providing the maximum power absorption (in fact the acoustic power injected by the source into the enclosure is a function of the resonator impedance). For combustion applications, dampers modeled as harmonic oscillators have been coupled to the oscillator represented by the mass of fluid in a fuel/air mixing nozzle [43]. The air in the combustor provided the compliance (equivalent spring in the mechanical analogy) for the oscillators. A negative combustor damping accounted for the amplification behavior of the flame. The optimum damping of eigenmodes was obtained with a resonance frequency of resonators aligned with the natural frequency of the combustor-nozzle system without resonators.

1.4 Thesis Overview

In the second Chapter of this thesis, thermoacoustic governing equations are derived by applying a perturbation technique to the fluid dynamic Navier-Stokes equations. Under certain assumptions, it is possible to split the perturbed fluid dynamic field into vorticity, entropy and acoustic disturbances. In particular, when the heat release process is unsteady thus heat release oscillations act as a source for the only acoustic field. In a gas turbine combustion system generally the low Mach number hypothesis holds. Using a low Mach number asymptotic expansion, the single components of the combustion system are described by means of different sets of governing equations, i.e. acoustic wave equation for hood and combustor chambers and linearized incompressible Navier-Stokes equations for burner and flame.
Using the further assumption of negligible dissipative effects in the perturbed burner flow, a thermoacoustic wave equation (including heat release fluctuations as a source term) is derived for modeling the entire combustion system. As a result of the use of this thermoacoustic wave equation in combination with heat release fluctuations dependent of the acoustic field, the Rayleigh criterion is recovered as a necessary condition for combustion instability.
The third Chapter presents the transfer matrix approach employed to represent burners and flames in the low-frequency range. The perturbation field is approximated as one-dimensional and then described by a two-port transfer matrix. Transfer matrices of an industrial burner have been measured in an atmospheric impedance tube and employed to validate burner transfer matrix models. For sufficiently low frequencies, analytical models derived by the linearized incompressible flow equations may be used. When frequency increases thus acoustic FEM must be used to represent wave propagation, the linearized incompressible flow model being employed to include the burner acoustic dissipation.
The flame transfer matrix model is closed when an expression is given for the heat release contribution depending of the acoustic field in front of the flame. In the fourth Chapter, analytical flame transfer

functions are derived by considering the physical mechanisms of fuel concentration oscillations (generated by velocity fluctuations at the fuel injection location) and oscillations of the flame area (induced by fluctuations of the flow velocity normal to the flame front). The analytical model is compared to flame transfer functions measured atmospherically in a combustion rig, where a lean premixed swirl burner was operated in both gas and oil operation.

Passive control techniques employing Helmholtz dampers are illustrated in the fifth Chapter. First, we show a nonlinear resonator model including bias flow effects. The model is calibrated by means of experiments performed in an impedance tube on resonators with different geometries and bias flow conditions. Then, we present an acoustic theory providing the pressure suppression achieved when applying Helmholtz resonators to combustion chambers. The theory predicts a maximization of the pressure suppression for a specific value of the resonator impedance.

Finally, in the sixth Chapter the ALSTOM acoustic network is presented. In the network, hood, burners and combustor are represented by means of three-dimensional FEM modal expansion. The flame is modeled as a gas dynamic discontinuity whose transfer function is measured atmospherically. The network can also simulate the effect of Helmholtz dampers applied to the combustion system for suppressing acoustic pulsations. All the network element models may be formulated in the frequency domain or in the time domain (using a state-space representation). The network is capable to compute both system eigenvalues (stability map) and pulsation spectra. The time domain solution is obtained by including non-linear saturation of the heat release term. The reported results show a very good agreement between simulations and pulsation spectra measured in an engine with and without resonators. Moreover, the network demonstrates a valid engineering tool to support the development of new burners by identifying the design parameters able to perform the thermoacoustic combustor tuning at engine level.

Chapter 2

Thermoacoustic Governing Equations

2.1 Flow Regions in Gas Turbine Combustion Systems

In the present work we focus on the gas turbine combustion system illustrated in Fig. 2.1, where different flow regions may be identified.

(i) The *hood* is the volume located upstream of the burner where the combustion air is collected.

(ii) The *burner* manages the mixing process between combustion air and fuel. Moreover the burner provides the aerodynamic stabilization of the flame, which is generally achieved by means of a burner induced swirled flow characterized by high levels of turbulence intensity [44].

(iii) Within the *flame* the heat release process occurs and temperature increases.

(iv) The *combustor* includes the flow downstream of the flame.

In the following Sections, thermoacoustic governing equations are derived for the gas turbine combustion system.

2.2 Navier-Stokes Equations

A reacting flow may be modeled as a continuum medium using the Navier-Stokes equations. The Navier-Stokes continuity, momentum and energy equations are written in non-conservative form respectively

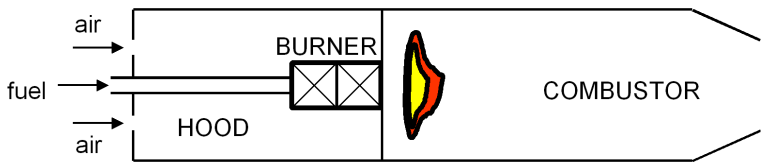

Figure 2.1: Schematic of gas turbine combustion system.

as [45]

$$\frac{D\rho}{Dt} + \rho \nabla \cdot \mathbf{u} = 0 \tag{2.1}$$

$$\rho \frac{D\mathbf{u}}{Dt} + \nabla p = \nabla \cdot \boldsymbol{\tau} \tag{2.2}$$

$$\rho T \frac{DS}{Dt} = \boldsymbol{\tau} : \nabla \mathbf{u} - \nabla \cdot \mathbf{q} + Q \tag{2.3}$$

where the Lagrangian derivative $D/Dt = \partial/\partial t + \mathbf{u} \cdot \nabla$ expresses the change of the derivative argument for a fluid element. The system of governing equations (2.1)-(2.3) is completed by the equation of state of perfect gases

$$p = \rho \mathcal{R} T \tag{2.4}$$

and the thermodynamic relation

$$S = C_v \ln\left(\frac{p}{\rho^\gamma}\right) + const \tag{2.5}$$

where $C_v = const$ according to the hypothesis of calorically perfect gas and

$$\gamma = C_p / C_v \tag{2.6}$$

with $C_p = C_v + \mathcal{R}$ ($\gamma = 1.4$ for perfect gases). The stress tensor $\boldsymbol{\tau}$ and the heat flux $\mathbf{q}$ are defined as

$$\boldsymbol{\tau} = \mu \left[\left(\nabla \mathbf{u} + \nabla \mathbf{u}^T \right) - \frac{2}{3} \left(\nabla \cdot \mathbf{u} \right) \mathbf{I} \right] \tag{2.7}$$

$$\mathbf{q} = -\kappa \nabla T \tag{2.8}$$

The bulk viscosity has been set equal to zero (this assumption is not valid in presence of non-equilibrium phenomena, as when vibrational modes of molecules are excited [45], [46]). The heat flux has been expressed by the Fourier law. The transport coefficients μ and κ are in general monotonic functions of the temperature only, being the dependence from the pressure usually negligible for gases [46]. In the following, both μ and κ are assumed to be constant. The heat release term Q depends on the chemical reactions of the combustion process and is determined by solving for the continuity equations of the chemical species [47]. The set of equations (2.1)-(2.5) is closed when appropriate initial and boundary conditions are prescribed.

Eqs. (2.1)-(2.3) may be also written in conservative form using the total energy E and the the total enthalpy B given by

$$E = C_v T + \frac{\mathbf{u} \cdot \mathbf{u}}{2}, \qquad B = C_p T + \frac{\mathbf{u} \cdot \mathbf{u}}{2} \tag{2.9}$$

It yields [47]

$$\frac{\partial \rho}{\partial t} + \nabla \cdot (\rho \mathbf{u}) = 0 \tag{2.10}$$

$$\frac{\partial(\rho\,\mathbf{u})}{\partial t} + \nabla\cdot(\rho\,\mathbf{u}\,\mathbf{u}) + \nabla p = \nabla\cdot\boldsymbol{\tau} \tag{2.11}$$

$$\frac{\partial(\rho\,E)}{\partial t} + \nabla\cdot(\rho\,B\,\mathbf{u}) = \nabla\cdot(\mathbf{u}\cdot\boldsymbol{\tau}) - \nabla\cdot\mathbf{q} + Q \tag{2.12}$$

By using Eqs. (2.1), (2.4) and (2.5), the energy equation (2.3) may be expressed in terms of pressure as

$$\frac{Dp}{Dt} + \gamma\,p\,\nabla\cdot\mathbf{u} = (\gamma-1)\,[\,\boldsymbol{\tau}:\nabla\mathbf{u} - \nabla\cdot\,\mathbf{q} + Q\,] \tag{2.13}$$

2.2.1 Helmholtz decomposition and flow vorticity

The Helmholtz decomposition applied to the differentiable vector field $\mathbf{u}$ writes as

$$\mathbf{u} = \mathbf{u}_i + \mathbf{u}_\Omega \tag{2.14}$$

where the vector fields $\mathbf{u}_i$ and $\mathbf{u}_\Omega$ are given by

$$\mathbf{u}_i = \nabla\,\phi\,, \qquad \mathbf{u}_\Omega = \nabla\times\boldsymbol{\pi} \tag{2.15}$$

being ϕ the scalar potential and $\boldsymbol{\pi}$ the vector potential [45], [48]. By definition $\mathbf{u}_i$ is irrotational ($\nabla\times\mathbf{u} = \nabla\times\mathbf{u}_\Omega$) and $\mathbf{u}_\Omega$ solenoidal ($\nabla\cdot\mathbf{u} = \nabla\cdot\mathbf{u}_i$). The divergence and curl of Eq. (2.14) give respectively[1]

$$\nabla^2\phi = \nabla\cdot\mathbf{u}\,, \qquad \nabla^2\boldsymbol{\pi} = -\boldsymbol{\Omega} \tag{2.16}$$

where the condition

$$\nabla\cdot\boldsymbol{\pi} = 0 \tag{2.17}$$

has been imposed and $\boldsymbol{\Omega}$ is the flow *vorticity* defined as

$$\boldsymbol{\Omega} = \nabla\times\mathbf{u} \tag{2.18}$$

When $\mathbf{u}_\Omega$ has zero normal component on the boundary ∂V of the domain of interest V, then the decomposition (2.14) is orthogonal (i.e. $\int_V \mathbf{u}_i\cdot\mathbf{u}_\Omega\,dV = 0$) and unique [49]. A vorticity transport equation may be obtained by making the curl of Eq. (2.2) with the viscous term on the right-hand side expressed as[2]

$$\nabla\cdot\boldsymbol{\tau} = \mu\left[\frac{4}{3}\,\nabla(\nabla\cdot\mathbf{u}) - \nabla\times(\nabla\times\mathbf{u})\right] \tag{2.19}$$

By assuming that the kinematic viscosity

$$\nu = \mu/\rho \tag{2.20}$$

is constant, one finds[3]

$$\frac{D\boldsymbol{\Omega}}{Dt} = \boldsymbol{\Omega}\cdot\nabla\mathbf{u} - \boldsymbol{\Omega}\,(\nabla\cdot\mathbf{u}) + \frac{1}{\rho^2}\,\nabla\rho\times\nabla p + \nu\,\nabla^2\,\boldsymbol{\Omega} \tag{2.21}$$

[1] $\nabla\times(\nabla\times\mathbf{a}) = \nabla(\nabla\cdot\mathbf{a}) - \nabla^2\mathbf{a}$.

[2] $\nabla\cdot[\nabla\mathbf{u}+\nabla\mathbf{u}^T - 2/3\,(\nabla\cdot\mathbf{u})\,\mathbf{I}] = \nabla^2\mathbf{u}+\nabla(\nabla\cdot\mathbf{u}) - 2/3\,\nabla(\nabla\cdot\mathbf{u}) = \nabla^2\mathbf{u}+1/3\,\nabla(\nabla\cdot\mathbf{u}) = \nabla(\nabla\cdot\mathbf{u}) - \nabla\times(\nabla\times\mathbf{u}) + 1/3\,\nabla(\nabla\cdot\mathbf{u})$.

[3] $\nabla\times(\mathbf{u}\cdot\nabla\mathbf{u}) = \nabla\times[\,\nabla(\mathbf{u}\cdot\mathbf{u})/2 + (\nabla\times\mathbf{u})\times\mathbf{u}\,] = \nabla\times(\boldsymbol{\Omega}\times\mathbf{u}) = -\boldsymbol{\Omega}\cdot\nabla\mathbf{u} + \mathbf{u}\cdot\nabla\boldsymbol{\Omega} + \boldsymbol{\Omega}(\nabla\cdot\mathbf{u})$ and $\nabla\times(\nabla p/\rho) = 1/\rho\nabla\times\nabla p + \nabla(1/\rho)\times\nabla p = -1/\rho^2\nabla\rho\times\nabla p$.

where the four terms on the right-hand side represent, respectively, the effects of vortex stretching, fluid dilatation, baroclinic vorticity generation and viscous diffusion [50]. It is possible to demonstrate that an initially irrotational flow remains irrotational if the flow is barotropic (i.e. $\rho = \rho(p)$) and inviscid [45]. In an incompressible flow $\nabla \cdot \mathbf{u} = 0$, $\rho = const$ and Eq. (2.21) reduces to

$$\frac{D\boldsymbol{\Omega}}{Dt} = \boldsymbol{\Omega} \cdot \nabla \mathbf{u} + \nu \nabla^2 \boldsymbol{\Omega} \tag{2.22}$$

the pressure being given by the Poisson equation

$$\nabla^2 p = -\rho \nabla \cdot (\mathbf{u} \cdot \nabla \mathbf{u}) \tag{2.23}$$

that is obtained by making the divergence of Eq. (2.2).

2.2.2 Bernoulli theorem and Crocco's equation

Using Eq. (2.19) into the momentum equation (2.2), we have[4]

$$\frac{\partial \mathbf{u}}{\partial t} + \frac{\nabla p}{\rho} + \nabla \left(\frac{\mathbf{u} \cdot \mathbf{u}}{2} \right) = \mathbf{u} \times \boldsymbol{\Omega} + \nu \left[\frac{4}{3} \nabla (\nabla \cdot \mathbf{u}) - \nabla \times \boldsymbol{\Omega} \right] \tag{2.24}$$

When the flow is barotropic, irrotational and inviscid, Eq. (2.24) gives the Bernoulli theorem

$$\frac{\partial \phi}{\partial t} + \int \frac{dp}{\rho} + \frac{\mathbf{u} \cdot \mathbf{u}}{2} = C(t) \tag{2.25}$$

where $C(t)$ is a function of time only. In an incompressible flow, the second term on the left-hand side of Eq. (2.25) reads as $\int dp/\rho = p/\rho$. By combining Eqs. (2.4) and (2.5), one can derive the thermodynamic expression

$$\frac{dp}{\rho} = \frac{\gamma}{\gamma - 1} d \left(\frac{p}{\rho} \right) - T \, dS \tag{2.26}$$

Thus in a homentropic flow (i.e. $S = const$), one has $\int dp/\rho = C_p T$. Eqs. (2.24) and (2.26) may be combined to give the Crocco's equation

$$\frac{\partial \mathbf{u}}{\partial t} + \nabla B = T \nabla S + \mathbf{u} \times \boldsymbol{\Omega} + \nu \left[\frac{4}{3} \nabla (\nabla \cdot \mathbf{u}) - \nabla \times \boldsymbol{\Omega} \right] \tag{2.27}$$

2.3 Classical Acoustics

In order to simplify the thermoacoustic modeling of the combustion system, linearized forms of the Navier-Stokes equations may be derived by expressing the generic flow variable φ (being φ a placeholder for p, ρ, T, S, $\mathbf{u}$, Q) as

$$\varphi(\mathbf{x}, t) = \overline{\varphi}(\mathbf{x}) + \varphi'(\mathbf{x}, t) \tag{2.28}$$

where the *mean flow* $\overline{\varphi}(\mathbf{x})$ is the steady solution of the steady Navier-Stokes equations and $\varphi'(\mathbf{x}, t)$ is the mean flow *perturbation*. In classical acoustics the mean flow is taken as a non-reacting uniform fluid

[4] $\mathbf{a} \cdot \nabla \mathbf{b} + \mathbf{b} \cdot \nabla \mathbf{a} = \nabla(\mathbf{a} \cdot \mathbf{b}) + (\nabla \times \mathbf{a}) \times \mathbf{b} + (\nabla \times \mathbf{b}) \times \mathbf{a}$

at rest, i.e. $\overline{\mathbf{u}} = \overline{Q} = 0$ and $\overline{\varphi} = const$ for $\overline{\varphi} = \overline{p}\,,\ \overline{\rho}\,,\ \overline{T}\,,\ \overline{S}\,$. Next the flow variables $p\,,\ \rho\,,\ T\,,\ S\,,\ \mathbf{u}$ are nondimensionalized using the constant mean flow values $\overline{p}\,,\ \overline{\rho}\,,\ \overline{T}\,,\ C_p\,,\ \overline{c}$ respectively, where c is the speed of sound defined as

$$c = \sqrt{\gamma\,\mathcal{R}\,T} = \sqrt{\gamma\,p/\rho} \tag{2.29}$$

(in an unperturbed fluid at rest the speed of sound is the only characteristic velocity). In order to apply the linearization process to the governing equations, all the nondimensional perturbations are supposed to be $\mathcal{O}(\varrho)$ with ϱ small parameter $\ll 1$ characterizing the intensity of disturbances [51], [52]. When substituting Eqs. (2.28) into the nondimensional form of Eqs. (2.1)-(2.5) and collecting terms of the same order in $\varrho\,$, at $\mathcal{O}(\varrho^0)$ and $\mathcal{O}(\varrho)$ one obtains the mean flow and perturbation equations respectively. In particular, the dimensional form of the perturbation equations reads as

$$\frac{\partial\,\rho'}{\partial t} + \overline{\rho}\,\nabla\cdot\,\mathbf{u}' = 0 \tag{2.30}$$

$$\overline{\rho}\,\frac{\partial\,\mathbf{u}'}{\partial t} + \nabla\,p' = \mu\left[\frac{4}{3}\,\nabla\,(\nabla\cdot\,\mathbf{u}') - \nabla\times\,(\nabla\times\,\mathbf{u}')\right] \tag{2.31}$$

$$\overline{\rho}\,\overline{T}\,\frac{\partial\,S'}{\partial t} = \kappa\,\nabla^2\,T' \tag{2.32}$$

$$\frac{p'}{\overline{p}} = \frac{\rho'}{\overline{\rho}} + \frac{T'}{\overline{T}} \tag{2.33}$$

$$\frac{S'}{C_p} = \frac{p'}{\gamma\,\overline{p}} - \frac{\rho'}{\overline{\rho}} \tag{2.34}$$

where Eq. (2.19) has been used to express the viscous term in the momentum equation.

2.3.1 Boundary layer problem

By making the divergence of Eq. (2.31), using Eq. (2.30) to express $\nabla\cdot\,\mathbf{u}'$ and eliminating ρ' by means of Eq. (2.34) gives

$$\left(\frac{\partial}{\partial t} - \frac{4}{3}\,\overline{\nu}\,\nabla^2\right)\frac{\partial}{\partial t}\left(\frac{p'}{\gamma\,\overline{p}} - \frac{S'}{C_p}\right) - \frac{\nabla^2\,p'}{\overline{\rho}} = 0 \tag{2.35}$$

When Eqs. (2.33) and (2.34) are employed into Eq. (2.32) to express T' as a function of p' and S', one has

$$\frac{1}{C_p}\,\frac{\partial\,S'}{\partial t} = \frac{\overline{\nu}}{Pr}\,\nabla^2\left(\frac{\gamma-1}{\gamma}\,\frac{p'}{\overline{p}} + \frac{S'}{C_p}\right) \tag{2.36}$$

where Pr is the Prandtl number defined as

$$Pr = \frac{\mu\,C_p}{\kappa} \tag{2.37}$$

($Pr = 0.72$ for air at ambient temperature). Eqs. (2.35) and (2.36) form a closed system in the variables p' and S'. Using Eq. (2.36) to express $\partial S'/\partial t$ into Eq. (2.35), one obtains

$$\frac{\partial^2 p'}{\partial t^2} - \overline{c}^2 \nabla^2 p' = \overline{\nu} \left[\left(\frac{4}{3} + \frac{\gamma - 1}{Pr} \right) \frac{\partial}{\partial t} \nabla^2 p' + \frac{\gamma \overline{p}}{C_p} \left(\frac{1}{Pr} - \frac{4}{3} \right) \frac{\partial}{\partial t} \nabla^2 S' \right] \tag{2.38}$$

Eq. (2.38) shows that the propagation of pressure waves is decoupled from entropy fluctuations when $Pr = 3/4$. To consider the general case $Pr \neq 3/4$, first the momentum equation (2.31) is split into two separate equations using the decomposition of $\mathbf{u}'$ into irrotational component $\mathbf{u}'_i$ and rotational component $\mathbf{u}'_\Omega$ [see Eq. (2.14)]. It yields

$$\overline{\rho} \frac{\partial \mathbf{u}'_i}{\partial t} = -\nabla \left[p' + \frac{4}{3} \mu \frac{\partial}{\partial t} \left(\frac{p'}{\gamma \overline{p}} - \frac{S'}{C_p} \right) \right] \tag{2.39}$$

$$\overline{\rho} \frac{\partial \mathbf{u}'_\Omega}{\partial t} = -\mu \nabla \times (\nabla \times \mathbf{u}'_\Omega) \tag{2.40}$$

where $\nabla \cdot \mathbf{u}'_i$ has been eliminated using Eqs. (2.30), (2.33) and (2.34). Note that the curl of Eq. (2.39) and the divergence of Eq. (2.40) give, respectively, $\partial t / \partial (\nabla \times \mathbf{u}'_i) = 0$ and $\partial t / \partial (\nabla \cdot \mathbf{u}'_\Omega) = 0$, i.e. an initially irrotational field $\mathbf{u}'_i$ remains irrotational and an initially solenoidal field $\mathbf{u}'_\Omega$ remains solenoidal. To investigate the characteristics of the system (2.35), (2.36), (2.39) and (2.40), we consider the harmonic solution [29]

$$\varphi'(\mathbf{x}, t) = \breve{\varphi} \exp(s\,t - i\,\mathbf{k} \cdot \mathbf{x}) \tag{2.41}$$

where $\mathbf{k}$ is the vector wave number and s the complex frequency. The solution (2.41) satisfies the conditions

$$\nabla^2 \varphi' = -|\mathbf{k}|^2 \varphi' \ , \qquad \frac{\partial \varphi'}{\partial t} = s\, \varphi' \tag{2.42}$$

The substitution of Eq. (2.41) into Eqs. (2.35)-(2.36) yields

$$\left(s + \frac{4}{3} \overline{\nu} |\mathbf{k}|^2 \right) s \left(\frac{p'}{\gamma \overline{p}} - \frac{S'}{C_p} \right) + |\mathbf{k}|^2 \frac{p'}{\overline{\rho}} = 0 \tag{2.43}$$

$$s \frac{S'}{C_p} = -\frac{\overline{\nu}}{Pr} |\mathbf{k}|^2 \left(\frac{\gamma - 1}{\gamma} \frac{p'}{\overline{p}} + \frac{S'}{C_p} \right) \tag{2.44}$$

The case $\mathbf{k}$ real and s complex corresponds to standing waves damped out in time by viscous and heat conduction effects. We analyze the regime response case, where $\mathbf{k}$ is complex and $s = i\omega$ with $\omega = 2\pi f$ circular frequency. This corresponds to a sinusoidal driven motion in time with waves attenuated in space. A non trivial solution may be searched by setting the determinant of the system (2.43)-(2.44) to zero. This leads to the characteristic relation between $|\mathbf{k}|^2$ and ω

$$|\mathbf{k}|^2 = i \left(\frac{\omega}{\overline{c}} \right)^2 \frac{Pr\, Sh^2}{2} \Upsilon \tag{2.45}$$

$$\Upsilon = \frac{-\left[1 + \frac{i}{Sh^2} \left(\frac{4}{3} + \frac{\gamma}{Pr} \right) \right] \mp \sqrt{\left[1 + \frac{i}{Sh^2} \left(\frac{4}{3} + \frac{\gamma}{Pr} \right) \right]^2 - \frac{4\,i}{Pr\, Sh^2} \left(1 + \frac{4}{3}\, i\, \frac{\gamma}{Sh^2} \right)}}{1 + \frac{4}{3}\, i\, \frac{\gamma}{Sh^2}}$$

where the shear number Sh is defined as

$$Sh = \frac{\overline{c}}{\sqrt{\overline{\nu}\,\omega}} \tag{2.46}$$

The continuum model is valid for the acoustic field when the acoustic Knudsen number Kn is $\ll 1$, being $Kn = \varsigma/\lambda$ with ς mean free path (i.e. distance between molecule collisions) and λ acoustic wavelength given by [46], [51]

$$\lambda = \overline{c}/\omega \tag{2.47}$$

Following the kinetic theory of gases, the kinematic viscosity may be written as $\overline{\nu} \sim \overline{c}\,\varsigma$ and thus the condition $Kn \ll 1$ is equivalent to

$$Sh^2 \gg 1 \tag{2.48}$$

(for air at room temperature $\overline{\nu} = 1.5 \times 10^{-5} m^2/s$ and $\overline{c} = 340 m/s$, so that for a frequency of $1kHz$ one gets $Sh^2 \simeq 10^6$). By using Eq. (2.48), the solution corresponding to the upper sign in Eq. (2.45) is obtained with $\Upsilon \simeq -2$. It reads as

$$k_d^2 \simeq -i \left(\frac{\omega}{\overline{c}}\right)^2 Pr\, Sh^2 \qquad \Rightarrow \qquad k_d \simeq \mp \left(\frac{\omega}{\overline{c}}\right) \sqrt{\frac{Pr}{2}}\, Sh\,(1-i) \tag{2.49}$$

The second of Eqs. (2.49) shows that perturbations are damped within propagation distances of the order of the small diffusion length

$$\delta_d = |k_d|^{-1} = \sqrt{2\ \overline{\nu}/(\omega\, Pr)} \tag{2.50}$$

where

$$\delta_d \ll \lambda \tag{2.51}$$

according to Eq. (2.48). Then, for the *diffusion mode* (2.49) the effect of boundary walls becomes negligible outside of the thin thermal boundary layer of thickness δ_d (for air at room temperature and a frequency $> 7Hz$ one has $\delta_d < 1mm$). The solution corresponding to the lower sign in Eq. (2.45) is obtained by expanding Υ in series of $1/Sh^2$. At second order, it gives[5]

$$k_p^2 \simeq \left(\frac{\omega}{\overline{c}}\right)^2 \left[1 - \frac{i}{Sh^2}\left(\frac{4}{3} + \frac{\gamma-1}{Pr}\right)\right] \ \Rightarrow\ k_p \simeq \mp \left(\frac{\omega}{\overline{c}}\right) \left[1 - \frac{i}{2\,Sh^2}\left(\frac{4}{3} + \frac{\gamma-1}{Pr}\right)\right] \tag{2.52}$$

The mode related to the wave number k_p is characterized by a small attenuation in space and is called *propagational mode*. When k_p^2 is substituted into Eqs. (2.42) (written for pressure fluctuations), Eq. (2.43) and the harmonic form of Eq. (2.39), one obtains at order $1/Sh^2$

$$\frac{\partial^2 p'_p}{\partial t^2} - \overline{c}^2\, \nabla^2 p'_p \simeq \overline{\nu}\left(\frac{4}{3} + \frac{\gamma-1}{Pr}\right) \frac{\partial}{\partial t} \nabla^2 p'_p \tag{2.53}$$

$$\frac{S'_p}{C_p} \simeq \frac{i}{\overline{\rho}\,\overline{T}\,Pr\,Sh^2}\ p'_p \tag{2.54}$$

$$\mathbf{u}'_p \simeq -\frac{1}{i\,\omega\,\overline{\rho}}\left(1 + \frac{4}{3}\frac{i}{Sh^2}\right) \nabla\, p'_p \tag{2.55}$$

[5] $\sqrt{1-i\theta} = 1/\sqrt{2}(\sqrt{\sqrt{1+\theta^2}+1} - i\sqrt{\sqrt{1+\theta^2}-1})$ where $\sqrt{\sqrt{1+\theta^2}+1} \simeq \sqrt{2}$ and $\sqrt{\sqrt{1+\theta^2}-1} \simeq \theta/\sqrt{2}$ when $\theta \to 0$.

where Eq. (2.53) represents the wave equation of the propagational mode. By introducing the (real) wave number

$$k = \omega / \overline{c} \tag{2.56}$$

and the damping coefficient $\alpha_p = \omega^2 \overline{\nu} / \{2 \overline{c}^3 [4/3 + (\gamma - 1)/Pr]\}$ we can rewrite Eqs. (2.52) as $k_p = \pm k(1 + i\alpha_p / k)$, i.e. λ is the characteristic length scale and visco-thermal attenuation becomes important only when waves propagate over distances of the order of magnitude of $1/\alpha_p$ (for air at room temperature and a frequency of $1kHz$ one has $1/\alpha_p \simeq 70km$). Finally, when a harmonic solution (2.41) is searched for $\mathbf{u}'_\Omega$ using Eq. (2.40), the characteristic equation gives the wave numbers $\mp\sqrt{\omega / 2\,\overline{\nu}}(1 - i)$ that define the viscous length scale

$$\delta_v = \sqrt{2\ \overline{\nu}/\omega} \tag{2.57}$$

Therefore, *shear mode* perturbations $\mathbf{u}'_\Omega$ generated at boundary walls become negligible outside of the viscous boundary layer of thickness δ_v. In conclusion, being the attenuation of the propagational mode very small and being the diffusion and shear modes damped within the thermal and viscous boundary layers, the total solution may be represented by the inviscid form of Eqs. (2.53)-(2.55)

$$\frac{\partial^2 p'_p}{\partial t^2} - \overline{c}^2 \nabla^2 p'_p = 0 \tag{2.58}$$

$$\overline{\rho} \frac{\partial \mathbf{u}'_p}{\partial t} + \nabla p'_p = 0 \tag{2.59}$$

$$S'_p = 0 \tag{2.60}$$

where Eq. (2.58) is the wave equation of classical acoustics [51]. By transforming to the frequency domain with $\varphi'(\mathbf{x}, t) = \widehat{\varphi}(\mathbf{x}) \exp(i\omega t)$, Eqs. (2.58) and (2.59) become

$$\nabla^2 \widehat{p}_p + k^2 \widehat{p}_p = 0 \tag{2.61}$$

$$\widehat{\mathbf{u}}_p = -\frac{1}{i\,\omega\,\overline{\rho}} \nabla \widehat{p}_p \tag{2.62}$$

$$\widehat{S}_p = 0 \tag{2.63}$$

where Eq. (2.61) is the Helmholtz equation.
However, the diffusion, propagational and shear modes can not be separately solved when boundary conditions introduce mode coupling (this happens when constrains on some flow variables can not be formulated separately upon the individual mode [29]). In case of solid walls, zero fluctuations of temperature and velocity are prescribed as boundary conditions. In general the propagational mode may be computed when assigning its velocity component normal to the wall $(\widehat{\mathbf{u}}_p \cdot \mathbf{n})_w$, being $\mathbf{n}$ the outward normal to the wall [such a condition is linked to a pressure gradient condition by means of Eq. (2.55)]. To force to zero the global velocity component normal to the wall, one must impose $(\widehat{\mathbf{u}}_p \cdot \mathbf{n})_w = -[(\widehat{\mathbf{u}}_d \cdot \mathbf{n})_w + (\widehat{\mathbf{u}}_\Omega \cdot \mathbf{n})_w]$ where $(\widehat{\mathbf{u}}_d \cdot \mathbf{n})_w$ and $(\widehat{\mathbf{u}}_\Omega \cdot \mathbf{n})_w$ are the velocity components normal to the wall induced by diffusion and shear mode respectively. $(\widehat{\mathbf{u}}_d \cdot \mathbf{n})_w$ is associated to the diffusion

mode solution obtained by forcing zero temperature fluctuations on the wall. $(\widehat{\mathbf{u}}_\Omega \cdot \mathbf{n})_w$ originates when the shear mode solution is adjusted to satisfy $(\widehat{\mathbf{u}}_\Omega \cdot \mathbf{t})_w = -(\widehat{\mathbf{u}}_p \cdot \mathbf{t})_w$, being $(\widehat{\mathbf{u}}_p \cdot \mathbf{t})_w$ the velocity component tangential to the wall induced by the propagational mode. As a result of this mode coupling, the propagational mode equation (2.61) must be solved using the boundary condition

$$\frac{\widehat{p}_p}{\widehat{\mathbf{u}}_p \cdot \mathbf{n}} = Z_w\,(\omega\,,\,\mathbf{x}) \tag{2.64}$$

where Z_w is the boundary impedance that depends on the solution of the diffusion and shear modes inside the boundary layers (when neglecting boundary layer effects, the solid wall impedance becomes $Z_w = \infty$). For instance, for plane waves incident on a plane solid wall at angle of incidence θ with respect to the normal to the plane, one finds [29]

$$Z_w = \overline{\rho}\;\overline{c}\;\frac{1+i}{\sqrt{2}}\,Sh\left(\frac{\gamma-1}{\sqrt{Pr}} + \sin^2\theta\right)^{-1} \tag{2.65}$$

2.3.2 Capillary duct

When considering a duct where the thicknesses of thermal and viscous boundary layers are not small with respect to the duct radius ("capillary duct"), the propagational mode alone can not approximate the global solution. This is the case of the axial-symmetric perturbation of a fluid at rest in a cylindrical tube of radius a, when a is much smaller than the acoustic wavelength λ [see Eq. (2.51)]. To study this problem, the governing equations (2.30)-(2.32) are written in cylindrical coordinates as

$$\frac{\partial\,\rho'}{\partial t} = -\,\overline{\rho}\left[\frac{\partial\,u'_x}{\partial x} + \frac{1}{r}\,\frac{\partial r\,u'_r}{\partial r}\right] \tag{2.66}$$

$$\frac{\partial\,u'_x}{\partial t} = -\frac{1}{\overline{\rho}}\,\frac{\partial\,p'}{\partial x} + \overline{\nu}\left[\frac{\partial^2\,u'_x}{\partial x^2} + \frac{1}{r}\,\frac{\partial}{\partial r}\left(r\,\frac{\partial\,u'_x}{\partial r}\right)\right] + \frac{1}{3}\,\overline{\nu}\,\frac{\partial}{\partial x}\left[\frac{\partial\,u'_x}{\partial x} + \frac{1}{r}\,\frac{\partial r\,u'_r}{\partial r}\right] \tag{2.67}$$

$$\frac{\partial\,u'_r}{\partial t} = -\frac{1}{\overline{\rho}}\frac{\partial\,p'}{\partial r} + \overline{\nu}\left[\frac{\partial^2\,u'_r}{\partial x^2} + \frac{1}{r}\frac{\partial}{\partial r}\left(r\frac{\partial\,u'_r}{\partial r}\right) - \frac{u'_r}{r^2}\right] + \frac{1}{3}\,\overline{\nu}\,\frac{\partial}{\partial r}\left[\frac{\partial\,u'_x}{\partial x} + \frac{1}{r}\frac{\partial r\,u'_r}{\partial r}\right] \tag{2.68}$$

$$\overline{\rho}\,C_p\,\frac{\partial\,T'}{\partial t} = \frac{\partial\,p'}{\partial t} + \kappa\,\left[\frac{\partial^2\,T'}{\partial x^2} + \frac{1}{r}\,\frac{\partial}{\partial r}\left(r\,\frac{\partial\,T'}{\partial r}\right)\right] \tag{2.69}$$

where x is the axial coordinate and r the radial coordinate. The solution of Eqs. (2.66)-(2.69) is searched in the harmonic form $\varphi'(\mathbf{x},t) = \widehat{\varphi}(\mathbf{x})\exp(i\omega t)$ by introducing the dimensionless quantities

$$\widetilde{\rho} = \widehat{\rho}/\,\overline{\rho}\,,\quad \widetilde{u}_x = \widehat{u}_x/\,\overline{c}\,,\quad \widetilde{u}_r = \widehat{u}_r/\,\overline{c}\,,\quad \widetilde{p} = \widehat{p}/\,\overline{p}\,,\quad \widetilde{T} = \widehat{T}/\,\overline{T} \tag{2.70}$$

and the dimensionless coordinates

$$\xi = k\,x\;,\qquad \eta = \frac{r}{a} \tag{2.71}$$

It gives

$$i\,He\;\widetilde{\rho} = -\left[He\,\frac{\partial\,\widetilde{u}_x}{\partial\xi} + \frac{1}{\eta}\,\frac{\partial\eta\,\widetilde{u}_r}{\partial\eta}\right] \tag{2.72}$$

$$i\,\widetilde{u}_x = -\frac{1}{\gamma}\,\frac{\partial\,\widetilde{p}}{\partial\xi} + \frac{1}{Sd^2}\left\{\left[He^2\,\frac{\partial^2\,\widetilde{u}_x}{\partial\xi^2} + \frac{1}{\eta}\,\frac{\partial}{\partial\eta}\left(\eta\,\frac{\partial\,\widetilde{u}_x}{\partial\eta}\right)\right] + \right.$$
$$\left. + \frac{1}{3}He\,\frac{\partial}{\partial\xi}\left[He\,\frac{\partial\,\widetilde{u}_x}{\partial\xi} + \frac{1}{\eta}\,\frac{\partial\eta\,\widetilde{u}_r}{\partial\eta}\right]\right\} \tag{2.73}$$

$$i\,He\,\widetilde{u}_r = -\frac{1}{\gamma}\,\frac{\partial\,\widetilde{p}}{\partial\eta} + \frac{He}{Sd^2}\left\{\left[He^2\,\frac{\partial^2\,\widetilde{u}_r}{\partial\xi^2} + \frac{1}{\eta}\,\frac{\partial}{\partial\eta}\left(\eta\,\frac{\partial\,\widetilde{u}_r}{\partial\eta}\right) - \frac{\widetilde{u}_r}{\eta^2}\right] + \right.$$
$$\left. + \frac{1}{3}\,\frac{\partial}{\partial\eta}\left[He\,\frac{\partial\,\widetilde{u}_x}{\partial\xi} + \frac{1}{\eta}\,\frac{\partial\eta\,\widetilde{u}_r}{\partial\eta}\right]\right\} \tag{2.74}$$

$$i\,\widetilde{T} = i\,\frac{\gamma-1}{\gamma}\,\widetilde{p} + \frac{1}{Pr\,Sd^2}\,\left[He^2\,\frac{\partial^2\,\widetilde{T}}{\partial\xi^2} + \frac{1}{\eta}\,\frac{\partial}{\partial\eta}\left(\eta\,\frac{\partial\,\widetilde{T}}{\partial\eta}\right)\right] \tag{2.75}$$

where the duct Helmholtz and Stokes numbers are given respectively by

$$He = k\,a\,, \qquad Sd = a\,\sqrt{\omega/\,\overline{\nu}} \tag{2.76}$$

The related boundary conditions are $\widetilde{u}_x = \widetilde{u}_r = \widetilde{T} = 0$ at $\eta = 1$ and $\widetilde{u}_r = 0$ at $\eta = 0$. Being the duct radius much smaller than acoustic wavelengths, one has $He \ll 1$. Moreover, the radial component of velocity is assumed to be much smaller than the axial component, i.e. $\widetilde{u}_r \ll \widetilde{u}_x$.[6] Using these assumptions, Eqs. (2.72)-(2.75) are reduced to

$$i\,He\,\widetilde{\rho} = -\left[He\,\frac{\partial\,\widetilde{u}_x}{\partial\xi} + \frac{1}{\eta}\,\frac{\partial(\eta\,\widetilde{u}_r)}{\partial\eta}\right] \tag{2.77}$$

$$i\,\widetilde{u}_x = -\frac{1}{\gamma}\,\frac{\partial\,\widetilde{p}}{\partial\xi} + \frac{1}{Sd^2}\,\frac{1}{\eta}\,\frac{\partial}{\partial\eta}\left(\eta\,\frac{\partial\,\widetilde{u}_x}{\partial\eta}\right) \tag{2.78}$$

$$\frac{\partial\,\widetilde{p}}{\partial\eta} = 0 \tag{2.79}$$

$$i\,\widetilde{T} = i\,\frac{\gamma-1}{\gamma}\,\widetilde{p} + \frac{1}{Pr\,Sd^2}\,\frac{1}{\eta}\,\frac{\partial}{\partial\eta}\left(\eta\,\frac{\partial\,\widetilde{T}}{\partial\eta}\right) \tag{2.80}$$

The solution of Eqs. (2.77)-(2.80) is given by [53]

$$\frac{d^2\,\widehat{p}}{dx^2} - \Gamma^2\,k^2\,\widehat{p} = 0 \tag{2.81}$$

$$\widehat{u}_A = \frac{1}{i\,\omega\,\overline{\rho}}\left(\frac{\gamma}{n\,\Gamma^2}\right)\frac{d\,\widehat{p}}{dx} \tag{2.82}$$

$$\frac{\widehat{T}_A}{\overline{T}} = \frac{n-1}{n}\,\frac{\widehat{p}}{\overline{p}} \tag{2.83}$$

[6] The analysis performed in Ref. [53] indicates that $\widetilde{u}_r \ll \widetilde{u}_x$ is equivalent to $Sh \gg 1$.

where $\widehat{\varphi}_A = 1/(\pi a^2) \int_0^a \widehat{\varphi}\, 2\pi r dr$ represents the cross-sectional average value and

$$n = \left[1 + \frac{\gamma - 1}{\gamma} \frac{J_2(i^{3/2}\sqrt{Pr}\, Sd)}{J_0(i^{3/2}\sqrt{Pr}\, Sd)}\right]^{-1}, \qquad \Gamma = \sqrt{\frac{\gamma\, J_0(i^{3/2}\, Sd)}{n\, J_2(i^{3/2}\, Sd)}} \tag{2.84}$$

with J_m Bessel function of first kind of order m. When $Sd \to \infty$, one has

$$\lim_{Sd\to\infty} \Gamma = i \tag{2.85}$$

that reduces Eq. (2.81) to the one-dimensional Helmholtz equation having the plane wave solution

$$\frac{\widehat{p}}{\overline{\rho}\,\overline{c}} = \mathcal{F}\, \exp(-i\, k\, x) + \mathcal{G}\, \exp(i\, k\, x) \tag{2.86}$$

$$\widehat{u} = \mathcal{F}\, \exp(-i\, k\, x) - \mathcal{G}\, \exp(i\, k\, x) \tag{2.87}$$

(the Riemann invariants $\mathcal{F}$ and $\mathcal{G}$ are determined by the boundary conditions in the x-direction). For large values of Sd, Eqs. (2.84) give the Kirchhoff solution [51], [53]

$$n \simeq \gamma\ , \qquad \Gamma \simeq i + \frac{1+i}{\sqrt{2}\, Sd}\left(1 + \frac{\gamma - 1}{\sqrt{Pr}}\right) \tag{2.88}$$

Using Eqs. (2.88), the general solution of Eqs. (2.81)-(2.83) writes as

$$\frac{\widehat{p}}{\overline{\rho}\,\overline{c}} = \mathcal{F}\, \exp(-\Gamma\, k\, x) + \mathcal{G}\, \exp(\Gamma\, k\, x) \tag{2.89}$$

$$\widehat{u}_A = \frac{i}{\Gamma}\left[\mathcal{F}\, \exp(-\Gamma\, k\, x) - \mathcal{G}\, \exp(\Gamma\, k\, x)\right] \tag{2.90}$$

$$\frac{\widehat{T}_A}{\overline{T}} = \frac{\gamma - 1}{\gamma}\, \frac{\widehat{p}}{\overline{p}} \tag{2.91}$$

where Eq. (2.91) represents the isentropic flow condition [see Eqs. (2.33)-(2.34)]. The damping coefficient α_d of the duct is defined by the expression

$$\alpha_d = \frac{\sqrt{\omega\, \overline{\nu}}}{\sqrt{2}\, \overline{c}\, a}\left(1 + \frac{\gamma - 1}{\sqrt{Pr}}\right) \tag{2.92}$$

that usually satisfies the condition $\alpha_d \ll k$ (e.g. $\alpha_d/k \simeq 10^{-4}$ for $1kHz$ waves in a duct of radius $a = 0.1m$ filled with air at room temperature). Using the approximation $\Gamma \simeq i + \alpha_d/k$, Eq. (2.81) is rewritten as

$$\frac{d^2\, \widehat{p}}{dx^2} + k^2\, \widehat{p} - 2\, i\, \alpha_d\, k\, \widehat{p} = 0 \tag{2.93}$$

that has the general solution

$$\frac{\widehat{p}}{\overline{\rho}\,\overline{c}} = \mathcal{F}\, \exp(-i\, k\, x)\, \exp(-\alpha_d\, x) + \mathcal{G}\, \exp(i\, k\, x)\, \exp(\alpha_d\, x) \tag{2.94}$$

Finally, for small values of Sd one has $\lim_{Sd\to 0} n = 1$ that, according to Eq. (2.83), corresponds to the isothermal condition. Moreover $\Gamma = 2(1+i)\sqrt{\gamma}/Sd$ and Eq. (2.82) gives $u_A = -a^2/(8\,\mu) dp/dx$, which is the Poiseuille's resistance for laminar flows in tubes.

2.4 Mode Decomposition in Uniform Mean Flows

The approach illustrated in Section 2.3.1 may be extended to the case of uniform mean flow ($\overline{\mathbf{u}} = const$) by replacing Eq. (2.41) and the second of Eqs. (2.42) with $\varphi'(\mathbf{x}, t) = \breve{\varphi} \exp[(s + \mathbf{k} \cdot \overline{\mathbf{u}})\, t - i\, \mathbf{k} \cdot \mathbf{x}]$ and $\overline{D}\,\varphi'/Dt = s\,\varphi'$ respectively, where

$$\frac{\overline{D}\,\varphi'}{Dt} = \frac{\partial\,\varphi'}{\partial t} + \overline{\mathbf{u}} \cdot \nabla\,\varphi' \tag{2.95}$$

is the Lagrangian derivative with respect to the mean flow. Thus, in the domain outside of the thermal and viscous boundary layers one can use the inviscid form of Eqs. (2.35), (2.36), (2.39) and (2.40) where the time derivatives are replaced by $\overline{D}/Dt$. Moreover, the perturbation flow may be decomposed into *acoustic*, *entropy* and *vorticity* modes defined as follows [10].

Acoustic mode

$$\frac{\overline{D}^2\,p'}{Dt^2} - \overline{c}^2\,\nabla^2\,p' = 0 \tag{2.96}$$

$$\overline{\rho}\,\frac{\overline{D}\,\mathbf{u}'_i}{Dt} + \nabla\,p' = 0 \tag{2.97}$$

$$\nabla \times \mathbf{u}'_i = 0 \tag{2.98}$$

Entropy mode

$$\frac{\overline{D}\,S'}{Dt} = 0 \tag{2.99}$$

Vorticity mode

$$\frac{\overline{D}\,\mathbf{u}'_\Omega}{Dt} = 0 \tag{2.100}$$

$$\nabla \cdot \mathbf{u}'_\Omega = 0 \tag{2.101}$$

Eq. (2.99) accounts for the convection of entropy waves that are generated at the domain inlet and propagate in the region outside of the boundary layers. The perturbation flow field upstream of the flame is usually assumed to be homentropic, i.e. $S' = 0$. On the contrary, downstream of the flame the heat release process acts as a time-dependent entropy boundary. In this case Eq. (2.99) describes the propagation of "hot spots" convected towards the combustor exit by the mean flow. The curl of Eq. (2.100) yields $\overline{D}\,\boldsymbol{\Omega}'/Dt = 0$, which describes the convection of the first-order incompressible vorticity $\boldsymbol{\Omega}' = \nabla \times \mathbf{u}'$ possibly introduced in the domain by inlet boundary conditions (e.g. at the downstream side of flame front). Note that the equation $\overline{D}\,\boldsymbol{\Omega}'/Dt = 0$ may be also obtained as first order perturbation of the inviscid form of the incompressible vorticity equation (2.22).

Higher order perturbation equations may be derived by replacing Eq. (2.28) with the expansion

$$\varphi\left(\mathbf{x},t\right)=\overline{\varphi}\left(\mathbf{x}\right)+\varphi^{(1)}\left(\mathbf{x},t\right)+\varphi^{(2)}\left(\mathbf{x},t\right)+\varphi^{(3)}\left(\mathbf{x},t\right)+\ldots \tag{2.102}$$

where $\varphi^{(m)}=\mathcal{O}(\varrho^m)$ with $\varrho\ll 1$ [in Eq. (2.102) we have used the notation $\varphi^{(1)}\equiv\varphi'$]. At the generic order m, Eqs. (2.96), (2.99) and (2.100) write as [10]

$$\frac{\overline{D}^2 p^{(m)}}{Dt^2}-\overline{c}^{\,2}\nabla^2 p^{(m)}=\gamma\,\overline{p}F^{(m)} \tag{2.103}$$

$$\frac{1}{C_p}\frac{\overline{D}S^{(m)}}{Dt}=q^{(m)} \tag{2.104}$$

$$\frac{\overline{D}\boldsymbol{\Omega}^{(m)}}{Dt}=\nabla\times\mathbf{f}^{(m)} \tag{2.105}$$

The left-hand sides (homogeneous parts) of Eqs. (2.103)-(2.105) are the same for all values of m, whereas the source terms on the right-hand sides depend on the order m of the perturbation system. At first order one has $F^{(1)}=q^{(1)}=\mathbf{f}^{(1)}=0$ [see Eqs. (2.96), (2.99) and (2.100)]. At order $m>1$, the source terms are functions of the products of the j-solutions with $j<m$ and mode coupling arises. In particular, for $m=2$ the second-order source terms $F^{(2)}$, $q^{(2)}$ and $\mathbf{f}^{(2)}$ are expressed as the sum of 18 interaction terms that are functions of first-order variables [10]. The second-order interaction terms are reported in Tab. 2.1 and discussed in detail in the following.

Acoustic-acoustic interaction
The interaction of the first-order acoustic mode with itself gives a contribution to the second-order acoustic mode only. When integrating the acoustic-acoustic interaction term on the entire domain and zero acoustic velocity is assumed at boundaries, the contribution from the terms $\nabla\cdot\nabla\cdot\mathbf{u}'_i\,\mathbf{u}'_i$ and $\nabla^2 p'^{\,2}$ is zero. That means that both the terms are just responsible for sound scattering by sound or nonlinear distortion of sound waves. On the contrary, the volume integral of $\partial^2 p'^{\,2}/\partial t^2$ is different from zero and is responsible for a net sound generation.

Acoustic-vorticity interaction
When velocity fluctuations are zero at boundaries, the integration of the term $\nabla\cdot\nabla\cdot\mathbf{u}'_\Omega\,\mathbf{u}'_i$ on the domain of interest vanishes. Thus, the vorticity-acoustic contribution to the acoustic source produces just a scattering of sound by rotational inhomogeneity of velocity. The vorticity-acoustic contribution to the generation of vorticity accounts for the production of vorticity by sound waves.

Acoustic-entropy interaction
The effects of the acoustic-entropy interaction are scattering of sound by temperature inhomogeneity, transfer of heat by sound waves and generation of vorticity by the interaction of entropy and pressure.

Entropy-vorticity interaction
The vorticity-entropy interaction leads only to a transfer of heat by vorticity in the entropy mode.

	Acoustic source $F^{(2)}$	Entropy source $q^{(2)}$	Vorticity source $\nabla \times \mathbf{f}^{(2)}$
Acoustic-acoustic	$\nabla \cdot \nabla \cdot \mathbf{u}'_i \mathbf{u}'_i +$ $+\nabla^2 p'^2/\overline{\rho} +$ $+(\gamma-1)/(2\gamma\overline{p})\ \partial^2 p'^2/\partial t^2$	0	0
Acoustic-vorticity	$2\ \nabla \cdot \nabla \cdot \mathbf{u}'_\Omega \mathbf{u}'_i$	0	$\nabla \times (\mathbf{u}'_i \times \boldsymbol{\Omega}')$
Acoustic-entropy	$\frac{1}{C_p}\frac{\partial}{\partial t}\nabla \cdot (S' \mathbf{u}'_i)$	$-\frac{1}{C_p}\mathbf{u}'_i \cdot \nabla S'$	$-\frac{1}{\overline{\rho} C_p}\nabla S' \times \nabla p'$
Entropy-entropy	0	0	0
Entropy-vorticity	0	$-\frac{1}{C_p}\mathbf{u}'_\Omega \cdot \nabla S'$	0
Vorticity-vorticity	$\nabla \cdot \nabla \cdot \mathbf{u}'_\Omega \mathbf{u}'_\Omega$	0	$\nabla \times (\mathbf{u}'_\Omega \times \boldsymbol{\Omega}')$

Table 2.1: Second-oder source terms.

Vorticity-vorticity interaction
The vorticity-vorticity interaction generates the source term $\nabla \cdot \nabla \cdot \mathbf{u}'_\Omega \mathbf{u}'_\Omega$ in the acoustic mode. This term represents the Lighthill's acoustic analogy, which is used to model the nonlinear generation of sound due to an incompressible vorticity field [54], [55].[7] When the other vorticity-vorticity interaction term $\nabla \times (\mathbf{u}'_\Omega \times \boldsymbol{\Omega}')$ is written as $\boldsymbol{\Omega}' \cdot \nabla \mathbf{u}'_\Omega - \mathbf{u}'_\Omega \cdot \nabla \boldsymbol{\Omega}'$, then the vorticity equation (2.105) with $m = 2$ corresponds to the nonlinear perturbation of the inviscid form of Eq. (2.22).

2.5 Linearized Navier-Stokes Equations

In this Section we consider the general case of a non-uniform mean flow. When the perturbation (2.28) and the nondimensionalization approach described in Section 2.3 are used into Eqs. (2.1)-(2.3), at first order one obtains

$$\frac{\partial \rho'}{\partial t} + \nabla \cdot (\overline{\rho}\, \mathbf{u}' + \rho' \overline{\mathbf{u}}) = 0 \tag{2.106}$$

[7]The Lighthill's acoustic analogy neglects the feedback of the acoustic field on the incompressible flow field and is employed when the source region is limited in space and the surrounding fluid is stagnant and unbounded (e.g. noise produced by a turbulent jet discharging in a uniform steady atmosphere).

$$\frac{\partial\,(\rho\,\mathbf{u})'}{\partial t}+\nabla\cdot\left[\,\overline{\rho}\left(\,\overline{\mathbf{u}}\;\mathbf{u}'+\;\mathbf{u}'\,\overline{\mathbf{u}}\right)+\;\rho'\,\overline{\mathbf{u}}\;\overline{\mathbf{u}}\,\right]+\nabla\,p'=\nabla\cdot\,\boldsymbol{\tau}'\tag{2.107}$$

$$\overline{\rho}\;\overline{T}\,\frac{D\,S'}{Dt}+\;(\rho\,T\,\mathbf{u})'\cdot\nabla\,\overline{S}=\;(\boldsymbol{\tau}:\nabla\mathbf{u})'+\kappa\,\nabla^2\,T'+\;Q'\tag{2.108}$$

The system (2.106)-(2.108) is closed by the perturbations of Eqs. (2.4) and (2.5), that are given by Eqs. (2.33) and (2.34) respectively. Note that Eqs. (2.106)-(2.108) are obtained by using reference speed of sound and acoustic wavelength to nondimensionalize mean flow velocity and mean flow spacial gradients respectively, i.e. we have assumed that the flow velocity is of the same order of magnitude as the speed of sound. In alternative to Eq (2.108), the perturbation of Eq. (2.12) may be employed. It reads as

$$\frac{\partial\,(\rho\,E)'}{\partial t}+\nabla\cdot\left[\,\overline{\rho}\;\overline{\mathbf{u}}\;B'+\left(\,\overline{\rho}\;\mathbf{u}'+\;\rho'\,\overline{\mathbf{u}}\right)\;\overline{B}\,\right]=\nabla\cdot\left(\,\mathbf{u}'\cdot\,\overline{\boldsymbol{\tau}}+\;\overline{\mathbf{u}}\cdot\,\boldsymbol{\tau}'\right)+\kappa\,\nabla^2\,T'+\;Q'\tag{2.109}$$

where the fluctuating total energy E' and the fluctuating total enthalpy B' are given by

$$E'=C_v\;T'+\;\overline{\mathbf{u}}\cdot\,\mathbf{u}'\,,\qquad\qquad B'=C_p\;T'+\;\overline{\mathbf{u}}\cdot\,\mathbf{u}'\tag{2.110}$$

Using Eqs. (2.33)-(2.34) into Eqs. (2.106)-(2.107) and eliminating $\overline{\mathbf{u}}\cdot\nabla\,\overline{\mathbf{u}}$ by means of the mean flow momentum equation, one finds[8]

$$\frac{\partial\,p'}{\partial t}+\;\overline{c}^{\,2}\,\nabla\cdot\left(\,\overline{\rho}\;\mathbf{u}'+\frac{\overline{\mathbf{u}}}{\overline{c}^{\,2}}\;p'\right)=\;\overline{c}^{\,2}\,\frac{\overline{\rho}}{C_p}\,\frac{\overline{D}\,S'}{Dt}\tag{2.111}$$

$$\frac{\partial\,\mathbf{u}'}{\partial t}+\nabla\left(\frac{p'}{\overline{\rho}}+\;\overline{\mathbf{u}}\cdot\,\mathbf{u}'\right)=\;T'\,\nabla\,\overline{S}-\;S'\,\nabla\,\overline{T}-\;(\boldsymbol{\Omega}\times\mathbf{u})'+\left(\frac{\nabla\cdot\boldsymbol{\tau}}{\rho}\right)'\tag{2.112}$$

[note that Eq. (2.112) represents the perturbation of the Crocco's equation (2.27)]. When the decomposition (2.14) is applied to both the velocity perturbation $\mathbf{u}'$ and the right-hand side of Eq. (2.112), Eqs. (2.111)-(2.112) may be rewritten as

$$\frac{\partial\,p'}{\partial t}+\;\overline{c}^{\,2}\,\nabla\cdot\left(\,\overline{\rho}\;\mathbf{u}'_i+\frac{\overline{\mathbf{u}}}{\overline{c}^{\,2}}\;p'\right)=\;F'\tag{2.113}$$

$$\frac{\partial\,\mathbf{u}'_i}{\partial t}+\nabla\left(\frac{p'}{\overline{\rho}}+\;\overline{\mathbf{u}}\cdot\,\mathbf{u}'_i\right)=\nabla\,\phi'\tag{2.114}$$

$$\frac{\partial\,\mathbf{u}'_\Omega}{\partial t}=\nabla\times\;\boldsymbol{\pi}'\tag{2.115}$$

where

$$F'=\overline{c}^{\,2}\left(\frac{\overline{\rho}}{C_p}\,\frac{\overline{D}\,S'}{Dt}-\;\mathbf{u}'_\Omega\cdot\nabla\,\overline{\rho}\right)\tag{2.116}$$

$$\nabla^2\,\phi'=\nabla\cdot\,\mathbf{f}'\,,\qquad\nabla^2\,\boldsymbol{\pi}'=-\nabla\times\,\mathbf{f}'\,,\qquad\nabla\cdot\,\boldsymbol{\pi}'=0\tag{2.117}$$

[8] $\mathbf{a}\cdot\nabla\mathbf{b}+\mathbf{b}\cdot\nabla\mathbf{a}=\nabla(\mathbf{a}\cdot\mathbf{b})+(\nabla\times\mathbf{a})\times\mathbf{b}+(\nabla\times\mathbf{b})\times\mathbf{a}$

with

$$\mathbf{f}' = T' \nabla \overline{S} - S' \nabla \overline{T} - \overline{\mathbf{\Omega}} \times \mathbf{u}'_i - \overline{\mathbf{u}} \cdot \nabla \mathbf{u}'_\Omega - \mathbf{u}'_\Omega \cdot \nabla \overline{\mathbf{u}} + \left(\frac{\nabla \cdot \boldsymbol{\tau}}{\rho} \right)' \tag{2.118}$$

The curl of Eq. (2.114) and the divergence of Eq. (2.115) give, respectively, $\partial t / \partial (\nabla \times \mathbf{u}'_i) = 0$ and $\partial t / \partial (\nabla \cdot \mathbf{u}'_\Omega) = 0$, i.e. an initially irrotational field $\mathbf{u}'_i$ remains irrotational and an initially solenoidal field $\mathbf{u}'_\Omega$ remains solenoidal. In Eqs. (2.113) and (2.114) the terms F' and $\nabla \phi'$ are the source terms for the acoustic mode $(p', \mathbf{u}'_i)$ propagating in the non-uniform mean flow $\overline{\mathbf{u}}$ [8]. In particular, in gas turbine combustors contributions to F' and $\nabla \phi'$ are given by

(i) solenoidal velocity perturbations related to turbulent fluctuations;

(ii) entropy fluctuations induced by unsteady combustion;

(iii) interaction between acoustic velocity and mean flow vorticity typical of swirl flows.

In general, it is not possible to reduce the system (2.113)-(2.114) to a wave equation. In the next Sections an approximate wave equation is derived under the hypothesis of low Mach number mean flow.

2.6 Low Mach number Flows

In gas turbine combustion systems the Mach number is usually small and thus it is of particular interest the case of low Mach number limit (the low Mach number assumption neglects Mach number effects occurring in the area contraction possibly located at the combustor exit, which may be modeled by means of a "compact nozzle" boundary condition when nozzle dimensions are small in comparison with acoustic wavelengths [56]). To apply the low Mach number limit, first the flow variables are nondimensionalized by using the reference pressure p_∞, the reference temperature T_∞, the reference burner flow velocity u_∞, the reference temperature jump across the flame ΔT_∞ and the reference flame thickness δ_{f_∞}. The nondimensional variables are expressed as

$$\widetilde{p} = \frac{p}{p_\infty} , \qquad \widetilde{T} = \frac{T}{T_\infty} , \qquad \widetilde{\rho} = \frac{\rho}{\rho_\infty} , \qquad \widetilde{S} = \frac{S}{C_p} , \qquad \widetilde{\mathbf{u}} = \frac{\mathbf{u}}{u_\infty} , \qquad \widetilde{Q} = \frac{Q}{Q_\infty} \tag{2.119}$$

where $\rho_\infty = p_\infty / (\mathcal{R} T_\infty)$ is the reference density and $Q_\infty = \rho_\infty u_\infty \mathcal{R} \Delta T_\infty / \delta_{f_\infty}$ the reference heat release. The nondimensional variables defined by Eqs. (2.119) remain $\mathcal{O}(1)$ for any low value of the reference Mach number

$$M_\infty = \frac{u_\infty}{c_\infty} \tag{2.120}$$

where $c_\infty = \sqrt{\gamma \, p_\infty / \rho_\infty}$ is the reference speed of sound.[9] To avoid the dependence on γ, we define

$$\epsilon = \sqrt{\gamma} \, M_\infty \tag{2.121}$$

The time scale of flow oscillations is supposed to be dominated by the evolution of the flame front and the reference time t_∞ of heat release oscillations is taken as a burner characteristic convective time.

[9] If the flow velocity is nondimensionalized using the speed of sound thus $|\mathbf{u}|/c_\infty \to 0$ when $M_\infty \to 0$, i.e. the low Mach number limit is not applicable.

Therefore we use $t_\infty = L_\infty/u_\infty$, with L_∞ burner length related to the physical mechanism responsible for heat release unsteadiness (e.g. when heat release oscillations are induced by vortex shedding occurring at burner exit, thus L_∞ is approximately given by the burner diameter [57]). By introducing the wavelength $\lambda = c_\infty/\omega$ with $\omega = 1/t_\infty$, then the condition $M_\infty \to 0$ may be written as $L_\infty \ll \lambda$ that means our analysis is restricted to a low-frequency range. The time scale L_∞/u_∞ and the length scale L_∞ define the time and length scale variables given respectively by

$$\widetilde{t} = t/(L_\infty/u_\infty)\,, \qquad \widetilde{\mathbf{x}} = \mathbf{x}/L_\infty \tag{2.122}$$

The nondimensional form of Eqs. (2.10), (2.11), (2.13) and (2.4) writes as

$$\frac{\partial \widetilde{\rho}}{\partial \widetilde{t}} + \widetilde{\nabla}\cdot(\widetilde{\rho}\,\widetilde{\mathbf{u}}) = 0 \tag{2.123}$$

$$\frac{\partial(\widetilde{\rho}\,\widetilde{\mathbf{u}})}{\partial \widetilde{t}} + \widetilde{\nabla}\cdot(\widetilde{\rho}\,\widetilde{\mathbf{u}}\,\widetilde{\mathbf{u}}) + \frac{1}{\epsilon^2}\,\widetilde{\nabla}\widetilde{p} = \frac{1}{Re_\infty}\,\widetilde{\nabla}\cdot\widetilde{\boldsymbol{\tau}} \tag{2.124}$$

$$\frac{\partial \widetilde{p}}{\partial \widetilde{t}} + \widetilde{\mathbf{u}}\cdot\widetilde{\nabla}\widetilde{p} + \gamma\,\widetilde{p}\,\widetilde{\nabla}\cdot\widetilde{\mathbf{u}} = \epsilon^2\,\frac{\gamma-1}{Re_\infty}\,\widetilde{\boldsymbol{\tau}} : \widetilde{\nabla}\widetilde{\mathbf{u}} + \frac{\gamma}{Pr\,Re_\infty}\,\widetilde{\nabla}^2\widetilde{T} + (\gamma-1)\,\Sigma_\infty\,\widetilde{Q} \tag{2.125}$$

$$\widetilde{p} = \widetilde{\rho}\,\widetilde{T} \tag{2.126}$$

where $\widetilde{\boldsymbol{\tau}} = [(\widetilde{\nabla}\widetilde{\mathbf{u}} + \widetilde{\nabla}\widetilde{\mathbf{u}}^T) - 2/3\,(\widetilde{\nabla}\cdot\widetilde{\mathbf{u}})\,\mathbf{I}]$. In Eqs. (2.124) and (2.125), the reference Reynolds number Re_∞, the Prandtl number Pr and the heat release number Σ_∞ are defined as

$$Re_\infty = \frac{\rho_\infty\,u_\infty\,L_\infty}{\mu}\,, \qquad Pr = \frac{\mu\,C_p}{\kappa}\,, \qquad \Sigma_\infty = \frac{\Delta T_\infty/T_\infty}{\delta_{f\,\infty}/L_\infty} \tag{2.127}$$

2.6.1 Asymptotic analysis

When the low Mach number limit $\epsilon \to 0$ is applied to Eqs. (2.123)-(2.126), a singularity arises in Eq. (2.124) because of the $\mathcal{O}(\epsilon^{-2})$ pressure gradient term. By assuming that the low Mach number asymptotic analysis is a regular perturbation problem, the singularity may be removed by expanding the generic nondimensional variable $\widetilde{\varphi}$ in asymptotic series of the form [58], [59], [60]

$$\widetilde{\varphi} = \widetilde{\varphi}_0 + \epsilon\,\widetilde{\varphi}_1 + \epsilon^2\,\widetilde{\varphi}_2 + \ldots \tag{2.128}$$

In order to apply correctly the low Mach number asymptotic expansion, the order of magnitude of the nondimensional numbers (2.127) must be specified with respect to ϵ.[10] Even though in general $1/Re_\infty \ll \epsilon$, viscous and heat conduction terms are retained into the asymptotic expansion of Eqs. (2.124)-(2.125) because they become $\mathcal{O}(1)$ inside the boundary layer, where the length scale of the diffusive effects is of the order of L_∞/Re_∞ [45]. Furthermore, the heat release terms $\widetilde{Q}_n$ may be included in the $\mathcal{O}(\epsilon^n)$ energy equations if we assume $\Sigma_\infty \gg \epsilon$, i.e.

$$\delta_{f\,\infty} \ll \lambda\,\frac{\Delta T_\infty}{T_\infty} \tag{2.129}$$

[10] For a differential equation involving two singular small parameters ε and σ, the asymptotic behavior as $\varepsilon, \sigma \to 0$ depends on the path to the origin in the (ε, σ) plane, i.e. on the "distinguished" limit that is imposed by the constraint $\sigma \sim \varepsilon^m$ with m integer ≥ 1 [61].

Being in heavy-duty gas turbines generally $\Delta T_\infty/T_\infty < 2$, Eq. (2.129) shows that the flame is supposed to be thin with respect to acoustic wavelengths. The low Mach number asymptotic expansion is performed by substituting Eqs. (2.128) into Eqs. (2.123)-(2.126) and collecting terms of the same order in ϵ.[11] It reads for the continuity equation as

$$\mathcal{O}(\epsilon^0): \quad \frac{\partial \widetilde{\rho}_0}{\partial \widetilde{t}} + \widetilde{\nabla} \cdot (\widetilde{\rho}_0 \widetilde{\mathbf{u}}_0) = 0 \tag{2.130}$$

$$\mathcal{O}(\epsilon^1): \quad \frac{\partial \widetilde{\rho}_1}{\partial \widetilde{t}} + \widetilde{\nabla} \cdot (\widetilde{\rho}\widetilde{\mathbf{u}})_1 = 0 \tag{2.131}$$

$$\mathcal{O}(\epsilon^2): \quad \frac{\partial \widetilde{\rho}_2}{\partial \widetilde{t}} + \widetilde{\nabla} \cdot (\widetilde{\rho}\widetilde{\mathbf{u}})_2 = 0 \tag{2.132}$$

where $(\widetilde{\rho}\widetilde{\mathbf{u}})_1 = \widetilde{\rho}_1 \widetilde{\mathbf{u}}_0 + \widetilde{\rho}_0 \widetilde{\mathbf{u}}_1$ and $(\widetilde{\rho}\widetilde{\mathbf{u}})_2 = \widetilde{\rho}_2 \widetilde{\mathbf{u}}_0 + \widetilde{\rho}_1 \widetilde{\mathbf{u}}_1 + \widetilde{\rho}_0 \widetilde{\mathbf{u}}_2$. The momentum equation is expanded as

$$\mathcal{O}(\epsilon^{-2}): \quad \widetilde{\nabla} \widetilde{p}_0 = 0 \tag{2.133}$$

$$\mathcal{O}(\epsilon^{-1}): \quad \widetilde{\nabla} \widetilde{p}_1 = 0 \tag{2.134}$$

$$\mathcal{O}(\epsilon^0): \quad \frac{\partial(\widetilde{\rho}_0 \widetilde{\mathbf{u}}_0)}{\partial \widetilde{t}} + \widetilde{\nabla} \cdot (\widetilde{\rho}_0 \widetilde{\mathbf{u}}_0 \widetilde{\mathbf{u}}_0) + \widetilde{\nabla} \widetilde{p}_2 = \frac{1}{Re_\infty} \widetilde{\nabla} \cdot \widetilde{\boldsymbol{\tau}}_0 \tag{2.135}$$

$$\mathcal{O}(\epsilon^1): \quad \frac{\partial(\widetilde{\rho}\widetilde{\mathbf{u}})_1}{\partial \widetilde{t}} + \widetilde{\nabla} \cdot (\widetilde{\rho}\widetilde{\mathbf{u}}\widetilde{\mathbf{u}})_1 + \widetilde{\nabla} \widetilde{p}_3 = \frac{1}{Re_\infty} \widetilde{\nabla} \cdot \widetilde{\boldsymbol{\tau}}_1 \tag{2.136}$$

where $\widetilde{\boldsymbol{\tau}}_j = [(\widetilde{\nabla} \widetilde{\mathbf{u}}_j + \widetilde{\nabla} \widetilde{\mathbf{u}}_j^T) - 2/3 (\widetilde{\nabla} \cdot \widetilde{\mathbf{u}}_j) \mathbf{I}]$. Eqs. (2.133) and (2.134) give $\widetilde{p}_0 = \widetilde{p}_0(\widetilde{t})$ and $\widetilde{p}_1 = \widetilde{p}_1(\widetilde{t})$ respectively, so that the expanded energy equations read as

$$\mathcal{O}(\epsilon^0): \quad \frac{d\widetilde{p}_0}{d\widetilde{t}} + \gamma \widetilde{p}_0 \widetilde{\nabla} \cdot \widetilde{\mathbf{u}}_0 = \frac{\gamma}{Pr\, Re_\infty} \widetilde{\nabla}^2 \widetilde{T}_0 + (\gamma - 1) \Sigma_\infty \widetilde{Q}_0 \tag{2.137}$$

$$\mathcal{O}(\epsilon^1): \quad \frac{d\widetilde{p}_1}{d\widetilde{t}} + \gamma (\widetilde{p} \widetilde{\nabla} \cdot \widetilde{\mathbf{u}})_1 = \frac{\gamma}{Pr\, Re_\infty} \widetilde{\nabla}^2 \widetilde{T}_1 + (\gamma - 1) \Sigma_\infty \widetilde{Q}_1 \tag{2.138}$$

$$\mathcal{O}(\epsilon^2): \quad \frac{\partial \widetilde{p}_2}{\partial \widetilde{t}} + \widetilde{\mathbf{u}}_0 \cdot \widetilde{\nabla} \widetilde{p}_2 + \gamma (\widetilde{p} \widetilde{\nabla} \cdot \widetilde{\mathbf{u}})_2 =$$

$$= \frac{\gamma - 1}{Re_\infty} \widetilde{\boldsymbol{\tau}}_0 : \widetilde{\nabla} \widetilde{\mathbf{u}}_0 + \frac{\gamma}{Pr\, Re_\infty} \widetilde{\nabla}^2 \widetilde{T}_2 + (\gamma - 1) \Sigma_\infty \widetilde{Q}_2 \tag{2.139}$$

Finally, the expansion of the equation of state leads to

$$\mathcal{O}(\epsilon^0): \quad \widetilde{p}_0 = \widetilde{\rho}_0 \widetilde{T}_0 \tag{2.140}$$

$$\mathcal{O}(\epsilon^1): \quad \widetilde{p}_1 = \widetilde{\rho}_1 \widetilde{T}_0 + \widetilde{\rho}_0 \widetilde{T}_1 \tag{2.141}$$

$$\mathcal{O}(\epsilon^2): \quad \widetilde{p}_2 = \widetilde{\rho}_2 \widetilde{T}_0 + \widetilde{\rho}_1 \widetilde{T}_1 + \widetilde{\rho}_0 \widetilde{T}_2 \tag{2.142}$$

[11] When the sequence terms L_n are independent of ϵ, the asymptotic statement $\sum_{n=0}^{N} \epsilon^n L_n = o(\epsilon^N)$, $\epsilon \to 0$ holds if and only if $L_n = 0$, $n = 0, \ldots, N$ [62] [we have used the notation $v(x) = o(w(x))$, $x \to x_0 \Leftrightarrow \lim_{x \to x_0} v(x)/w(x) = 0$].

The leading-order pressure $\widetilde{p}_0$ is a thermodynamic variable that may be obtained by integrating Eq. (2.137) over the flow field volume V. It gives

$$\frac{d\widetilde{p}_0}{d\widetilde{t}}\,V+\gamma\,\widetilde{p}_0\oint_{\partial V}\widetilde{\mathbf{u}}_0\cdot\mathbf{n}\,d\partial V=\frac{\gamma}{Pr\,Re_\infty}\oint_{\partial V}\widetilde{\nabla}\,\widetilde{T}_0\cdot\mathbf{n}\,d\partial V+(\gamma-1)\,\Sigma_\infty\int_V\widetilde{Q}_0\,dV \tag{2.143}$$

where $\mathbf{n}$ is the outward normal to ∂V. Eq. (2.143) shows that the time evolution of $\widetilde{p}_0$ is related to the balance between the heat released in the volume by the combustion process and the heat exchanged throughout the boundaries by convection and conduction. By assuming $\widetilde{p}_0$ constant at the flow field inlet, one gets $\widetilde{p}_0 = const$. The role of the pressure $\widetilde{p}_2$ is that of the "hydrodynamic" pressure balancing inertial forces in order to satisfy the local continuity constraint [$\widetilde{p}_2$ may be computed by means of a Poisson-like equation obtained by making the divergence of Eq. (2.135)]. Noting that the $\mathcal{O}(\epsilon^0)$ and $\mathcal{O}(\epsilon^1)$ equations have the same structure, we can replace $\widetilde{\varphi}_0$ ($\varphi = p, \rho, \mathbf{u}, T, Q$) and $\widetilde{p}_2$ with $\widetilde{\varphi}_0+\epsilon\,\widetilde{\varphi}_1$ and $\widetilde{p}_2+\epsilon\,\widetilde{p}_3$ respectively and avoid to consider separately the first-order quantities. Finally, the "quasi-incompressible" fluid dynamic equations write as [60]

$$\frac{\partial\,\widetilde{\rho}_0}{\partial\,\widetilde{t}}+\widetilde{\nabla}\cdot(\,\widetilde{\rho}_0\,\widetilde{\mathbf{u}}_0)=0 \tag{2.144}$$

$$\frac{\partial(\,\widetilde{\rho}_0\,\widetilde{\mathbf{u}}_0)}{\partial\,\widetilde{t}}+\widetilde{\nabla}\cdot(\,\widetilde{\rho}_0\,\widetilde{\mathbf{u}}_0\,\widetilde{\mathbf{u}}_0)+\widetilde{\nabla}\,\widetilde{p}_2=\frac{1}{Re_\infty}\,\widetilde{\nabla}\cdot\widetilde{\boldsymbol{\tau}}_0 \tag{2.145}$$

$$\gamma\,\widetilde{p}_0\,\widetilde{\nabla}\cdot\,\widetilde{\mathbf{u}}_0=\frac{\gamma}{Pr\,Re_\infty}\,\widetilde{\nabla}^2\,\widetilde{T}_0+(\gamma-1)\,\Sigma_\infty\,\widetilde{Q}_0 \tag{2.146}$$

$$\widetilde{p}_0=\,\widetilde{\rho}_0\,\widetilde{T}_0=const \tag{2.147}$$

For a non-reacting flow, Eqs. (2.144), (2.146) and (2.147) may be combined to give

$$\frac{\partial\,\widetilde{T}_0}{\partial\,\widetilde{t}}+\,\widetilde{\mathbf{u}}_0\cdot\,\widetilde{\nabla}\,\widetilde{T}_0=\frac{1}{Pr\,Re_\infty}\left(\frac{\widetilde{T}_0}{\widetilde{p}_0}\right)\,\widetilde{\nabla}^2\,\widetilde{T}_0 \tag{2.148}$$

When boundaries are adiabatic and the inlet thermodynamic temperature is constant, Eqs. (2.144), (2.145), (2.147) and (2.148) reduce to

$$\widetilde{\nabla}\cdot\,\widetilde{\mathbf{u}}_0=0 \tag{2.149}$$

$$\widetilde{\rho}_0\frac{\partial\,\widetilde{\mathbf{u}}_0}{\partial\,\widetilde{t}}+\,\widetilde{\rho}_0\,\widetilde{\nabla}\cdot(\,\widetilde{\mathbf{u}}_0\,\widetilde{\mathbf{u}}_0)+\,\widetilde{\nabla}\,\widetilde{p}_2=\frac{1}{Re_\infty}\,\widetilde{\nabla}\cdot\widetilde{\boldsymbol{\tau}}_0 \tag{2.150}$$

$$\widetilde{p}_0=const\,,\qquad\widetilde{\rho}_0=const\,,\qquad\widetilde{T}_0=\,\widetilde{p}_0/\,\widetilde{\rho}_0 \tag{2.151}$$

that are the classical "incompressible" fluid dynamic equations [45]. For an incompressible flow, Eqs. (2.132) and (2.139) may be combined to give

$$\gamma\,\widetilde{p}_0\,\frac{\widetilde{D}_0\,\widetilde{S}_2}{D\,\widetilde{t}}=\frac{\gamma-1}{Re_\infty}\,\widetilde{\boldsymbol{\tau}}_0:\,\widetilde{\nabla}\,\widetilde{\mathbf{u}}_0+\frac{\gamma}{Pr\,Re_\infty}\,\widetilde{\nabla}^2\,\widetilde{T}_2 \tag{2.152}$$

where $\widetilde{S}_2 = \widetilde{p}_2/\gamma\,\widetilde{p}_0 - \widetilde{\rho}_2/\widetilde{\rho}_0$ is the second-order flow entropy and $\widetilde{D}_0/D\widetilde{t} = \partial/\partial\widetilde{t} + \widetilde{\mathbf{u}}_0 \cdot \widetilde{\nabla}$ the nondimensional Lagrangian derivative with respect to the incompressible flow velocity. When neglecting the visco-thermal terms on the right-hand side of Eq. (2.152), one has

$$\frac{\widetilde{\rho}_2}{\widetilde{\rho}_0} = \frac{\widetilde{p}_2}{\gamma\,\widetilde{p}_0} + const \tag{2.153}$$

where the second-order quantity $\widetilde{\rho}^{(2)}$ represents the "pseudosound" density oscillations associated to the incompressible flow [63]. The related second-order temperature is given by Eq. (2.142) and is expressed as

$$\frac{\widetilde{T}_2}{\widetilde{\rho}_0} = \frac{\gamma-1}{\gamma}\,\frac{\widetilde{p}_2}{\widetilde{p}_0} + const \tag{2.154}$$

2.6.2 Flow perturbation

Next we introduce the flow variable perturbation

$$\begin{aligned}
\widetilde{p} &= \widetilde{p}_0 + \epsilon^2\,\widetilde{p}_2 + \epsilon^2\,\widetilde{p}^{(2)} \\
\widetilde{\mathbf{u}} &= \widetilde{\mathbf{u}}_0 + \epsilon\,\widetilde{\mathbf{u}}^{(1)} \\
\widetilde{\rho} &= \widetilde{\rho}_0 + \epsilon^2\,\widetilde{\rho}_2 + \epsilon^a\,\widetilde{\rho}^{(a)} \\
\widetilde{T} &= \widetilde{T}_0 + \epsilon^2\,\widetilde{T}_2 + \epsilon^a\,\widetilde{T}^{(a)} \\
\widetilde{Q} &= \widetilde{Q}_0 + \epsilon\,\widetilde{Q}^{(1)}
\end{aligned} \tag{2.155}$$

where the flow field $(\,\widetilde{\varphi}_0\,,\,\widetilde{\varphi}_2\,)$ is the steady quasi-incompressible mean flow and $\widetilde{\varphi}^{(j)}$ represent the unsteady perturbations [52]. In Eqs. (2.155) the linearized acoustics is introduced as a correction to the incompressible flow equations that may contribute to pressure at the same order as the incompressible hydrodynamic pressure, this choice retaining the boundeness of $\partial\,\widetilde{\mathbf{u}}/\partial\,\widetilde{t}$ at the initial instant of time [see Eqs. (2.124)] and then preventing any infinite acceleration of fluid particles [59], [63], [64]. Moreover, pressure oscillations of order ϵ^2 are consistent with the values usually measured in gas turbine combustors far away from resonance or combustion instability conditions (e.g. with $p_\infty = 20bar$ and $M_\infty = 0.05$, the dimensional second-order perturbation pressure is $\epsilon^2\,\widetilde{p}^{(2)}p_\infty \ll 70mbar$). Heat release perturbations of order ϵ may be induced by the first-order velocity perturbation $\widetilde{\mathbf{u}}^{(1)}$. Density and temperature perturbations are $\mathcal{O}(\epsilon^a)$, the cases $a = 1$ and $a = 2$ being considered in detail in the following.
When the dimensions of the flow field domain are sufficiently large to allow for acoustic wave propagation, thus variable perturbations may also vary over the acoustic wavelength $\lambda = c_\infty/\omega$ that defines the length scale variable

$$\boldsymbol{\xi} = \mathbf{x}\,\sqrt{\gamma}/\lambda = \widetilde{\mathbf{x}}\,\epsilon \tag{2.156}$$

In the low Mach number limit $\epsilon \to 0$ the length scales L_∞ and λ become widely separated. Then, the generic perturbation $\widetilde{\varphi}^{(j)}$ and its spatial gradient may be written respectively as [62], [64], [65]

$$\widetilde{\varphi}^{(j)}\,(\,\widetilde{\mathbf{x}}\,,\,\widetilde{t}\,) = \widetilde{\varphi}^{(j)}\,(\,\boldsymbol{\eta}\,,\,\boldsymbol{\xi}\,,\,\widetilde{t}\,) \tag{2.157}$$

and

$$\widetilde{\nabla}\,\widetilde{\varphi}^{(j)}\,(\,\widetilde{\mathbf{x}}\,,\,\widetilde{t}\,)=\,\widetilde{\nabla}_{\eta}\,\widetilde{\varphi}^{(j)}\,(\,\boldsymbol{\eta}\,,\,\boldsymbol{\xi}\,,\,\widetilde{t}\,)+\epsilon\,\widetilde{\nabla}_{\xi}\,\widetilde{\varphi}^{(j)}\,(\,\boldsymbol{\eta}\,,\,\boldsymbol{\xi}\,,\,\widetilde{t}\,) \tag{2.158}$$

where $\boldsymbol{\eta}\equiv\,\widetilde{\mathbf{x}}$.
In the following, different sets of linear perturbation equations are separately derived for non-reacting and reacting zones.

2.6.3 Non-reacting compact flow

By assuming overall dimensions of the flow field comparable to L_∞, in the perturbation analysis the long scale variable $\boldsymbol{\xi}$ becomes void (this situation is typical for the burner zone). Moreover we use $a=2$ into Eqs. (2.155), i.e. density and temperature perturbations are correlated to pressure perturbations and thus thermal fluctuations only "modify" the departure from incompressibility [7], [59], [63], [64]. The "single time scale - multiple length scale" perturbation is then obtained by substituting Eqs. (2.155) into Eqs. (2.123)-(2.125) and using the steady form of Eqs. (2.149)-(2.151). It yields

$$\epsilon\left\{\,\widetilde{\nabla}\cdot\,\widetilde{\mathbf{u}}^{\,(1)}\right\}+\mathcal{O}(\epsilon^{2})=0 \tag{2.159}$$

$$\left\{\,\widetilde{\nabla}\,\widetilde{p}^{(2)}\right\}+\epsilon\,\widetilde{\rho}_{0}\left\{\frac{\partial\,\widetilde{\mathbf{u}}^{\,(1)}}{\partial\,\widetilde{t}}+\,\widetilde{\nabla}\cdot(\,\widetilde{\mathbf{u}}_{0}\,\widetilde{\mathbf{u}}^{\,(1)}+\,\widetilde{\mathbf{u}}^{\,(1)}\,\widetilde{\mathbf{u}}_{0})-\frac{1}{Re_{\infty}}\,\frac{\widetilde{\nabla}\cdot\,\widetilde{\boldsymbol{\tau}}^{\,(1)}}{\widetilde{\rho}_{0}}\right\}+\mathcal{O}(\epsilon^{2})=0 \tag{2.160}$$

where $\widetilde{\boldsymbol{\tau}}^{\,(1)}=[(\,\widetilde{\nabla}\,\widetilde{\mathbf{u}}^{\,(1)}+\,\widetilde{\nabla}\,\widetilde{\mathbf{u}}^{\,(1)\,T})-2/3\,(\,\widetilde{\nabla}\cdot\,\widetilde{\mathbf{u}}^{\,(1)})\,\mathbf{I}\,]$. At $\mathcal{O}(\epsilon)$, Eqs. (2.159)-(2.160) write in dimensional form as

$$\nabla\cdot\,\mathbf{u}\,'=0 \tag{2.161}$$

$$\frac{\partial\,\mathbf{u}\,'}{\partial t}+\nabla\cdot(\,\overline{\mathbf{u}}\,\mathbf{u}\,'+\,\mathbf{u}\,'\overline{\mathbf{u}}\,)+\frac{\nabla\,p\,'}{\overline{\rho}}=\frac{\nabla\cdot\,\boldsymbol{\tau}\,'}{\overline{\rho}} \tag{2.162}$$

where $\mathbf{u}\,'=\epsilon\,\widetilde{\mathbf{u}}^{\,(1)}\,u_{\infty}$, $p\,'=\epsilon^{\,2}\,\widetilde{p}^{(2)}\,p_{\infty}$, $\overline{\rho}=\,\widetilde{\rho}_{\,0}\,\rho_{\infty}=const.$ The mean flow velocity $\overline{\mathbf{u}}=\,\widetilde{\mathbf{u}}_{\,0}\,u_{\infty}$ is given by the solution of the incompressible flow system

$$\nabla\cdot\,\overline{\mathbf{u}}=0\,,\qquad\nabla\cdot(\,\overline{\mathbf{u}}\,\overline{\mathbf{u}}\,)+\nabla\,\overline{p}^{\,*}/\,\overline{\rho}=0 \tag{2.163}$$

with $\overline{p}^{\,*}=\,\widetilde{p}_{\,2}\,p_{\infty}$ being the dimensional hydrodynamic pressure. Note that Eq. (2.160) may be also expressed in Crocco's form as[12]

$$\frac{\partial\,\mathbf{u}\,'}{\partial t}+\nabla\left(\,\overline{\mathbf{u}}\cdot\,\mathbf{u}\,'+\frac{p\,'}{\overline{\rho}}\right)=-\,\overline{\boldsymbol{\Omega}}\times\,\mathbf{u}\,'-\,\boldsymbol{\Omega}\,'\times\,\overline{\mathbf{u}}+\frac{\nabla\cdot\,\boldsymbol{\tau}\,'}{\overline{\rho}} \tag{2.164}$$

[12]When $\nabla\cdot\mathbf{a}=0$ and $\nabla\cdot\mathbf{b}=0$, one has $\nabla\cdot(\mathbf{ba}+\mathbf{ab})=\mathbf{a}\cdot\nabla\mathbf{b}+\mathbf{b}\cdot\nabla\mathbf{a}=\nabla(\mathbf{a}\cdot\mathbf{b})+(\nabla\times\mathbf{a})\times\mathbf{b}+(\nabla\times\mathbf{b})\times\mathbf{a}$

2.6.4 Reacting compact flow

When the flame thickness is lower than L_∞, in the flame zone we can use the single length scale asymptotic analysis and neglect visco-thermal effects (we have seen in Section 2.3 that visco-thermal effects become important when fluctuation waves travel over distances that are much longer than fluctuation wavelengths). Moreover we use $a = 1$ into Eqs. (2.155), i.e. we assume that thermal fluctuations "dominate" the departure from incompressibility with density and temperature perturbations one order of magnitude larger than pressure perturbations [64]. By substituting Eqs. (2.155) into Eqs. (2.123)-(2.126) and using the steady form of Eqs. (2.144)-(2.147), the perturbation equations read as

$$\epsilon \left\{ \frac{\partial \widetilde{\rho}^{(1)}}{\partial \widetilde{t}} + \widetilde{\nabla} \cdot (\widetilde{\rho}_0 \, \widetilde{\mathbf{u}}^{(1)} + \widetilde{\rho}^{(1)} \, \widetilde{\mathbf{u}}_0) \right\} + \mathcal{O}(\epsilon^2) = 0 \tag{2.165}$$

$$\left\{ \widetilde{\nabla} \, \widetilde{p}^{(2)} \right\} + \epsilon \left\{ \widetilde{\rho}_0 \frac{\partial \widetilde{\mathbf{u}}^{(1)}}{\partial \widetilde{t}} + \widetilde{\mathbf{u}}_0 \frac{\partial \widetilde{\rho}^{(1)}}{\partial \widetilde{t}} + \widetilde{\nabla} \cdot [\widetilde{\rho}_0 \, (\widetilde{\mathbf{u}}_0 \, \widetilde{\mathbf{u}}^{(1)} + \widetilde{\mathbf{u}}^{(1)} \, \widetilde{\mathbf{u}}_0 \, \widetilde{\rho}^{(1)} \, \widetilde{\mathbf{u}}_0 \, \widetilde{\mathbf{u}}_0)] \right\} +$$

$$+ \mathcal{O}(\epsilon^2) = 0 \tag{2.166}$$

$$\epsilon \left\{ \gamma \, \widetilde{p}_0 \, \widetilde{\nabla} \cdot \, \widetilde{\mathbf{u}}^{(1)} - (\gamma - 1) \, \Sigma_\infty \, \widetilde{Q}^{(1)} \right\} + \mathcal{O}(\epsilon^2) = 0 \tag{2.167}$$

$$\epsilon \left\{ \widetilde{\rho}^{(1)} \, \widetilde{T}_0 + \widetilde{\rho}_0 \, \widetilde{T}^{(1)} \right\} + \mathcal{O}(\epsilon^2) = 0 \tag{2.168}$$

Eq. (2.168) shows that when using $a = 1$, then $\widetilde{\rho}^{(1)}$ and $\widetilde{T}^{(1)}$ are anticorrelated at $\mathcal{O}(\epsilon)$. The dimensional form of Eqs. (2.166) and (2.167) writes at $\mathcal{O}(\epsilon^0)$ as

$$\nabla \, p' = 0 \tag{2.169}$$

$$\nabla \cdot \mathbf{u}' = \frac{\gamma - 1}{\gamma \, \overline{p}} \, Q' \tag{2.170}$$

with

$$\nabla \cdot (\overline{\rho} \, \overline{\mathbf{u}}) = 0 \, , \qquad \nabla \cdot (\overline{\rho} \, \overline{\mathbf{u}} \, \overline{\mathbf{u}}) + \nabla \, \overline{p}^* = 0 \, , \qquad \nabla \cdot \overline{\mathbf{u}} = (\gamma - 1) \, \overline{Q} / \gamma \, \overline{p} \tag{2.171}$$

2.6.5 Non-reacting acoustic region

In hood and combustor elements we assume that the overall dimensions of the flow domain are $\geq L_\infty / \epsilon$, i.e. long wave phenomena can appear on the scale $\boldsymbol{\xi}$. To get more physical insights into the perturbed equations, we introduce the operator

$$\langle \, g \, \rangle = \frac{1}{\widetilde{V}_\eta} \int_{\widetilde{V}_\eta} g \, d\boldsymbol{\eta} \tag{2.172}$$

performing the average of the generic flow variable $g(\boldsymbol{\eta} \, , \, \boldsymbol{\xi} \, , \, \widetilde{t} \,)$ over the local $\boldsymbol{\eta}$-scale structures. Taking $\widetilde{V}_\eta$ as a volume of diameter $\mathcal{O}(1/\epsilon)$, one gets

$$\langle \, \widetilde{\nabla}_\eta \, g \, \rangle = \frac{1}{\widetilde{V}_\eta} \int_{\widetilde{V}_\eta} \widetilde{\nabla}_\eta g \, d\boldsymbol{\eta} = \frac{1}{\widetilde{V}_\eta} \oint_{\partial \widetilde{V}_\eta} g \, \mathbf{n} \, d\partial \widetilde{V}_\eta = \frac{g(\boldsymbol{\eta} \in \partial \widetilde{V}_\eta)}{\mathcal{O}(\epsilon^{-3})} \, \mathcal{O}(\epsilon^{-2}) = o \, (1) \tag{2.173}$$

where $\mathbf{n}$ is the outward normal to $\partial \widetilde{V}_\eta$ and we have used the boundness of the quantity g over $\partial \widetilde{V}_\eta$. Equation (2.173) represents the "sublinear growth condition" [62], [65]. The long scale perturbation equations are obtained by substituting Eqs. (2.155) with $a = 2$ and Eqs. (2.158) into Eqs. (2.123)-(2.126), subtracting the steady form of Eqs. (2.149)-(2.151) and performing the $\boldsymbol{\eta}$-average using the sublinear growth condition. It yields

$$\frac{\partial \langle \widetilde{\rho}^{(2)} \rangle}{\partial \widetilde{t}} + \widetilde{\rho}_0 \, \widetilde{\nabla}_\xi \cdot \langle \widetilde{\mathbf{u}}^{(1)} \rangle + \mathcal{O}(\epsilon) = 0 \tag{2.174}$$

$$\widetilde{\rho}_0 \frac{\partial \langle \widetilde{\mathbf{u}}^{(1)} \rangle}{\partial \widetilde{t}} + \widetilde{\nabla}_\xi \langle \widetilde{p}^{(2)} \rangle + \mathcal{O}(\epsilon) = 0 \tag{2.175}$$

$$\frac{\partial \langle \widetilde{p}^{(2)} \rangle}{\partial \widetilde{t}} + \gamma \, \widetilde{p}_0 \, \widetilde{\nabla}_\xi \cdot \langle \widetilde{\mathbf{u}}^{(1)} \rangle - \frac{\gamma - 1}{Re_\infty} \langle \widetilde{\boldsymbol{\tau}}_0 : \widetilde{\nabla}_\eta \widetilde{\mathbf{u}}_0 \rangle + \mathcal{O}(\epsilon) = 0 \tag{2.176}$$

By combining Eqs. (2.174)-(2.176), one finds in dimensional form at $\mathcal{O}(\epsilon^0)$

$$\frac{\partial^2 p'}{\partial t^2} - \overline{c}^2 \nabla_\xi^2 p' = 0 \tag{2.177}$$

$$\overline{\rho} \frac{\partial \mathbf{u}'}{\partial t} + \nabla_\xi p' = 0 \tag{2.178}$$

$$\overline{\rho} \, \overline{T} \frac{\partial S'}{\partial t} = \langle \overline{\boldsymbol{\tau}} : \nabla \overline{\mathbf{u}} \rangle \tag{2.179}$$

where $\overline{c} = \sqrt{\gamma \overline{p} / \overline{\rho}} = const$, $\mathbf{u}' = \epsilon \langle \widetilde{\mathbf{u}}^{(1)} \rangle u_\infty$ and $p' = \epsilon^2 \langle \widetilde{p}^{(2)} \rangle p_\infty$. Eq. (2.177) shows that the second-order pressure p' has (over the long scale $\boldsymbol{\xi}$) the role of the acoustic pressure influencing the flow velocity at order ϵ. In Eqs. (2.177)-(2.178) the averaging process on the short scale together with the sublinear growth condition have eliminated any visco-thermal effect, these effects remaining important only within the viscous and thermal boundary layers [29]. On the contrary the entropy perturbation equation (2.179) includes the dissipative term $\langle \overline{\boldsymbol{\tau}} : \nabla \overline{\mathbf{u}} \rangle$, which represents the production of heat by viscous dissipation occurring in the mean flow.

2.6.6 Zone matching

According to the perturbation analysis presented in the previous Sections, burner and flame may be modeled by means of Eqs. (2.161)-(2.162) and Eqs. (2.169)-(2.170), respectively. These systems of equations describe the perturbation flow in terms of second-oder pressure and first-order velocity disturbances. At burner inlet and flame downstream side, the $\mathcal{O}(\epsilon^2)$ pressure perturbation and $\mathcal{O}(\epsilon)$ velocity perturbation represent boundary conditions for the acoustic propagation in hood and combustor of the averages of $\widetilde{p}^{(2)}$ and $\widetilde{\mathbf{u}}^{(1)}$ made over the short-scale structures.

2.7 Combustion System Stability Analysis

When mean flow and visco-thermal effects are neglected inside the burner, then Eqs. (2.161)-(2.162) lead to $\nabla^2 p' = 0$. In the burner, the nondimensional form of Eq. (2.177) reads as $\epsilon^2 \partial^2 \widetilde{p}^{(2)} / \partial t^2 -$

$\widetilde{c}_0^2\,\widetilde{\nabla}^2\,\widetilde{p}^{(2)} = 0$. Then, both burner and hood/combustor zones may be modeled by means of the system (2.177)-(2.178). By lumping the flame into a one-dimensional element concentrated at the burner exit, Eqs. (2.169)-(2.170) give the jump relations $[\,p'\,] = 0$ (zero flame pressure drop) and $[\,u'\,] = (\gamma-1)/\gamma\,\overline{p}\int Q'\,dx$. Under such hypothesis, the combustion system formed by hood, burner, flame and combustor may be described by the system[13]

$$\frac{\partial^2 p'}{\partial t^2} - \overline{c}^{\,2}\,\nabla^2 p' = (\gamma-1)\,\frac{\partial Q'}{\partial t} \tag{2.180}$$

$$\overline{\rho}\,\frac{\partial \mathbf{u}'}{\partial t} + \nabla p' = 0 \tag{2.181}$$

By transforming Eqs. (2.180) and (2.181) to the frequency domain, one has

$$\nabla^2 \widehat{p} + \left(\frac{\omega}{\overline{c}}\right)^2 \widehat{p} = -i\,\omega\,\frac{\gamma-1}{\overline{c}^{\,2}}\,\widehat{Q} \tag{2.182}$$

$$\widehat{\mathbf{u}} = -\frac{1}{i\,\omega\,\overline{\rho}}\nabla\,\widehat{p} \tag{2.183}$$

with the boundary condition

$$\frac{\widehat{p}}{\widehat{\mathbf{u}}\cdot\mathbf{n}} = Z\,(\omega\,,\,\mathbf{x}) \qquad \text{on } \partial V \tag{2.184}$$

where $\mathbf{n}$ is the outward normal to ∂V. On solid walls the boundary impedance Z includes the damping effects occurring in boundary layers [see Eq. (2.64)]. In Eq. (2.182), the heat release source term $\widehat{Q}$ may be in general decomposed into the two terms $\widehat{Q}_N$ and $\widehat{Q}_I$. The contribution $\widehat{Q}_N$ represents heat release oscillations independent of the acoustic field ("loudspeaker" behavior of the combustion acoustic source). Vice versa, $\widehat{Q}_I$ is a function of the acoustic field and represents the "amplifier" behavior of sources. The contributions $\widehat{Q}_N$ and $\widehat{Q}_I$ are responsible for *combustion noise* and *combustion instability* respectively. In the next Sections, the mathematical treatment of combustion noise and combustion instability is separately studied.

2.7.1 Combustion noise

To study combustion noise and combustion instability, it is more convenient to transform the governing equations to the frequency domain by means of the Laplace transform, which accounts for solutions possibly damped or amplified in time. The Laplace transform is defined as [66]

$$\mathcal{L}[\varphi(s)] = \int_{0^-}^{\infty} e^{-st}\,\varphi(t)\,dt \tag{2.185}$$

where

$$s = i\,\omega + \upsilon \tag{2.186}$$

is the Laplace variable (complex frequency).

[13] The integration of Eq. (2.180) between the boundaries of the flame (treated as a gasdynamic interface) gives [47] $[\,\overline{c}^{\,2}\,\nabla\,p'\,] = -(\gamma-1)\int \partial\,Q'/\partial t\,dx$ where according to Eq. (2.181) $[\,\overline{c}^{\,2}\,\nabla\,p'\,] = -\gamma\,\overline{p}\,\partial/\partial t\,[\,\mathbf{u}'\,]$

For combustion noise, the Laplace transforms of Eqs. (2.182)-(2.182) read as

$$\nabla^2 \widehat{p} - \left(\frac{s}{\overline{c}}\right)^2 \widehat{p} = -s\,\frac{\gamma-1}{\overline{c}^{\,2}}\;\widehat{Q}_N(s\,,\,\mathbf{x}) \tag{2.187}$$

$$\widehat{\mathbf{u}} = -\frac{1}{s\,\overline{\rho}}\nabla\,\widehat{p} \tag{2.188}$$

where $\widehat{\varphi}$ indicates the Laplace tranform of φ'. First, we define a Green function G as the solution of the following problem (Ref. [66] p. 804, Ref. [29] p. 321)

$$\nabla^2_{\mathbf{x}}\, G(s\,|\,\mathbf{x}\,,\,\mathbf{x}_0) - \left(\frac{s}{\overline{c}}\right)^2 G(s\,|\,\mathbf{x}\,,\,\mathbf{x}_0) = -\delta(\mathbf{x}-\mathbf{x}_0) \tag{2.189}$$

$$\nabla_{\mathbf{x}}\, G\cdot\mathbf{n} = 0 \quad \text{ on } \partial V \tag{2.190}$$

where $\mathbf{n}$ is the outward normal to ∂V. By subtracting Eq. (2.189) multiplied by $\widehat{p}$ from Eq. (2.187) multiplied by G and making the volume integral gives

$$\widehat{p}\,(s\,,\,\mathbf{x}_0) = s\,\frac{\gamma-1}{\overline{c}^{\,2}}\int_V G(s\,|\,\mathbf{x}\,,\,\mathbf{x}_0)\;\widehat{Q}_N(s\,,\,\mathbf{x})\,dV(\mathbf{x}) +$$

$$+\int_V \left[G(s\,|\,\mathbf{x}\,,\,\mathbf{x}_0)\,\nabla^2\,\widehat{p}\,(s\,,\,\mathbf{x}) - \,\widehat{p}\,(s\,,\,\mathbf{x})\,\nabla^2_{\mathbf{x}}\,G(s\,|\,\mathbf{x}\,,\,\mathbf{x}_0)\right] dV(\mathbf{x}) \tag{2.191}$$

The last term on the right-hand side of Eq. (2.191) may be tranformed using the Green's theorem. It reads as

$$\int_V \left[G(s\,|\,\mathbf{x}\,,\,\mathbf{x}_0)\,\nabla^2\,\widehat{p}\,(s\,,\,\mathbf{x}) - \,\widehat{p}\,(s\,,\,\mathbf{x})\,\nabla^2_{\mathbf{x}}\,G(s\,|\,\mathbf{x}\,,\,\mathbf{x}_0)\right] dV(\mathbf{x}) =$$

$$= \int_V \left\{\nabla_{\mathbf{x}}\left[G(s\,|\,\mathbf{x}\,,\,\mathbf{x}_0)\,\nabla\,\widehat{p}\,(s\,,\,\mathbf{x})\right] - \nabla_{\mathbf{x}}\left[\,\widehat{p}\,(s\,,\,\mathbf{x})\,\nabla_{\mathbf{x}}\,G(s\,|\,\mathbf{x}\,,\,\mathbf{x}_0)\right]\right\} dV(\mathbf{x}) =$$

$$= \oint_{\partial V} \left[G(s\,|\,\mathbf{x}\,,\,\mathbf{x}_0)\,\nabla\,\widehat{p}\,(s\,,\,\mathbf{x}) - \,\widehat{p}\,(s\,,\,\mathbf{x})\,\nabla_{\mathbf{x}}\,G(s\,|\,\mathbf{x}\,,\,\mathbf{x}_0)\right]\cdot\mathbf{n}\;d\partial V(\mathbf{x}) \tag{2.192}$$

Using the symmetry property $G(s\,|\,\mathbf{x}\,,\,\mathbf{x}_0) = G^*(s\,|\,\mathbf{x}_0\,,\,\mathbf{x})$ with G^* complex conjugate of G, one has

$$\widehat{p}\,(s\,,\,\mathbf{x}) = s\,\frac{\gamma-1}{\overline{c}^{\,2}}\int_V G^*(s\,|\,\mathbf{x}_0\,,\,\mathbf{x})\;\widehat{Q}_N(s\,,\,\mathbf{x}_0)\,dV(\mathbf{x}_0) +$$

$$+\oint_{\partial V} G^*(s\,|\,\mathbf{x}_0\,,\,\mathbf{x})\,\nabla\,\widehat{p}\,(s\,,\,\mathbf{x}_0)\cdot\mathbf{n}\;d\partial V(\mathbf{x}_0) \tag{2.193}$$

The Green function may be determined using the eigenfunction approach (Ref. [66] p. 820, Ref. [29] p. 554). The system eigenfunctions are defined as the non trivial solutions of the problem

$$\nabla^2\psi_j + k_j^2\,\psi_j = 0 \tag{2.194}$$

$$\psi_j = Z_\psi\,(\nabla\psi_j\cdot\mathbf{n}) \quad \text{ on } \partial V \tag{2.195}$$

The generic eigenmode ψ_j obtained in correspondence of the eigenfrequency $\omega_j = k_j\,\overline{c}$ is characterized by the following properties.

(i) When the boundary impedance Z_ψ is a function of s, thus k_j and ψ_j also depend on s.

(ii) The base formed by ψ_j is orthogonal, i.e.

$$\int_V \psi_j \, \psi_m^* \, dV = V \, \Lambda_j \, \delta_{j,m} \quad \text{with} \quad \Lambda_j = \frac{1}{V} \int_V \psi_j^2 \, dV \tag{2.196}$$

(iii) If Z_ψ is real, both eigenfunctions ψ_j and eigenfrequencies ω_j are solutions of the real problem (2.194)-(2.195) and then are real functions.

In the following we assume eigenmodes related to solid wall boundaries, i.e. $Z_\psi = \infty$ and $\nabla\psi_j \cdot \mathbf{n} = 0$ on ∂V. In this case both ω_j and ψ_j are real and frequency independent. When the Green function $G(\omega|\,\mathbf{x}, \mathbf{x}_0)$ is expanded in an eigenmode series of the form

$$G(s\,|\,\mathbf{x}\,,\,\mathbf{x}_0) = \sum_{m=0}^{\infty} g_m(s\,,\,\mathbf{x}_0)\,\psi_m(\mathbf{x}) \tag{2.197}$$

and Eq. (2.197) is substituted into Eq. (2.189) multiplied by $\psi_j(\mathbf{x})$, one finds

$$\int_V \left\{ \sum_{m=0}^{\infty} \left[g_m(s,\mathbf{x}_0)\nabla^2\psi_m(\mathbf{x}) - \frac{s^2}{\overline{c}^{\,2}}\, g_m(s,\mathbf{x}_0)\psi_m(\mathbf{x}) \right] \right\} \psi_j(\mathbf{x}) dV(\mathbf{x}) = -\psi_j(\mathbf{x}_0) \tag{2.198}$$

Using Eqs. (2.194) and (2.196) into Eq. (2.198) yields

$$g_j(s,\mathbf{x}_0) = \frac{\overline{c}^{\,2}\,\psi_j(\mathbf{x}_0)}{V\,\Lambda_j\,(s^2+\omega_j^2\,)} \tag{2.199}$$

and finally

$$G(s\,|\,\mathbf{x}\,,\,\mathbf{x}_0) = \overline{c}^{\,2} \sum_{j=0}^{\infty} \frac{\psi_j(\mathbf{x}_0)\,\psi_j(\mathbf{x})}{V\,\Lambda_j\,(s^2+\omega_j^2\,)} \tag{2.200}$$

The substitution of the Green function expansion (2.200) into Eq. (2.193) leads to

$$\widehat{p}\,(s\,,\,\mathbf{x}) = \sum_{j=0}^{\infty} \widehat{\eta}_j(s)\,\psi_j(\mathbf{x}) \tag{2.201}$$

where the modal amplitude $\widehat{\eta}_j(s)$ is defined as

$$\widehat{\eta}_j(s) = \frac{s\,\overline{\rho}\,\overline{c}^{\,2}}{(s^2+\omega_j^2\,)\,V\Lambda_j} \left[\frac{\gamma-1}{\overline{\rho}\,\overline{c}^{\,2}} \int_V \widehat{Q}_N(s,\mathbf{x})\,\psi_j(\mathbf{x})\,dV - \oint_{\partial V} \frac{\widehat{p}\,(s,\mathbf{x})}{Z(s,\mathbf{x})}\,\psi_j(\mathbf{x})\,d\partial V \right] \tag{2.202}$$

The surface integral on the right-hand side of Eq. (2.201) is zero both for open ($\widehat{p}\,=0$) and closed ($\widehat{\mathbf{u}}\cdot\mathbf{n}=0$) boundaries. In this case, Eq. (2.201) provides directly the solution of the acoustic field. In general, the boundary impedance effect may be modeled by means of the complex coefficient

$$z_j\,(s) = \xi_j\,(s) + i\,\varsigma_j\,(s) = \frac{1}{2\,k_j} \oint_{\partial V} \frac{\psi_j^2(\mathbf{x})/V\Lambda_j}{Z(s,\mathbf{x})/\,\overline{\rho}\,\overline{c}}\,d\partial V \tag{2.203}$$

where ξ_j is the *modal damping coefficient*.[14] For frequencies close to ω_j one can neglect mode coupling and use the approximation $\widehat{p} \simeq \widehat{\eta}_j \psi_j$ into Eq. (2.202). It gives

$$\widehat{\eta}_j(s) \simeq \left(\frac{s}{s^2 + 2\, z_j\, \omega_j\, s + \omega_j^2} \right) \frac{\gamma - 1}{V \Lambda_j} \int_V \widehat{Q}_N(s, \mathbf{x})\, \psi_j(\mathbf{x})\, dV \tag{2.204}$$

Being the heat release term related to a one-dimensional flame concentrated in a single plane located at $\mathbf{x}_0$, we can write $\int_V \widehat{Q}_N\, \psi_j\, dV = \widehat{Q}_0(s)\, \psi_j(\mathbf{x}_0)$ and express the modal amplitude (2.204) as

$$\widehat{\eta}_j(s) = W_j(s)\ \widehat{Q}_0(s) = \left[\frac{(\gamma - 1)\, \psi_j(\mathbf{x}_0)}{V\, \Lambda_j} \left(\frac{s}{s^2 + 2\, z_j\, \omega_j\, s + \omega_j^2} \right) \right] \widehat{Q}_0(s) \tag{2.205}$$

where $W_j(s)$ is the modal transfer function. When the heat release is a delta of Dirac at $t = 0$, then $\widehat{Q}_0(s) = 1$ and thus

$$W_j(s) = \frac{(\gamma - 1)\, \psi_j(\mathbf{x}_0)}{2\, V\, \Lambda_j} \left(\frac{1}{s - s_j} + \frac{1}{s - s_j^*} \right) \tag{2.206}$$

The poles s_j and s_j^* of $W_j(s)$ are obtained from the characteristic equation $s^2 + 2\, z_j\, \omega_j\, s + \omega_j^2 = 0$ that may be solved using the hypothesis of slightly damped system $|z_j| \simeq const \ll 1$. One finds

$$s_j \simeq -\xi_j\, \omega_j + i\, \omega_j\ , \qquad s_j^* \simeq -\xi_j\, \omega_j - i\, \omega_j \tag{2.207}$$

By antitransforming Eq. (2.206) to the time domain gives the *impulsive response*

$$w_j^i(t) = \frac{(\gamma - 1)\, \psi_j(\mathbf{x}_0)}{V\, \Lambda_j}\, e^{-\upsilon_j\, t}\, \cos(\omega_j\, t) \tag{2.208}$$

that is a sinusoidal oscillation with frequency ω_j and amplitude decaying in time because of the damping term $-\upsilon_j = -\xi_j \omega_j$.
A sinusoidal heat release oscillation of frequency Ω is expressed in time and frequency domain as $Q_0(t) = |Q| \sin(\Omega t)$ and $\widehat{Q}_0(s) = |Q|\Omega/(s^2 + \Omega^2)$ respectively. In this case, the time domain antitransform of Eq. (2.205) reads as [66]

$$\eta_j(t) = w_j^t(t) + |W_j(i\,\Omega)|\, \sin\{\Omega\, t + \arg[W_j(i\,\Omega)]\} \tag{2.209}$$

In Eq. (2.209), $w_j^t(t)$ is the *transient response* that is again a sinusoidal oscillation with frequency ω_j damped in time by the term $e^{-\upsilon_j\, t}$. The second term on the right-hand side of Eq. (2.209) represents the *harmonic response*, which oscillates in time with the excitation frequency Ω. After a sufficiently long time interval, only the harmonic response survives. The amplitude of the harmonic response writes as

$$|W_j(i\,\Omega)| = \frac{(\gamma - 1)\, \psi_j(\mathbf{x}_0)}{V\, \Lambda_j} \left| \frac{i\,\Omega}{\left(\omega_j^2 - \Omega^2\right) + 2\, i\, z_j\, \omega_j\, \Omega} \right| \tag{2.210}$$

Being $|z_j| \ll 1$, when Ω is equal to one of the pole frequencies ω_j then the amplitude of the harmonic response is maximum, i.e. the system is in *resonance*. Hence, when combustion noise occurs at a frequency matching one of the system eigenfrequencies, in correspondence of such a frequency a resonance peak is generated in the pressure spectrum.

[14] As an alternative to ξ_j, a complex eigenfrequency $\breve{\omega}_j$ may be defined using the identity $s^2 + 2\,\xi_j\,\omega_j\, s + \omega_j^2 = s^2 + \breve{\omega}_j^2$ that gives $\breve{\omega}_j \simeq \omega_j + \xi_j\, s$. Moreover, Eq. (2.187) may be also written as $\nabla^2\, \widehat{p} + (s/c_c)^2\, \widehat{p} = -s\,(\gamma - 1)\ \widehat{Q}/\,\overline{c}^{\,2}$ where $c_c = \overline{c} + i\, Im(c_c)$ is the complex speed of sound with $Im(c_c) \simeq \xi_j \omega_j / \omega$.

2.7.2 Combustion instability

In this Section we consider heat release sources dependent of the acoustic field, i.e. Eq. (2.187) writes as

$$\nabla^2 \widehat{p} - \left(\frac{s}{\overline{c}}\right)^2 \widehat{p} = -s\,\frac{(\gamma-1)}{\overline{c}^{\,2}}\,(\,\widehat{Q}_N + \,\widehat{Q}_I) \tag{2.211}$$

where $\widehat{Q}_I$ is in general a function of the acoustic velocity and acoustic pressure fields. The system response may be studied by means of the Galerkin's method. For the combustion instability case, Eq. (2.204) writes as

$$\widehat{\eta}_j(s) \simeq \left(\frac{s}{s^2 + 2\,z_j\,\omega_j\,s + \omega_j^2}\right)\,\frac{\gamma-1}{V\Lambda_j}\,\int_V (\,\widehat{Q}_N + \,\widehat{Q}_I)\,\psi_j\,dV \tag{2.212}$$

The heat release fluctuations of a zero thickness flame may be expressed as

$$Q'_I = \left[K_p\;p'(\mathbf{x}\,,\,t-\tau_p) + K_u\;\mathbf{u}'(\mathbf{x}\,,\,t-\tau_u)\cdot\mathbf{n}(\,\overline{\mathbf{x}}_f)\right]\cdot\delta(\mathbf{x} - \,\overline{\mathbf{x}}_f) \tag{2.213}$$

where K_p and K_u are positive real constants, $\overline{\mathbf{x}}_f$ is the average flame location and $\mathbf{n}(\,\overline{\mathbf{x}}_f)$ the normal to the average flame location in the direction of combustion products. In Eq. (2.213), heat release fluctuations depend of acoustic pressure and velocity at the time $t-\tau_p$ and $t-\tau_u$ respectively, being τ_p and τ_u the time-lags. In the frequency domain, Eq. (2.213) writes as

$$\widehat{Q}_I = \left[K_p\;\widehat{p}\,(s\,,\,\mathbf{x})\,e^{-s\,\tau_p} + K_u\;\widehat{\mathbf{u}}\,(s\,,\,\mathbf{x})\cdot\mathbf{n}(\,\overline{\mathbf{x}}_f)\,e^{-s\,\tau_u}\right]\cdot\delta(\mathbf{x} - \,\overline{\mathbf{x}}_f) \tag{2.214}$$

Moreover, $\widehat{Q}_I$ is supposed to be small in the sense that for frequencies close to ω_j the acoustic field may be still approximated by the acoustic mode $\eta_j\psi_j$ [67]. Hence, by using in Eq. (2.214) the approximations

$$\widehat{p} \simeq \,\widehat{\eta}_j\,\psi_j\,, \qquad \widehat{\mathbf{u}} \simeq -\frac{\widehat{\eta}_j\,\nabla\psi_j}{\overline{\rho}\,s} \tag{2.215}$$

one can write

$$s\,\frac{\gamma-1}{V\,\Lambda_j}\,\int_V \widehat{Q}_I\,\psi_j\,dV = \left(s\,e^{-s\,\tau_p}\,C_j^p + e^{-s\,\tau_u}\,C_j^u\right)\,\widehat{\eta}_j \tag{2.216}$$

where

$$C_j^p = \frac{\gamma-1}{V\,\Lambda_j}\,K_p\int_V {\psi_j}^2(\mathbf{x})\,\delta(\mathbf{x} - \,\overline{\mathbf{x}}_f)\,dV \tag{2.217}$$

$$C_j^u = -\frac{\gamma-1}{\overline{\rho}\,V\,\Lambda_j}\,K_u\,\int_V \psi_j(\mathbf{x})\,\nabla\psi_j(\mathbf{x})\cdot\mathbf{n}(\,\overline{\mathbf{x}}_f)\,\delta(\mathbf{x} - \,\overline{\mathbf{x}}_f)\,dV \tag{2.218}$$

The right-hand side of Eq. (2.216) may be expanded in Taylor series at $s = i\omega_j$ using $se^{-s\tau_p} \simeq e^{-i\omega_j\tau_p}[s(1-i\omega_j\tau_p) - \omega_j^2\tau_p]$ and $e^{-s\tau_u} \simeq e^{-i\omega_j\tau_p}[-s\tau_u + (1+i\omega_j\tau_u)]$. It gives

$$s\,\frac{\gamma-1}{V\,\Lambda_j}\,\int_V \widehat{Q}_I\,\psi_j\,dV \simeq \left(s\,F_j^I + F_j^0\right)\,\widehat{\eta}_j \tag{2.219}$$

where

$$F_j^I = C_j^p\,(1 - i\,\omega_j\,\tau_p)\,e^{-i\,\omega_j\,\tau_p} - C_j^u\,\tau_u\,e^{-i\,\omega_j\,\tau_u} \tag{2.220}$$

$$F_j^0 = -C_j^p\,\omega_j^2\,\tau_p\,e^{-i\,\omega_j\,\tau_p} + C_j^u\,(1 + i\,\omega_j\,\tau_u)\,e^{-i\,\omega_j\,\tau_u} \tag{2.221}$$

[note that if $\widehat{Q}_I$ depends on $s^2\,\widehat{\eta}_j$, Eq. (2.219) may be still employed by using the approximation $\ddot{\eta}_j \simeq -\omega_j^2\eta_j$ that in frequency domain writes as $s^2\,\widehat{\eta}_j \simeq -\omega_j^2\,\widehat{\eta}_j$]. Eqs. (2.212) and (2.219) lead to the equation

$$\widehat{\eta}_j(s) \simeq \left[\frac{s}{s^2 + (2\,z_j\,\omega_j - F_j^I)\,s + (\omega_j^2 - F_j^0)}\right] \frac{\gamma-1}{V\Lambda_j} \int_V \widehat{Q}_N\,\psi_j\,dV \tag{2.222}$$

Hence, the stability of the system is determined by the poles of the characteristic equation

$$s^2 + \left(2\,z_j\,\omega_j - F_j^I\right)\,s + \left(\omega_j^2 - F_j^0\right) = 0 \tag{2.223}$$

For a slightly damped or amplified system we can use the assumptions $|z_j| \simeq const \ll 1$, $|F_j^I| \ll \omega_j$ and $|F_j^0| \ll \omega_j^2$. Therefore, Eq. (2.223) may be rewritten as

$$(s - s_j)\left(s - s_j^*\right) = 0 \tag{2.224}$$

the poles s_j and s_j^* being given by

$$s_j \simeq \upsilon_j + i\,\omega_j\ , \qquad s_j^* \simeq \upsilon_j - i\,\omega_j \tag{2.225}$$

where

$$\upsilon_j = -\xi_j\,\omega_j + \frac{Re(F_j^I)}{2} + \frac{Im(F_j^0)}{2\,\omega_j} \tag{2.226}$$

is the *growth rate*. The impulse response of the modal amplitude has the general solution

$$\eta_j(t) = e^{\upsilon_j\,t}\left[A_j\,e^{i\,\omega_j\,t} + B_j\,e^{-i\,\omega_j\,t}\right] \tag{2.227}$$

showing that when the growth rate υ_j is positive, thus the j-eigenmode becomes unstable. In this case the heat release term $\widehat{Q}_I$ is responsible for a combustion instability, the response of the linear system being amplified in time without any limit. Positive values of υ_j may be achieved for values of $Re(F_j^I)$ and $Im(F_j^0)$ positive and sufficiently larger than the physical damping $\xi_j\omega_j$. The substitution of Eqs. (2.220) and (2.221) into Eq. (2.226) yields

$$\upsilon_j = -\xi_j\,\omega_j + \frac{C_j^p}{2}\,\cos(\omega_j\,\tau_p) - \frac{C_j^u}{2\,\omega_j}\,\sin(\omega_j\,\tau_u) \tag{2.228}$$

Equation (2.228) shows that when $\widehat{Q}_I$ depends only on acoustic pressure (i.e. $C_j^u = 0$), a necessary condition for instability is

$$-\pi/2 < \omega_j\,\tau_p < \pi/2 \tag{2.229}$$

(note that we have defined $C_j^p > 0$). The instability condition (2.229) represents the Rayleigh criterion [68] and shows that the most favorable condition for combustion instability is $\tau_p = 0$. When $\widehat{Q}_I$ depends only on acoustic velocity (i.e. $C_j^p = 0$), then the necessary conditions for instability become

$$0 < \omega_j\,\tau_u < \pi \ \text{ if } \ C_j^u < 0 \tag{2.230}$$

$$\pi < \omega_j\,\tau_u < 2\,\pi \ \text{ if } \ C_j^u > 0 \tag{2.231}$$

In this case the system can become unstable only when there is a time delay between heat release and velocity fluctuations and the most favorable condition for combustion instability is $\omega_j \tau_u = \pi/2$. Being the acoustic velocity $\pi/2$ phase-shifted with respect to the acoustic pressure [see Eqs. (2.215)], the Rayleigh criterion is recovered for the case $C_j^p = 0$ too. In general, the time-lags between $\widehat{Q}_I$ and acoustic quantities are the physical mechanism responsible for making the system sensitive to combustion instabilities, which are generated when the values of the time-lags belong to certain ranges of variation [1].

Chapter 3

Transfer Matrix Approach

3.1 Transfer Matrix Definition

When the acoustic fields upstream and downstream of an acoustic element are both one-dimensional, the element may be acoustically described by the 2×2 *transfer matrix* $\mathbf{T}(\omega)$ that linearly relates acoustic pressure and acoustic velocity at the upstream side 1 and downstream side 2 of the element. The transfer matrix is defined by the relation

$$\begin{bmatrix} \dfrac{\widehat{p}_2}{\overline{\rho}_2\,\overline{c}_2} \\ \widehat{u}_2 \end{bmatrix} = \begin{bmatrix} T_{11} & T_{12} \\ T_{21} & T_{22} \end{bmatrix} \begin{bmatrix} \dfrac{\widehat{p}_1}{\overline{\rho}_1\,\overline{c}_1} \\ \widehat{u}_1 \end{bmatrix} \tag{3.1}$$

3.2 Duct Transfer Matrix

The transfer matrix approach may be employed to model acoustic elements for which it exists an analytical solution of the acoustic field. For a duct of length L, the Kirchhoff solution (2.89)-(2.90) yields

$$\frac{\widehat{p}_2}{\overline{\rho}\,\overline{c}} = \frac{1}{2}\left(\frac{\widehat{p}_1}{\overline{\rho}\,\overline{c}} + \frac{\Gamma\,\widehat{u}_1}{i}\right)\exp\left(-\Gamma\,k\,L\right) + \frac{1}{2}\left(\frac{\widehat{p}_1}{\overline{\rho}\,\overline{c}} - \frac{\Gamma\,\widehat{u}_1}{i}\right)\exp\left(\Gamma\,k\,L\right) \tag{3.2}$$

$$\widehat{u}_2 = \frac{i}{\Gamma}\left[\frac{1}{2}\left(\frac{\widehat{p}_1}{\overline{\rho}\,\overline{c}} + \frac{\Gamma\,\widehat{u}_1}{i}\right)\exp\left(-\Gamma\,k\,L\right) - \frac{1}{2}\left(\frac{\widehat{p}_1}{\overline{\rho}\,\overline{c}} - \frac{\Gamma\,\widehat{u}_1}{i}\right)\exp\left(\Gamma\,k\,L\right)\right] \tag{3.3}$$

The upstream and downstream impedances of the duct are defined as $Z_1 = \widehat{p}_1/\,\widehat{u}_1$ and $Z_2 = \widehat{p}_2/\,\widehat{u}_2$ respectively. Thus, using Eqs. (3.2)-(3.3) one has

$$Z'_2 = \frac{\dfrac{\Gamma}{i}\left[\exp\left(-\Gamma kL\right) - \exp\left(\Gamma kL\right)\right] + Z'_1\,\left[\exp\left(-\Gamma kL\right) + \exp\left(\Gamma kL\right)\right]}{\left[\exp\left(-\Gamma kL\right) + \exp\left(\Gamma kL\right)\right] + \dfrac{iZ'_1}{\Gamma}\,\left[\exp\left(-\Gamma kL\right) - \exp\left(\Gamma kL\right)\right]} \tag{3.4}$$

where $Z' = Z/\,\overline{\rho}\,\overline{c}$ is the normalized impedance. When $Sd \to \infty$, Eq. (2.85) may be used into Eq. (3.4). It yields

$$Z'_2 = -\frac{i\,\sin\left(kL\right) - Z'_1\,\cos\left(kL\right)}{\cos\left(kL\right) - i\,Z'_1\,\sin\left(kL\right)} \tag{3.5}$$

The compactness condition for the duct is

$$k\,L \ll 1 \tag{3.6}$$

being kL the Helmholtz number based on duct length. Using Eq. (3.6), the first order expansion of Eqs. (3.2)-(3.3) in kL gives

$$\widehat{p}_2 = \widehat{p}_1 \left(1 + \frac{i\,\Gamma^2}{Z'_1}\,kL\right) + \mathcal{O}[(kL)^2] = \widehat{p}_1 + i\,\Gamma^2\,\omega\,\overline{\rho}\,L\,\widehat{u}_1 + \mathcal{O}[(kL)^2] \tag{3.7}$$

$$\widehat{u}_2 = \widehat{u}_1\left(1 - i\,Z'_1\,kL\right) + \mathcal{O}[(kL)^2] = \widehat{u}_1 - i\,\frac{\omega\,L}{\overline{\rho}\,\overline{c}^2}\,\widehat{p}_1 + \mathcal{O}[(kL)^2] \tag{3.8}$$

The condition $|Z'_1| \ll 1$ is usually verified by an open end (i.e. $\widehat{p}_1 = 0$) or a large expansion at the boundary 1 [29]. In this case, Eqs. (3.7)-(3.8) lead to the model

$$\widehat{p}_2 = \widehat{p}_1 + i\,\Gamma^2\,\omega\,\overline{\rho}\,L\,\widehat{u}_1 \tag{3.9}$$

$$\widehat{u}_2 = \widehat{u}_1 \tag{3.10}$$

that corresponds to a linear incompressible duct flow with a pressure loss coefficient

$$\zeta_D = -Im(\Gamma^2)\omega L \tag{3.11}$$

On the contrary, when $|Z'_1| \gg 1$ Eqs. (3.7)-(3.8) write as

$$\widehat{p}_2 = \widehat{p}_1 \tag{3.12}$$

$$\widehat{u}_2 = \widehat{u}_1 - i\,\frac{\omega\,L}{\overline{\rho}\,\overline{c}^2}\,\widehat{p}_1 \tag{3.13}$$

In case of closed end or strong contraction at the boundary 1 (i.e. $Z'_1 \simeq \infty$), Eqs. (3.12)-(3.13) give

$$Z'_2 = \frac{i}{k\,L} \tag{3.14}$$

that represents the "spring model" in the mechanical analogy ($\widehat{p}_2 \propto \widehat{u}_2/(i\omega) = \widehat{x}_2$).

3.3 Burner Transfer Matrix

3.3.1 Analytical model

Figure 3.1 shows the schematic of a burner of radius $a_I = \sqrt{A_I/\pi}$ connected upstream and downstream to two ducts of radii a_I and $a_{II} = \sqrt{A_{II}/\pi}$ respectively (that means an area change occurs at the element exit). When both a_I and a_{II} are $< 1.84\,\overline{c}/\omega$, thus the acoustic field is one-dimensional upstream of the cross-section I and downstream of the cross-section II ($\omega \simeq 1.84\,\overline{c}/a$ is the "cut-off" frequency for plane wave propagation in a duct of radius a [51]). The Mach number inside the element is assumed to be low and thus the incompressible flow model is used. The integration of Eq. (2.161) over the volume comprised between the sections I and II gives

$$u'_{II}\,A_{II} = u'_I\,A_I \tag{3.15}$$

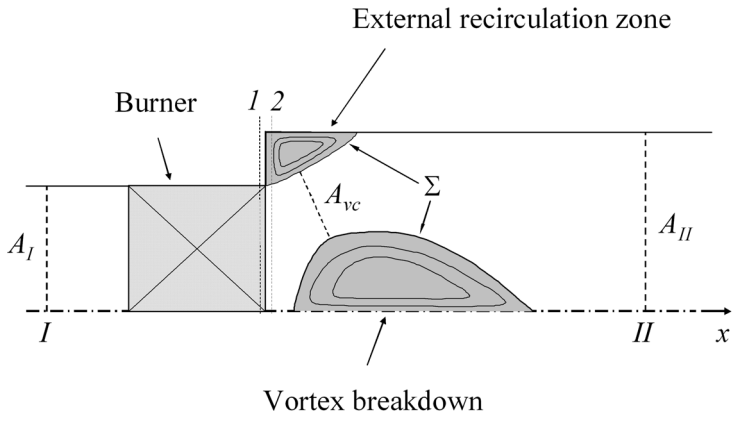

Figure 3.1: Schematic of ducts connected by an acoustic element.

where u' is the axial component of the perturbation velocity. In industrial swirl burners, the flow field downstream of the burner exit is usually characterized by two recirculation regions: an external one generated by the vorticity released by the boundary layer separation occurring at the burner exit lip and an internal recirculation bubble (vortex breakdown) that appears when the burner swirl number is sufficiently high [44]. The two recirculation regions bound the streamtube Σ of Fig. 3.1. For high Reynolds numbers, in the part of the streamtube Σ upstream of the *vena contracta* cross-section A_{vc} (minimum cross-sectional area) the flow may be approximated as inviscid [29], [45]. Under the further assumption of mean and perturbation flow uniform over A_{vc}, the integration of Eq. (2.164) along a streamline leads to

$$p'_I - p'_{vc} = \overline{\rho} \frac{d}{dt} \int_I^{vc} u'_s \, ds + \Phi' \tag{3.16}$$

where s is the streamline coordinate, u'_s the component of the perturbation velocity along s and

$$\Phi' = \overline{\rho} \, (\, \overline{\mathbf{u}}_{vc} \cdot \mathbf{u}'_{vc} - \overline{u}_I \, u'_I \,) \tag{3.17}$$

the pressure loss perturbation with $\overline{u}$ axial component of the mean flow velocity (note that both $\overline{\mathbf{\Omega}} \times \mathbf{u}'$ and $\mathbf{\Omega}' \times \overline{\mathbf{u}}$ are orthogonal to $\overline{\mathbf{u}}$). The pressure loss term Φ' is in general related to the dissipative processes occurring inside the element, i.e. visco-thermal acoustic damping and conversion of acoustic energy into shedding of vortices generated at solid boundaries, the vortices being convected downstream and dissipated into heat by turbulence [69]. When p'_{vc} is approximated with the value p'_{II} at the element downstream section [29], Eqs. (3.15) and (3.16) may be written in the frequency domain as

$$\widehat{u}_{II} \, A_{II} = \widehat{u}_I \, A_I \tag{3.18}$$

$$\widehat{p}_I - \widehat{p}_{II} = i \, \omega \, \overline{\rho} \, L_{eff} \, \widehat{u}_I + \widehat{\Phi} \tag{3.19}$$

where the *effective length* L_{eff} is defined as $L_{eff} = \int_I^{vc} \widehat{u}_s / \widehat{u}_I \, ds$. The inviscid form of Eqs. (3.9)-(3.10) may be used to recompute the transfer matrix (3.18)-(3.19) across the sections 1 and 2 that are defined, respectively, as the upstream and downstream sides of the outflow section of the element (see Fig. 3.1).

It yields

$$\widehat{u}_2\, A_{II} = \widehat{u}_1\, A_I \tag{3.20}$$

$$\widehat{p}_1 - \widehat{p}_2 = i\,\omega\,\overline{\rho}\,\ell\,\widehat{u}_1 + \widehat{\Phi} \tag{3.21}$$

where the *end-correction* ℓ is defined as

$$\ell = L_{eff} - L_1 - (A_I/A_{II})\, L_2 \tag{3.22}$$

with $L_1 = x_1 - x_I$ and $L_2 = x_{II} - x_2$. By using the continuity equations $\overline{u}_{vc}A_{vc} = \overline{u}_I A_I$ and $u'_s A_\Sigma = u'_I A_I$ with $A_\Sigma(s)$ cross-sectional area of the streamtube Σ, the effective length and the pressure drop may be expressed respectively as

$$\ell = \int_I^{vc} \frac{A_I}{A_\Sigma(s)}\, ds - L_1 - (A_I/A_{II})\, L_2 \tag{3.23}$$

and

$$\widehat{\Phi} = \zeta_1\,\overline{\rho}\,\overline{u}_1\,\widehat{u}_1 \tag{3.24}$$

where

$$\zeta_1 = \left(\frac{A_I}{A_{vc}}\right)^2 - 1 \tag{3.25}$$

is the pressure drop coefficient [70], [71]. When time dependence is harmonic, the perturbation velocity reverses its direction periodically. Therefore, a correct expression for the pressure loss in time domain becomes

$$\Phi' = \frac{1}{2}\,\zeta_1^{\pm}\,\overline{\rho}\left\{\,|\,\overline{u}_1 + u'_1|\,(\,\overline{u}_1 + u'_1) - |\,\overline{u}_1|\,\overline{u}_1\right\} \tag{3.26}$$

where the pressure loss coefficients ζ_1^+ and ζ_1^- account for pressure losses due to a flow in the $x > 0$ and $x < 0$ direction respectively. To transform the nonlinear term Φ' to the frequency domain, the derivative is taken with respect to time. It gives

$$\frac{d\,\Phi'}{dt} = \zeta_1^{\pm}\,\overline{\rho}\,|\,\overline{u}_1 + u'_1|\,\frac{d\,u'_1}{dt} \tag{3.27}$$

where $\zeta_1^{\pm}$ have been assumed time-independent. Being Eq. (3.27) nonlinear, a sinusoidal velocity signal does not lead to a sinusoidal derivative $d\Phi'/dt$. In fact, when $u'_1 = |\,\widehat{u}_1|\sin(\omega t)$ is substituted into Eq. (3.27) and a Fourier series expansion is performed, one obtains

$$\frac{d\Phi'}{dt} = \omega\,\overline{\rho}\,g\,(\,\overline{u}_1/|\,\widehat{u}_1|)\,|\,\widehat{u}_1|^2\,\cos(\omega t) + \sum_{m=2}^{\infty}\left[C_m\,\cos(m\omega t) + D_m\,\sin(m\omega t)\right] \tag{3.28}$$

where the function $g(\varphi)$ is defined as

$$g(\varphi) = \begin{cases} \zeta_1^+\,|\varphi| & \text{if } \varphi > 1 \\ \dfrac{\zeta_1^+ + \zeta_1^-}{\pi}\left[\varphi\arcsin(\varphi) + \dfrac{\sqrt{1-\varphi^2}}{3}\left(2+\varphi^2\right)\right] + \dfrac{\zeta_1^+ - \zeta_1^-}{2}\,\varphi & \text{if } |\varphi| \le 1 \\ \zeta_1^-\,|\varphi| & \text{if } \varphi < -1 \end{cases} \tag{3.29}$$

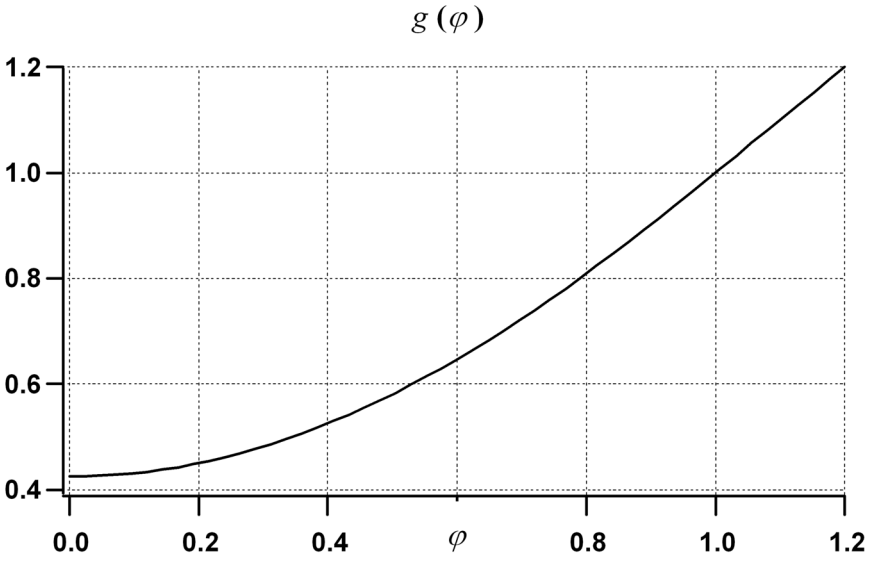

Figure 3.2: Pressure loss function.

By neglecting Fourier components of order higher than one in Eq. (3.28), one has

$$\Phi' = \overline{\rho}\, g(\,\overline{u}_1/|\,\widehat{u}_1|)|\,\widehat{u}_1|^2\,\sin(\omega t) \tag{3.30}$$

and finally

$$\widehat{\Phi} = \overline{\rho}\, g\,(\,\overline{u}_1/|\,\widehat{u}_1|)\;|\,\widehat{u}_1|\;\widehat{u}_1 \tag{3.31}$$

Figure 3.2 shows the function $g(\varphi)$ for the case $\zeta_1^+ = \zeta_1^-$. When $|\,\widehat{u}_1| > |\,\overline{u}_1|$ (e.g. in absence of a mean flow or close to resonance), the vortex-shedding dissipation mechanism is nonlinear because the acoustic field is responsible for the convection and dissipation of the acoustically produced vorticity (in this case $\widehat{\Phi}$ depends of the acoustic pressure). When a mean flow is maintained throughout the element, the convection and dissipation of vorticity due to the mean flow gives a linear contribution to the pressure loss term and for $|\,\widehat{u}_1| < |\,\overline{u}_1|$ Eq. (3.31) reduces to the "quasi-steady" linear expression

$$\widehat{\Phi}_{lin} = \zeta_1\;\overline{\rho}\;\overline{u}_1\;\widehat{u}_1 \tag{3.32}$$

that leads to $\ell - \zeta$ *model* expressed as

$$\widehat{u}_2\, A_{II} = \widehat{u}_1\, A_I \tag{3.33}$$

$$\widehat{p}_1 - \widehat{p}_2 = (\,i\,\omega\;\overline{\rho}\;\ell + \zeta_1\;\overline{\rho}\;\;\overline{u}_1\,)\;\widehat{u}_1 \tag{3.34}$$

In first approximation, the $\ell - \zeta$ pressure loss coefficient ζ_1 may be approximated with the steady flow value $\overline{\zeta}_1$.

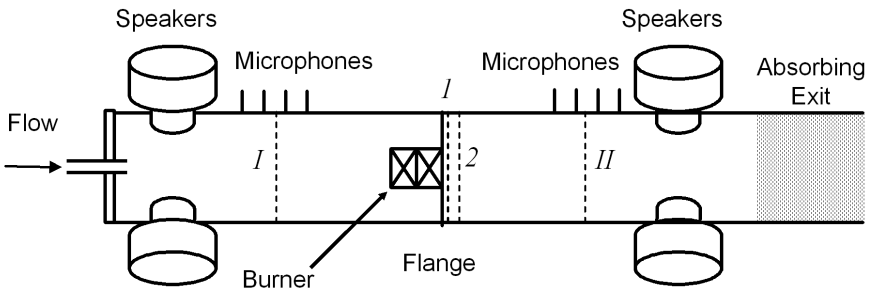

Figure 3.3: Schematic of impedance tube test rig.

3.3.2 Impedance tube experiments

The transfer matrix model presented in the previous Section has been applied to a gas turbine burner and validated by means of transfer matrix measurements performed by installing the burner in the atmospheric impedance tube shown in Figs. 3.3-3.4. The test rig consists of two hollow steel tubes having a circular cross section. The tube diameters ensure that plane wave propagation occurs for frequencies below the maximum frequency of interest (cut-off frequency). The burner is mounted on a flange reproducing the combustor front panel and an air flow may be maintained through the burner to simulate engine conditions. On the downstream end, an extension is bolted and filled with sound absorbing material to reduce the acoustic reflection from the open end of the test rig. Four loudspeakers emitting pure toned frequency signals at various frequency intervals are used for the acoustic forcing upstream and downstream of the burner. The response to this excitation is measured using arrays of microphones mounted along the top side of the tube. The minimum distance between microphones and burner is set in order to avoid near field effects. To take into account the atmospheric test conditions under which the tests are performed, the microphones are calibrated before every set of tests using a Brüel & Kjaer Type 4231 Acoustic Calibrator inducing an acoustic signal directly into the microphone

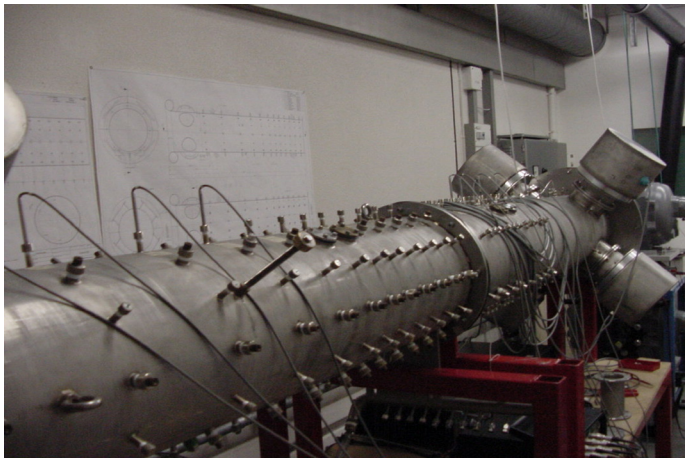

Figure 3.4: Photo of impedance tube test rig.

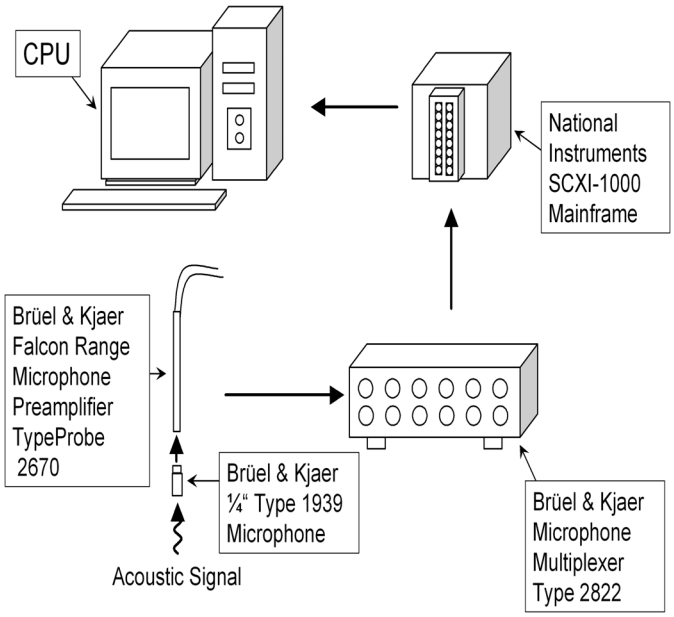

Figure 3.5: Data acquisition system.

probe at $94dB$ and $1000Hz$. The data acquisition system is illustrated in Fig. 3.5. From the microphone data, acoustic pressure and acoustic velocity can be calculated at the cross sections I and II of Fig 3.3 using the Multi-Microphone Method [16]. Fig 3.3 also defines the sections 1 and 2 as, respectively, the upstream and downstream sides of the outflow section of the burner. The acoustic field in 1 and 2 may be computed by using plane wave solution in $I-1$ and $II-2$ respectively, so that the burner is modeled as an acoustic discontinuity located between 1 and 2. By assuming the acoustic fields in 1 and 2 linearly related, one can write

$$\begin{bmatrix} \dfrac{\widehat{p}_2}{\overline{\rho}\,\overline{c}} \\ \widehat{u}_2 \end{bmatrix} = \begin{bmatrix} T_{11}(\omega) & T_{12}(\omega) \\ T_{21}(\omega) & T_{22}(\omega) \end{bmatrix} \begin{bmatrix} \dfrac{\widehat{p}_1}{\overline{\rho}\,\overline{c}} \\ \widehat{u}_1 \end{bmatrix} + \begin{bmatrix} S_p(\omega) \\ S_u(\omega) \end{bmatrix} \tag{3.35}$$

where $\mathbf{T}(\omega)$ is the burner transfer matrix and $[S_p, S_u]^T$ the pressure and velocity source terms responsible for noise generation (note that these source terms are, by definition, linearly independent of the excitation signal). To reconstruct transfer matrix elements and sources from $[\widehat{p}_1, \widehat{u}_1]$ and $[\widehat{p}_2, \widehat{u}_2]$ measurements, first the four elements of the transfer matrix are extracted from acoustic pressure and velocity signals by using the response to the loudspeaker excitation (in this case the source terms $[S_p, S_u]^T$ vanish). Since Eq. (3.35) provides two equations and four unknowns, at least two independent test states are required in order to extract the transfer matrix elements. In general, independent test states can be obtained by changing the acoustic boundary conditions or by consecutively forcing upstream and downstream of the acoustic element with loudspeakers. In our measurements the upstream and downstream forcing is employed. An important aspect is that the microphones do not only measure the response to the loudspeakers, being considerable levels of stochastic contributions (background noise and turbulence)

also present in the flow field. The stochastic contributions can be reduced to arbitrary small values by using for the loudspeakers a pure tone forcing signal and measuring for a sufficiently long time (this measurement technique is explained in detail in [16]). An additional independent state is required for the determination of the source terms $[S_p, S_u]^T$. The third required test state is obtained by applying no forcing to the loudspeakers.

3.3.3 ALSTOM EV burner

Transfer matrix measurements have been performed for the double-cone ALSTOM premix EV burner shown in Fig. 3.6 [72]. As illustrated in Fig. 3.7, the EV burner consists of two half cone shells that are displaced parallel to the axis, generating two tangential slots. The swirl strength of the flow entering through the tangential slots increases in the axial direction and is adjusted such that a vortex breakdown of the core flow occurs close to the burner exit. In the EV premix burner, no specific flame stabilizer hardware exists that is exposed upstream to the ignitable mixture and downstream to the flame stabilization zone. As a result, the EV burner has an inherent safety against autoignition and flame flashback events. When the burner operates in "gas premix mode", the gaseous fuel is injected through a row of holes in cross flow direction into the air entering the tangential burner slots. Each gas injection jet has to penetrate only a small portion of the air and has to be mixed only with its own small portion of the incoming air. Since the air which enters the burner slots is equally distributed along the length of the slot, the gas jets have to mix with the same portion of the air. This means that the mixing boundary conditions are equal and therefore the gas to air mixing performance is equally distributed in the whole flow field of the burner. The gas injection concept in the air slot stands for an inherent, equal distribution of the fuel into the incoming air, and is therefore the precondition for the high mixing effectiveness, which leads to a homogeneous air to fuel mixture in spite of the extremely compact mixing section of the EV burner. The relatively small volume in the cone is sufficient to generate a very homogeneous air-fuel mixture, which is a precondition to achieve premix combustion with ultra-low dry NO_x emissions. Note that no or little dilution air is needed when using EV burners. It is also possible to operate the burner

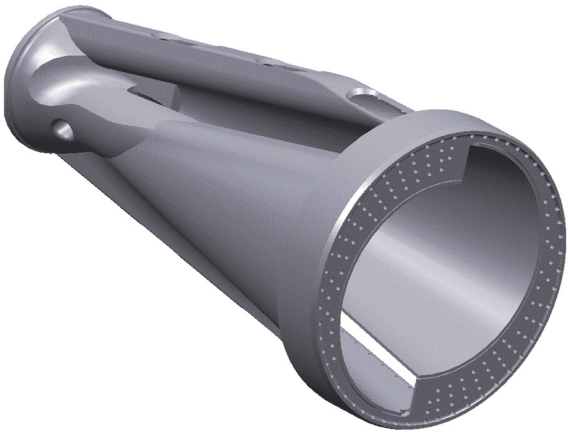

Figure 3.6: EV burner.

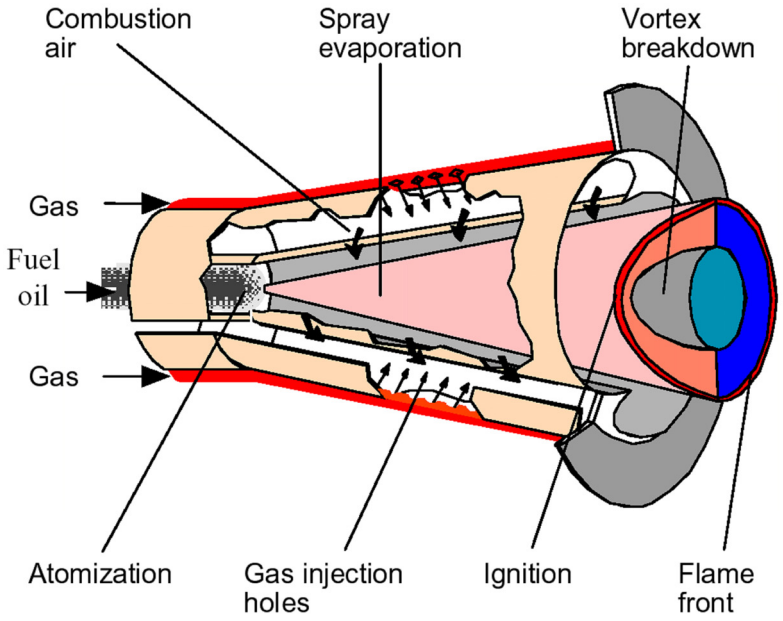

Figure 3.7: EV burner principle.

in "oil mode" by injecting liquid fuel throughout a "fuel lance" located in the cone head. The liquid jet disintegrates into small droplets within the burner leading cone and the swirling air flow distributes the droplets in the whole flow field, the flame stabilization occurring near to the burner outlet with the help of the inner recirculation zone.

3.3.4 EV burner transfer matrices

The measured magnitudes and phases of the burner transfer matrix elements reported in Fig. 3.9 refer to a case without burner mean flow. Vice versa, the experimental results presented in Fig. 3.10 have been obtained using a burner mean flow velocity set to a value providing the same Mach number in the impedance tube and in engine conditions. Figs. 3.9 and 3.10 also report the transfer matrices computed using a Finite Element Method (FEM) to solve the Helmholtz equation [73]. The FEM transfer matrices have been computed by simulating two independent test states obtained by applying an acoustic source at the tube end and an anechoic condition (i.e. impedance equal to $\overline{\rho}\,\overline{c}$) at the other end. To simulate the case with burner mean flow, the FEM result (containing no mean flow effect) has been modified by adding a $\ell - \zeta$ element (3.33)-(3.34) at the burner exit with $\ell = 0$ and ζ_1 obtained from steady flow measurements of the burner pressure drop (in the range of variation of the burner velocity, no significant variation of ζ_1 was observed). The results show the good accuracy achieved by simulating the burner matrix elements T_{11}, T_{21} and T_{22} by means of FEM and $\ell - \zeta$ model. The use of a constant value of ζ_1 leads to a good accuracy of the T_{22} numerical results only in the low-frequency range. Moreover, for

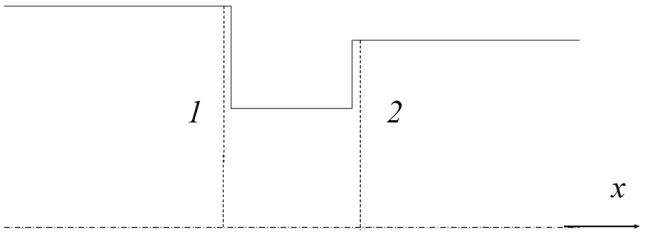

Figure 3.8: Schematic of orifice.

sufficiently low frequencies the only $\ell - \zeta$ transfer matrix

$$\mathbf{T}(\omega) = \begin{bmatrix} 1 & i\,\omega\,\rho\,\ell + \overline{\zeta}_1\ \overline{\rho}\ \overline{u}_1 \\ 0 & 1 \end{bmatrix} \tag{3.36}$$

may be used to represent the burner, i.e. the acoustic behavior of the burner is the same of a compact area change.

3.4 Area Jump and Orifice Flow

For simple area changes the $\ell - \zeta$ model (3.34) may be still employed. When ζ_1 is expressed by means of the steady flow value $\overline{\zeta}_1$, for high Reynolds number one can use [70], [71]

$$\overline{\zeta}_1 = \begin{cases} \left(\dfrac{A_I}{A_{II}}\right)^2 - 1 + \left(1 - \dfrac{A_I}{A_{II}}\right)^2 & \text{for area expansions} \\ 1 - \left(\dfrac{A_I}{A_{II}}\right)^2 + \dfrac{1}{2}\left(1 - \dfrac{A_I}{A_{II}}\right) & \text{for area contractions} \end{cases} \tag{3.37}$$

where A_I/A_{II} is the area jump ratio.
For the orifice flow shown in Fig. 3.8, Eqs. (3.20)-(3.21) may be applied to the two area changes occurring at the orifice extremities. It yields

$$\widehat{u}_2\,A_2 = \widehat{u}_1\,A_1 \tag{3.38}$$

$$\widehat{p}_1 - \widehat{p}_2 = \left[\, i\,\omega\,\overline{\rho}\,L'_n + \zeta_{neck}\ \overline{\rho}\ \overline{u}_n + (\,\widehat{\Phi}_1 + \widehat{\Phi}_2)/\,\widehat{u}_n \right]\ \widehat{u}_n \tag{3.39}$$

where Eqs. (3.9)-(3.10) with $Re(\Gamma^2) \simeq 0$ have been used to model the orifice pressure drop, $L'_n = \ell_1 + L_n + \ell_2$ with L_n orifice length, ℓ_1 and ℓ_2 are the area change end-corrections, ζ_{neck} is the neck pressure loss coefficient given by Eq. (3.11) and the pressure loss terms $\widehat{\Phi}_1$ and $\widehat{\Phi}_2$ refer to the orifice cross section.

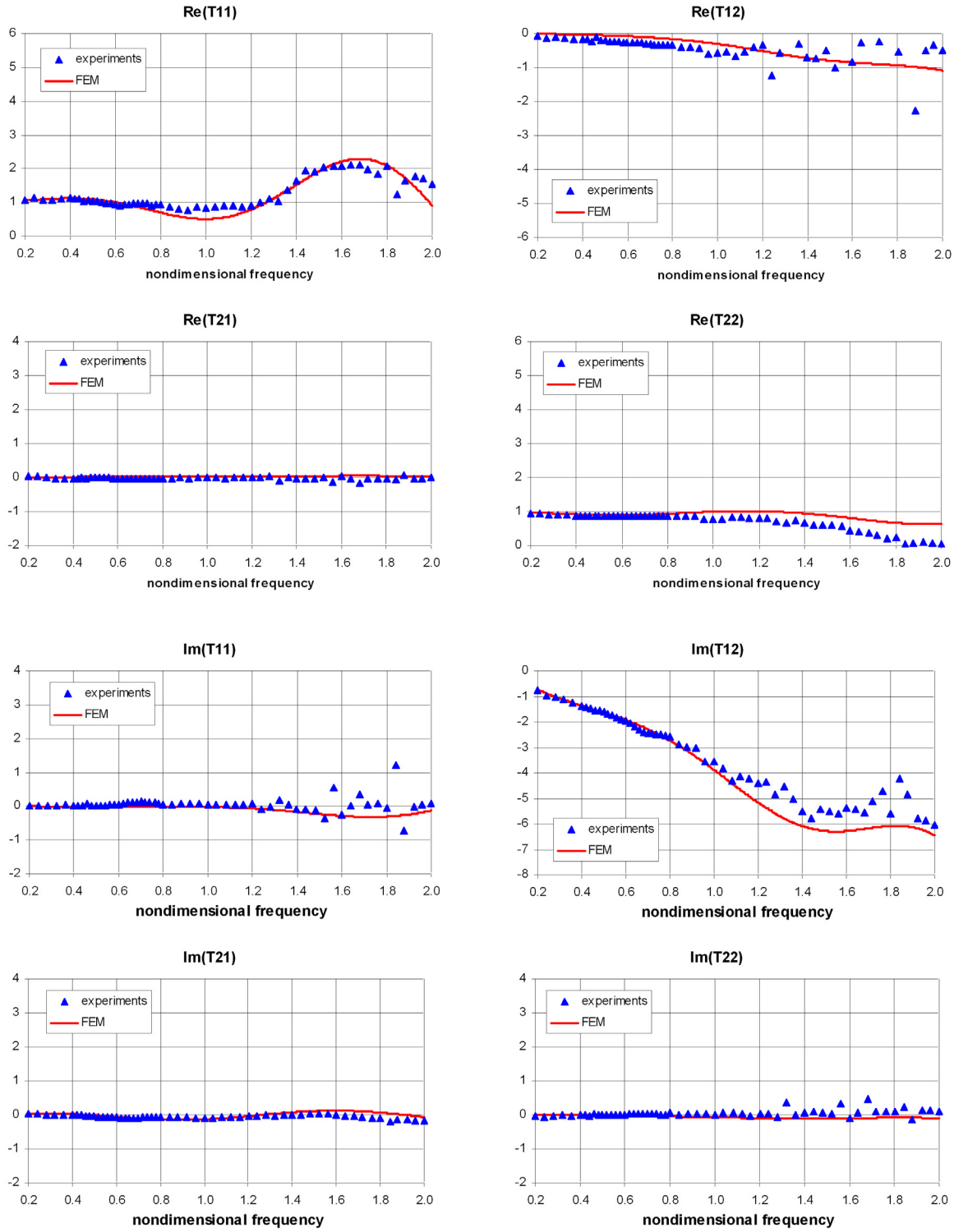

Figure 3.9: EV burner transfer matrix elements: no burner mean flow.

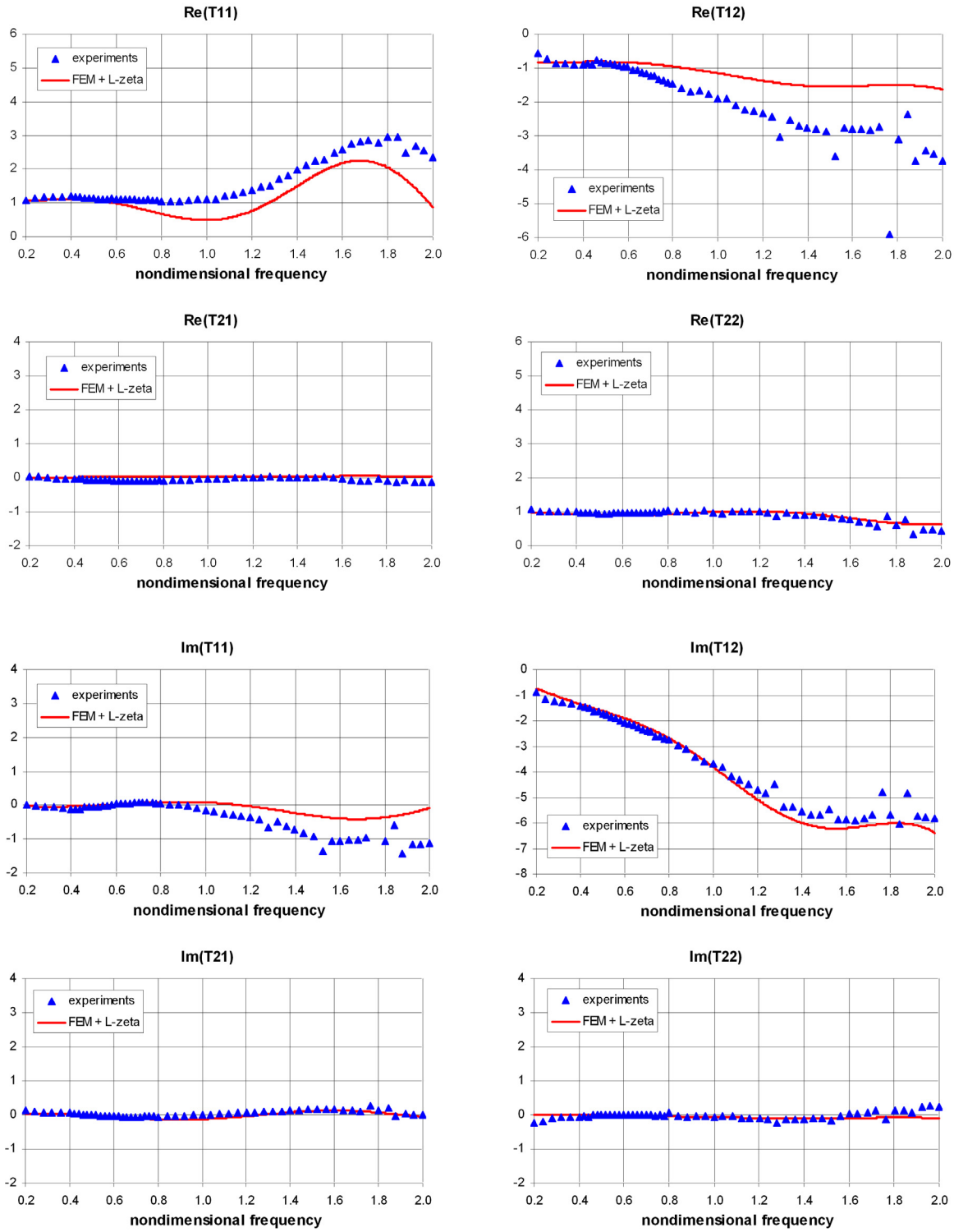

Figure 3.10: EV burner transfer matrix elements: burner mean flow case.

3.5 Flame Transfer Matrix

We consider in the following the one-dimensional flame shown in Fig. 3.11. The integration of the inviscid one-dimensional form of Eqs. (2.10)-(2.12) between the upstream boundary 1 and downstream boundary 2 of the flame front gives [47]

$$[\,m\,]_1^2 = -\frac{d}{dt}\int_1^2 \rho\, dx \tag{3.40}$$

$$[\,mu + p\,]_1^2 = -\frac{d}{dt}\int_1^2 \rho u\, dx \tag{3.41}$$

$$\left[m\left(C_pT + \frac{u^2}{2} \right) \right]_1^2 = -\frac{d}{dt}\int_1^2 \rho \left(C_vT + \frac{u^2}{2} \right) dx + Q_A \tag{3.42}$$

where m is the mass flux defined as

$$m = \rho\,(u - U_f) \tag{3.43}$$

with U_f velocity of the flame boundary and $Q_A = \int_1^2 Q dx$ is the heat flux per unit area and time. Note that the flame boundary velocity is related to the flame speed S_f by the relation

$$S_f = u - U_f \tag{3.44}$$

For the steady mean flow $\overline{\varphi}(x)$, Eqs. (3.40)-(3.42) lead to

$$\overline{\rho}_1\,\overline{u}_1 = \overline{\rho}_2\,\overline{u}_2 = \overline{m} \tag{3.45}$$

$$\overline{m}\,[\,\overline{u}\,]_1^2 + [\,\overline{p}\,]_1^2 = 0 \tag{3.46}$$

$$\left[\,\overline{C}_p\,\overline{T} + \frac{\overline{u}^2}{2}\,\right]_1^2 = \overline{Q}_M \tag{3.47}$$

where $Q_M = Q_A/m$ is the heat release per unit mass of reactants. Note that in steady conditions $\overline{U}_{f1} = \overline{U}_{f2} = 0$, i.e. the flame boundaries have a fixed mean position. The equation of state (2.4) yields

$$\overline{p} = \overline{\rho}\,\mathcal{R}\,\overline{T} \tag{3.48}$$

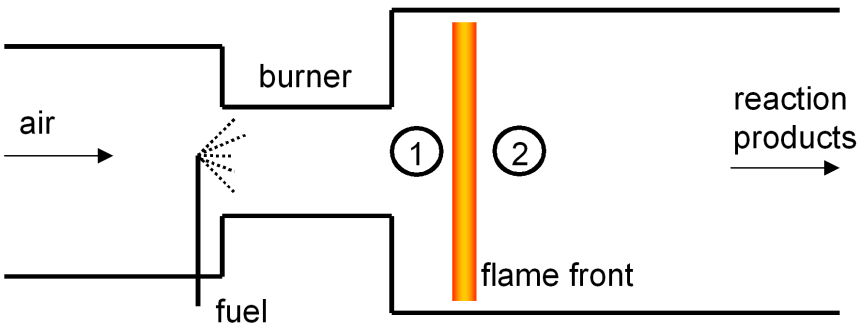

Figure 3.11: Sketch of the flame front.

The mean flow quantities downstream of the combustion region may be expressed as a function of the mean flow quantities upstream of the flame. For assigned values of $\overline{T}_2$ and $\overline{\mathcal{R}}_2$ (i.e. when the chemical composition of combustion products is given), from Eqs. (3.45)-(3.46) and (3.48) one has

$$\overline{p}_2 - \overline{p}_1 = \overline{m}^2 \left(\frac{1}{\overline{\rho}_1} - \frac{\overline{\mathcal{R}}_2 \, \overline{T}_2}{\overline{p}_2} \right) \tag{3.49}$$

Solving Eq. (3.49) for the mean pressure $\overline{p}_2$, yields

$$\overline{p}_2 = \frac{\overline{m}^2 + \overline{p}_1 \, \overline{\rho}_1 + \sqrt{\left(\overline{m}^2 + \overline{p}_1 \, \overline{\rho}_1 \right)^2 - 4 \, \overline{m}^2 \, \overline{\mathcal{R}}_2 \, \overline{T}_2 \, \overline{\rho}_1}}{2 \, \overline{\rho}_1} \tag{3.50}$$

Using Eqs. (3.48) and (3.45), the density and velocity downstream of the flame are computed. Finally, Eq. (3.47) may be employed to obtain the mean heat release $\overline{Q}_M$.

For a "compact flame", the perturbation flow equations may be obtained by linearizing Eqs. (3.40)-(3.42) [this coincides with the integration of the inviscid one-dimensional form of Eqs. (2.106), (2.107) and (2.109) across the flame] by neglecting the contributions from the right-hand side integrals. Therefore, in a compact flame the jumps of acoustic pressure and velocity across the flame correspond to a concentrated heat release input and the flame may be modeled as a gasdynamic discontinuity with respect to both acoustic and entropy waves. A subsonic flame with any assigned space distribution of heat release fluctuations $Q'_M(x)$ may be approximated as compact when [74]

$$\frac{\omega \delta_f}{\overline{c}_1} \ll 1 \quad \text{and} \quad \begin{cases} \dfrac{\omega \delta_f}{\overline{c}_1} \left(\dfrac{\overline{T}_2}{\overline{T}_1} - 1 \right)^2 \ll 1 \quad \text{with} \quad \dfrac{\omega \delta_f}{\overline{u}_1} \ll 1 \\ \overline{M}_1 \left(\dfrac{\overline{T}_2}{\overline{T}_1} - 1 \right)^2 \ll 1 \quad \text{with} \quad \dfrac{\omega \delta_f}{\overline{u}_1} \gg 1 \end{cases} \tag{3.51}$$

where δ_f is the flame thickness and $\overline{M}_1$ the upstream mean flow Mach number. In heavy-duty gas turbines $\overline{T}_2 / \overline{T}_1 < 3$ and then the compact flame hypothesis holds when

$$\delta_f \ll \overline{u}_1 / \omega \tag{3.52}$$

or

$$\overline{M}_1 \ll 1 \qquad \text{and} \qquad \delta_f \ll \overline{c}_1 / \omega \tag{3.53}$$

Eqs. (3.52)-(3.53) state that a subsonic flame is compact when the flame thickness is much smaller than the entropy length scale $\overline{u}_1 / \omega$, whereas for low Mach number flames the compactness condition reduces to a flame thickness much smaller than acoustic wavelengths.

3.5.1 Subsonic compact flames

For a compact subsonic flame, Eqs. (3.40)-(3.42) give

$$\rho'_1 \, \overline{u}_1 + \overline{\rho}_1 (u'_1 - U'_f) = \rho'_2 \, \overline{u}_2 + \overline{\rho}_2 (u'_2 - U'_f) = m' \tag{3.54}$$

$$\overline{m} \left[u' \right]_1^2 + m' \left[\overline{u} \right]_1^2 + \left[p' \right]_1^2 = 0 \tag{3.55}$$

$$\left[C_p \, T' + \overline{u} \, u' \right]_1^2 = Q'_M \tag{3.56}$$

where $U_{f_1} = U_{f_2} = U_f$ and fluctuations of C_p (and then of $\mathcal{R}$ and γ) have been neglected according to the calorically perfect gas assumption. The linearized equation of state reads as

$$\frac{p'}{\overline{p}} = \frac{\rho'}{\overline{\rho}} + \frac{T'}{\overline{T}} \tag{3.57}$$

A perturbation energy equation alternative to Eq. (3.56) may be obtained by using Eqs. (3.40)-(3.41) to write Eq. (3.42) in the form [75]

$$\left[\frac{p}{(\gamma-1)\rho} \right]_1^2 = -\frac{p_1 + p_2}{2} \left[\frac{1}{\rho} \right]_1^2 + Q_M \tag{3.58}$$

Eq. (3.58) leads to the perturbation energy equation [18]

$$\left[A_p\, p' - A_\rho\, \rho' \right]_1^2 = Q'_M \tag{3.59}$$

where the coefficients $A_{p_{1,2}}$ and $A_{\rho_{1,2}}$ are defined as

$$A_{p_{1,2}} = \frac{(\gamma_{1,2}+1)/\,\overline{\rho}_{1,2} - (\gamma_{1,2}-1)/\,\overline{\rho}_{2,1}}{2(\gamma_{1,2}-1)} \tag{3.60}$$

$$A_{\rho_{1,2}} = \frac{(\gamma_{1,2}+1)\,\overline{p}_{1,2} + (\gamma_{1,2}-1)\,\overline{p}_{2,1}}{2\,\overline{\rho}_{1,2}^2(\gamma_{1,2}-1)} \tag{3.61}$$

Eqs. (3.54)-(3.57) [or (3.54), (3.55), (3.57) and (3.59)] may be used to obtain p'_2, ρ'_2, T'_2 and u'_2 as functions of p'_1, ρ'_1, T'_1, u'_1, Q'_M and U'_f. When the flow upstream of the flame is isentropic (i.e. $S'_1 = 0$), density fluctuations upstream and downstream of the flame are respectively expressed as [see Eq. (2.34)]

$$\rho'_1 = \frac{p'_1}{\overline{c}_1^2} \tag{3.62}$$

$$\rho'_2 = \frac{p'_2}{\overline{c}_2^2} - \frac{\overline{\rho}_2}{C_{p_2}}\, S'_2 \tag{3.63}$$

Using Eq. (3.63) to eliminate ρ'_2 and providing the expressions $Q'_M(p'_1, u'_1)$ and $U'_f(p'_1, u'_1)$, the system (3.54)-(3.57) [or (3.54), (3.55), (3.57) and (3.59)] may be written in the final form

$$\begin{bmatrix} \dfrac{p'_2}{\overline{\rho}_2\,\overline{c}_2} \\ u'_2 \end{bmatrix} = \begin{bmatrix} T_{11}(s) & T_{12}(s) \\ T_{21}(s) & T_{22}(s) \end{bmatrix} \begin{bmatrix} \dfrac{p'_1}{\overline{\rho}_1\,\overline{c}_1} \\ u'_1 \end{bmatrix} + \begin{bmatrix} S_p(s) \\ S_u(s) \end{bmatrix} \tag{3.64}$$

$$S'_2 = S'_2\,(p'_1, u'_1) \tag{3.65}$$

where the transfer matrix elements $T_{ij}(s)$ include heat release fluctuations responsible for combustion instabilities, whereas the source terms $[S_p(s), S_u(s)]^T$ model heat release fluctuations related to combustion noise.

3.5.2 Low Mach number compact flames

When $\overline{M}_1 \ll 1$ and Eq. (2.129) is satisfied, Eqs. (2.169)-(2.170) may be integrated across the flame front [note that Eq. (2.129) coincides with the second of conditions (3.53)]. As an example, for laminar premixed flames burning natural gas one can use $\delta_f \approx 0.01cm$, $\overline{c}_1 \approx 500m/s$, $\overline{u}_1 \approx 30cm/s$ and $\overline{T}_2/\overline{T}_1 \approx 2.5$ so that the condition (2.129) yields $f \ll 500Hz$. Thus, for one-dimensional low Mach number compact flames one has

$$p'_2 - p'_1 = 0 \tag{3.66}$$

$$u'_2 - u'_1 = \overline{u}_1 \left(\frac{\overline{T}_2}{\overline{T}_1} - 1 \right) \frac{Q'_A}{\overline{Q}_A} \tag{3.67}$$

where [see Eqs. (2.171)]

$$\overline{Q}_A = \frac{\overline{\rho}_1 \, \overline{c}_1^2}{\gamma - 1} \, \overline{u}_1 \left(\frac{\overline{T}_2}{\overline{T}_1} - 1 \right) \tag{3.68}$$

Eqs. (3.66)-(3.67) may be also obtained by using the following approach. From Eqs. (3.45)-(3.47) one can derive $\overline{\rho}_2 = \overline{m}/\overline{u}_2$, $\overline{p}_2 = \overline{p}_1 + \overline{m}(\overline{u}_1 - \overline{u}_2)$, $\overline{T}_2 = \overline{p}_2/\overline{\rho}_2 \mathcal{R}_2$ and then

$$-\frac{\gamma_1 \, \overline{M}_1^2}{\gamma_2 - 1} \left(\frac{\overline{u}_2}{\overline{u}_1} \right)^2 + \left(1 + \gamma_1 \, \overline{M}_1^2 \right) \frac{\gamma_2}{\gamma_2 - 1} \left(\frac{\overline{u}_2}{\overline{u}_1} \right) = \frac{\gamma_1}{\gamma_1 - 1} + \frac{\gamma_1 \, \overline{M}_1^2}{2} + \frac{\gamma_1 \, \overline{Q}_M}{\overline{c}_1^2} \tag{3.69}$$

Then, by assuming $\gamma_1 \simeq \gamma_2$ and $\mathcal{R}_1 \simeq \mathcal{R}_2$ one finds

$$\frac{\overline{p}_2}{\overline{p}_1} = 1 - \gamma \, \overline{M}_1^2 \frac{\overline{Q}_M}{C_{p_1} \, \overline{T}_1} + \mathcal{O}(\overline{M}_1^4) \tag{3.70}$$

$$\frac{\overline{u}_2}{\overline{u}_1} = 1 + \frac{\overline{Q}_M}{C_{p_1} \, \overline{T}_1} + \mathcal{O}(\overline{M}_1^2) \tag{3.71}$$

that can be used into equations (3.54)-(3.56) to get [19]

$$\frac{p'_2}{\overline{p}_1} - \frac{p'_1}{\overline{p}_1} = \mathcal{O}(\overline{M}_1^2) \tag{3.72}$$

$$\frac{u'_2}{\overline{u}_1} - \frac{u'_1}{\overline{u}_1} = \left(\frac{\overline{T}_2}{\overline{T}_1} - 1 \right) \left(\frac{Q'_A}{\overline{Q}_A} - \frac{p'_1}{\overline{p}_1} \right) + \mathcal{O}(\overline{M}_1^2) \tag{3.73}$$

When using $u'_1/\overline{u}_1 = \mathcal{O}(\overline{M}_1)$ and $p'_1/\overline{p}_1 = \mathcal{O}(\overline{M}_1^2)$ (see Section 2.6.4), the $\mathcal{O}(\overline{M}_1)$ form of Eq. (3.73) reduces to Eq. (3.67).

The model (3.66)-(3.67) is closed when an expression is given for heat release fluctuations according to the characteristics of the combustion process. In general, the response of the heat release to acoustic perturbations depends on the several physical mechanisms affecting the combustion process (fuel injection, mixing, convective and diffusive transport, flame stabilization, chemical kinetics. etc.). As we have seen in the previous Chapter, heat release fluctuations may be expressed as $Q'_A = Q'_{A,N} + Q'_{A,I}$ where $Q'_{A,N}$ and $Q'_{A,I}$ are the contributions related to combustion noise and combustion instability respectively. By

expressing the combustion instability term as $Q'_{A,I}/\overline{Q}_A = (Q'_{A,I}/\overline{Q}_A)_p\, p'_1/\overline{p} + (Q'_{A,I}/\overline{Q}_A)_u\, u'_1/\overline{u}_1$, according to Eqs. (3.66)-(3.67) the flame is modeled as an active acoustic two-port in which the state variables pressure and velocity are coupled in the frequency domain by the expression

$$\begin{bmatrix} \dfrac{\widehat{p}_2}{\overline{\rho}_2\,\overline{c}_2} \\ \widehat{u}_2 \end{bmatrix} = \begin{bmatrix} \sqrt{\overline{T}_2/\overline{T}_1} & 0 \\ T_{21} & T_{22} \end{bmatrix} \begin{bmatrix} \dfrac{\widehat{p}_1}{\overline{\rho}_1\,\overline{c}_1} \\ \widehat{u}_1 \end{bmatrix} + \begin{bmatrix} 0 \\ S_u \end{bmatrix} \tag{3.74}$$

where

$$T_{21} = \gamma\, \overline{M}_1 \left(\frac{\overline{T}_2}{\overline{T}_1} - 1 \right) \left(\frac{\widehat{Q}_{A,I}}{\overline{Q}_A} \right)_p$$

$$T_{22} = 1 + \left(\frac{\overline{T}_2}{\overline{T}_1} - 1 \right) \left(\frac{\widehat{Q}_{A,I}}{\overline{Q}_A} \right)_u$$

$$S_u = \overline{u}_1 \left(\frac{\overline{T}_2}{\overline{T}_1} - 1 \right) \frac{\widehat{Q}_{A,N}}{\overline{Q}_A}$$

In Eq. (3.74) the transfer matrix elements T_{ij} model the amplifier behavior of the flame (responsible for eventual combustion instabilities), whereas the source term S_u depends only on frequency and represents the combustion noise contribution.

3.6 Linear Stability

Using the transfer matrix approach, the thermoacoustic stability of the premixed combustion system illustrated in Fig. 2.1 may be easily investigated. The analysis is performed in the frequency domain by applying the Laplace transform with zero initial conditions. For sufficiently low frequencies, the acoustic fields upstream and downstream of the flame (locations 1 and 2 respectively) may be assumed as one-dimensional. Therefore, the acoustics of hood and combustor may be respectively represented by means of the impedances $Z_1(s)$ and $Z_2(s)$, where $Z(s) = \widehat{p}(s)/\widehat{u}(s)$ is the ratio of the Laplace transforms of acoustic pressure $p'(t)$ and acoustic velocity $u'(t)$. By neglecting mean flow effects, Z_1 and Z_2 depend only on geometry, speed of sound and boundary impedances of hood and combustor. In case of low Mach number compact flame with heat release fluctuations independent of pressure oscillations, Eq. (3.74) may be used to express the acoustic velocity jump across the flame as

$$\widehat{u}_2(s) = T_{22}(s)\ \widehat{u}_1(s) + S_u(s) \tag{3.75}$$

The acoustic-heat release coupling is thus represented by the block diagram reported in Fig. 3.12, which is equivalent to the block diagram in Fig. 3.13 showing explicitely the feedback loop inherent to the thermoacoustic process. The link between acoustic field and source term S_u is given by

$$\widehat{u}_2(s) = H(s)\, S_u(s) \tag{3.76}$$

where

$$H(s) = \frac{1}{1 - T_{22}(s)\, Z_2(s)/Z_1(s)} \tag{3.77}$$

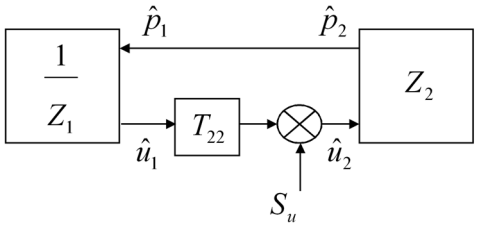

Figure 3.12: Thermoacoustic block diagram.

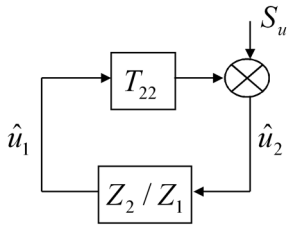

Figure 3.13: Feedback block diagram.

is the closed loop transfer function. Using the modal expansion (2.201), $Z_1(s)$ and $Z_2(s)$ may be approximated by rational functions. Thermoacoustic effects are usually associated to time delay terms $e^{-s\tau}$ [see Eq. (2.213)] appearing in the flame transfer matrix element T_{22}, which may be expressed as a rational function by means of the Padé approximation of accuracy h [76]

$$e^{-s\tau} \approx \left(\frac{-s\tau + 2\,h}{s\tau + 2\,h} \right)^h \qquad\qquad h \in (1, 2, \ldots) \tag{3.78}$$

Using Eq. (3.78), the closed loop transfer function may be written as a ratio of rational functions also for time-delayed systems, i.e.

$$H(s) = \frac{b_0 + b_1\,s + b_2\,s^2 + \ldots + b_m\,s^m}{a_0 + a_1\,s + a_2\,s^2 + \ldots + a_n\,s^n} \tag{3.79}$$

In the following analysis we assume that $m < n$ (real systems almost always satisfy this condition) and that the poles

$$s_j = i\,\Omega_j + \upsilon_j \tag{3.80}$$

(given by $a_0 + a_1\,s + a_2\,s^2 + \ldots + a_n\,s^n = 0$) are distinct, i.e. of multiplicity one. Under these hypothesis, Eq. (3.79) may be written in the form

$$H(s) = \sum_{j=1}^{n} \frac{K_j}{s - s_j} \tag{3.81}$$

The impulse response (i.e. the response to the input $S_u = \mathcal{L}[\delta(t)] = 1$) is obtained by applying the inverse Laplace transform to Eq. (3.81). It gives [66]

$$u'_2(t) = \sum_{j=1}^{n} K_j\,e^{\upsilon_j t}\,[\cos(\Omega_j\,t) + i\,\sin(\Omega_j\,t)] \tag{3.82}$$

The harmonic response is obtained by prescribing the sinusoidal input $S_u = \mathcal{L}[\sin(\Omega t)] = \Omega/(s^2 + \Omega^2)$, which leads to [66]

$$u'_2(t) = \sum_j \widetilde{K}_j \, e^{s_j t} + |H(i\,\Omega)| \sin\{\Omega\, t + \arg[H(i\,\Omega)]\} \tag{3.83}$$

where the constants $\widetilde{K}_j$ are obtained from the limit $\widetilde{K}_j = \lim_{s\to s_j}(s - s_j)H(s)$. According to Eqs. (3.82) and (3.83), the stability of the system is related to the sign of the growth rate υ_j as follows.

(i) $\upsilon_j < 0$: oscillations are damped in time (*stable system*);

(ii) $\upsilon_j = 0$: oscillations are stable in time (system at *stability border*);

(iii) $\upsilon_j > 0$: oscillations are amplified in time (*unstable system*).

When no combustion process takes place, then $T_{22} = 1$ the poles are given by

$$Z_2(s) = Z_1(s) \tag{3.84}$$

The real and imaginary part of the impedance Z define the *resistance* $R = Re(Z)$ and *reactance* $X = Im(Z)$ respectively. By assuming pure acoustic propagation in the volumes upstream and downstream of the flame (i.e. no generation of acoustic power), thus at the locations 1 and 2 one has $R_1 \leq 0$ and $R_2 \geq 0$ (i.e. acoustic power may be only absorbed). With no acoustic power absorption $R_1 = R_2 = 0$ and Eq. (3.84) reduces to $X_1(s) = X_2(s)$, which is a real equation giving real poles (stability border). When acoustic power is absorbed by the boundaries upstream and downstream of the flame (i.e. $R_1 < 0$ and/or $R_2 > 0$), then $\upsilon_j < 0$ and the system is stable. When combustion takes place, the flame transfer matrix may generate poles with $\upsilon_j > 0$. Within the limit of the current linear theory, poles with $\upsilon_j > 0$ lead to an impulse response amplitude growing unbounded in time (in real combustion systems the unbounded amplitude growth is limited by nonlinear effects). In this case the amplifier behavior of the flame leads to a combustion instability occurring at the frequency Ω_j and the related pressure spectrum is characterized by a high pulsation peak contained in a very narrow frequency band around Ω_j.

Chapter 4

Heat Release Fluctuations in Gas Turbine Flames

4.1 Quasi-Steady Premixed Flames

The low Mach number compact flame model (3.74) is closed when the heat release fluctuation $\widehat{Q}_{A,I}$ is given as a function of ($\widehat{p}_1$, $\widehat{u}_1$) and when the combustion noise term S_u is expressed as a function of the frequency. In general, $\widehat{Q}_{A,I}$ depends on the perturbation of the internal structure of the flame due to acoustic oscillations in the upstream flow field. We focus here on a laminar one-dimensional premixed flame whose chemistry is described by means of a one-step exothermic reaction. The governing equations for such a flame are Eqs. (2.1)-(2.3) that may be written as

$$\frac{\partial \rho}{\partial t} + \frac{\partial (\rho\, u)}{\partial x} = 0 \tag{4.1}$$

$$\rho \left(\frac{\partial u}{\partial t} + u \frac{\partial u}{\partial x} \right) + \frac{\partial p}{\partial x} = \frac{4}{3} \frac{\partial}{\partial x} \left(\mu \frac{\partial u}{\partial x} \right) \tag{4.2}$$

$$\rho\, C_p \left(\frac{\partial T}{\partial t} + u \frac{\partial T}{\partial x} \right) = \left(\frac{\partial p}{\partial t} + u \frac{\partial p}{\partial x} \right) + \frac{4}{3} \mu \left(\frac{\partial u}{\partial x} \right)^2 + \frac{\partial}{\partial x} \left(\kappa \frac{\partial T}{\partial x} \right) + Q \tag{4.3}$$

The system (4.1)-(4.3) is completed by the equation of state (2.4) and the equation [47]

$$\rho \left(\frac{\partial Y_F}{\partial t} + u \frac{\partial Y_F}{\partial x} \right) = \frac{\partial}{\partial x} \left(\rho\, D_F \frac{\partial Y_F}{\partial x} \right) - \dot{w}_F \tag{4.4}$$

where $Y_F = \rho_F / \rho$ is the fuel mass fraction with ρ_F fuel density, D_F the fuel molecular diffusion coefficient and $\dot{w}_F$ the reaction rate expressed as

$$\dot{w}_F = C\, \rho\, Y_F\, \exp(-\mathcal{E}/R^0 T) \tag{4.5}$$

where C is a constant, $\mathcal{E}$ the activation energy of the one-step chemical reaction *Fuel* $\rightarrow$ *Products* and R^0 the universal gas constant ($R^0 = \mathcal{R}\, \overline{W}$ with $\overline{W}$ average molecular weight of the mixture). The volumetric heat release Q is related to the fuel consumption by the relation

$$Q = \dot{w}_F\, \Delta h_F \tag{4.6}$$

where Δh_F is heat of reaction per unit mass of fresh mixture. When the Mach number is low, compressibility effects related to pressure variations may be neglected in Eq. (4.3) [47]. Furthermore, a steady solution may be searched for values of the activation energy $\mathcal{E}$ much larger than the thermal energy $R^0 T_b$, where the suffix b refers to the burned mixture. This leads to the Zel'dovich & Frank-Kamenetskii (ZFK) solution that is mathematically obtained by applying the asymptotic limit $Ze \rightarrow \infty$, being Ze the Zel'dovich number defined as

$$Ze = \frac{\mathcal{E}\,(T_b - T_u)}{R^0\,T_b^2} \tag{4.7}$$

where the suffix u refers to the fresh mixture. In the ZFK solution the flame structure is made of two different regions: the upstream convective-diffusive zone and the downstream reactive-diffusive zone [47]. In the upstream convective-diffusive region the reaction rate is negligible and convection is in balance with diffusion (the gas is preheated by heat diffusion coming from the reactive-diffusive zone). The thickness of the convective-diffusive region is

$$\delta_f \sim \frac{\rho_b}{\rho_u}\sqrt{D_{Fb}\,\tau_t} \tag{4.8}$$

where τ_t is the transit time

$$\tau_t \sim \frac{\delta_f}{S_f} \tag{4.9}$$

with S_f flame speed. In the thin reactive-diffusive zone of thickness δ_f/Ze, convection is negligible and the reactant concentration is depleted by diffusion.

The response of the ZFK flame solution to acoustic perturbations of the mass burning rate $m = \rho u$ has been studied in Ref. [77] for the system (4.1)-(4.4). The resulting flame transfer matrix corresponds to Eq. (3.74) with

$$\frac{Q'_{A,I}}{\overline{Q}_A} = \frac{\sqrt{1 + 4\,i\,\omega\tau_t} - 1}{2\,i\,\omega\tau_t}\,\frac{m'}{\overline{m}} \tag{4.10}$$

Eq. (4.10) is plotted in Fig. 4.1. For a compact premixed flame, the integration of Eq. (4.4) across the flame writes as

$$Q_A = m\,\Delta h_F\,[\,Y_F\,]_2^1 \tag{4.11}$$

(the term $d/dt\int_1^2 \rho Y_F dx$ has been neglected according to the compactness assumption). The perturbation of Eq. (4.11) with constant mass fractions yields the "quasi-steady" behavior $Q'_{A,I}/\overline{Q}_A = m'/\overline{m}$, which is equivalent to Eq. (4.10) when $\omega\tau_t \rightarrow 0$ (see Fig. 4.1). Therefore, a large activation energy premixed flame is quasi-steady in terms of heat release fluctuations when the acoustic time is much smaller than the transit time.

Under the quasi-steady heat release hypothesis and by assuming complete combustion (i.e. zero fuel mass fraction downstream of the flame), for a three-dimensional flame the heat release per unit of flame area may be expressed as

$$Q_A = \frac{1}{A_C}\oint_{A_f} \rho_f\,Y_{F,f}\,S_f\,\Delta h_F\,dA_f \tag{4.12}$$

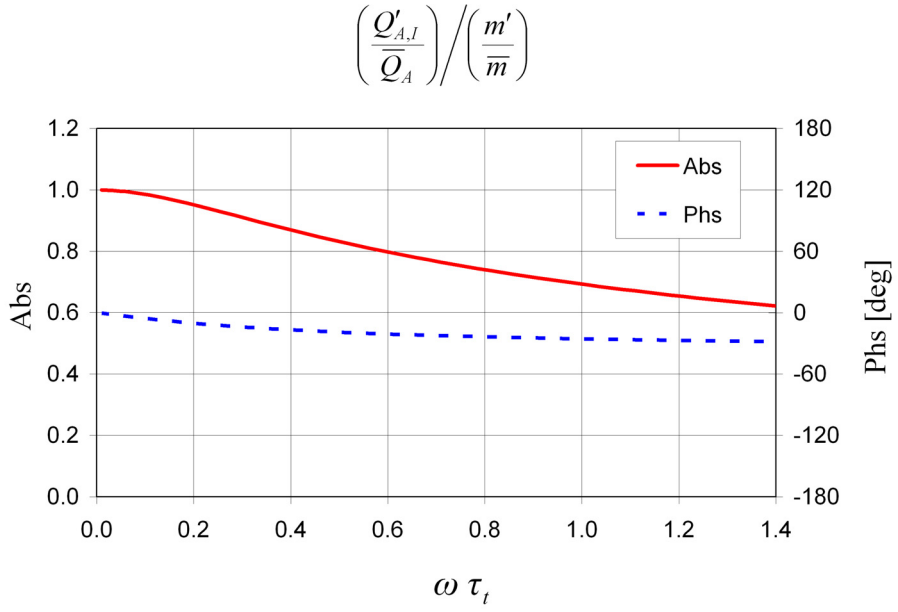

Figure 4.1: Transfer function of ZFK solution.

where A_f is the area of the flame front, A_C the cross-sectional combustor area and for the generic flow variable φ we have $\varphi_f = \varphi(\mathbf{x}_f, t)$ where $\mathbf{x}_f$ is the coordinate of the upstream flame front. By assuming $\overline{\rho}_f$, $\overline{S}_f$ and $\overline{Y}_{F,f}$ uniform over the upstream flame front, the perturbation of Eq. (4.12) gives

$$\frac{Q'_{A,I}}{\overline{Q}_A} = \left(\frac{Q'}{\overline{Q}}\right)_Y + \left(\frac{Q'}{\overline{Q}}\right)_{S_f} + \left(\frac{Q'}{\overline{Q}}\right)_\xi \tag{4.13}$$

where

$$\left(\frac{Q'}{\overline{Q}}\right)_Y = \frac{1}{\overline{A}_f}\oint_{\overline{A}_f} \frac{Y'_{F,f}}{\overline{Y}_{F,f}}\, d\overline{A}_f \tag{4.14}$$

$$\left(\frac{Q'}{\overline{Q}}\right)_{S_f} = \frac{1}{\overline{A}_f}\oint_{\overline{A}_f} \frac{S'_f}{\overline{S}_f}\, d\overline{A}_f \tag{4.15}$$

$$\left(\frac{Q'}{\overline{Q}}\right)_\xi = \frac{A'_f}{\overline{A}_f} \tag{4.16}$$

In Eq. (4.13) we have neglected heat release fluctuations induced by density fluctuations. In fact, if the perturbation flow is approximated as isentropic upstream of the flame, Eq. (2.34) yields $\rho'_f/\overline{\rho}_f = p'_f/\gamma\overline{p}_f$ with $p'_f/\overline{p}_f = \mathcal{O}(\overline{M}_1^2)$ (see Section 2.6.4). The modeling of the contributions (4.14)-(4.16) is discussed in the following Sections.

4.2 Fuel Concentration Fluctuations

The three-dimensional form of Eq. (4.4) written upstream of the flame (where $\dot{w}_F = 0$) is expressed for an inviscid flow as

$$\frac{\partial Y_F}{\partial t} + \mathbf{u} \cdot \nabla Y_F = 0 \tag{4.17}$$

By assuming $\overline{Y}_F \simeq const$, the acoustic perturbation of Eq. (4.17) reads as

$$\frac{\overline{D}\, Y'_F}{Dt} = 0 \tag{4.18}$$

that has the solution

$$Y'_{F,f} = Y'_F\,(\,\overline{\mathbf{x}}_f\,,\,t\,) = Y'_F\,(\mathbf{x}_{in}\,,\,t - \tau_f\,) \tag{4.19}$$

where $\mathbf{x}_{in}(\,\overline{\mathbf{x}}_f)$ is the injection point coordinate for the fuel element reaching the flame front at the mean flame front location $\overline{\mathbf{x}}_f$ and

$$\tau_f(\,\overline{\mathbf{x}}_f) = \int_{\mathbf{x}_{in}}^{\overline{\mathbf{x}}_f} \frac{d\chi}{|\,\overline{\mathbf{u}}\,|} \tag{4.20}$$

the mean time that the fluid element needs to travel from the injector to the flame front along the trajectory χ. In the frequency domain, Eq. (4.19) reads as

$$\widehat{Y}_F\,(\,\overline{\mathbf{x}}_f\,,\,\omega\,) = \exp\,[-i\,\omega\,\tau_f\,]\;\widehat{Y}_F\,(\mathbf{x}_{in}\,,\,\omega\,) \tag{4.21}$$

When turbulent diffusion effects are taken into consideration, instead of a single-value time-lag one has to consider a probability distribution of delays. According to Eq. (4.19), the time-domain impulse response $Y'_{F\delta}\,(\,\overline{\mathbf{x}}_f, t)$ writes as

$$Y'_{F\delta}\;(\,\overline{\mathbf{x}}_f\,,\,t\,) = \delta\,(\,t - \tau_f\,) \tag{4.22}$$

In case of particle diffusing in stationary and homogeneous turbulent fields, the probability distribution of delays has a Gaussian form [78]. Hence Eq. (4.22) may be replaced by the expression

$$Y'_{F\delta}\;(\,\overline{\mathbf{x}}_f\,,\,t\,) = \frac{1}{\sqrt{2\,\pi}\sigma_f} \exp\left[-\frac{(\,t - \tau_f)^2}{2\,\sigma_f^2}\right] \tag{4.23}$$

where $\sigma_f(\,\overline{\mathbf{x}}_f)$ is the variance of the time-lag distribution. The Laplace transform of Eq. (4.23) yields the impulsive response that leads to the frequency domain response

$$\widehat{Y}_F\,(\,\overline{\mathbf{x}}_f\,,\,\omega\,) = \exp\left(-i\,\omega\,\tau_f - \frac{1}{2}\,\omega^2\,\sigma_f\right)\;\widehat{Y}_F\,(\mathbf{x}_{in}\,,\,\omega\,) \tag{4.24}$$

To close the model, the fuel concentration fluctuations $\widehat{Y}_{F,in} = \widehat{Y}_F(\mathbf{x}_{in}, \omega\,)$ computed at the injector location must be computed. Being m_O and m_F the mass flow rate of air (oxidant) and fuel respectively, one can write

$$\frac{Y'_{F,in}}{\overline{Y}_{F,in}} = \frac{[m_F/(m_O + m_F)]'}{\overline{m}_F/(\,\overline{m}_O + \overline{m}_F)} = \frac{m'_F/\,\overline{m}_F - m'_O/\,\overline{m}_O}{1 + \overline{m}_f/\,\overline{m}_O} \simeq \frac{m'_F}{\overline{m}_F} - \frac{m'_O}{\overline{m}_O} \tag{4.25}$$

where the lean combustion condition $\overline{m}_O \gg \overline{m}_F$ has been used. The air density fluctuations in Eq. (4.25) may be expressed as

$$\frac{m'_O}{\overline{m}_O} \simeq \frac{u'_{in}}{\overline{u}_{in}} \tag{4.26}$$

where u_{in} is the flow velocity at the injector location and density fluctuations have been again neglected. Fuel mass flow rate fluctuations may be expressed in the frequency domain as

$$\frac{\widehat{m}_F}{\overline{m}_F} \simeq \frac{\widehat{u}_{F,in}}{\overline{u}_{F,in}} = \frac{\widehat{p}_{in}}{\overline{u}_{F,in}\, Z_{in}} \tag{4.27}$$

where $\widehat{p}_{in}$ is the pressure perturbation at the injector location and Z_{in} the impedance of the fuel supply system. Using Eqs. (4.24) and (4.27), the heat release fluctuation (4.14) may be expressed as

$$\left(\frac{\widehat{Q}}{\overline{\overline{Q}}}\right)_Y = \frac{1}{\overline{A}_f} \oint_{\overline{A}_f} \exp\left(-i\,\omega\,\tau_f - \frac{1}{2}\,\omega^2\,\sigma_f^2\right) \left(\frac{\widehat{p}_{in}}{\overline{u}_{F,in}\, Z_{in}} - \frac{\widehat{u}_{in}}{\overline{u}_{in}}\right) d\,\overline{A}_f \tag{4.28}$$

The application of the mean value theorem to the integral on the right-hand side of Eq. (4.28) yields

$$\left(\frac{\widehat{Q}}{\overline{\overline{Q}}}\right)_Y = \exp\left(-i\,\omega\,\tau_Y - \frac{1}{2}\,\omega^2\,\sigma_Y^2\right) \left(\frac{\widehat{p}_B}{\overline{u}_{F,B}\, Z_{FDS}} - \frac{\widehat{u}_B}{\overline{u}_B}\right) \tag{4.29}$$

where τ_Y and σ_Y are computed for the mean value point of the flame front, the quantities $(\cdot)_B$ are taken as averaged values over the fuel injection zone and Z_{FDS} represents the impedance of the fuel delivery system (FDS).
Under the incompressibility hypothesis, the fuel mass flow rate through the injector is given by

$$m_F = \sqrt{\frac{2\,\rho_F\,\Delta p_{F,in}}{\zeta_{in}}}\,A_{in} \tag{4.30}$$

where ρ_F is the fuel density, $\Delta p_{F,in}$ the injector pressure drop, A_{in} the injector cross-sectional area and ζ_{in} the injector pressure loss coefficient. The perturbation of Eq. (4.30) reads in the frequency domain as

$$\frac{\widehat{m}_F}{\overline{m}_F} = \frac{1}{2}\,\frac{\Delta\,\widehat{p}_{F,in}}{\Delta\,\overline{p}_{F,in}} \tag{4.31}$$

For stiff injectors $\Delta\,\overline{p}_{F,in} \gg |\Delta\,\widehat{p}_{F,in}|$ and thus fuel mass flow rate fluctuations may be neglected in Eq. (4.25). When this approximation holds, Eq. (4.29) writes as

$$\left(\frac{\widehat{Q}}{\overline{\overline{Q}}}\right)_Y = -\exp\left(-i\,\omega\,\tau_Y - \frac{1}{2}\,\omega^2\,\sigma_Y^2\right)\,\frac{\widehat{u}_B}{\overline{u}_B} \tag{4.32}$$

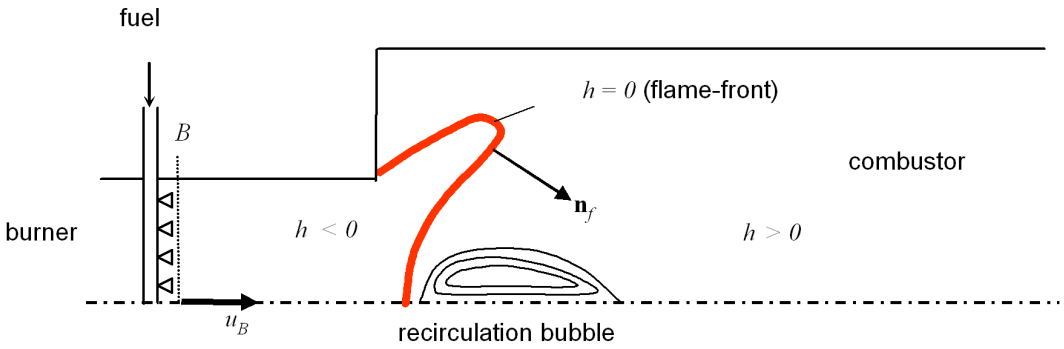

Figure 4.2: Axisymmetric flame front.

4.3 Flame Speed Fluctuations

In laminar flames, the flame speed of a specific fuel is a function of pressure, temperature and fuel concentration. When the temperature dependency is eliminated using the isentropic condition (3.62), one has

$$\frac{S'_f}{\overline{S}_f} = \vartheta_p \frac{p'_f}{\overline{p}_f} + \vartheta_Y \frac{Y'_{F,f}}{\overline{Y}_{F,f}} \tag{4.33}$$

For instance, for lean methane flames (i.e. equivalent ratio values greater than 0.5) ϑ_p falls in the range $0.4 < \vartheta_p < 0.5$ and $\vartheta_Y > 1$ [79], [80]. At high Damköhler numbers (i.e. with a chemical reaction time much larger than the turbulent time) the flame speed depends mainly on the turbulent velocity [47]. When the turbulence field is weakly affected by acoustic fluctuations, thus $S'_f = 0$ and then $(Q'/\overline{Q})_{S_f} = 0$.

4.4 Flame Area Fluctuations

In this Section we focus on the axisymmetric flame shown in Fig. 4.2. A flame front may be in general described by means of the function $h(\mathbf{x}, t)$ that is chosen such that $h < 0$ on the reactant side, $h > 0$ on the product side and $h = 0$ on the flame front that is supposed to move with the velocity $\mathbf{U}_f$. If the flame front is parameterized by $\mathbf{x}_f(\phi, \psi, t)$, then the trajectories of the material points defining the flame front are determined by the equation

$$\frac{\partial \mathbf{x}_f}{\partial t}(\phi, \psi, t) = \mathbf{U}_f\left(\mathbf{x}_f(\phi, \psi, t), t\right) \tag{4.34}$$

Since $h(\mathbf{x}_f(\phi, \psi, t), t) = 0$ for all (ϕ, ψ, t), on the flame front we have

$$\frac{dh(\mathbf{x}_f, t)}{dt} \equiv \nabla h \cdot \frac{\partial \mathbf{x}_f}{\partial t} + \partial h/\partial t = \nabla h \cdot \mathbf{U}_f + \partial h/\partial t = 0 \tag{4.35}$$

The flame front velocity may be expressed by means of the following kinematic balance

$$\mathbf{U}_f \cdot \mathbf{n}_f = \mathbf{u} \cdot \mathbf{n}_f - S_f \tag{4.36}$$

where $\mathbf{n}_f = \nabla h/|\nabla h|$ is the unit normal to the flame surface in the direction of products, $\mathbf{u}$ the flow velocity and S_f the burning velocity relative to the unburned gas. Using Eq. (4.36), Eq. (4.35) writes as

$$\frac{\partial h}{\partial t} + \mathbf{u} \cdot \nabla h = S_f \, |\nabla h| \tag{4.37}$$

that is known in combustion as G-equation [26], [81]. Note that Eq. (4.37) is valid only on the flame interface $\mathbf{x} = \mathbf{x}_f$.

4.4.1 V-flame model

The average position of the flame in Fig. 4.2 is approximated by the external (+) and internal (-) conical flame fronts (V-flame shape) illustrated in Fig. 4.3 (both the mean and instantaneous flame fronts are supposed to be axisymmetric). Therefore, in the cylindrical coordinate system (x, r, θ) of Fig. 4.4 the flame position is given by the axial displacement $\xi(r,t)$ (see Fig. 4.5) and the h function may be expressed as $h = \pm[\xi(r,t) - x]$, where the signs + and − stand for external and internal flame front respectively. The radius is taken as the independent variable because both external and internal flame fronts are supposed to have the same maximum radius b that remains constant when the flame oscillates. By expressing Eq. (4.37) as

$$\frac{\partial \xi}{\partial t} - u_x + u_r \, \frac{\partial \xi}{\partial r} = \pm S_f \sqrt{1 + \left(\frac{\partial \xi}{\partial r}\right)^2} \tag{4.38}$$

the mean flow and perturbation equations are expressed respectively as [27], [28]

$$\overline{V} = \mp \, \overline{S}_f \tag{4.39}$$

$$\frac{\partial \, \xi'}{\partial t} + \overline{U} \, \sin\beta \, \frac{\partial \, \xi'}{\partial r} = \frac{V' \pm S'_f}{\sin\beta} \tag{4.40}$$

where U and V are, respectively, the velocity component tangential to the steady flame front in the X-direction and the velocity component normal to the steady flame front in the Y-direction, being the axis X and Y shown in Fig. 4.5 where the flame angle β is also defined. In the frequency domain Eq. (4.40) reads as

$$\frac{d \, \widehat{\xi}}{dr} + \frac{i \, \omega}{\overline{U} \, \sin\beta} \, \widehat{\xi} = \frac{\widehat{V} \pm \widehat{S}_f}{\overline{U} \, \sin^2\beta} \tag{4.41}$$

In the following, the steady flow velocity component $\overline{U}$ is supposed to be constant on the average flame front. Being a the burner rim radius, Eq. (4.41) may be solved for the external flame front $\widehat{\xi}^{+}(r)$ and internal flame front $\widehat{\xi}^{-}(r)$ using the boundary conditions $\widehat{\xi}^{+}(a) = 0$ and $\widehat{\xi}^{-}(0) = \widehat{\xi}_0$ respectively. We obtain

$$\widehat{\xi}^{+}(r) = \frac{\tau^{+}}{(b-a) \, \sin\beta^{+}} \int_a^r \left[\widehat{V}^{+}(\widetilde{r}) + \widehat{S}_f^{+}(\widetilde{r}) \right] e^{-i\,\omega\,\tau^{+}\,(r-\widetilde{r})/(b-a)} \, d\,\widetilde{r} \tag{4.42}$$

$$\widehat{\xi}^{-}(r) = e^{-i\,\omega\,\tau^{-}\,r/b} \, \widehat{\xi}_0 + \frac{\tau^{-}}{b \, \sin\beta^{-}} \int_0^r \left[\widehat{V}^{-}(\widetilde{r}) - \widehat{S}_f^{-}(\widetilde{r}) \right] e^{-i\,\omega\,\tau^{-}\,(r-\widetilde{r})/b} \, d\,\widetilde{r} \tag{4.43}$$

where the characteristic time τ^+ of the external flame front and the characteristic time τ^- of the internal flame front are defined as

$$\tau^+ = \frac{(b-a)/\sin\beta^+}{\overline{U}^+}\,, \qquad \tau^- = \frac{b/\sin\beta^-}{\overline{U}^-} \tag{4.44}$$

The times τ^+ and τ^- represent the time needed to transit along the external and internal flame fronts with the tangential velocities $\overline{U}^+$ and $\overline{U}^-$ respectively.
Next, the flame area is expressed as[1]

$$A_f = 2\,\pi \int_a^b \sqrt{1+\left(\frac{\partial \xi^+}{\partial r}\right)^2}\, r\, dr + 2\,\pi \int_0^b \sqrt{1+\left(\frac{\partial \xi^-}{\partial r}\right)^2}\, r\, dr \tag{4.45}$$

Eq. (4.45) shows that the perturbation of the area element is associated to the fluctuation of the flame front slope. Using Eq. (4.45), the linear fluctuation of the flame front is expressed in the frequency domain as

$$\widehat{A}_f = 2\,\pi\,\cos\beta^+ \int_a^b \frac{\partial\,\widehat{\xi}^+}{\partial r}\, r\, dr + 2\,\pi\,\cos\beta^- \int_0^b \frac{\partial\,\widehat{\xi}^-}{\partial r}\, r\, dr =$$

$$= 2\,\pi\,\cos\beta^+ \left[b\,\widehat{\xi}(b) - \int_a^b \widehat{\xi}^+\, dr\right] + 2\,\pi\,\cos\beta^- \left[b\,\widehat{\xi}(b) - \int_0^b \widehat{\xi}^-\, dr\right] \tag{4.46}$$

By using Eqs. (4.42) and (4.43) into Eq. (4.46) with $\widehat{V}^+$, $\widehat{V}^-$ and $\widehat{S}_f$ taken as constant on the flame front, one obtains

$$\frac{\widehat{A}_f}{\overline{A}} = \Theta^+ \frac{\widehat{V}^+ + \widehat{S}_f^+}{\overline{U}^+ \tan\beta^+}\, F_\xi(a/b\,,\,\omega\tau^+) + \Theta^- \left[\frac{\widehat{V}^- - \widehat{S}_f^-}{\overline{U}^- \tan\beta^-} - \frac{i\omega\tau^- \sin(2\beta^-)\,\widehat{\xi}_0}{2b}\right] F_\xi(0\,,\,\omega\tau^-) \tag{4.47}$$

where

$$F_\xi(\psi\,,\,\omega\tau) = \frac{2}{1+\psi}\,\frac{(1-\psi+i\,\omega\,\tau)\;e^{-i\,\omega\,\tau} - 1 + (1-i\,\omega\,\tau)\;\psi}{(\omega\,\tau)^2} \tag{4.48}$$

and

$$\Theta^+ = \left[1+\left(\frac{\sin\beta^+}{\sin\beta^-}\right)\frac{b^2}{b^2-a^2}\right]^{-1}\,, \qquad \Theta^- = \left[1+\left(\frac{\sin\beta^-}{\sin\beta^+}\right)\frac{b^2-a^2}{b^2}\right]^{-1} \tag{4.49}$$

The magnitude and phase of $F_\xi(\psi\,,\,\omega\tau)$ are respectively plotted in Figs. 4.6 and 4.7 for $\psi = 0$ and $\psi = 0.5$. In Eq. (4.47), we can define $\widehat{u}_0 = i\omega\,\widehat{\xi}_0$ as the velocity of the axial point of the flame front. By

[1] Being the standard parameterization of the flame surface given by $x = \xi(\phi,\psi)$, $y = \chi(\phi,\psi)$, $z = \zeta(\phi,\psi)$, one has

$$dA_f = \sqrt{EG - F^2}\, d\phi\, d\psi$$

where $E = \xi_\phi^2 + \chi_\phi^2 + \zeta_\phi^2$, $G = \xi_\psi^2 + \chi_\psi^2 + \zeta_\psi^2$ and $F = \xi_\phi\xi_\psi + \chi_\phi\chi_\psi + \zeta_\phi\zeta_\psi$. When $x = \xi(r)$, $y = r\cos\theta$ and $z = r\,\sin\theta$, it gives

$$dA_f = r\,\sqrt{1+\xi_r^2}\, dr\, d\theta$$

using the approximation $\Theta^+ \ll \Theta^-$ and the high Damköhler number condition $\widehat{S}_f = 0$ (i.e. flame area fluctuations are supposed to be related only to the flame wrinkling associated to the oscillations of the velocity normal to the flame front), one can write

$$\left(\frac{\widehat{Q}}{\overline{Q}}\right)_\xi = n_\xi(\omega)\, F_\xi(0\,,\,\omega\tau_\xi)\,\frac{\widehat{u}_B}{\overline{u}_B} \tag{4.50}$$

where the interaction index $n_\xi(\omega)$ is defined as

$$n_\xi(\omega) = \Theta^- \,\frac{\left(\widehat{V}^- - \widehat{u}_0 \sin\beta^-\right)/(\overline{U}^- \tan\beta^-)}{\widehat{u}_B/\overline{u}_B} \tag{4.51}$$

with u_B burner velocity at the injection point location (see Fig. 4.2) and $\tau_\xi \equiv \tau^-$. Being $(\widehat{Q}/\overline{Q})_{S_f} = 0$, thus one must have $\lim_{\omega\to 0}(\widehat{Q}/\overline{Q})_\xi = \widehat{u}_B/\overline{u}_B$ that leads to the condition

$$\lim_{\omega\to 0} n_\xi(\omega) = 1 \tag{4.52}$$

Eqs. (4.32) and (4.50) may be combined to give

$$\frac{\widehat{Q}_{A,I}}{\overline{Q}_A} = \left[n_\xi\, F_\xi(0\,,\,\omega\tau_\xi) - \exp\left(-i\,\omega\,\tau_Y - \frac{1}{2}\,\omega^2\,\sigma_Y^2\right)\right]\frac{\widehat{u}_B}{\overline{u}_B} \tag{4.53}$$

Eqs. (4.52) and (4.53) yield $\lim_{\omega\to 0}\widehat{Q}_{A,I}/\overline{Q}_A = 0$, which is consistent with the hypothesis of no fluctuations of injected fuel mass flow rate that has been employed to derive Eq. (4.32).

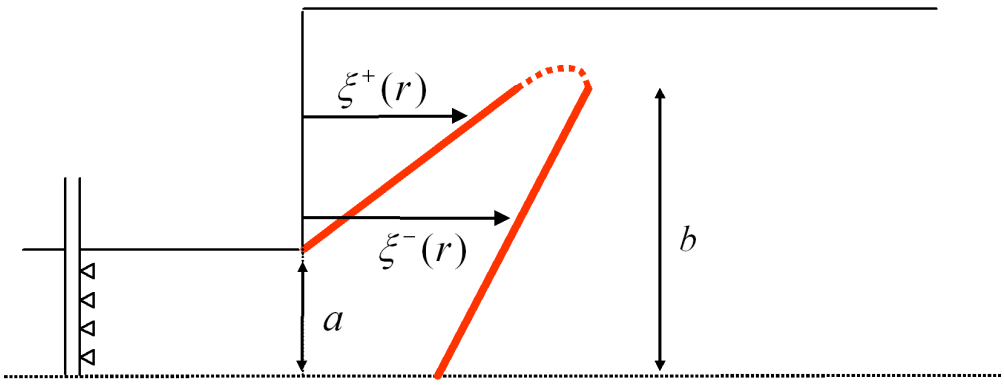

Figure 4.3: V-flame model of axisymmetric flame front.

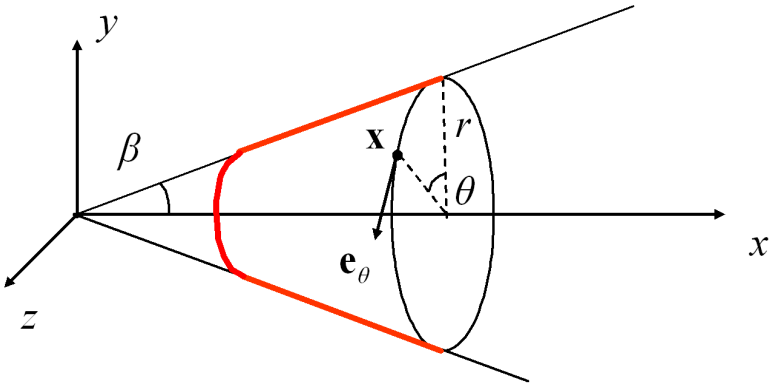

Figure 4.4: Cylindrical coordinate system.

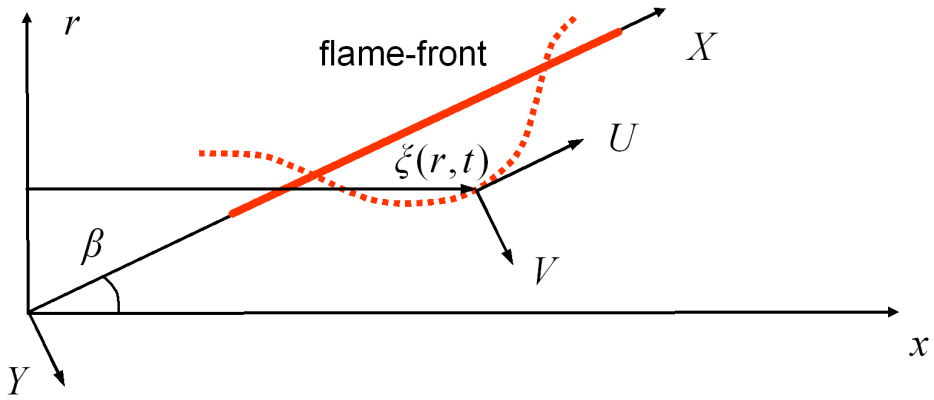

Figure 4.5: Sketch of V-flame.

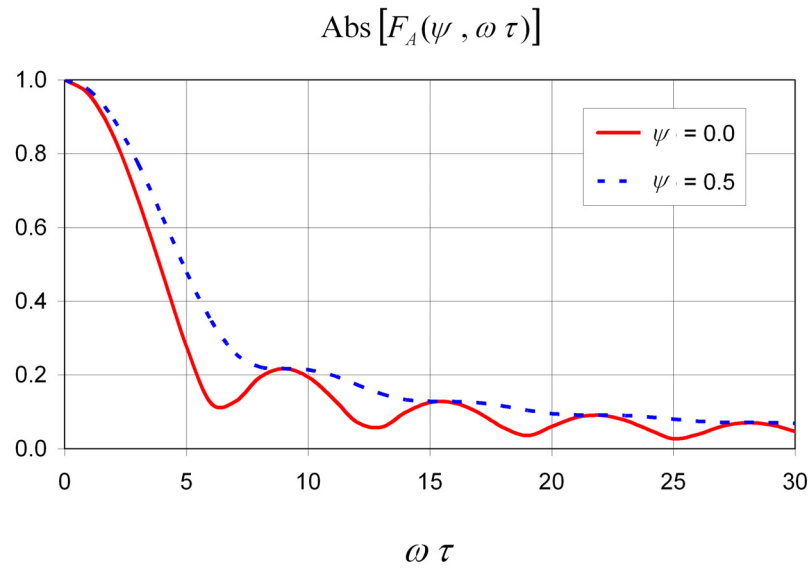

Figure 4.6: Magnitude of characteristic function for heat release fluctuations induced by flame area oscillations.

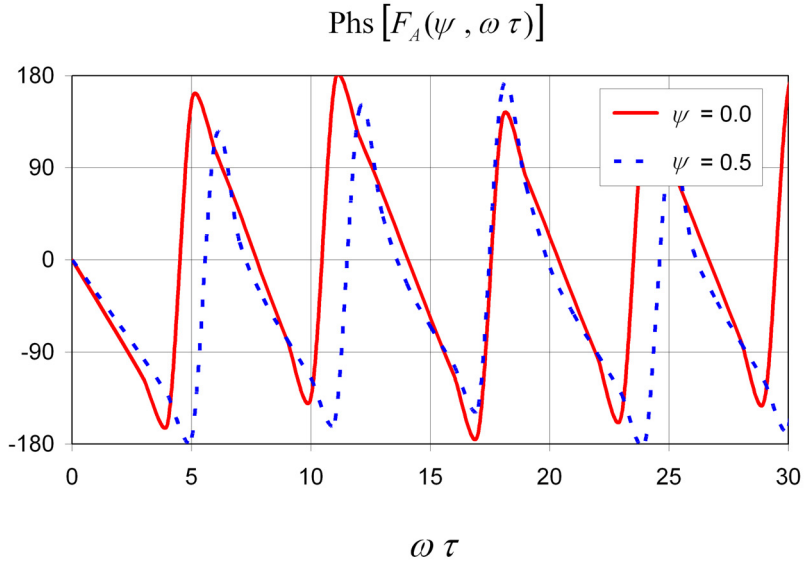

Figure 4.7: Phase ([*deg*]) of characteristic function for heat release fluctuations induced by flame area oscillations.

4.5 Transfer Matrix Measurements

In combination with the low-order models presented in the previous Sections, flame transfer matrices have been also measured under atmospheric conditions in the combustion facility shown in Fig. 4.8. Both the plenum chamber upstream of the burner and the combustion chamber downstream of the burner were circular tubes of diameter d. The plenum chamber contained perforated plates to reduce the turbulence level of the flow. The combustion chamber consisted either of an air cooled double wall metal liner or of an air cooled double wall quartz glass to provide full visual access to the flame. The exhaust system was an air-cooled tube with the same cross-section as the combustion chamber to avoid acoustic reflections at area discontinuities. The length of the exhaust tube was adjustable. The acoustic boundary condition of the exhaust system could be adjusted from almost anechoic (reflection coefficient < 0.15) to open end reflection using orifices of different diameters. Controlled excitation of the burner flow was accomplished by circumferential arrays of loudspeakers equally spaced in polar angle. Two sets of loudspeakers were placed in the plenum and combustion chamber at a distance of $4.2\,d$ and $6.8\,d$ respectively upstream and downstream of the burner exit plane. Pressure fluctuations were measured using Brüel & Kjær water-cooled microphones. The arrays of water-cooled 1/4" condenser microphones (four in the plenum chamber and five in the combustion chamber) were flush-mounted along the walls (using condenser microphones rather than piezoelectric pressure probes gave the advantage of highly accurate phase and amplitude data that is necessary for acoustic measurements). The microphone holders consisted of small orifices (diameter of 0.5 mm) open to the plenum and combustion chamber. The microphone diaphragm was placed in a small cavity and was heat radiation protected. The resonance frequency of the holder was larger than $20kHz$. The frequency response of the microphones in probe

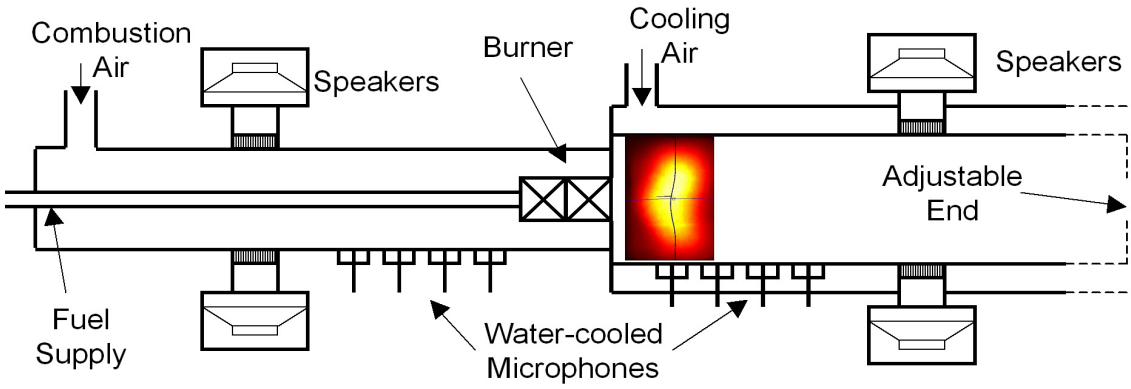

Figure 4.8: Combustion test facility for flame transfer function measurements.

holders were compared against standard B&K microphones and showed good agreement. Following the approach of Section 3.3.2, the Multi-Microphone Method applied to three independent test states (upstream loudspeaker forcing, downstream loudspeaker forcing and no forcing) was used to reconstruct the transfer matrix of the combined burner and flame element. In particular, by assuming plane wave propagation from the upstream microphone location I to the upstream side 1 of the burner exit and from the downstream microphone location II to the downstream side 2 of the burner exit (see Fig. 4.9), the transfer matrix $\mathbf{T}_{bf}^{ex}$ relating the cross-sections 1 and 2 was obtained. The measurement repeated in absence of combustion provided the transfer matrix of the burner only $\mathbf{T}_{b}^{ex}$, so that the experimental flame transfer matrix $\mathbf{T}_{f}^{ex}$ could be obtained by using the relation [11]

$$\mathbf{T}_{f}^{ex} = \mathbf{T}_{bf}^{ex} \cdot \mathbf{T}_{b}^{ex\,-1} \tag{4.54}$$

(the underlying assumption was that the transfer matrix $\mathbf{T}_{b}^{ex}$ did not change because of the combustion process).

4.6 Transfer Matrix Fits

In the present Section, analytical transfer matrix models are fit to transfer matrix measurements. By using Eqs. (4.29) and (4.50) to express the heat release fluctuations into Eq. (3.67), one gets

$$\widehat{u}_2 = \widehat{u}_1 + \overline{u}_1 \left(\frac{\overline{T}_2}{\overline{T}_1} - 1 \right) \left\{ [H_\xi(\omega) - H_Y(\omega)] \, \frac{\widehat{u}_B}{\overline{u}_B} + H_Y(\omega) \, \frac{\widehat{p}_B}{\overline{u}_{F,B} \, Z_{FDS}} \right\} \tag{4.55}$$

where

$$H_\xi(\omega) = n_\xi(\omega) \, F_\xi(0\,,\, \omega\tau_\xi)\,, \qquad H_Y(\omega) = \exp\left(-i\,\omega\,\tau_Y - \frac{1}{2}\,\omega^2\,\sigma_Y^2 \right)$$

(the burner cross-section B is indicated in Fig. 4.9). Using the measured burner transfer matrix $\mathbf{T}_{b}^{ex}$, the acoustic fields in B and 1 may be related by means of the expressions

$$\frac{\widehat{p}_B}{\overline{\rho}_1 \, \overline{c}_1} \simeq (T_b^{ex})_{11}^{-1} \, \frac{\widehat{p}_1}{\overline{\rho}_1 \, \overline{c}_1} + (T_b^{ex})_{12}^{-1} \, \widehat{u}_1 \tag{4.56}$$

$$\frac{\widehat{u}_B}{\overline{u}_B} \simeq \frac{\widehat{u}_1}{\overline{u}_1} \tag{4.57}$$

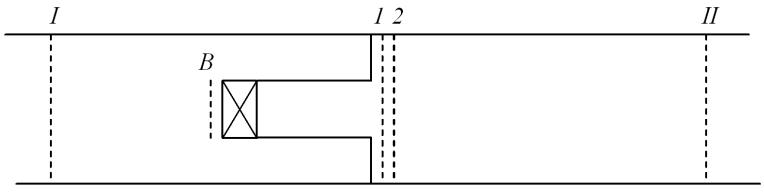

Figure 4.9: Schematic of burner in combustion test rig.

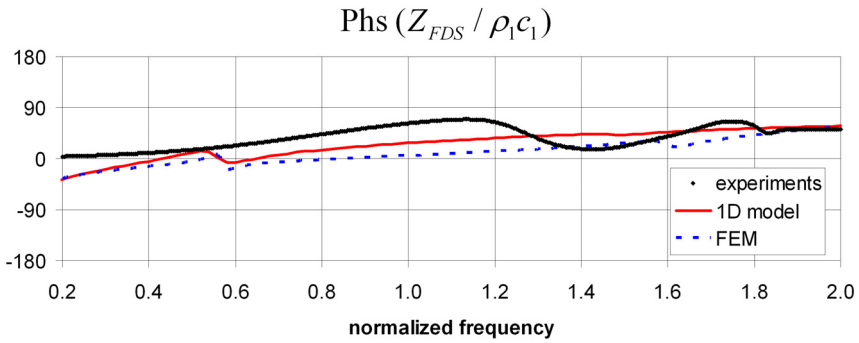

Figure 4.10: Phase [deg] of normalized fuel delivery system impedance.

so that Eqs. (4.55) may be rewritten as

$$\widehat{u}_2 = (T_f^{an})_{21} \frac{\widehat{p}_1}{\overline{\rho}_1 \overline{c}_1} + (T_f^{an})_{22} \widehat{u}_1 \tag{4.58}$$

where the elements of the analytical flame transfer function $\mathbf{T}_f^{an}$ are given by

$$(T_f^{an})_{21} = \left(\frac{\overline{T}_2}{\overline{T}_1} - 1 \right) \frac{\overline{u}_1 \, (T_b^{ex})_{11}^{-1}}{\overline{u}_{F,B} \, Z_{FDS} / \overline{\rho}_1 \, \overline{c}_1} H_Y(\omega) \tag{4.59}$$

$$(T_f^{an})_{22} = 1 + \left(\frac{\overline{T}_2}{\overline{T}_1} - 1 \right) [H_\xi(\omega) - H_Y(\omega)] + \frac{(T_b^{ex})_{12}^{-1}}{(T_b^{ex})_{11}^{-1}} (T_f^{an})_{21} \tag{4.60}$$

A transfer matrix $\mathbf{T}_e$ may be defined where the effect of the fuel delivery system is removed. For analytical and experimental transfer matrices, the elimination of the FDS effect from the 22−element reads respectively as

$$(T_e^{an})_{22} = 1 + \left(\frac{\overline{T}_2}{\overline{T}_1} - 1 \right) [H_\xi(\omega) - H_Y(\omega)] \tag{4.61}$$

$$(T_e^{ex})_{22} = (T_f^{ex})_{22} - \frac{(T_b^{ex})_{12}^{-1}}{(T_b^{ex})_{11}^{-1}} (T_f^{ex})_{21} \tag{4.62}$$

Fig. 4.10 shows an example of the phase of Z_{FDS} obtained from Eq. (4.59) by imposing $(T_f^{an})_{21} = (T_f^{ex})_{21}$. The FDS removal approach has been validated in Fig. 4.10 by also modeling the FDS by means of an acoustic network composed by one-dimensional ducts [see Eq. (3.4)] connected by area changes ("1D model" plot) and by means of an acoustic Finite Element Method ("FEM" plot) [73].
In the following, analytical flame transfer matrix elements $(T_e^{an})_{22}$ are fitted to experimental ones $(T_e^{ex})_{22}$ obtained with different hardware and under different combustion operation conditions.

4.6.1 Pre-premix test cases

The flame transfer matrices have been measured for a modified version of the EV burner (see Section 3.3.3). First, measurements were performed by operating the burner in "pre-premix" conditions,

i.e. gas fuel was injected far upstream of the burner in order to suppress fuel concentration fluctuations at the burner location (this is in contrast with the standard "premix" mode where the gas is injected directly inside the burner). In Figs. 4.11-4.13, the magnitude and phase of the transfer matrix elements $(T_f^{ex})_{22}$ measured in pre-premix conditions for three different flame temperatures are compared to the analytical results obtained by fitting Eq. (4.61) (with $H_Y = 0$) to the experimental plots [with no fuel injection inside the burner we do not need to apply Eq. (4.62) and include the fuel concentration term into the analytical model]. Both the parameter n_ξ and τ_ξ have been taken as constant in the fitting procedure. In spite of these and the other approximations employed to derive Eq. (4.50), the agreement between measurements and analytical model is good specially in the low frequency range. The analytical curves are characterized by values of the interaction index n_ξ comprises between 2 and 2.5, whereas the time-lags τ_ξ are consistent with the values obtained from steady CFD simulations. In particular, when increasing the flame temperature an increase in n_ξ and a decrease in τ_ξ is observed.

4.6.2 Premix test cases

Measurements have been also performed in premix conditions for different versions of the modified EV burner. Even at full load, the comparison between $(T_e^{ex})_{22}$ and $(T_f^{ex})_{22}$ has demonstrated that the pressure drop across the premix injectors is not sufficiently large to avoid fluctuations of fuel mass flow rate, so that 22-elements given by Eqs. (4.61) and (4.62) have been compared. The results of Figs. 4.15 and 4.16 differ from those reported in Fig. 4.14 because of the use of a different fuel lance geometry and fuel lance axial position respectively (see Section 3.3.3), whereas Fig. 4.17 presents the results related to the use of a different swirler. Even if no liquid fuel is injected throughout the fuel lance, Figs. 4.14-4.16 show that a different lance geometry or lance position may modify the aerodynamic field and then the flame dynamics in premix operation. The analytical fits reported in Figs. 4.14-4.17 have been obtained by using Eq. (4.61). As a result of the fitting process, we have found $|n_\xi| = 1-2$ with $n_\xi < 0$ for the case in Fig. 4.17. Note that a difference in the sign of n_ξ means that velocity perturbations normal to the flame front respond in opposite way to a given perturbation of velocity in the burner, this effect being probably related to a different response of the recirculation bubble (see Fig. 4.2) that is responsible for flame stabilization. The fuel concentration time-lag values τ_Y were in agreement with those provided by steady CFD computations. The analytical fit of Fig. 4.15 has values of n_ξ and τ_ξ similar to those of the pre-premix cases and larger than those of the analytical fits in Figs. 4.14 and 4.16, whereas the case in Fig. 4.17 is associated to the largest τ_ξ (that means the flame is more elongated and/or with a large tangential flow velocity).

4.6.3 Oil test cases

Finally, measurements have been performed using oil injection throughout the central fuel lance shown in Figs. 3.6 and 3.7. Figs. 4.18-4.20 and Figs. 4.21-4.22 report oil measurements obtained by varying flame temperature and air temperature respectively. In order to account for the acoustic influence of the oil delivery system, the measurements have been post-processed by means of Eq. (4.62) and compared with the analytical model (4.61), including both flame area and fuel concentration fluctuations. In the analytical fits of Figs. 4.18-4.20, when the flame temperature increases thus n_ξ decreases from 2 to 1.5 whereas both τ_ξ and τ_Y increase. The results in Figs. 4.17 and 4.18 refer to the same burner operating at

the same conditions (air and flame temperature) with gas and oil respectively. With respect to the gas transfer matrix fit reported in Fig. 4.17, the oil fit in Fig. 4.18 is characterized by a positive value of n_ξ (indicating a different response of the aerodynamic field to perturbations of the axial burner velocity), a smaller τ_ξ and a larger τ_Y.

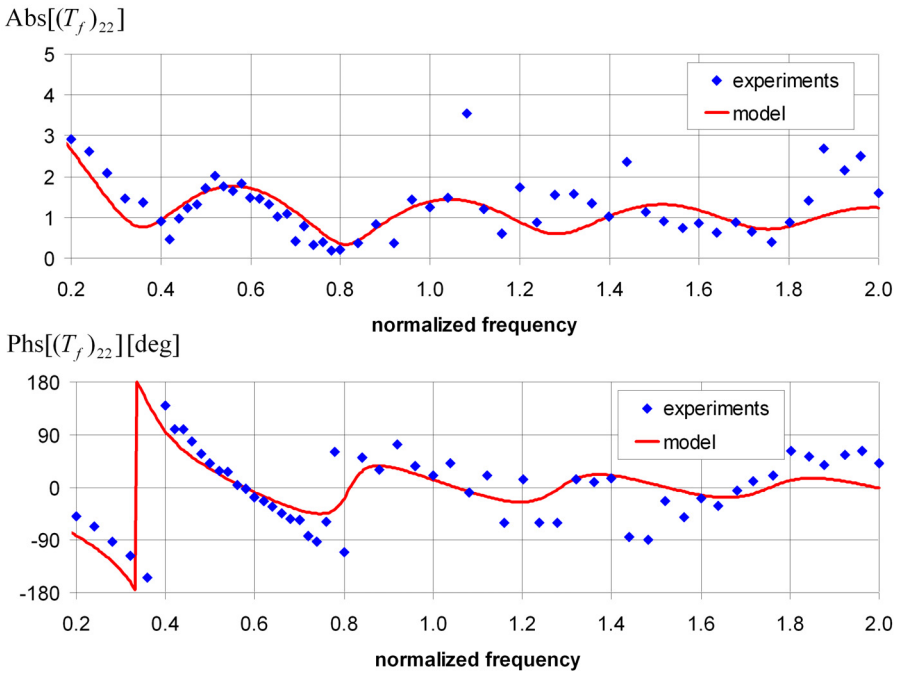

Figure 4.11: Magnitude (top) and phase (bottom) of $(T_f)_{22}$ flame transfer function element. Pre-premix test case with flame temperature $(T_{flame})_{ref}$.

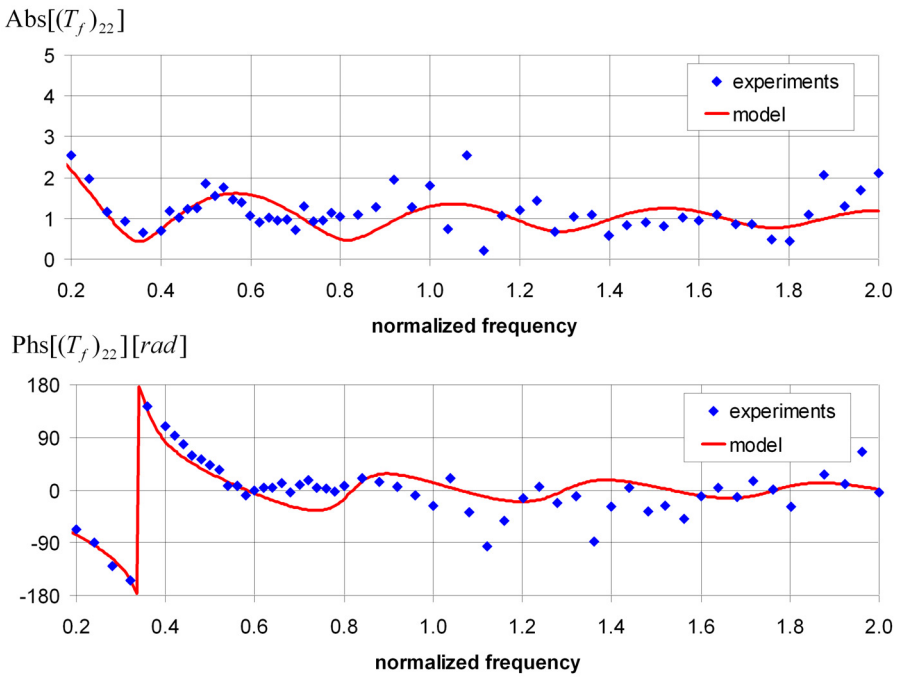

Figure 4.12: Magnitude (top) and phase (bottom) of $(T_f)_{22}$ flame transfer function element. Pre-premix test case with flame temperature $(T_{flame})_{ref} - 50K$.

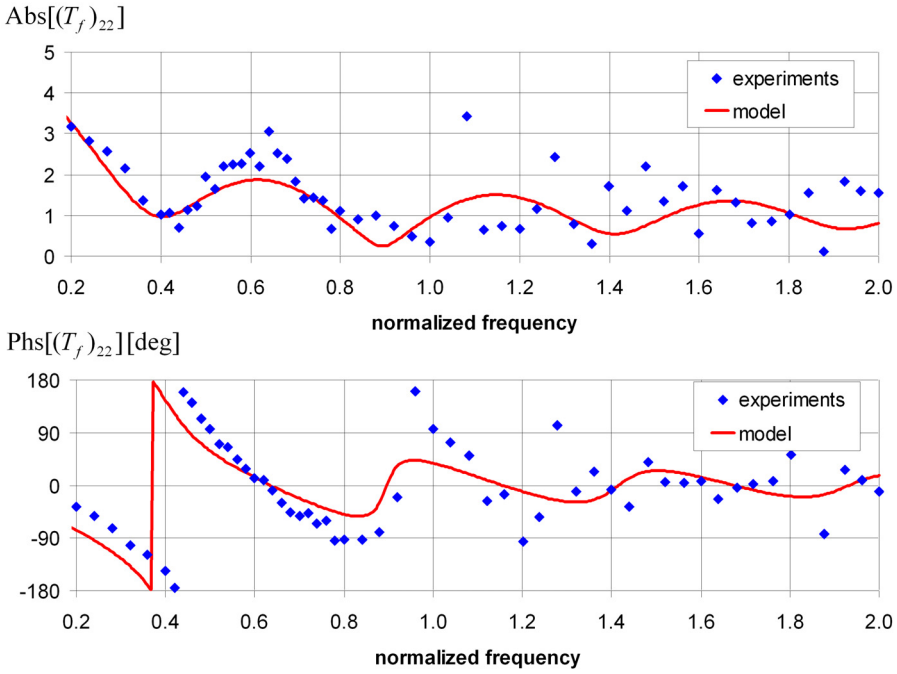

Figure 4.13: Magnitude (top) and phase (bottom) of $(T_f)_{22}$ flame transfer function element. Pre-premix test case with flame temperature $(T_{flame})_{ref} + 50K$.

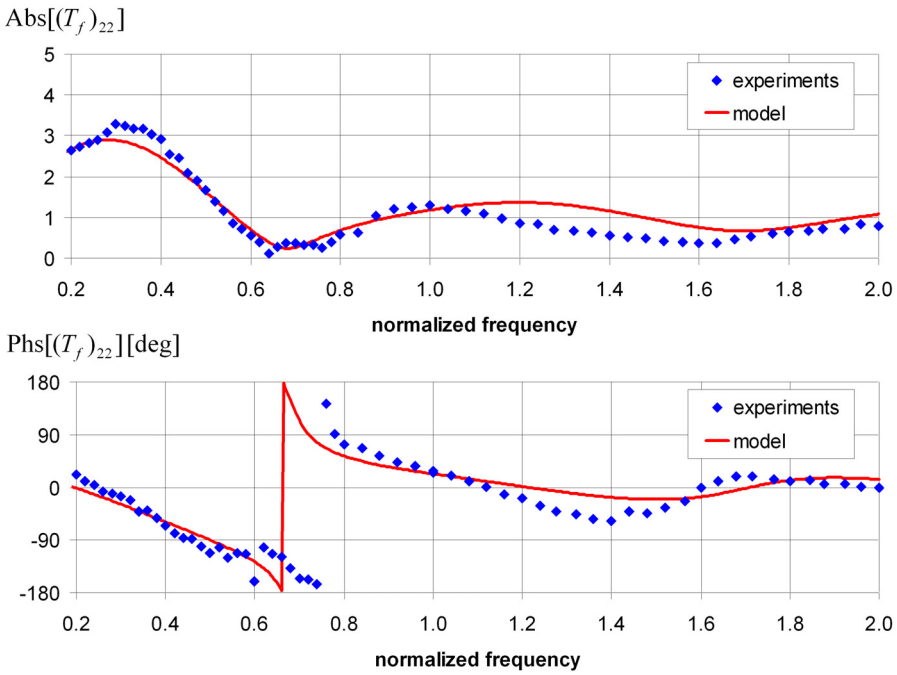

Figure 4.14: Magnitude (top) and phase (bottom) of $(T_e)_{22}$ flame transfer function element. Premix test case with reference fuel lance and swirler.

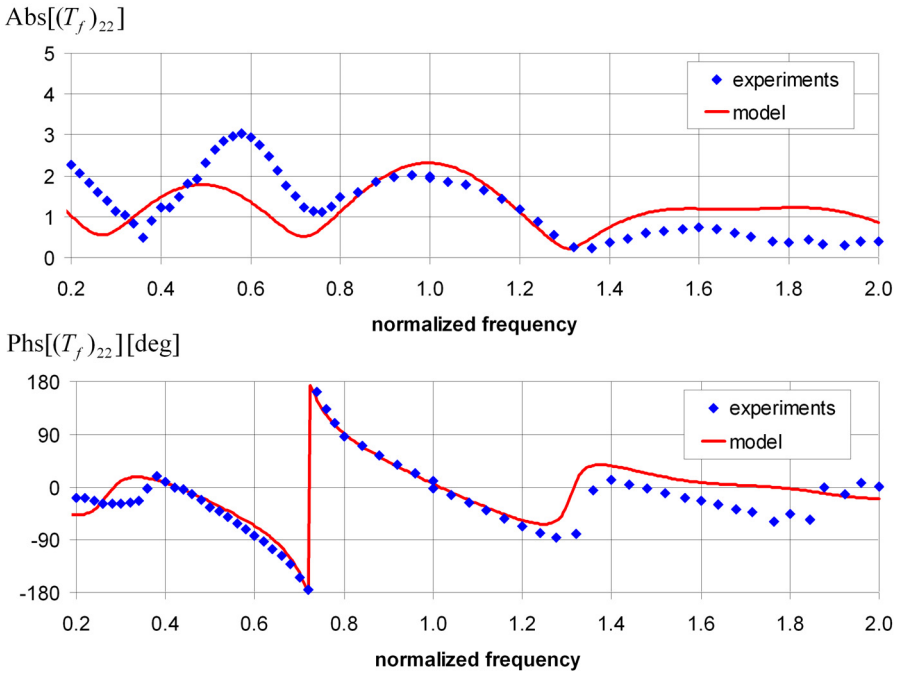

Figure 4.15: Magnitude (top) and phase (bottom) of $(T_e)_{22}$ flame transfer function element. Premix test case with modified fuel lance geometry.

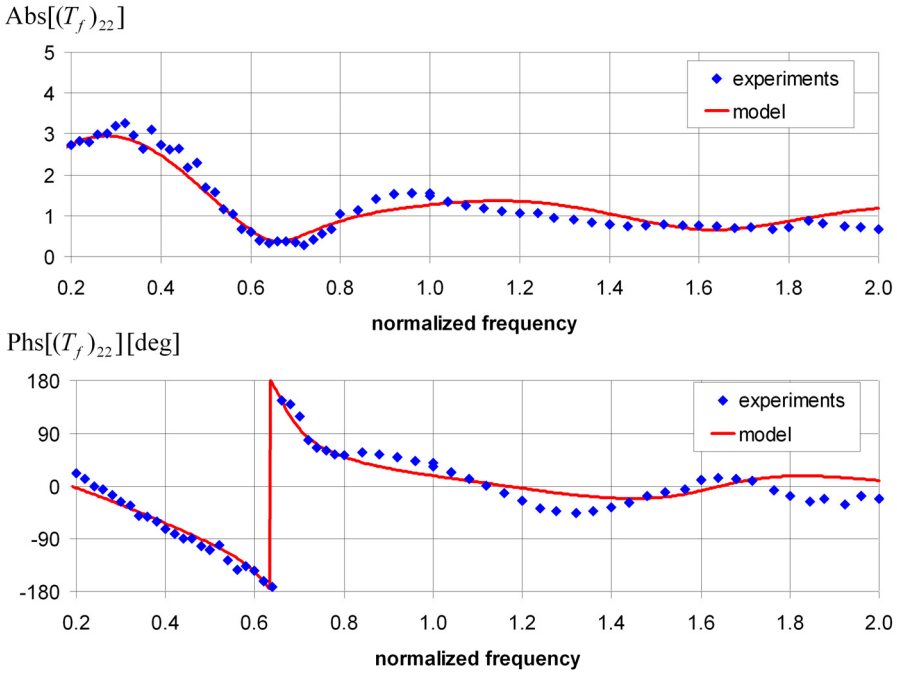

Figure 4.16: Magnitude (top) and phase (bottom) of $(T_e)_{22}$ flame transfer function element. Premix test case with modified fuel lance axial position.

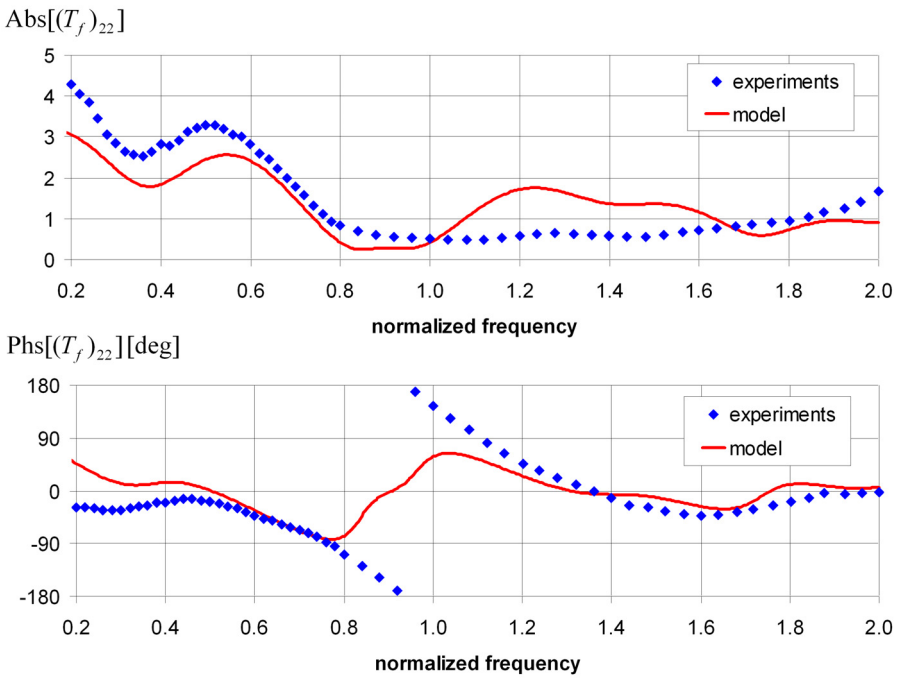

Figure 4.17: Magnitude (top) and phase (bottom) of $(T_e)_{22}$ flame transfer function element. Premix test case with modified swirler (same hardware than the hardware used in the oil tests reported in Figs. 4.18-4.22).

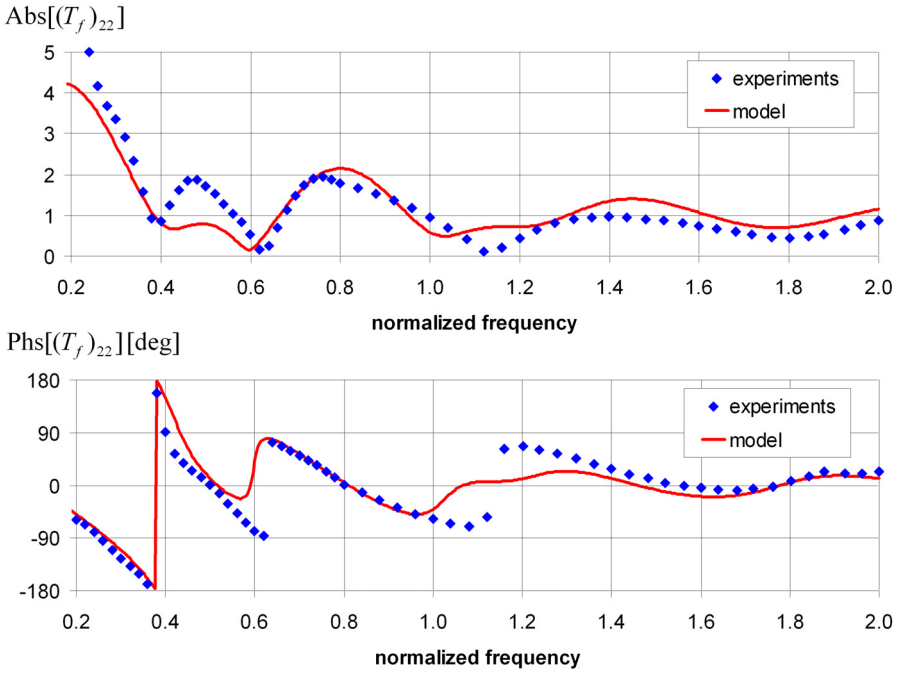

Figure 4.18: Magnitude (top) and phase (bottom) of $(T_e)_{22}$ flame transfer function element. Oil test case with air temperature $(T_a)_{ref}$ and flame temperature $(T_{flame})_{ref}$.

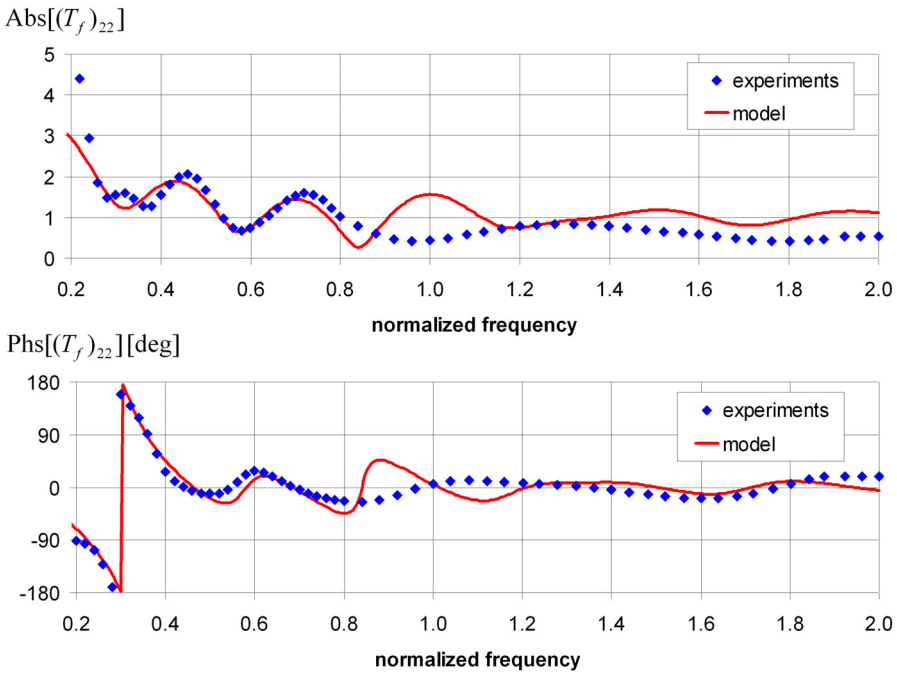

Figure 4.19: Magnitude (top) and phase (bottom) of $(T_e)_{22}$ flame transfer function element. Oil test case with air temperature $(T_{air})_{ref}$ and flame temperature $(T_{flame})_{ref} - 130K$.

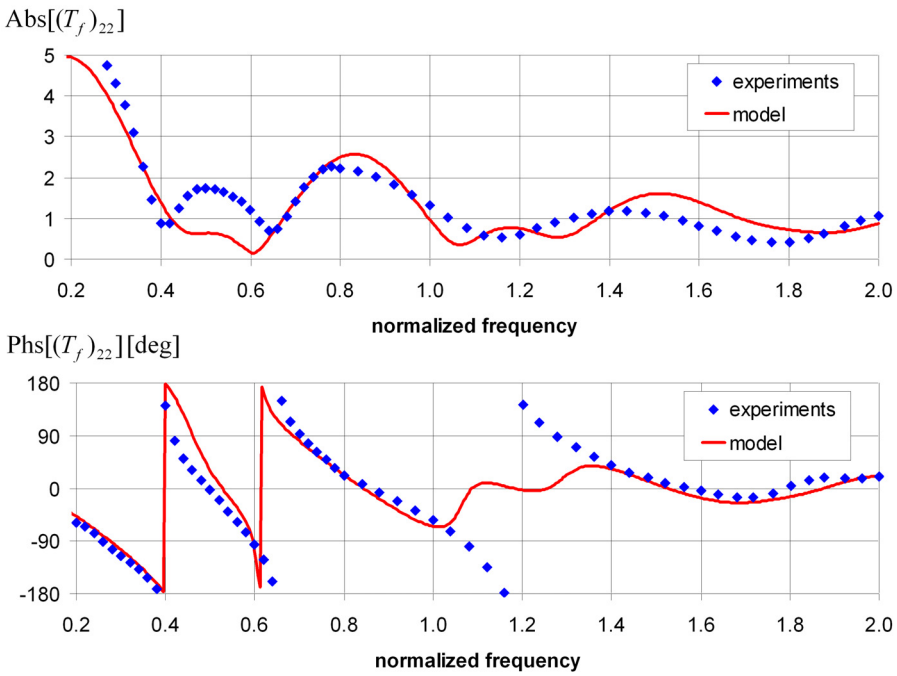

Figure 4.20: Magnitude (top) and phase (bottom) of $(T_e)_{22}$ flame transfer function element. Oil test case with air temperature $(T_{air})_{ref}$ and flame temperature $(T_{flame})_{ref} + 100K$.

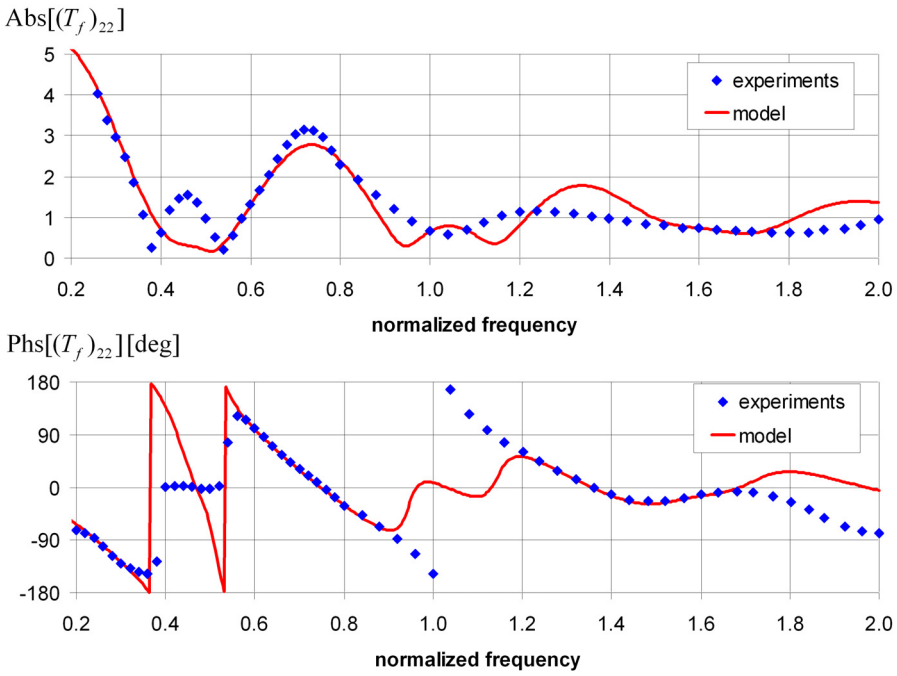

Figure 4.21: Magnitude (top) and phase (bottom) of $(T_e)_{22}$ flame transfer function element. Oil test case with air temperature $(T_{air})_{ref} - 60K$ and flame temperature $(T_{flame})_{ref}$.

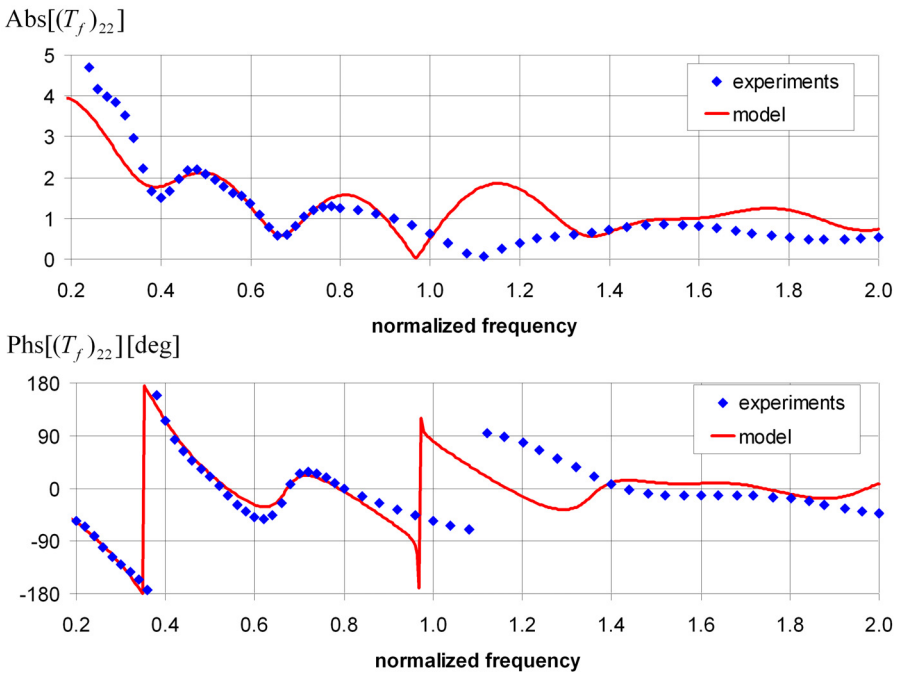

Figure 4.22: Magnitude (top) and phase (bottom) of $(T_e)_{22}$ flame transfer function element. Oil test case with air temperature $(T_{air})_{ref} + 30K$ and flame temperature $(T_{flame})_{ref}$.

Chapter 5

Passive Control

5.1 Helmholtz Damper Impedance Model

In this Chapter we discuss the use of Helmholtz resonators to dampen thermoacoustic pulsations occurring in gas turbine combustion chambers. First, a nonlinear model of the Helmholtz resonator impedance is presented and validated by means of atmospheric experiments. Then, the physical mechanism behind the sound attenuation achieved by the application of Helmholtz dampers to combustion chambers is analyzed.
As shown in Fig. 5.1, a Helmholtz resonator consists of a volume with a neck through which the fluid inside the resonator communicates with an external medium [29], [30], [51]. With respect to classical acoustics, in combustion applications a cooling flow must be maintained through the resonator in order to prevent overheating. When a Helmholtz resonator is applied to an enclosure, in correspondence of the neck mouth a frequency dependent boundary is realized. The acoustic behavior of the resonator is defined through the damper impedance $Z_n = R_n + iX_n$, i.e. the ratio in the frequency domain between acoustic pressure and normal component of acoustic velocity computed on the neck mouth.

5.1.1 Harmonic oscillator model

When the neck is short and narrow with respect to acoustic wavelengths (low-frequency range), all the fluid particles in the neck are assumed to fluctuate with the same acoustic speed. Thus the air in the neck may be modeled as a zero-mass solid piston fluctuating and then radiating acoustic energy outside of the neck. For a compact neck, in the linear regime Eqs. (3.38)-(3.39) give

$$A_{fl}\,\widehat{u}_{fl} = A_n\,\widehat{u}_n = A_V\,\widehat{u}_V \tag{5.1}$$

$$\widehat{p}_{fl} = \widehat{p}_V + \left[i\,\omega\,\overline{\rho}\,L'_n + \zeta_{neck}\,\overline{\rho}\,\overline{u}_n + (\,\widehat{\Phi}_1 + \,\widehat{\Phi}_2)/\,\widehat{u}_n \right]\,\widehat{u}_n \tag{5.2}$$

where the suffixes n, fl and V refer to resonator neck, flange and volume respectively (see Fig. 5.2). Moreover,

$$L'_n = \ell_V + L_n + \ell_{fl} \tag{5.3}$$

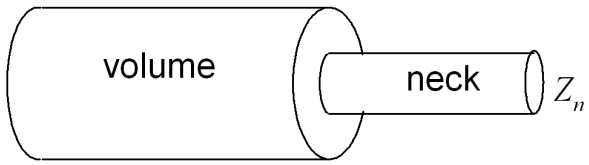

Figure 5.1: Helmholtz resonator schematic.

with ℓ_V and ℓ_{fl} end-corrections at the neck-volume and neck-flange interface respectively. Eq. (3.14) may be used to express the pressure $\widehat{p}_V$ (i.e. the damper volume is acoustically compact) if

$$L_V \leq \lambda/16 \tag{5.4}$$

where L_V is the length of the resonator volume and $\lambda = 2\pi\,\overline{c}/\omega$ the acoustic wavelength [32]. When the assumption (5.4) holds, Eqs. (5.2)-(5.1) yield

$$Z_{fl} = \frac{\widehat{p}_{fl}}{\widehat{u}_{fl}} = R_{fl} + i\,X_{fl} = \frac{A_{fl}}{A_n}\left[\zeta_{neck}\;\overline{\rho}\;\overline{u}_n + (\,\widehat{\Phi}_1 + \,\widehat{\Phi}_2)/\,\widehat{u}_n + i\,\left(\omega\;\overline{\rho}\,L'_n - \frac{\overline{\rho}\;\overline{c}^2\,A_n}{\omega\,V_R}\right)\right] \tag{5.5}$$

where $V_R = A_V L_V$ is the resonator volume. The resonance frequency of the damper (i.e. the frequency for which $X_{fl} = 0$) is given by

$$\omega_{res} = \overline{c}\sqrt{\frac{A_n}{V_R\,L'_n}} \tag{5.6}$$

As we will see in the following, a Helmholtz resonator is able to dampen pulsations occurring at the damper resonance frequency. Thus the slope of the reactance curve at resonance

$$\left.\frac{\partial X_{fl}}{\partial \omega}\right|_{\omega_{res}} = \frac{A_{fl}}{A_n}\left(2\;\overline{\rho}\,L'_n\right) \tag{5.7}$$

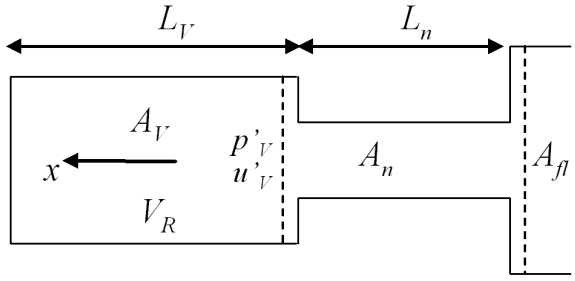

Figure 5.2: Helmholtz resonator characteristic quantities.

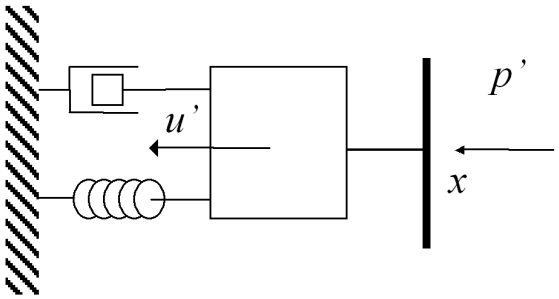

Figure 5.3: Harmonic oscillator.

indicates how fast the damper behavior deviates from the resonance condition when the frequency moves away from ω_{res}.
Helmholtz developed originally Eq. (5.5) by using the "harmonic oscillator" analogy, where the fluid in the neck is seen as an equivalent mass fluctuating under the effect of a spring force related to the compressibility of the fluid in the volume and a dissipative force related to viscous and thermal conduction losses [30] (see Fig. 5.3).

5.1.2 Nonlinear model

When a Helmholtz resonator is applied to a combustion chamber, the accurate prediction of the resonator impedance is fundamental for the correct resonator design. In the model we present in this Section, the neck is modeled by means of Eq. (3.4) (one-dimensional wave propagation) including the Kirchhoff visco-thermal acoustic damping (2.88). For the damper volume we use Eq. (3.5) (one-dimensional wave propagation without damping), the assumption $Sd \rightarrow \infty$ being justified by a sufficiently large radius of the damper volume. Eq. (5.2) shows that the damper reactance depends of the end-corrections ℓ_V and ℓ_{fl} , which represent the inertia of the fluid induced to fluctuate into combustor and resonator volume by the acoustic fluctuations occurring into the neck. The presence of a mean flow (maintained for cooling reasons) also affects the end-correction. Various models have been proposed for modeling the end-correction of an area change in absence of mean flow [29], [31], [82], [83]. The end-correction ℓ_∞ of a tube without mean flow terminating in a half-space (infinite flange) may be computed as the reactance of a piston of radius $a = \sqrt{A_n/\pi}$ set on an infinite boundary plane. By introducing the duct Helmholtz number $He = \omega a/\,\overline{c}$, in the limit $He \rightarrow 0$ one obtains [29]

$$\lim_{He \rightarrow 0} \ell_\infty = \frac{8}{3\,\pi}\,a \tag{5.8}$$

The effect of a finite value of He is considered in the expression [82]

$$\ell_\infty = 0.8216\,a\left[1 + \frac{(0.77He)^2}{1 + 0.77He}\right]^{-1} \tag{5.9}$$

In case of finite area jump (flanged end) it is possible to use $\ell = \ell_\infty \chi(P)$, where P is the area ratio (defined as less than one) and [83]

$$\chi(P) = 1 - 1.47\,P^{0.5} + 0.47\,P^{1.5} \tag{5.10}$$

Finally, for the end correction of a piston of radius a communicating with an infinite space (unflanged end) one has [82]

$$\ell_{unfl} = 0.6133\ a\ \frac{1 + 0.044\,He^2}{1 + 0.19\,He^2} \tag{5.11}$$

As reported in several experimental investigations, in the presence of a mean flow ℓ decreases when increasing the mean flow velocity until a limit values is reached [84], [85], [86]. In our model the area changes at neck ends are modeled by means of the semi-empirical relation

$$\ell = \ell_\infty(He)\ \chi(P)\ \psi(St) \tag{5.12}$$

where $\ell_\infty(He)$ and $\chi(P)$ are given by Eqs. (5.9) and (5.10) respectively, whereas the factor $\psi(St)$ accounts for the decrease in ℓ when $|\,\overline{u}_n| \to \infty$ with

$$St = \omega a/|\,\overline{u}_n| \tag{5.13}$$

mean flow Strouhal number [85]. An expression fitting well our experiments is

$$\psi(St) = \frac{\ell_{lim}\,(\beta/St^2) + 1}{\beta/St^2 + 1} \tag{5.14}$$

where ℓ_{lim} and β are constants. At high cooling flow velocities, Eq. (5.14) gives an end-correction that is ℓ_{lim} times the end-correction value at $|\,\overline{u}_n| = 0$.
Next, the theory derived in Section 3.3.1 is used to express the nonlinear behavior of the resonator resistance R_{fl}. In particular, Eq. (3.31) may be used to model $\widehat{\Phi}_n = \widehat{\Phi}_1 + \widehat{\Phi}_2$ into Eq. (5.5) with the simplification $\zeta_n^+ \simeq \zeta_n^- = \zeta_n$ applied into Eq. (3.29). When an expression for the pressure loss coefficient ζ_n is provided, Eq. (3.31) models the transition from the linear to the nonlinear regime occurring when the mean flow velocity in the damper neck becomes smaller than the neck acoustic velocity. Previous investigations have been oriented to model separately the linear and nonlinear regimes in the case of low Mach number and low-Helmholtz-number flows using one-dimensional fluid dynamic models [33], [34], [35], [36], [37], [38]. With or without mean flow, the "quasi-steady" assumption $\zeta_n = const$ holds if $St_{ac} \ll 1$ or $St \ll 1$ respectively, being the mean flow Strouhal number St defined in Eq. (5.13) and the acoustic Strouhal number St_{ac} given by

$$St_{ac} = \omega a/|\,\widehat{u}_n| \tag{5.15}$$

Under the quasi-steady assumption, the acoustic characteristic displacement $|\,\widehat{u}_n|/\omega$ or the fluid dynamic characteristic displacement $|\,\overline{u}_n|/\omega$ are supposed to be much larger than the neck radius a. Quasi-steady models without mean flow have been proposed for orifices using a constant "discharge coefficient" $C_D = 1/\sqrt{\zeta_n}$ [33], [34], [37] [see for instance Eqs. (3.37)]. Without mean flow and for large values of St_{ac}, the pressure loss term may be obtained by modeling the acoustic power transformed into shedding of

ℓ_{lim}	β	ζ_0	C_0	D_0	ζ_u	C_u	D_u
0.3	6	2	0.36	1.05	1	0.20	1.10

Table 5.1: Parameters for end-correction and pressure loss coefficient fits.

vorticity by means of a vortex-sheet model [36]. By assuming that the only viscous effect is the release of a vortex sheet from the area change lip in order to fulfill the Kutta condition, one can use

$$\zeta_n = 0.6\,\frac{3\pi}{4}\,St_{ac}^{1/3} \tag{5.16}$$

that gives good agreement with experiments performed on ducts connected to an infinite space [36]. In linear regimes with large St, the pressure loss coefficient has been found to be a function of St only [69], [84].
According to the above considerations, in the present work we model the pressure loss coefficient ζ_n as follow. Without mean flow we use

$$\zeta_{nonlin} = \max(\zeta_0\,,\, C_0 \cdot St_{ac}^{D_0}) \tag{5.17}$$

where ζ_0 represents the quasi-steady value and for large St_{ac} an expression similar to Eq. (5.16) is used with C_0 and D_0 constants. In the linear regime we use

$$\zeta_{lin} = \max(\zeta_u\,,\, C_u \cdot St^{\,D_u}) \tag{5.18}$$

where again C_u and D_u are two constants. In the intermediated regime $0 < |\,\overline{u}_n| < |\,\widehat{u}_n|$ we use the linear interpolation

$$\zeta_n = \frac{\zeta_{nonlin}\,(1 - g_{nonlin}) + \zeta_{lin}\,(g_{nonlin} - 4/3\pi)}{1 - 4/3\pi} \tag{5.19}$$

where the function g_{nonlin} is given by [see Eq. (3.29)]

$$g_{nonlin}(\varphi) = \begin{cases} |\varphi| & \text{if } |\varphi| > 1 \\ \dfrac{2}{\pi}\left[\varphi\arcsin(\varphi) + \dfrac{\sqrt{1-\varphi^2}}{3}\left(2+\varphi^2\right)\right] & \text{if } |\varphi| \le 1 \end{cases} \tag{5.20}$$

The values of the parameters used in Eqs. (5.14), (5.17) and (5.18) have been obtained by fitting the damper experiments reported in the following Sections and are presented in Tab. 5.1.
Finally, Eq. (5.5) provides the equation

$$\sqrt{R_{fl}^2(|\,\widehat{u}_{fl}|) + X_{fl}^2(|\,\widehat{u}_{fl}|)}\cdot|\,\widehat{u}_{fl}| - |\,\widehat{p}_{fl}| = 0 \tag{5.21}$$

that is nonlinear because both end-corrections and pressure losses are functions of $|\,\widehat{u}_{fl}|$. Eq. (5.21) is solved for $|\,\widehat{u}_{fl}|$ by applying a Newton-Raphson method where the acoustic pressure on the damper

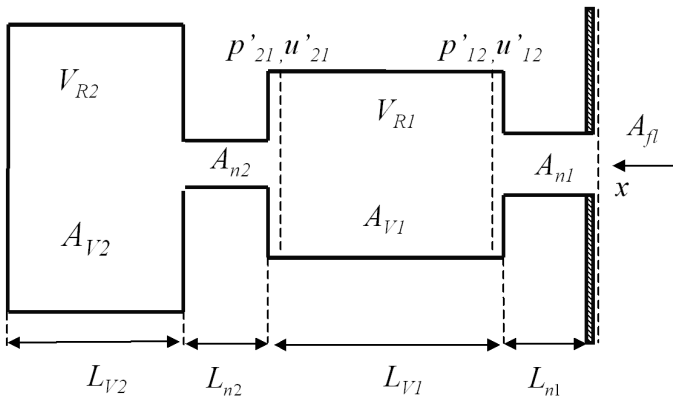

Figure 5.4: Two-volume resonator.

flange $|\widehat{p}_{fl}|$ is an input parameter (e.g. obtained from experiments). In alternative to the resonator impedance Z_{fl}, the damper max be characterized in terms of the reflection coefficient r_f given by

$$r_f = \frac{Z'_{fl}+1}{Z'_{fl}-1}\,. \tag{5.22}$$

The reflection coefficient r_f defines the acoustic absorption $1-|r_f|^2$ that corresponds to the ratio between the reflected and incoming acoustic power of a normally incident plane wave [51].

5.1.3 Two-volume resonator

The nonlinear model presented in the previous Section may be easily extended to multi-volume resonators. In particular, the two-volume resonator illustrated in Fig. 5.4 has the advantage to have two resonance frequencies and then it has the possibility to dampen two pulsation peaks simultaneously. In order to simplify the analysis, we consider linear pressure losses. According to Fig. 5.4, the following area ratios can be defined

$$P_{fl} = \frac{A_{n1}}{A_{fl}}\,, \qquad P_{12} = \frac{A_{n1}}{A_{V1}}\,, \qquad P_{21} = \frac{A_{n2}}{A_{V1}}\,, \qquad P_{22} = \frac{A_{n2}}{A_{V2}} \tag{5.23}$$

Eq. (5.5) is then used to determine the pressure $\widehat{p}_{21}$ at the upstream end of the volume 1. It gives

$$\widehat{p}_{21} = \left[i\left(\omega\,\overline{\rho}\,L'_{n2} - \frac{\overline{\rho}\,\overline{c}^2\,P_{22}}{\omega\,L_{V2}}\right) + \zeta_2\,\overline{\rho}\,\overline{u}_{n2}\right]\,\widehat{u}_{n2} \tag{5.24}$$

Next, using Eqs. (3.12)-(3.13) (the volume 1 is assumed to be compact and with small area ratio P_{21}) we obtain

$$\widehat{p}_{21} = \widehat{p}_{12} = -i\,\overline{\rho}\,\overline{c}^2\,\frac{P_{12}\,\widehat{u}_{n1} - P_{21}\,\widehat{u}_{n2}}{\omega\,L_{V1}} \tag{5.25}$$

Using again Eqs. (3.12)-(3.13) for the first neck, the acoustic pressure at the resonator flange $\widehat{p}_{fl}$ is given by

$$\widehat{p}_{fl} = \left(i\,\omega\,\overline{\rho}\,L'_{n1} + \zeta_1\,\overline{\rho}\,\overline{u}_{n1}\right)\,\widehat{u}_{n1} + \widehat{p}_{12} \tag{5.26}$$

The two-volume resonator may be considered as made by the combination of two single-volume resonators with resonance frequencies

$$\omega_1 = \overline{c}\sqrt{\frac{P_{12}}{L'_{n1}\,L_{V1}}}\,, \qquad\qquad \omega_2 = \overline{c}\sqrt{\frac{P_{22}}{L'_{n2}\,L_{V2}}} \tag{5.27}$$

Using Eqs. (5.24), (5.25) and (5.27), the relationship between the acoustic velocities in the resonator necks writes as

$$\widehat{u}_{n2} = \frac{\omega_1^2\,L'_{n1}/L'_{n2}}{\omega_2^2\,(1+\theta) - \omega^2 + i\,\omega\,\zeta_2\;\overline{u}_{n2}/L_{n2}}\;\widehat{u}_{n1} \tag{5.28}$$

where θ is the volume ratio defined as

$$\theta = \frac{V_{R2}}{V_{R1}} \tag{5.29}$$

Finally, Eqs. (5.25), (5.26) and (5.28) can be combined to give the damper impedance

$$\begin{aligned} Z_{fl} &= \frac{1}{P_{fl}}\left(i\,\omega\;\overline{\rho}\,L'_{n1} + \zeta_1\;\overline{\rho}\;\overline{u}_{n1} + \frac{\widehat{p}_{12}}{\widehat{u}_{n1}}\right) = \\ &= \frac{1}{P_{fl}}\left\{i\omega\,\overline{\rho}L'_{n1}\left(1-\frac{\omega_1^2}{\omega^2}\right) + \zeta_1\,\overline{\rho}\,\overline{u}_{n1} + \frac{i\,\omega\;\overline{\rho}\,L'_{n1}\,\omega_1^2\,\omega_2^2\,\theta}{\omega^2\left[\omega_2^2\,(1+\theta) - \omega^2 + i\omega\zeta_2\,\overline{u}_{n2}/L'_{n2}\right]}\right\} \end{aligned} \tag{5.30}$$

from which one obtains

$$X_{fl} = Im(Z_{fl}) = \frac{1}{P_{fl}}\,\omega\;\overline{\rho}\,L'_{n1}\left\{\left(1-\frac{\omega_1^2}{\omega^2}\right) + \frac{\omega_1^2\,\omega_2^2\,\theta\;\left[\omega_2^2\;(1+\theta) - \omega^2\right]/\omega^2}{\left[\omega_2^2\;(1+\theta) - \omega^2\right]^2 + \left(\omega\,\zeta_2\;\overline{u}_{n2}/L'_{n2}\right)^2}\right\} \tag{5.31}$$

The condition $X_{fl} = 0$ gives the resonance frequencies $\omega_{res1,2}$ of the two-volume resonator. In order to have resonance frequencies independent of the mean flow, in the following we assume $\overline{u}_{n2} = 0$ (i.e. no mean flow through the second neck). In this case Eq. (5.31) gives

$$\omega_{res1,2} = \left\{\frac{1}{2}\left[\omega_1^2 + \omega_2^2\,(1+\theta) \pm \sqrt{\omega_1^4 + \omega_2^4\,(1+\theta)^2 - 2\omega_1^2\omega_2^2\,(1-\theta)}\right]\right\}^{1/2} \tag{5.32}$$

The two resonance frequencies given by Eq. (5.32) satisfy the conditions $\omega_{res2} < \min(\omega_1, \omega_2)$ and $\omega_{res1} > \max(\omega_1, \omega_2)$. The slope of the reactance curve at resonance is

$$\left.\frac{\partial X_{fl}}{\partial \omega}\right|_{\omega_{res12}} = \frac{1}{P_{fl}}\left(2\;\overline{\rho}\,L'_{n1}\right)\frac{\omega_{res1,2}^2 - \omega_{res2,1}^2}{\omega_{res1,2}^2 - \omega_2^2\;(1+\theta)} \tag{5.33}$$

For a single-volume resonator one has $\omega_2 = 0$ and Eq. (5.32) gives $\omega_{res1,1} \equiv \omega_1$.

Finally, we consider the "two-throat resonator" shown in Fig. 5.5 that is realized by replacing the second volume of a two-volume resonator with an open end. Note that in this case one has zero acoustic pressure at the second neck inlet and thus the end-correction contribution $\ell_0(He, P)$ in Eq. (5.12) must be computed according to Eq. (5.11). For the two-throat resonator $\omega_2^2 \to 0$ ($V_{R2} \gg V_{R1}$) whereas $\omega_2^2\theta$ remains finite. In this case Eqs. (5.32)-(5.33) give

$$\omega_{res} = \overline{c}\sqrt{\frac{1}{V_R}\left(\frac{A_{n1}}{L'_{n1}} + \frac{A_{n2}}{L'_{n2}}\right)} \tag{5.34}$$

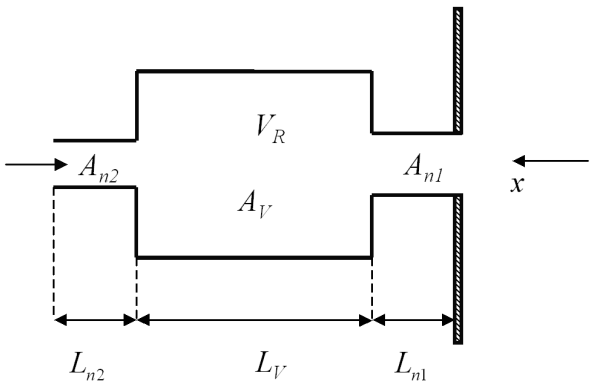

Figure 5.5: Two-throat resonator.

and

$$\left.\frac{\partial X_{fl}}{\partial \omega}\right|_{\omega_{res}} = \frac{1}{P_{fl}} \left(2\,\overline{\rho}\,L'_{n1}\right) \frac{\omega_{res}^2}{\omega_1^2} \tag{5.35}$$

5.2 Resonator Experiments for Impedance Model Validation

Experiments for validating the nonlinear resonator model have been conducted in the atmospheric impedance tube test rig already described in Section 3.3.2. Figs. 5.6 and Fig. 5.7 show the rig set-up for measuring damper impedances, the resonators being mounted on the resonator flange located on one end of the tube. Using the Multi-Microphone-Method (see Section 3.3.2), both the acoustic pressure on the resonator flange $|\widehat{p}_{fl}|$ and the reflection coefficient r_f were obtained over the range of frequencies of interest.

5.2.1 Cylindrical resonator

The nonlinear resonator model has been first validated with experiments performed on the cylindrical resonator illustrated in Fig.5.8. The resonator volume was composed of a cylinder whose length could be varied by means of a movable piston in order to obtain different resonance frequencies. As shown in Fig. 5.7, an inlet tube (second neck) exited the resonator volume on the piston surface in order to inject air inside the resonator volume.

Initially the inlet tube was closed on the resonator piston side. Tab. 5.2 reports the test conditions in terms of nondimensional volume length $\widetilde{L}_V$ and related nondimensional resonance frequency $\widetilde{f}_{res}$, being $\widetilde{L}_V$ and $\widetilde{f}_{res}$ normalized using the maximum volume length achievable moving the piston and the minumum frequency measured in the impedance tube. Figs. 5.9-5.10 show the comparison between simulations and measurements in terms of magnitude and phase of the reflection coefficient measured on the resonator flange. The resonance frequencies are characterized by a minimum of the reflection

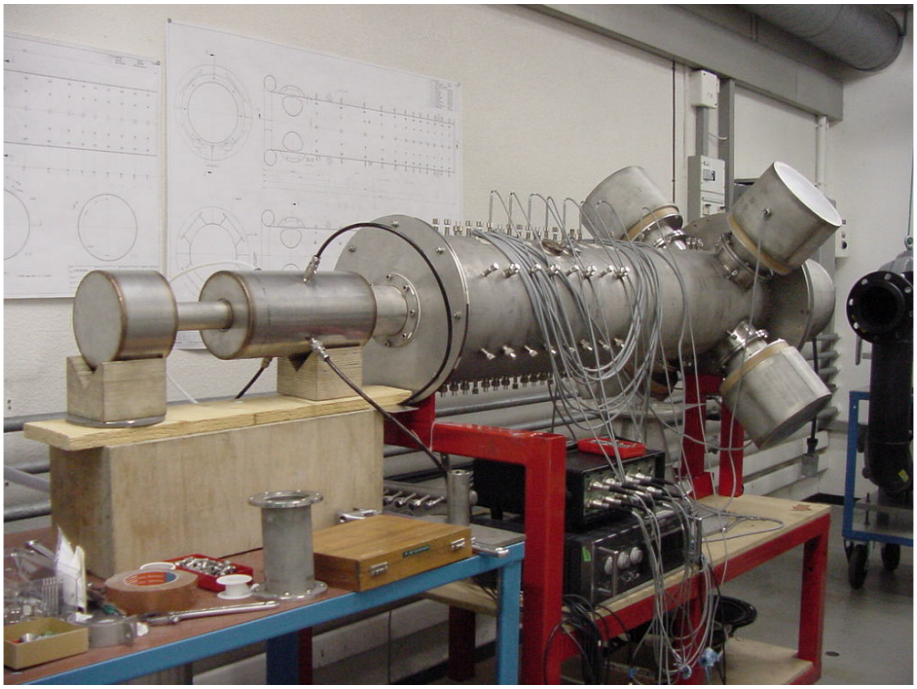

Figure 5.6: Impedance tube test rig.

coefficient magnitude and a phase equal to $\pm 180^o$. The agreement between experiments and simulations is very good for the entire frequency range. The decrease in resonance frequency when increasing $\widetilde{L}_V$ [see Eq. (5.6)] is well captured. For the longest resonator volume $\widetilde{L}_V = 0.69$, the second resonance frequency at $\widetilde{f}_{res} = 7.80$ (zero phase point) is also predicted.
By opening the inlet tube, a two-throat resonator was realized (see Fig. 5.5). This design is suitable for gas turbine applications, where the resonator must be cooled to prevent overheating. In gas turbine

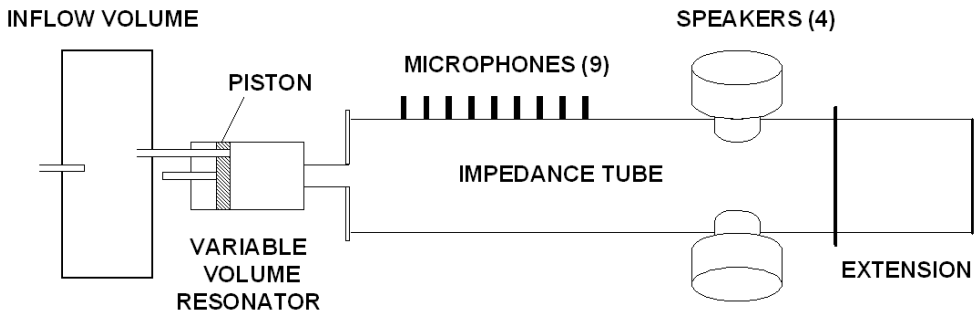

Figure 5.7: Schematic of impedance tube test rig.

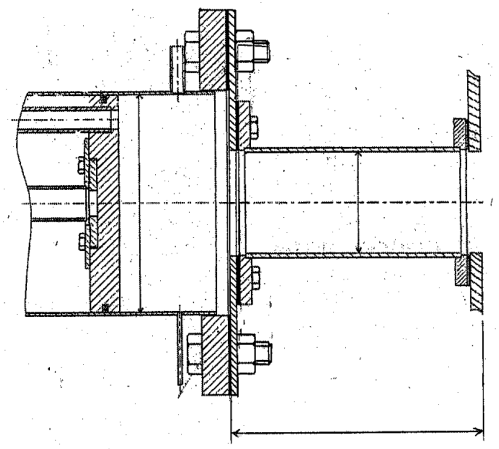

Figure 5.8: Cylindrical resonator.

applications the neck mouth communicates directly with the combustion chamber and the cooling air is supplied from the hood, the cooling mass flow rate being fixed by the pressure drop realized by the inlet tube. The nondimensional inlet tube lenght was $\widetilde{L}_{n2} = 1.53$. As illustrated in Fig. 5.7, the upstream end of the inlet tube was connected to an inflow volume that realized a zero acoustic pressure boundary (open end) in order to simulate the gas turbine hood chamber. The inflow volume was connected to the rotameter, manometer and thermometer set-up shown in Fig. 5.11. This measurement apparatus was then connected to an air supply valve, which produced airflow at various pressures. By allowing air to flow through the measurement apparatus, pressure, temperature and the height of the float within the rotameter were used to determine the mass flow within the air line and thus within the neck of the Helmholtz resonator. The test conditions are reported in Tab. 5.3, where $\widetilde{\overline{u}}_{n1}$ represents the cooling flow velocity in the damper neck normalized by means of the maximum velocity used in experiments. Figs. 5.12-5.13 show the results for the case without cooling flow. As for the closed inlet tube case, with $\widetilde{L}_V = 0.69$ a secondary resonance frequency is generated at $\widetilde{f}_{res} = 7.80$. Moreover, for small volumes two other resonance frequencies at $\widetilde{f}_{res} = 3.30$ and $\widetilde{f}_{res} = 6.80$ appear in addition to the main minima of $|r_f|$. These resonance frequencies do not change with $\widetilde{L}_V$, depend on the inlet tube geometry

$\widetilde{L}_V$	$\widetilde{f}_{res}$
0.05	5.44
0.08	4.54
0.23	2.80
0.46	1.96
0.69	1.58

Table 5.2: Cylindrical Helmholtz resonator with closed inlet tube. Measurement summary.

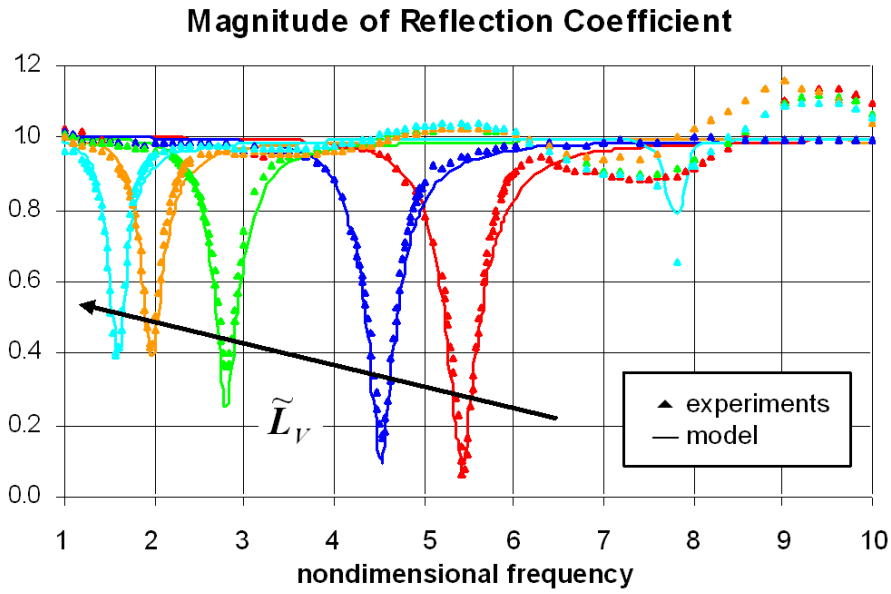

Figure 5.9: Cylindrical Helmholtz resonator with closed inlet tube. Volume length variation.

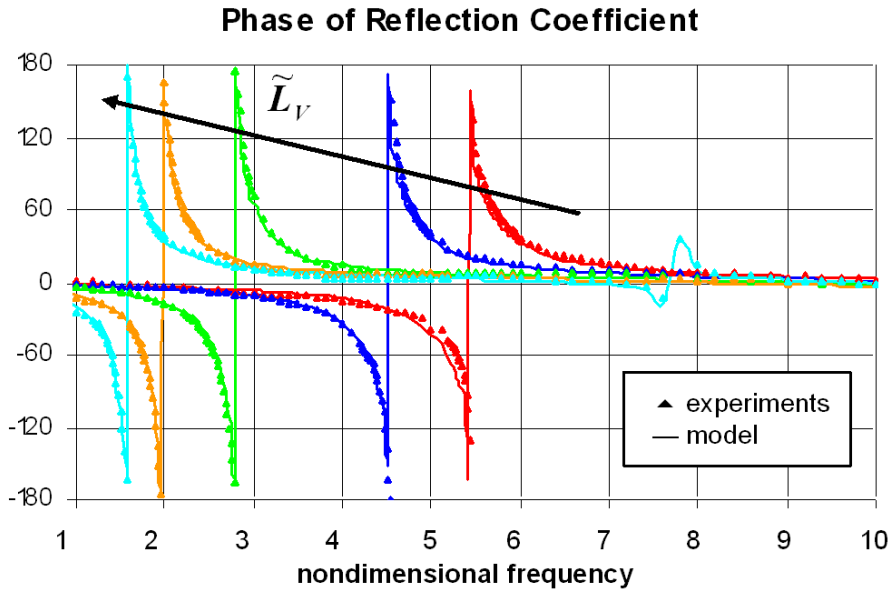

Figure 5.10: Cylindrical Helmholtz resonator with closed inlet tube. Volume length variation.

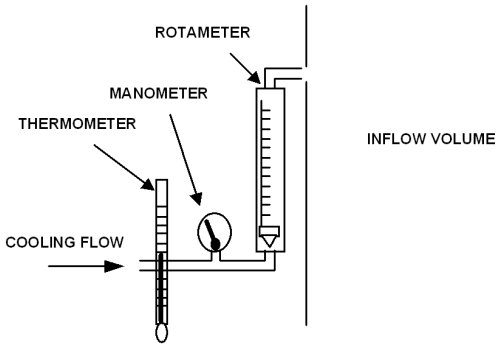

Figure 5.11: Flow measurement set-up.

and the related minima in $|r_f|$ disappear when $\widetilde{L}_V$ increases. The cooling flow cases are illustrated in Figs. 5.14-5.17. For a certain volume, the main resonance frequency showed a very small dependency on the cooling flow (see also Tab. 5.3), the cooling flow influencing meanly the resonator resistance. When increasing the cooling flow velocity, the $|r_f|$ curves became wider. Furthermore, with cooling flow the $|r_f|$ minima due to inlet tube resonance ($\widetilde{f}_{res} = 3.30$ and $\widetilde{f}_{res} = 6.80$) were suppressed because of the damping provided by the cooling flow.

$\widetilde{\overline{u}}_{n1}$	$\widetilde{L}_V$	$\widetilde{f}_{res}$
0.0	0.05	5.36
0.0	0.08	4.62
0.0	0.23	2.76
0.0	0.46	1.96
0.0	0.69	1.58
0.5	0.05	5.36
0.5	0.08	4.60
0.5	0.23	2.78
0.5	0.46	1.96
0.5	0.69	1.58
1.0	0.05	5.38
1.0	0.08	4.58
1.0	0.23	2.80
1.0	0.46	2.00
1.0	0.69	1.60

Table 5.3: Cylindrical Helmholtz resonator with open inlet tube. Measurement summary.

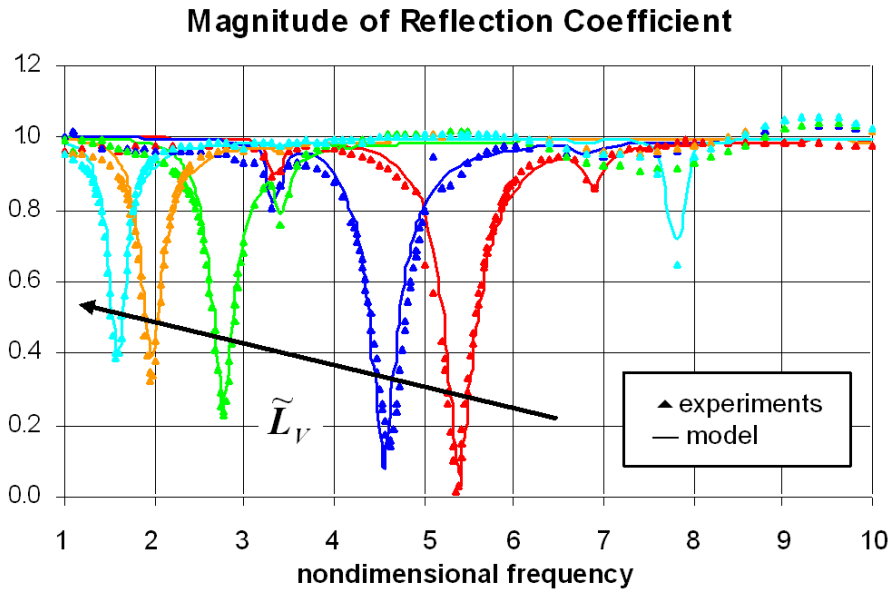

Figure 5.12: Cylindrical Helmholtz resonator, $\widetilde{\overline{u}}_{n1} = 0$. Volume length variation.

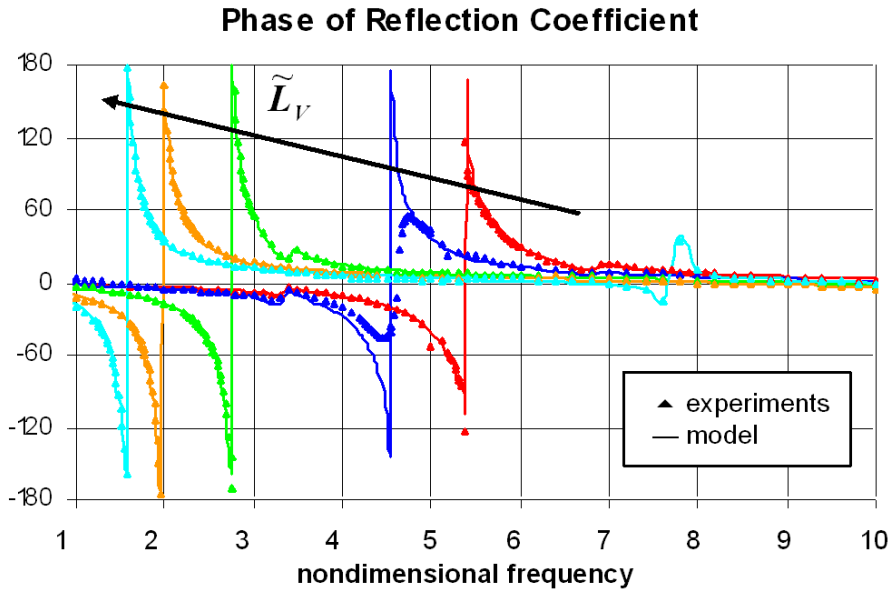

Figure 5.13: Cylindrical Helmholtz resonator, $\widetilde{\overline{u}}_{n1} = 0$. Volume length variation.

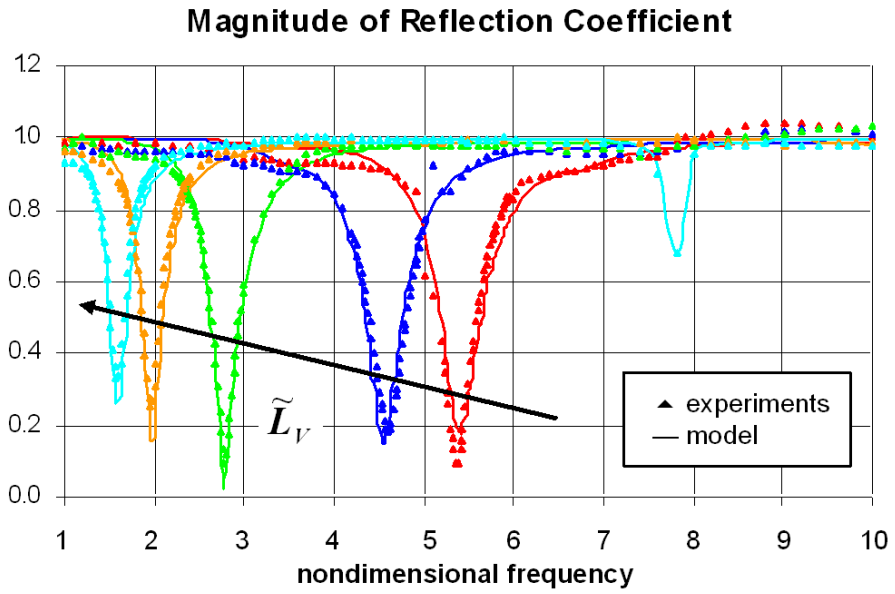

Figure 5.14: Cylindrical Helmholtz resonator, $\widetilde{u}_{n1} = 0.5$. Volume length variation.

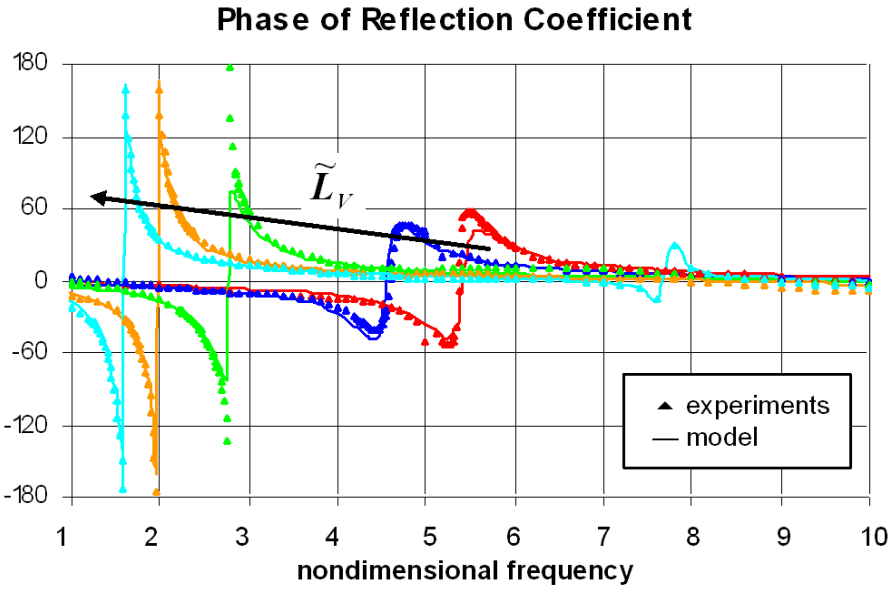

Figure 5.15: Cylindrical Helmholtz resonator, $\widetilde{u}_{n1} = 0.5$. Volume length variation.

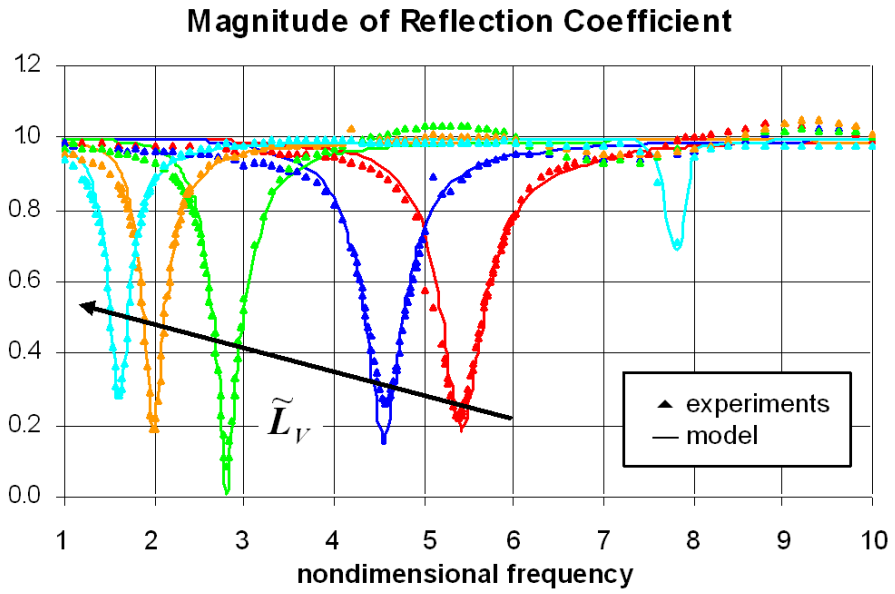

Figure 5.16: Cylindrical Helmholtz resonator, $\widetilde{\overline{u}}_{n1} = 1$. Volume length variation.

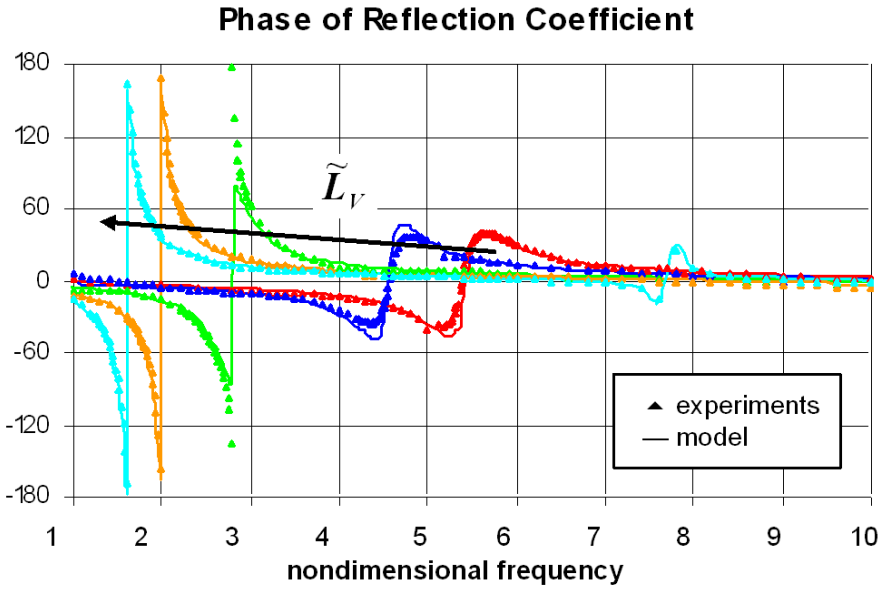

Figure 5.17: Cylindrical Helmholtz resonator, $\widetilde{\overline{u}}_{n1} = 1$. Volume length variation.

5.2.2 Conical resonator

Fig. 5.18 shows the conical resonator that was obtained from the cylindrical one by replacing the volume-neck area jump with a cone. The end-correction modeling of the nonlinear model reported in Section 5.1.2 has been developed for area discontinuities at neck ends. Thus, the end-correction ℓ_V at the conical connection joining neck and resonator volume was computed by replacing the length of the volume (including the cone) $\widetilde{L}_V$ with a corrected length $(\widetilde{L}_V)_{cone}$. The corrected length was calculated as a function of $\widetilde{L}_V$ in order to have good agreement with experimental results. Such function was found to be the linear expression

$$(\widetilde{L}_V)_{cone} = \widetilde{L}_V - b \tag{5.36}$$

with $b = const.$ The conical resonator was also tested with the inlet tube lengths $\widetilde{L}_{n2} = 1.53$ and $\widetilde{L}_{n2} = 0.68$. Tab. 5.4 reports the test conditions related to the results presented in Figs. 5.19-5.26, proving that Eq. (5.36) is capable to predict the damper resonance frequency for all flow conditions and geometries.

The extended neck shown in Fig. 5.27 was also tested. The neck extension inside the resonator volume led to a shorter resonator volume and to a different end-correction. In particular, on the volume side the neck had an unflanged end and then the end-correction ℓ_V was expressed by means of Eq. (5.11). Moreover, the following corrected volume length $(L_V)_{unfl}$ was employed

$$(\widetilde{L}_V)_{unfl} = \widetilde{L}_V + b_{unfl} \tag{5.37}$$

where $b_{unfl} = const$ and $\widetilde{L}_V$ is the distance between neck end and volume end. The results in Figs. 5.28-5.29 refer to the measurement points of Tab. 5.5.

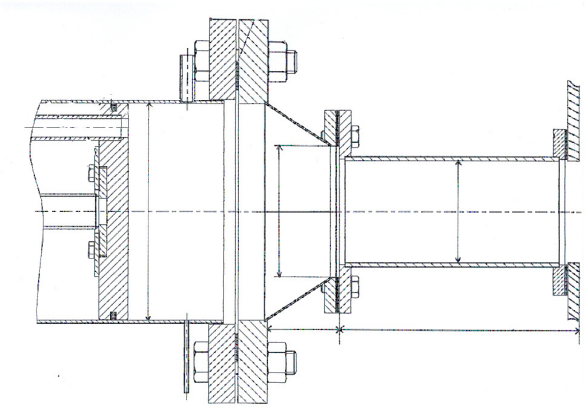

Figure 5.18: Conical resonator.

$\widetilde{L}_{n2}$	$\widetilde{\overline{u}}_{n1}$	$\widetilde{L}_V$	$\widetilde{f}_{res}$
1.53	0.0	0.16	3.80
1.53	0.0	0.69	1.62
1.53	0.5	0.16	3.74
1.53	0.5	0.23	2.98
1.53	0.5	0.35	2.40
1.53	0.5	0.46	2.04
1.53	0.5	0.58	1.80
1.53	0.5	0.69	1.62
1.53	1.0	0.16	3.78
1.53	1.0	0.23	3.06
0.68	0.0	1.0	1.32
0.68	0.5	1.0	1.32
0.68	1.0	1.0	1.32

Table 5.4: Conical Helmholtz resonator. Measurement summary.

The conical resonator was finally tested by closing the inlet tube and removing the piston seal. In previous tests, the resonator piston had a seal thickness equal to $6.7 \cdot 10^{-3} D_P$ with D_P piston diameter. The piston-cylinder clearance was of $6.7 \cdot 10^{-4} D_P$ and it was neglected in the acoustic simulations, where the only inlet tube opening was considered. By closing the inlet tube and removing the seal, a clearance of $7.4 \cdot 10^{-3} D_P$ was obtained. In this case the resonator was modeled as a nonlinear two-volume resonator, where the clearance represented the equivalent (in cross section and length) second neck and the closed volume upstream of the piston was the second resonator volume. Figs. 5.30-5.31 report the results related to the test conditions illustrated in Tab. 5.6. Figs. 5.30-5.31 show the good accuracy obtained using the equivalent duct approximation for the clearance.

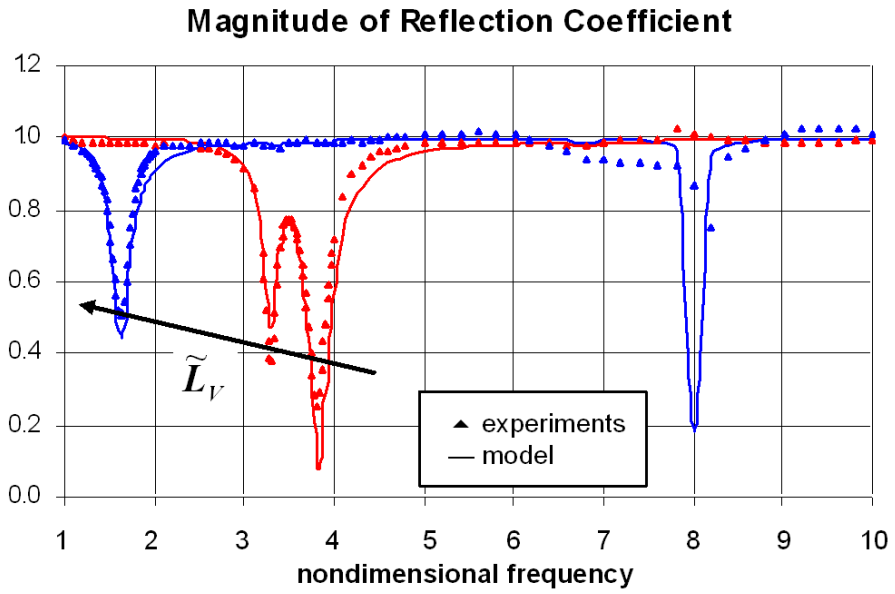

Figure 5.19: Conical Helmholtz resonator, $\widetilde{L}_{n2} = 1.53$ and $\widetilde{\overline{u}}_{n1} = 0$. Volume length variation.

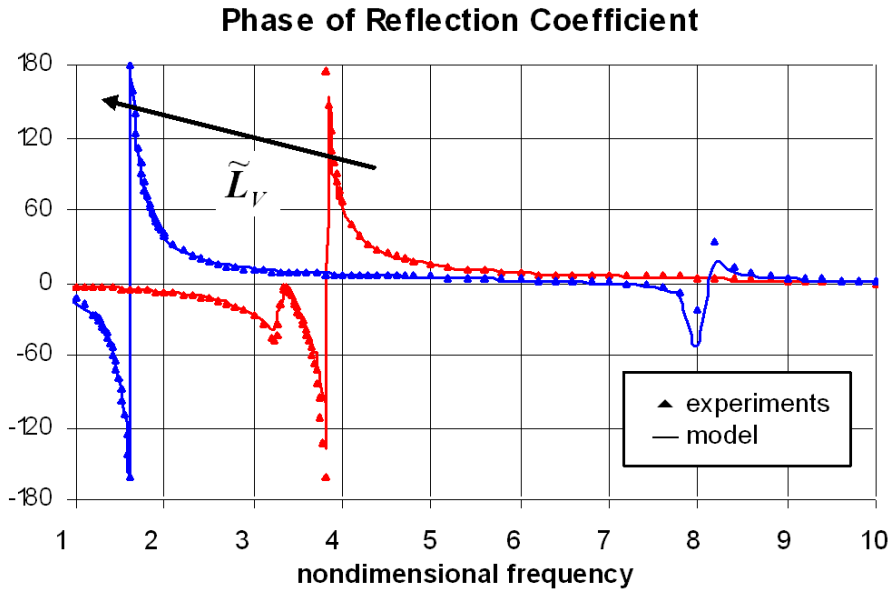

Figure 5.20: Conical Helmholtz resonator, $\widetilde{L}_{n2} = 1.53$ and $\widetilde{\overline{u}}_{n1} = 0$. Volume length variation.

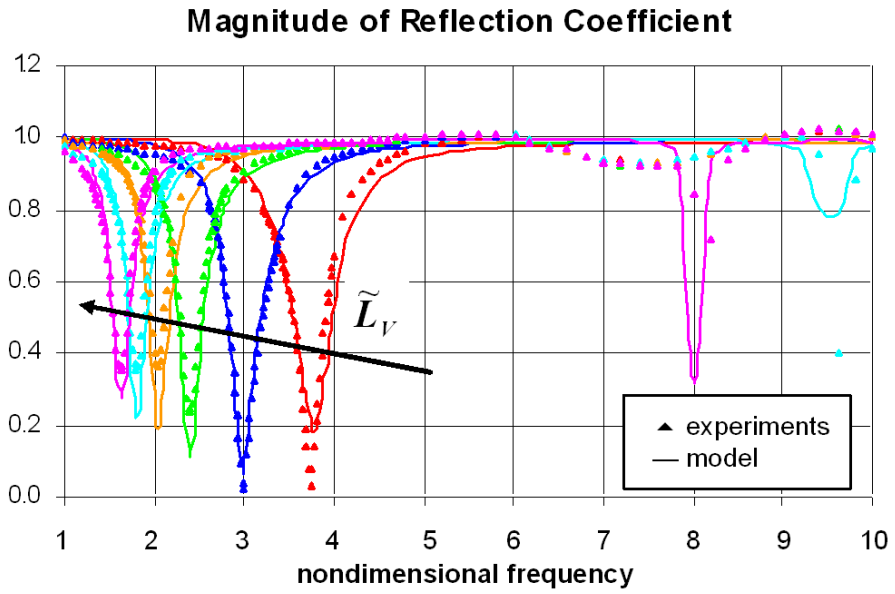

Figure 5.21: Conical Helmholtz resonator, $\widetilde{L}_{n2} = 1.53$ and $\widetilde{\overline{u}}_{n1} = 0.5$. Volume length variation.

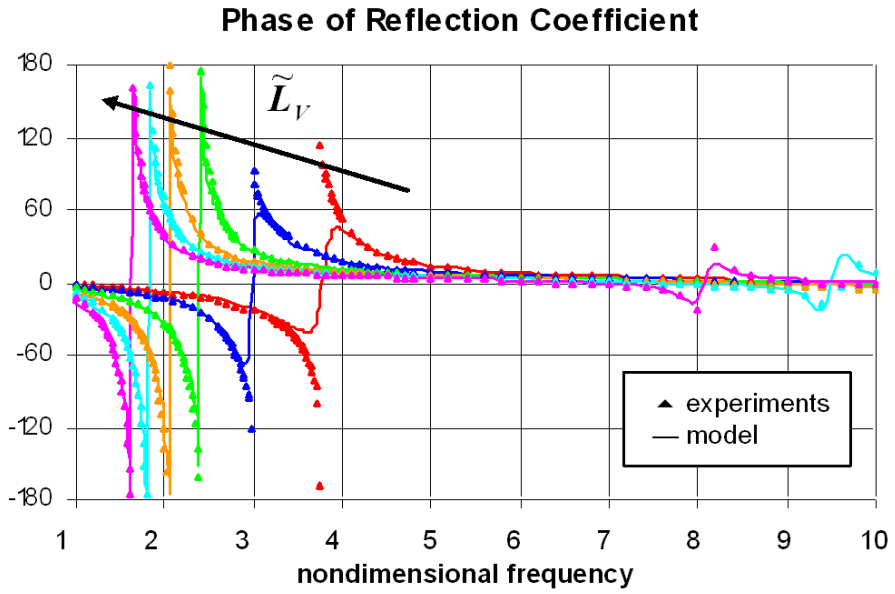

Figure 5.22: Conical Helmholtz resonator, $\widetilde{L}_{n2} = 1.53$ and $\widetilde{\overline{u}}_{n1} = 0.5$. Volume length variation.

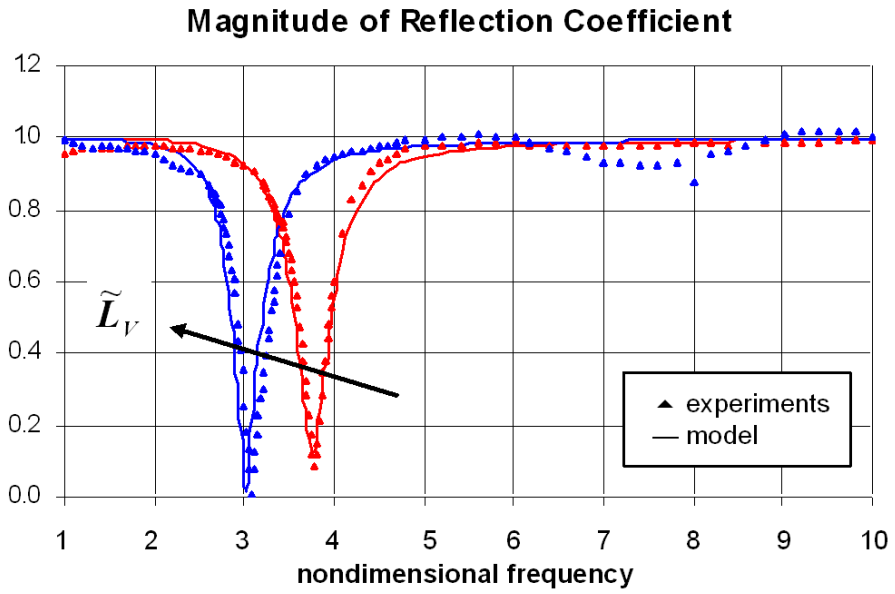

Figure 5.23: Conical Helmholtz resonator, $\widetilde{L}_{n2} = 1.53$ and $\widetilde{\overline{u}}_{n1} = 1$. Volume length variation.

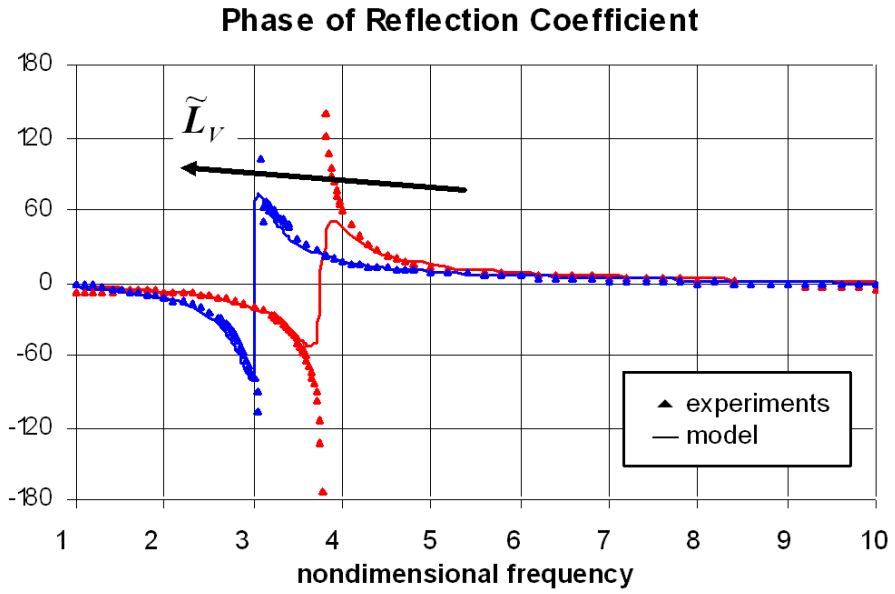

Figure 5.24: Conical Helmholtz resonator, $\widetilde{L}_{n2} = 1.53$ and $\widetilde{\overline{u}}_{n1} = 1$. Volume length variation.

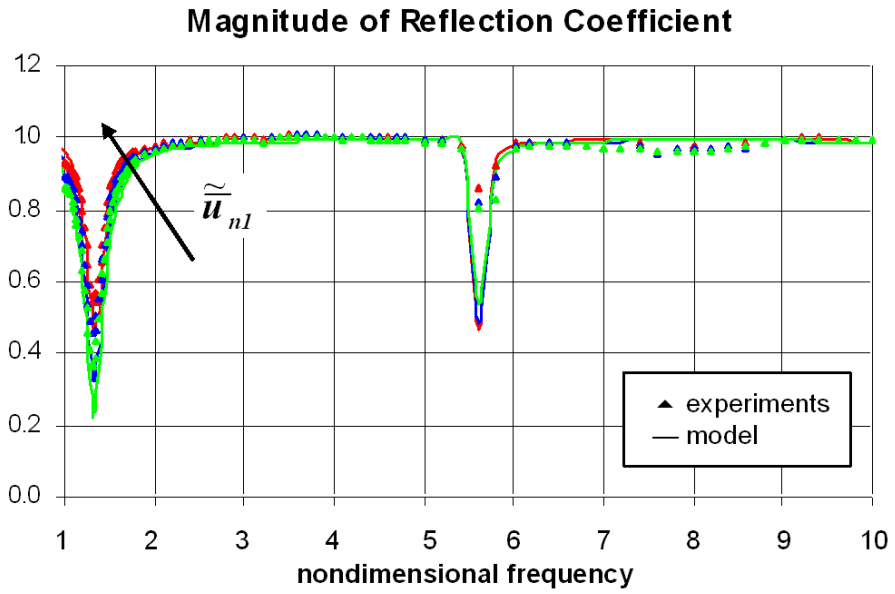

Figure 5.25: Conical Helmholtz resonator, $\widetilde{L}_{n2} = 0.68$ and $\widetilde{L}_V = 1$. Cooling flow velocity variation.

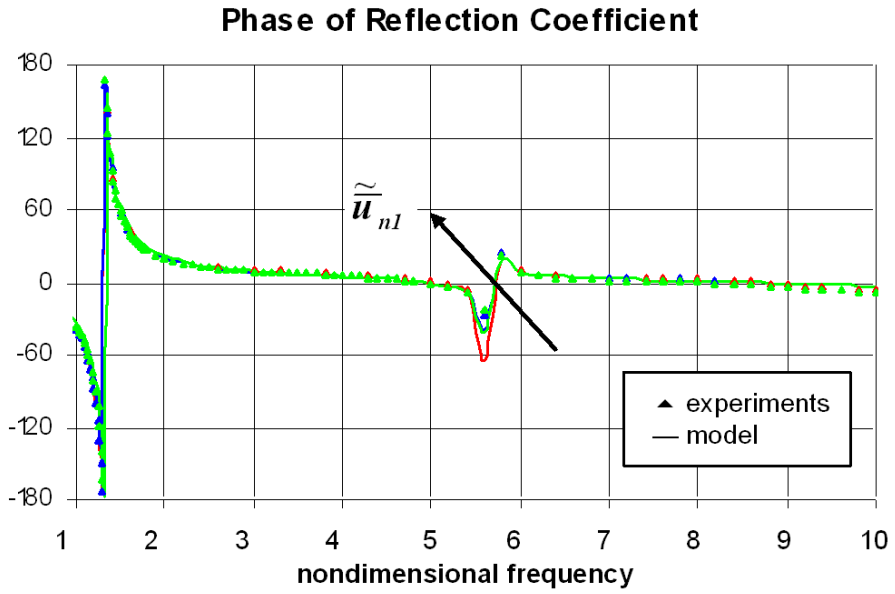

Figure 5.26: Conical Helmholtz resonator, $\widetilde{L}_{n2} = 0.68$ and $\widetilde{L}_V = 1$. Cooling flow velocity variation.

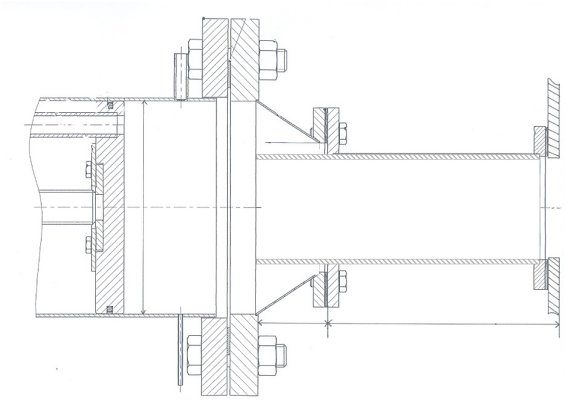

Figure 5.27: Conical resonator with extended neck.

$\widetilde{L}_{n2}$	$\widetilde{\overline{u}}_{n1}$	$\widetilde{L}_V$	$\widetilde{f}_{res}$
1.53	1	0.08	3.6
1.53	1	0.15	2.8
1.53	1	0.27	2.28
1.53	1	0.38	1.92
1.53	1	1	1.18

Table 5.5: Conical Helmholtz resonator with extended neck. Measurement summary.

$\widetilde{L}_{n2}$	$\widetilde{\overline{u}}_{n1}$	$\widetilde{L}_V$	$\widetilde{f}_{res}$
0.68	0.0	1	1.16
0.68	0.5	1	1.16
0.68	1.0	1	1.16

Table 5.6: Conical Helmholtz resonator without seal. Measurement summary.

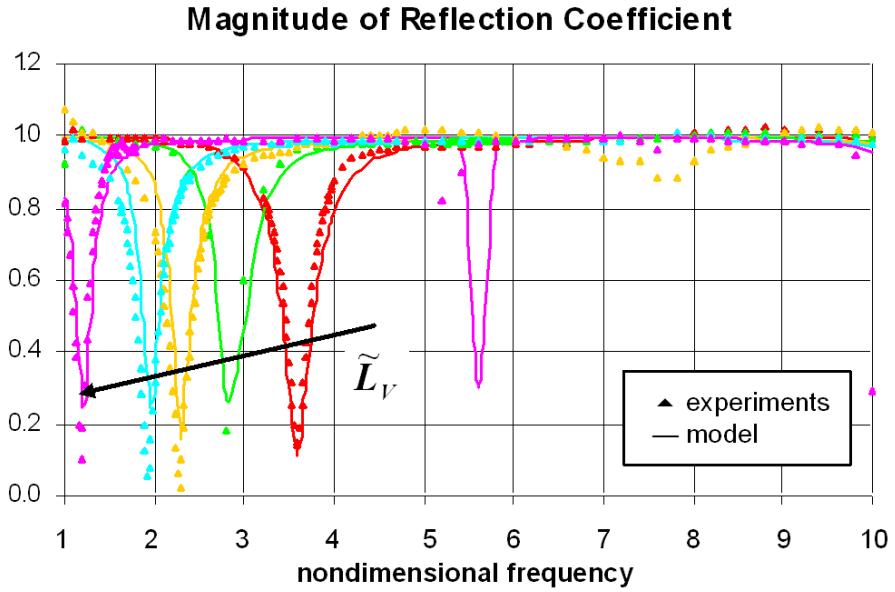

Figure 5.28: Conical Helmholtz resonator with extended neck, $\widetilde{L}_{n2} = 1.53$ and $\widetilde{\overline{u}}_{n1} = 1$. Volume length variation.

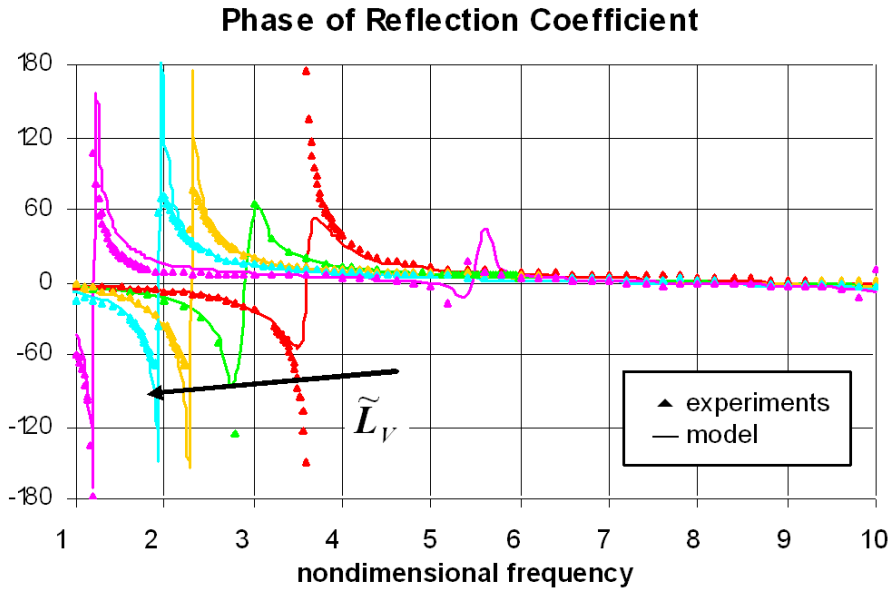

Figure 5.29: Conical Helmholtz resonator with extended neck, $\widetilde{L}_{n2} = 1.53$ and $\widetilde{\overline{u}}_{n1} = 1$. Volume length variation.

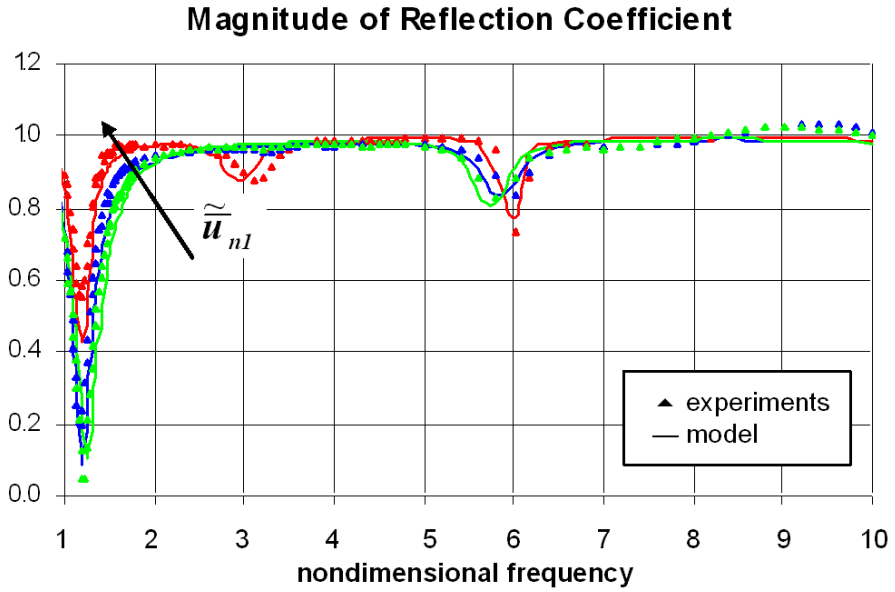

Figure 5.30: Conical Helmholtz resonator, no seal, $\widetilde{L}_{n2} = 0.68$ and $\widetilde{L}_V = 1$. Cooling flow velocity variation.

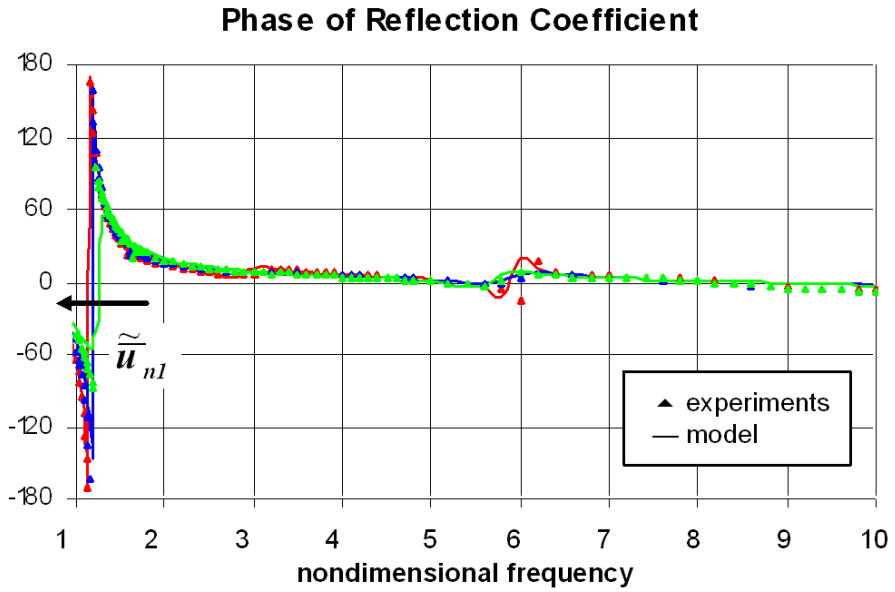

Figure 5.31: Conical Helmholtz resonator, no seal, $\widetilde{L}_{n2} = 0.68$ and $\widetilde{L}_V = 1$. Cooling flow velocity variation.

5.3 Resonators Coupled to Combustion Chambers

In room acoustics, Helmholtz resonators are coupled to enclosures in order to suppress acoustic modes excited by sound sources [29]. The mechanism responsible for the damping may be analyzed by replacing the solid wall boundary A_n of the enclosure with the resonator impedance Z_n [41], [42]. In our analysis we concentrate on the suppression of the acoustic mode $\psi_j(\mathbf{x})$ associated to the resonance frequency ω_j belonging to the low frequency range, where the average separation between eigenfrequencies is much larger than the average modal bandwidth. The enclosure we consider is equipped with N_R equal resonators that are acoustically "compact", i.e. both the mode value ψ_j and the resonator impedance Z_n are constant on the k-resonator mouth of area A_n located at $\mathbf{x}_k$ (low frequency hypothesis). Thus, for frequencies close to ω_j we neglect the modal coupling so that Eqs. (2.201), (2.202), (2.203) and (2.224) lead to the relation

$$\widehat{p}\,(s,\mathbf{x}) \simeq \left[C_1(s) - C_2(s) \sum_{k=1}^{N_R} \psi_j(\mathbf{x}_k)\; \widehat{p}\,(s,\mathbf{x}_k) \right] \psi_j(\mathbf{x}) \tag{5.38}$$

where

$$C_1(s) = \left(\frac{s}{s^2 - 2\,\upsilon_j\,s + \omega_j^2} \right) \frac{\gamma_E - 1}{V_E\,\Lambda_j} \int_{V_E} \widehat{Q}_N\,(s,\mathbf{x})\,\psi_j(\mathbf{x})\,dV$$

$$C_2(s) = \left(\frac{s}{s^2 - 2\,\upsilon_j\,s + \omega_j^2} \right) \frac{\overline{\rho}_E\,\overline{c}_E^{\,2}\,A_n}{V_E\,\Lambda_j\,Z_n(s)}$$

the suffix E being related to enclosure conditions and V_E being the volume of the enclosure. Moreover, the growth rate υ_j defined in Eq. (2.226) has been supposed to be

$$|\upsilon_j| \ll \omega_j \tag{5.39}$$

where $\upsilon_j < 0$ in stable systems and $\upsilon_j > 0$ when a combustion instability occurs. Eq. (5.38) written on resonator mouths lead to the linear system

$$\widehat{p}\,(s,\mathbf{x}_m) = \left[C_1(s) - C_2(s) \sum_{k=1}^{N_R} \psi_j(\mathbf{x}_k)\; \widehat{p}\,(s,\mathbf{x}_k) \right] \psi_j(\mathbf{x}_m) \qquad\qquad (m = 1,\ldots,N_R) \tag{5.40}$$

By multiplying each equation of the system (5.40) by $\psi_j(\mathbf{x}_m)$ and making the sum yields

$$\sum_{m=1}^{N_R} \psi_j(\mathbf{x}_m)\; \widehat{p}\,(s,\mathbf{x}_m) = \frac{C_1(s)\,\sum_{m=1}^{N_R}\,\psi_j^2(\mathbf{x}_m)}{1 + C_2(s)\,\sum_{m=1}^{N_R}\,\psi_j^2(\mathbf{x}_m)} \tag{5.41}$$

The substitution of Eq. (5.41) into Eq. (5.38) gives finally

$$\widehat{p}\,(s,\mathbf{x}) \simeq \frac{-2\,\upsilon_j\,s\;\widehat{p}_0(s,\mathbf{x})}{(s^2 - 2\,\upsilon_j\,s + \omega_j^2) + \dfrac{s\;\overline{\rho}_E\,\overline{c}_E^{\,2}\,A_n\,\sum_{m=1}^{N_R}\,\psi_j^2(\mathbf{x}_m)}{V_E\,\Lambda_j\,Z_n(s)}} \tag{5.42}$$

where

$$\widehat{p}_0(s,\mathbf{x}) = -\frac{1}{2\,\upsilon_j}\;\psi_j(\mathbf{x})\,\frac{\gamma_E-1}{V_E\,\Lambda_j}\;\int_{V_E}\;\widehat{Q}_N\,(s,\mathbf{x})\,\psi_j(\mathbf{x})\,dV \tag{5.43}$$

In the following we assume $\widehat{Q}_N$ as frequency independent ("white noise" case), i.e. $\widehat{p}_0 = \widehat{p}_0(\mathbf{x})$.
To express the resonator impedance Z_n, we write Eq. (5.5) in the form

$$Z_n\,(s) = \frac{\overline{\rho}_R\;\overline{c}_R^2\,A_n}{s\,\omega_{res}^2\,V_R}\left(s^2+\frac{\omega_{res}}{q_R}\,s+\omega_{res}^2\right) \tag{5.44}$$

where the suffix R refers to resonator conditions, V_R is the resonator volume and q_R the resonator quality-factor defined as

$$q_R = \omega_{res}\,\overline{\rho}_R L_n'/R_n = \;\overline{\rho}_R\,\overline{c}_R^2 A_n/\omega_{res} V_R R_n \tag{5.45}$$

with R_n supposed to be independent of frequency.
Next, we introduce the quality-factor of the enclosure without resonators $q_E = \omega_j/\Delta\omega_j$ where $\Delta\omega_j$ is defined so that at $\omega_j \pm \Delta\omega_j/2$ the pressure amplitude in case of stable system ($\upsilon_j < 0$) is $1/\sqrt{2}$ times the peak amplitude at ω_j. Eq. (5.38) written for $Z_n = \infty$ reads as

$$\left|\frac{2\,i\,\upsilon_j\;(\omega_j \pm \Delta\omega_j/2)}{(\omega_j \pm \Delta\omega_j/2)^2 + 2\,i\,\upsilon_j\;(\omega_j \pm \Delta\omega_j/2) - \omega_j^2}\right| = \frac{1}{\sqrt{2}} \tag{5.46}$$

that may be solved for $\Delta\omega_j$ using Eq. (5.39). It yields $\Delta\omega_j \simeq -2\,\upsilon_j$ and thus

$$q_E \simeq -\frac{\omega_j}{2\,\upsilon_j} \tag{5.47}$$

where $q_E > 0$ for stable systems and $q_E < 0$ for unstable systems. In the following we assume that the modal damping coefficient ξ_j of the enclosure with dampers may be approximated by the value of ξ_j computed without dampers.
By using Eqs. (5.44), (5.45) and (5.47) into Eq. (5.42) and noting that

$$\overline{\rho}_E\;\overline{c}_E^2 = \gamma_E\;\overline{p}_E \approx\;\overline{\rho}_R\;\overline{c}_R^2 = \gamma_R\;\overline{p}_R \tag{5.48}$$

one obtains finally

$$\frac{\widehat{p}}{\widehat{p}_0}(s) \simeq \frac{s\,\omega_j/q_E}{(s^2 + s\,\omega_j/q_E + \omega_j^2) + \dfrac{s^2\,\varepsilon^2\,\omega_{res}^2}{s^2 + s\,\omega_{res}/q_R + \omega_{res}^2}} \tag{5.49}$$

where we have introduced the nondimensional parameter

$$\varepsilon = \sqrt{\frac{V_R\;\sum_{m=1}^{N_R}\;\psi_j^2(\mathbf{x}_m)}{V_E\,\Lambda_j}} \tag{5.50}$$

In an initially stable systems $q_E > 0$ and $\widehat{p}_0(\mathbf{x})$ represents the pressure at $s = i\omega = i\omega_j$ in the enclosure without resonators. In this case Eq. (5.49) writes at $\omega = \omega_j$ as

$$\left[\frac{\widehat{p}}{\widehat{p}_0}\right]_{\omega=\omega_j} = \left[1 - \frac{i\,\varepsilon^2}{(\omega_j^2/\omega_{res}^2 - 1)/q_E - i\omega_j/(\omega_{res}\,q_E\,q_R)}\right]^{-1} \tag{5.51}$$

Eq. (5.51) shows that the neck mouths may act as "pseudo-sources" performing sound cancelation on the acoustic field produced by sound sources inside the enclosure. When $1/q_R \to 0$ (slightly damped resonator) thus $|\,\widehat{p}/\,\widehat{p}_0|_{\omega=\omega_j}$ is minimized provided that $\omega_{res} = \omega_j$ ("well tuned" resonators).

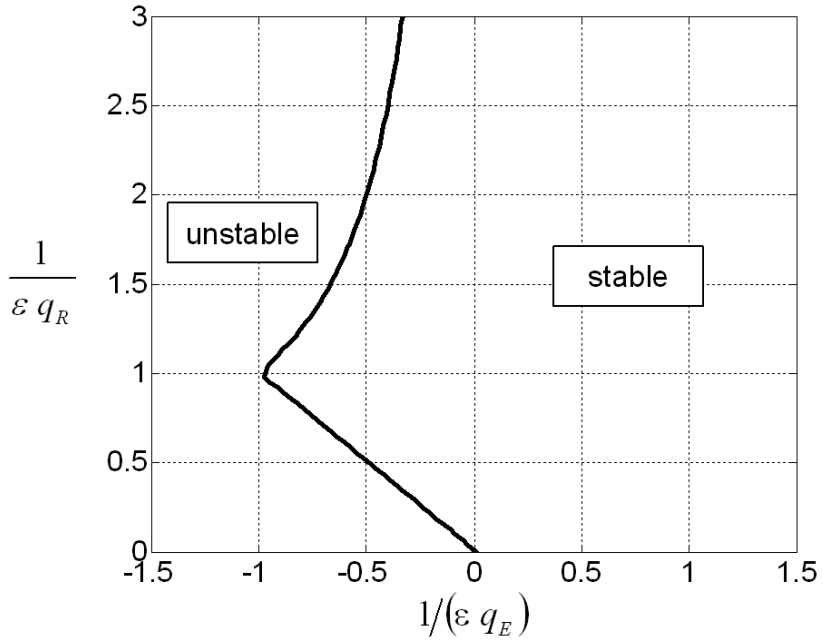

Figure 5.32: Stability plot for $\omega_{res} = \omega_j$.

5.3.1 Unstable systems

In unstable systems, the main goal of the dampers is to suppress the instability. Well tuned resonators may make the system stable if the poles of the characteristic equation

$$(s^2 + s\,\omega_j/q_E + \omega_j^2)\,(s^2 + s\,\omega_j/q_R + \omega_j^2) + s^2\,\varepsilon^2\,\omega_j^2 = 0 \tag{5.52}$$

have a negative real part. By substituting $s = i\omega$ into Eq. (5.52) and setting to zero both the real and imaginary part, one obtains the (necessary) stability border conditions $1/(\varepsilon q_R) = -1/(\varepsilon q_E)$ and $1/(\varepsilon q_R) = -[1/(\varepsilon q_E)]^{-1}$. When computing the stability plot (see Fig. 5.32), one finds that the stability condition is given by

$$-\frac{1}{\varepsilon\,q_E} < \frac{1}{\varepsilon\,q_R} < -\frac{1}{1/(\varepsilon\,q_E)} \qquad (q_E < 0) \tag{5.53}$$

5.3.2 Pressure amplitude minimization

For a stable system ($q_E > 0$) or for an unstable system verifying Eq. (5.53), Eq. (5.51) writes as

$$\left[\frac{\widehat{p}}{\widehat{p}_0}\right]_{\omega=\omega_{res}=\omega_j} = \frac{1}{1+\varepsilon^2\,q_R\,q_E} \tag{5.54}$$

Eq. (5.54) shows that the maximum pressure reduction at $\omega = \omega_j$ is obtained by maximizing ε and q_R, i.e. by locating large volume lightly damped resonators close to mode antinodes. Note that at ω_j the condition of maximum pressure amplitude reduction does not correspond to that of maximum

absorption of acoustic power $\varepsilon^2\, q_R q_E = 1$, the application of the resonators to the enclosure having the effect of retuning the acoustic power injected by the sources into the domain [41].
When considering frequencies close to ω_j, Eq. (5.49) may be written as

$$\left[\frac{\widehat{p}}{\widehat{p}_0}\right]_{\omega_{res}=\omega_j} = \frac{i/\varepsilon q_E}{(\widetilde{\omega} - i/\varepsilon q_R)^{-1} - (\widetilde{\omega} - i/\varepsilon q_E)} \tag{5.55}$$

where we have used $s = i\omega$ and

$$\widetilde{\omega} = \frac{\omega^2 - \omega_j^2}{\omega\, \omega_j\, \varepsilon} \tag{5.56}$$

Eq. (5.55) indicates that the pressure reduction is a function of the three nondimensional numbers $\widetilde{\omega}$, $1/(\varepsilon\, q_R)$ and $1/(\varepsilon\, q_E)$. Figs. 5.33-5.34 report respectively the H_∞ and H_2 norms of the pressure ratio $[\,\widehat{p}/\,\widehat{p}_0]_{\omega_{res}=\omega_j}$ as a function of $1/(\varepsilon q_R)$ and $1/(\varepsilon q_E)$.[1] Figs. 5.33-5.34 indicate that the pressure reduction is larger when $1/(\varepsilon q_E)$ is lower, that means the parameter ε should be always maximized. Fig. 5.35 presents the curves $1/(\varepsilon q_R)_\infty$ and $1/(\varepsilon q_R)_2$ where the minimum values of the H_∞ and H_2 norms are respectively achieved. In Fig. 5.35, the minimum values of the H_∞ and H_2 norms are also plotted as a function of $1/(\varepsilon q_E)$. The $1/(\varepsilon q_R)_\infty$ and $1/(\varepsilon q_R)_2$ curves are well interpolated by the linear fits

$$1/(\varepsilon q_R)_\infty = 0.1967/(\varepsilon\, q_E) + 1.235 \tag{5.57}$$

$$1/(\varepsilon q_R)_2 = 1 \tag{5.58}$$

Eqs. (5.57)-(5.58) suggest that when maximizing the pressure reduction with white noise excitation, besides ω_j other frequencies may be excited. These additional frequencies are obtained by means of the following theoretical analysis. For a stable system we can set to zero Eq. (5.52) where damping terms are neglected. It yields

$$\widetilde{\omega}^2 = 1 \Longleftrightarrow (\omega^2 - \omega_j^2)^2 = \omega^2\, \omega_j^2\, \varepsilon^2 \tag{5.59}$$

that has the real solutions

$$\omega_\pm = \omega_j \left(\sqrt{\frac{\varepsilon^2}{4} + 1} \pm \frac{\varepsilon}{2}\right) \tag{5.60}$$

In general one has $0 < \psi_j^2/\Lambda_j < 1$, $V_E = \mathcal{O}(\lambda_j)$ and from model assumptions $V_R \ll \lambda_j$ with $\lambda_j = 2\pi\, \overline{c}/\omega_j$. Therefore $\varepsilon \ll 1$ and Eq. (5.60) may be approximated by

$$\omega_\pm \simeq \omega_j \left(1 \pm \frac{\varepsilon}{2}\right) \tag{5.61}$$

The resonance frequencies $\omega_\pm$ replace the resonance frequency ω_j of the enclosure without resonators, $\omega_\pm$ being symmetrically located with respect to ω_j (when considering the acoustic damping thus the frequencies of maximum modal response are slightly shifted with respect to $\omega_\pm$). The pressure reduction at ω_+ and ω_- computed using Eqs. (5.55) and (5.59) is given by

$$\left|\frac{\widehat{p}}{\widehat{p}_0}\right|^2_{\substack{\omega_{res}=\omega_j \\ \omega=\omega_\pm}} = \left|\frac{1 \pm i\, \varepsilon\, q_R}{1 \pm i\, \varepsilon\, (q_R + q_E)}\right|^2 = \frac{1 + \varepsilon^2\, q_R^2}{1 + \varepsilon^2 (q_R + q_E)^2} \tag{5.62}$$

[1] $||\,\widehat{p}/\,\widehat{p}_0||_\infty = \max\{|(\,\widehat{p}/\,\widehat{p}_0)|\}$ for $\widetilde{\omega} \in [-\infty, \infty]$ and $||\,\widehat{p}/\,\widehat{p}_0||_2 = \sqrt{1/2\pi \int_{-\infty}^{\infty} |(\,\widehat{p}/\,\widehat{p}_0)|^2 d\,\widetilde{\omega}}$.

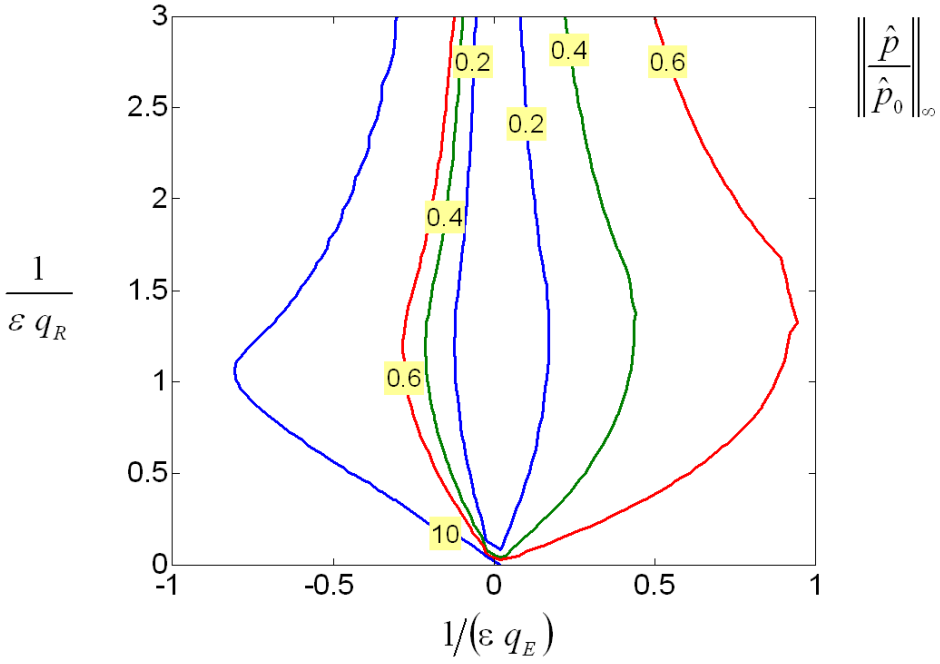

Figure 5.33: H_∞-norm of pressure ratio $[\widehat{p}/\,\widehat{p}_0]_{\omega_{res}=\omega_j}$.

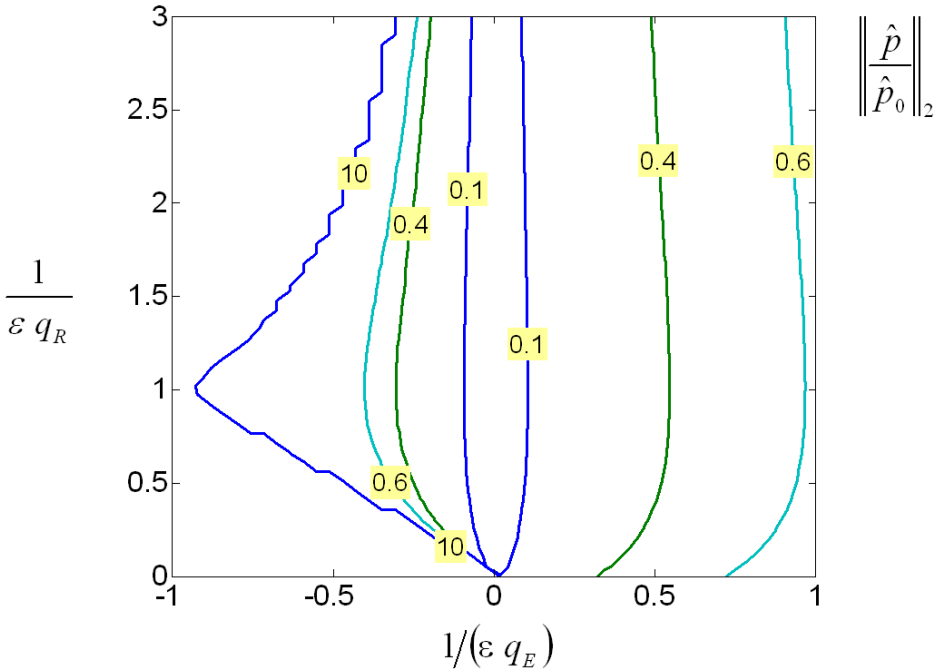

Figure 5.34: H_2-norm of pressure ratio $[\widehat{p}/\,\widehat{p}_0]_{\omega_{res}=\omega_j}$.

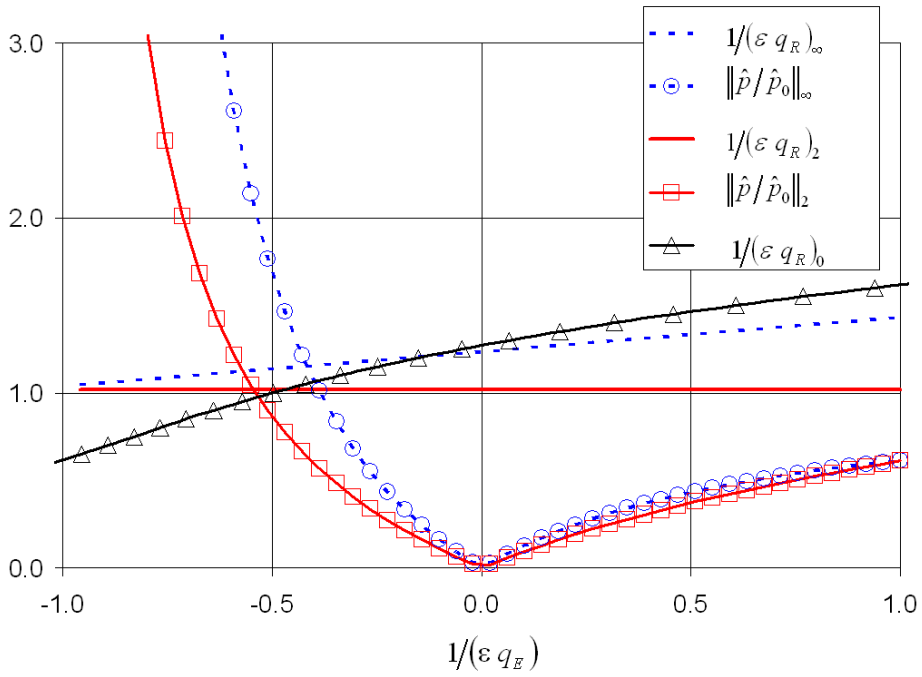

Figure 5.35: Points in the plane $1/(\varepsilon q_E) - 1/(\varepsilon q_R)$ where the H_∞ and H_2 norms of $[\widehat{p}/\widehat{p}_0]_{\omega_{res}=\omega_j}$ are minimum. H_∞ and H_2 minima given as a function of $1/(\varepsilon q_E)$.

Eq. (5.62) shows that the maximum pressure reduction is achieved at ω_+ and ω_- when

$$\varepsilon\, q_R = \sqrt{\left(\frac{\varepsilon\, q_E}{2}\right)^2 + 1} - \frac{\varepsilon\, q_E}{2} \tag{5.63}$$

In Ref. [41] a resonator design criterion was obtained by imposing the same value of $|\widehat{p}/\widehat{p}_0|$ at ω_j, ω_+ and ω_-. Using Eqs. (5.54) and (5.62), it reads as

$$\varepsilon\, q_E = \frac{2\,(\varepsilon\, q_R)_0^3}{1 - (\varepsilon\, q_R)_0^2 - (\varepsilon\, q_R)_0^4} \tag{5.64}$$

The curve $1/(\varepsilon q_R)_0$ is also reported in Fig. 5.35. Fig. 5.36 illustrates typical frequency responses for a fixed value of (εq_E) when varying (εq_R). Fig. 5.36 shows that when $(\varepsilon q_R) > (\varepsilon q_R)_0$ two pulsation peaks appear, whereas when $(\varepsilon q_R) < (\varepsilon q_R)_0$ the pressure spectrum has a maximum at $\omega = \omega_j$. The maximum pressure reduction is achieved with $(\varepsilon q_R)_\infty$. However, a similar sound reduction is obtained with $(\varepsilon q_R)_2$ and $(\varepsilon q_R)_0$. For instance, when imposing the minimization of the H_2-norm (5.58) together to the stability condition (5.53), one obtains $q_R = 1/\varepsilon$ with ε as large as possible and however $> -1/q_E$ if $q_E < 0$.

It is important to remark that the present theory is suitable for gas turbine combustion chambers where the temperature inside the damper (related to the cooling flow purging the resonator) differs from the combustion chamber temperature [see Eq. (5.48)]. In agreement with the classical resonator design rules, the theory predicts that the maximum pressure reduction is obtained by tuning the resonator resonance frequency to the pulsation peak frequency and by locating large volume lightly damped resonators

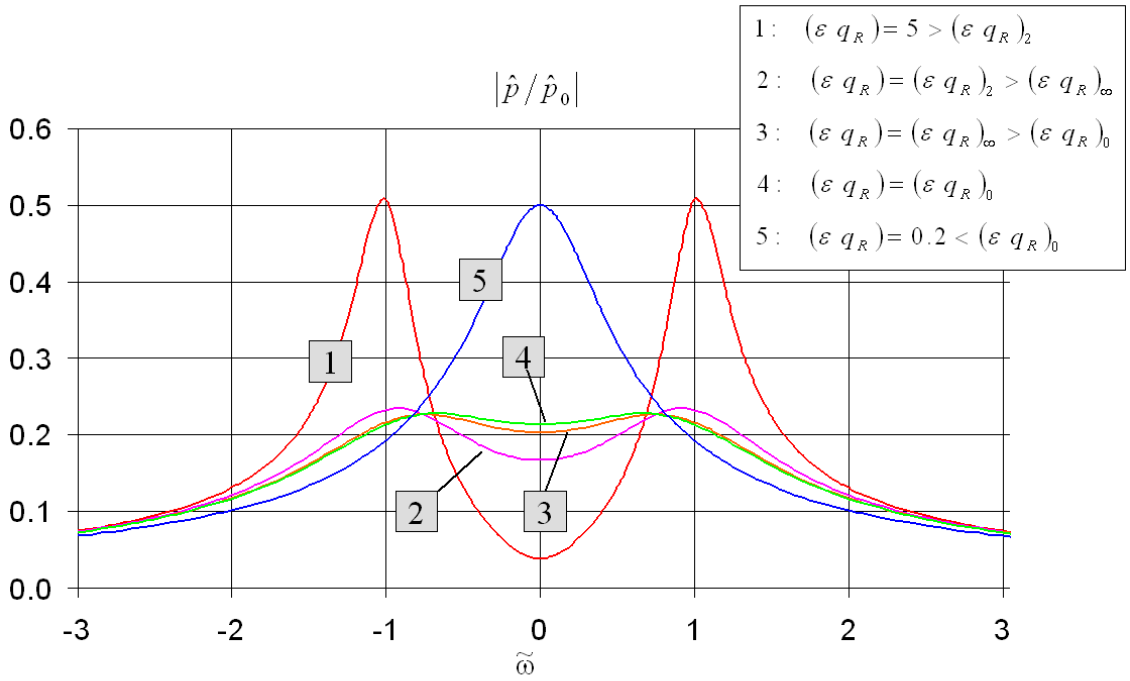

Figure 5.36: Pressure ratio for $1/(\varepsilon q_E) = 0.2$. Effect of (εq_R) variation.

close to mode antinodes. For an excitation not confined to ω_j, the theory shows that the maximum suppression of acoustic amplitude is achieved when a specific value is assigned to the damper resistance. This demonstrates the importance of predicting the damper impedance with the maximum possible accuracy.

5.3.3 Theory validation

The validation of the acoustic theory for pressure reduction maximization has been performed on the cylindrical resonator with inlet tube illustrated in Section 5.2.1. In order to increase the range of variation of the neck flow velocity, the neck diameter was reduced of a factor two. Pressure spectra were measured on the resonator flange of the impedance tube, which represented the enclosure in which acoustic pulsations had to be suppressed. The impedance tube end on the other side of the resonator flange was an open end. By acting on the movable piston, the resonator volume was varied in order to tune the resonator resonance frequency to the frequency of the first axial mode of the impedance tube [87]. Furthermore, air was injected inside the resonator volume in order to tune the resonator resistance. The quality factor of the enclosure was determined by using the impedance tube spectrum measured without resonator. Fig. 5.37 reports pressure spectra without and with the cylindrical resonator. In the latter case, the neck velocity was varied from $0m/s$ to $19m/s$. In the experiments, $\overline{u}_n = 13m/s$ was found to give the maximum damping $||\,\widehat{p}/\,\widehat{p}_0||_\infty = 0.27$. According to Eq. (5.57) (H_∞-norm minimization), the minimum achievable pressure ratio was $||\,\widehat{p}/\,\widehat{p}_0||_\infty = 0.26$ in correspondence of a neck velocity (extracted

from the impedance model presented in Section 5.1.2) $\overline{u}_n = 11m/s$. Pulsation amplitudes computed with Eq. (5.55) for $\overline{u}_n = 11m/s$ have been also reported in Fig. 5.37, showing good agreement with experiments.

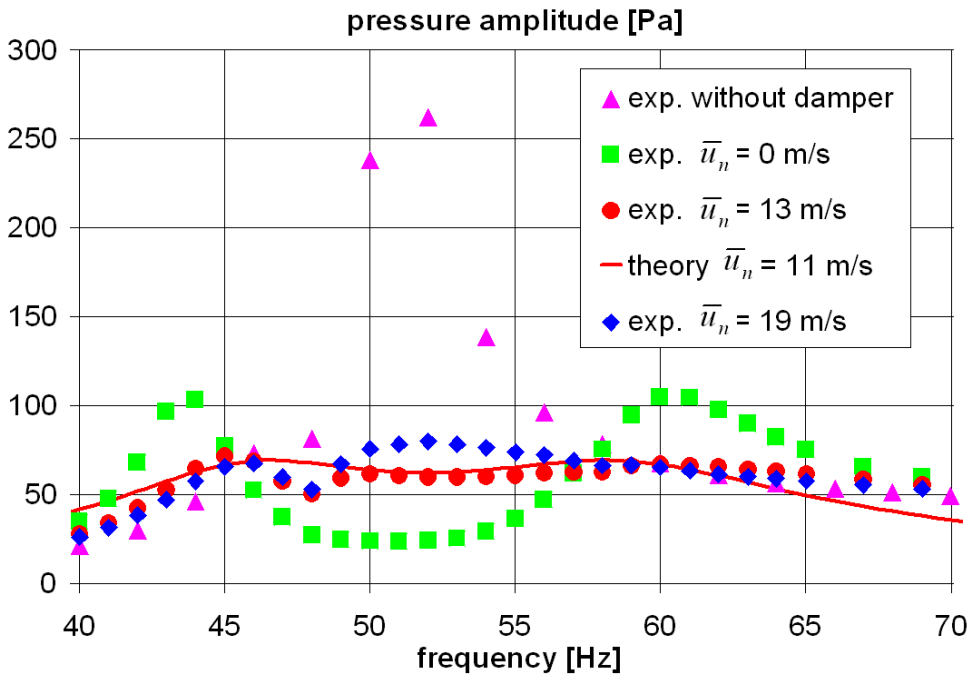

Figure 5.37: Pressure spectra of impedance tube with and without dampers. Neck velocity variation.

Chapter 6

Thermoacoustic Network Approach

6.1 Network Description

In this Section we describe the ALSTOM Thermo-Acoustic 3-dimensional (*TA3*) network used for simulating the thermoacoustic response of a heavy-duty gas turbines. In the *TA3* approach, the combustion system is lumped into several elements (e.g. air supply, burner, flame, combustor, cooling channels, etc.). The use of the thermoacoustic network modeling has the advantage that the different network elements may be described by different acoustic models singularly validated.
In *TA3*, hood and combustor are modeled by means of Finite Element Method (FEM) modal analysis that is applied to the chamber geometries by taking as only openings on the boundary surface those corresponding to burners and (eventually) acoustic dampers (see Fig. 6.1). Therefore both hood air supply channels and combustor exit are assumed acoustic closed boundaries, this simplification being motivated by the large area jump between air supply channels and hood and by the large flow Mach number at the combustor exit. The FEM description of hood and combustor accounts for the geometrical complexity of the two elements, the physics being described by the wave equation without mean flow effects. By assuming acoustic wavelengths much larger than burner and damper dimensions, the acoustic pressure $\widehat{p}_j$ and normal acoustic velocity $\widehat{u}_j$ are assumed uniform over the opening area A_j centered at the average opening location $\mathbf{x}_j$. The acoustic unknowns $\widehat{p}_j$ and $\widehat{u}_j$ are expressed by making use of Green functions and modal expansion according to Eq. (2.201). It reads as

$$\widehat{p}_j = i\,\omega\,\overline{\rho}\,\overline{c}^2 \sum_{k=0}^{K} G(\,\mathbf{x}_j\,,\,\mathbf{x}_k)\,A_k\,\widehat{u}_k\,, \qquad j = 1\,,\ldots,K \tag{6.1}$$

where the Green function $G(\mathbf{x}_j, \mathbf{x}_k)$ of the Multiple Input-Multiple Output (MIMO) system is defined as

$$G(\,\mathbf{x}_j\,,\,\mathbf{x}_k) = \sum_{n=0}^{N} \frac{\psi_n(\mathbf{x}_j)\,\psi_n(\mathbf{x}_k)}{V\,\Lambda_n\,(\omega^2 - 2\,i\,\xi_n\,\omega_n\,\omega - \omega_n^2)} \tag{6.2}$$

(note that in our notation, the acoustic velocity is defined as positive when its direction points outside the volume). Eqs. (6.1) relate the K velocities to the K pressures at volume openings without including mean flow effects, being such effects considered negligible because of the small flow Mach number. The

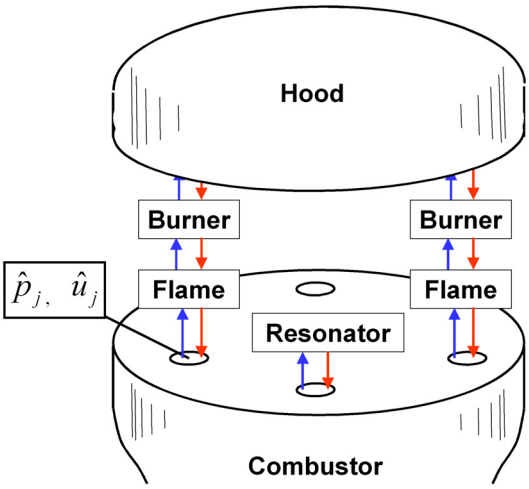

Figure 6.1: Thermoacoustic network elements.

eigenfunctions ψ_n and eigenfrequencies ω_n are the solutions of the problem (2.194)-(2.195) and are obtained numerically by applying FEM [73] (as a solution of a real problem, both eigenfunctions and eigenfrequencies are real functions). An example of FEM model is shown in Fig. 6.2 for an ALSTOM GT11N2 combustion system. Fig. 6.2 also reports a computed acoustic mode corresponding to an engine pulsation peak (see next Section). Eq. (6.1) yields the exact solution for $N = \infty$. However, a limited number of modes (depending on the frequency range of interest) is generally sufficient to represent the network element.

Under the assumption of geometrical extent small compared to acoustic wavelengths, plane wave propagation is usually considered in burners, flames and resonators (this "compactness" assumption restricts the application of the network approach to the low-frequency regime). Compact burners, flames and dampers are treated as two-ports elements, where acoustic pressure and acoustic velocity upstream and downstream the element are coupled linearly via a four-element transfer matrix. In particular, burners are acoustically modeled by including them within the hood FEM geometry (see Fig. 6.2). Moreover, following the analysis performed in Section 3.3, the end-correction effect and the losses due to the mean flow are also modeled by applying the $L - \zeta$ model (3.33)-(3.34) between hood openings and flames. In Eq. (3.34), the pressure loss coefficient obtained by fitting impedance tube measurements (see Section 3.3) is also employed in engine simulations (in general, in the range of variation of the burner velocity no significant ζ variations are observed). On the contrary, the end-correction ℓ is a function of the combustor geometry and thus the value measured in the impedance tube can not directly employed in engine simulations. To obtain the burner end-correction for the engine geometry, a method based on the FEM analysis of the "cold" (i.e. without flame) combustion system is proposed. In our approach, FEM and *TA3* simulations of the cold combustion system model including hood, burners and combustor are performed. Then, the burner end-correction of the *TA3* model is tuned to obtain the same eigenfrequencies of the FEM model. An example of this end-correction calibration is illustrated in Fig. 6.3.

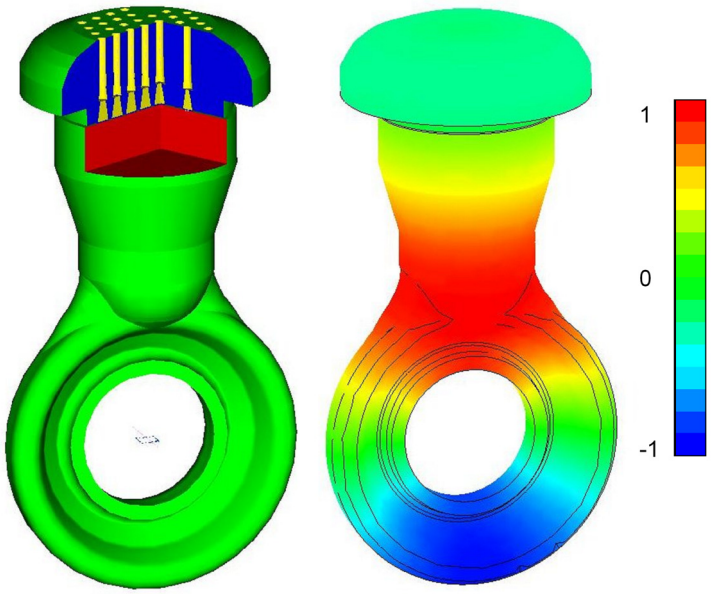

Figure 6.2: FEM model (left) and example of acoustic mode (right) of the combustion system.

The end-correction calibration does not account for flow effects, in agreement with the small sensitivity shown by impedance tube measurements with respect to burner speed.

The amplifier behavior of the flame makes it an "active" acoustic two-port. We have seen that the flame dynamics depends on the several physical mechanisms affecting the heat release process (fuel injection, mixing, convective and diffusive transport, flame stabilization, chemical kinetics). All these effects may be implicitly included when modeling the flame as a gas dynamic discontinuity by means of its transfer function, which represents the crucial element to perform accurate thermoacoustic simulations. Therefore, in our network approach we employ flame transfer functions and source terms measured in the atmospheric combustion test rig described in Section 4.5.

The thermoacoustic network is also able to model Helmholtz dampers eventually applied to the combustion chamber. In this case, the damper impedance (5.5) is used to express the link between $\widehat{p}_j$ and $\widehat{u}_j$ at the combustor openings connected to resonators.

In the *TA3* network, all the network element models are formulated in the frequency domain and assembled together in the MATLAB environment [88]. In the frequency domain formulation, the stability analysis of the combustion system is performed by computing the eigenvalues of the resulting linear system [76]. The real part of eigenvalues gives the frequency of pulsation peaks. The growth rate (i.e. the eigenvalue imaginary part) determines the stability of the system. A the time domain solution may be also obtained from *TA3* when nonlinearities are included in order to limit the amplitude growth when the system is unstable. Then, pulsation spectra may be computed by post-processing the time domain solution. For instance, the time domain representation of Eq. (6.1) corresponds to K second order differential equations relating $2K$ unknowns. Noting that a differential equation of any order can be represented as a system of first order differential equations and that all the terms of the Green function (6.2) have the same poles ω_n, Eq. (6.1) can be expressed in the time domain by a *state-space* formulation

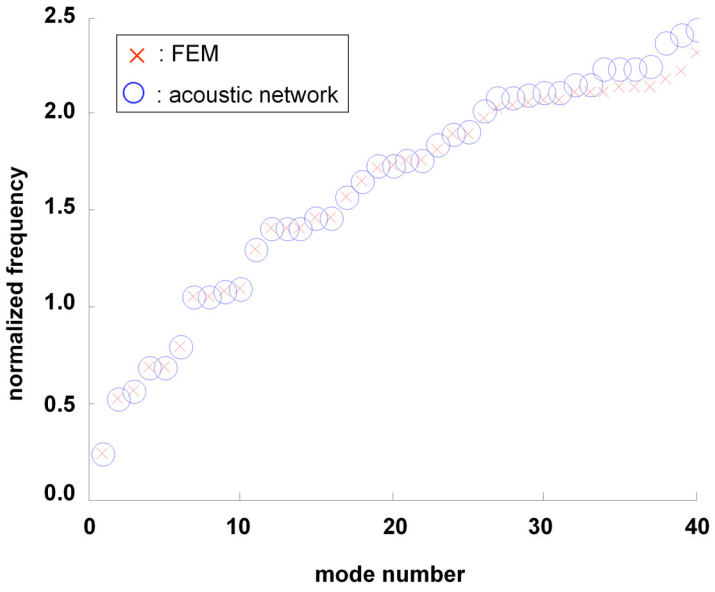

Figure 6.3: Comparison of combustion system eigenfrequencies: FEM vs. network results.

consisting of $2N + K$ first order differential equations in $2N + 2K$ unknowns. It reads as [76]

$$\frac{\partial \mathbf{y}}{\partial t} = \mathbf{A}\mathbf{y} + \mathbf{B}\mathbf{u}' , \tag{6.3}$$

$$\mathbf{p}' = \mathbf{C}\mathbf{y} + \mathbf{D}\mathbf{u}' , \tag{6.4}$$

where

$$\mathbf{y} = [y_1 , \ldots , y_{2N}]^T , \qquad \mathbf{p}' = \left[p'_1 , \ldots , p'_K\right]^T , \qquad \mathbf{u}' = \left[u'_1 , \ldots , u'_K\right]^T , \tag{6.5}$$

and

$$\mathbf{A} = \begin{bmatrix} 0 & -\omega_n & & & \\ \omega_n & -2\xi_n\omega_n & & & \\ & & \ddots & & \\ & & & 0 & -\omega_n \\ & & & \omega_n & -2\xi_n\omega_n \end{bmatrix}$$

$$\mathbf{B} = \begin{bmatrix} 0 & \ldots & 0 \\ -\psi_1(\mathbf{x}_1)A_1 & \ldots & -\psi_1(\mathbf{x}_K)A_K \\ & \vdots & \\ 0 & \ldots & 0 \\ -\psi_N(\mathbf{x}_1)A_1 & \ldots & -\psi_N(\mathbf{x}_K)A_K \end{bmatrix}$$

$$\mathbf{C} = \frac{\rho c^2}{V} \begin{bmatrix} 0 & \frac{\psi_1(\mathbf{x}_1)}{\Lambda_1} & & 0 & \frac{\psi_N(\mathbf{x}_1)}{\Lambda_N} \\ \vdots & \vdots & \cdots & \vdots & \vdots \\ 0 & \frac{\psi_1(\mathbf{x}_K)}{\Lambda_1} & & 0 & \frac{\psi_N(\mathbf{x}_K)}{\Lambda_N} \end{bmatrix}$$

$$\mathbf{D} = 0$$

The state-space representation is also used to model burners, flames and resonators. In particular, the flame model contains a time delay term and is of infinite order in time domain. In order to avoid systems of infinite order, the time delay is approximated by means of the Padé approximation (3.78). The entire system can now be modeled by interconnecting all the outputs of the subsystems to the inputs of their "neighbors" (see Fig. 6.1). Special care is taken to ensure that the system is causal and stable. The source terms in the flame module provides the external excitation. Unbounded amplitude growth in time is avoided by non-linear fuel saturation, that is introduced by applying the saturation function H to the velocity fluctuation u'_1 occurring at the upstream flame front side [see Eq. (3.74)]. The function H is defined as [14], [17]

$$H\{\, u'_1(t)\,\} = \begin{cases} u'_1(t) & \text{if} \quad |\, u'_1(t)| < u'_{lim} \\ sign[\, u'_1(t)]\ u'_{lim} & \text{if} \quad |\, u'_1(t)| > u'_{lim} \end{cases} \tag{6.6}$$

where the saturation parameter u'_{lim} is fitted to engine spectra. The computational time for a single spectrum simulation is in MATLAB of the order of minutes.

6.2 ALSTOM GT11N2 Gas Turbine Simulation

In this Section we present the application of the *TA3* network to the thermoacoustic simulation of an ALSTOM GT11N2 heavy-duty gas turbine (see Fig. 6.4). The combustion chamber is a silo combustor (see also Fig. 6.2), on the top of which both EV burners (see Section 3.3.3) and Helmholtz resonators are mounted. A hood and a combustor mode of the engine are shown in Fig. 6.5. The *TA3* GT11N2 model has been used to simulate baseload conditions. Both engine and *TA3* spectra reported in Fig. 6.6 were obtained without employing any resonator tuned at the pulsation peak frequency. The atmospheric flame transfer function was employed without any pressure scaling, assuming the natural gas chemical kinetics independent of pressure. After having calibrated the model, different engine operating conditions could be successfully simulated without any variation of the calibration parameters. This shows as the experimental-numerical combined process behind the *TA3* network is able to provide very fast and accurate engine spectrum computation.
Fig. 6.7 presents *TA3* and engine spectra for an engine configuration with seven resonators tuned to the pulsation peak frequency. Fig. 6.7 demonstrates the correct prediction of the effects of acoustic dampers applied to gas turbine combustors. The pulsation amplitude reduction with resonators is about 50%, showing the effectiveness of using Helmholtz resonators for gas turbine acoustic damping.

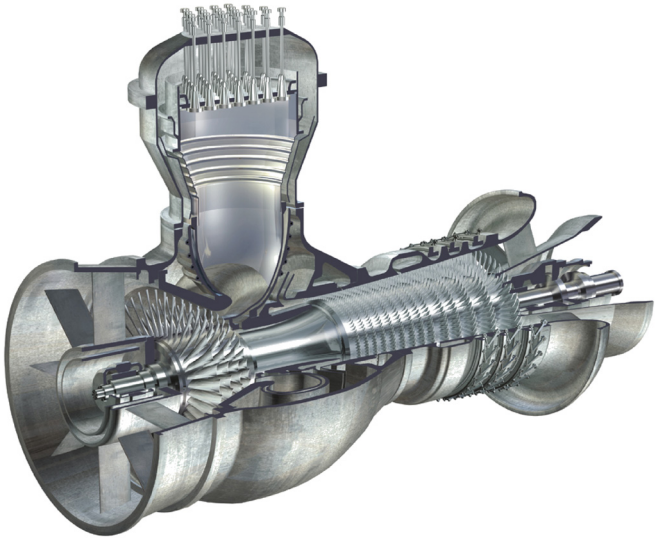

Figure 6.4: GT11N2 ALSTOM gas turbine.

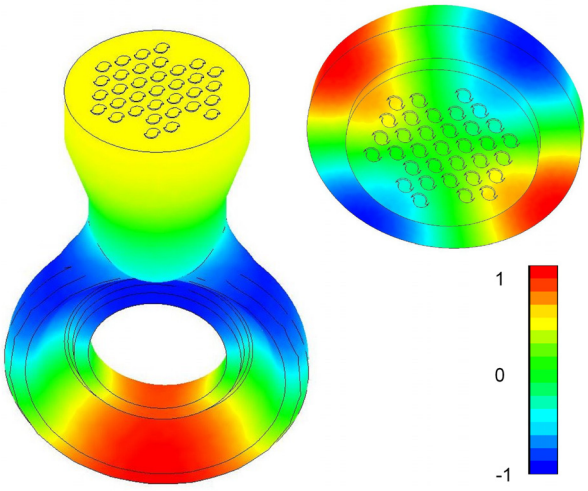

Figure 6.5: Example of combustor mode (left) and hood mode (right).

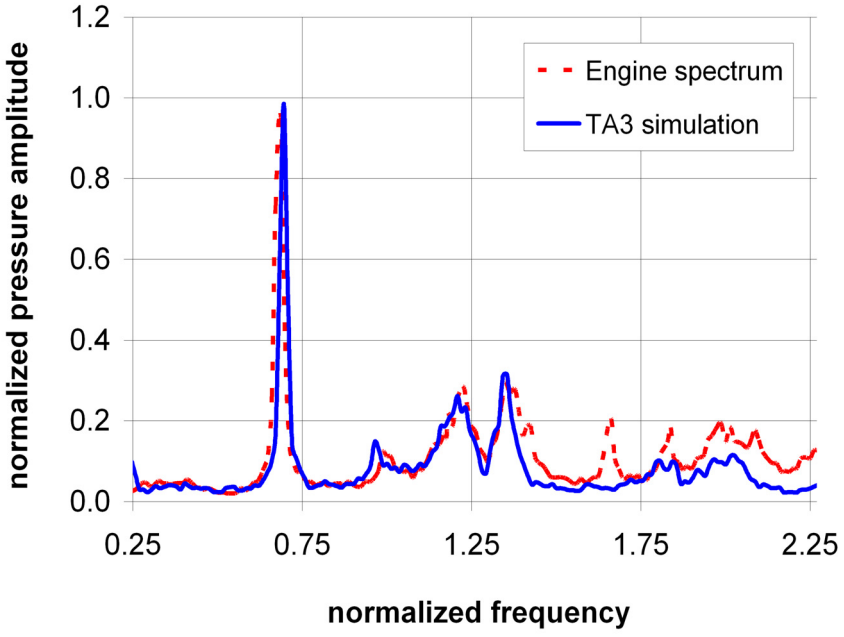

Figure 6.6: GT11N2 spectrum without resonators at peak frequency: engine vs. TA3 network.

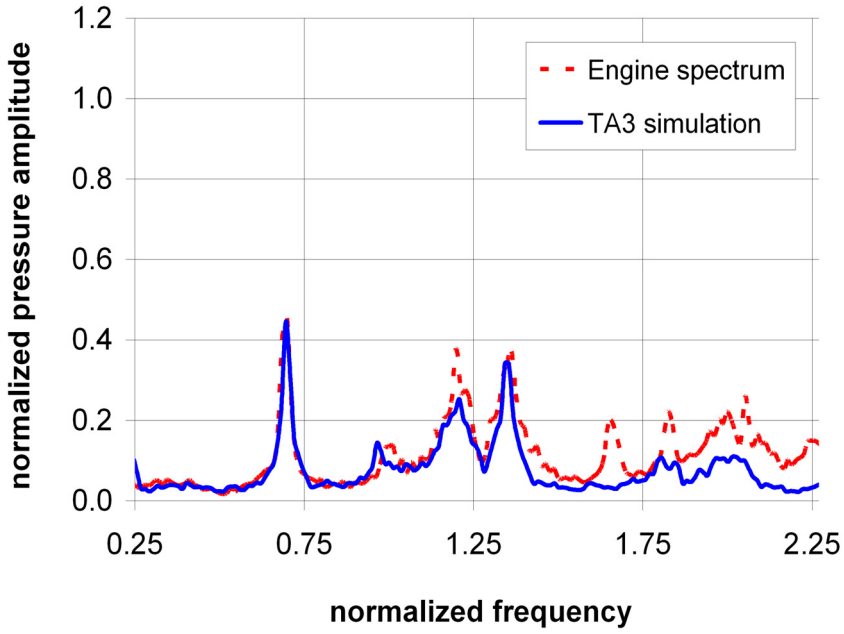

Figure 6.7: GT11N2 spectrum with resonators at peak frequency: engine vs. TA3 network.

6.3 ALSTOM LEV Burner Design

The thermoacoustic approach based on a combination of numerical analysis (CFD and three-dimensional acoustics), acoustic network models and dedicated measurements of acoustic flame response is well accepted across the industry. However, its application to specific combustor upgrade or development programs in "prediction mode" as opposed to "analysis mode" remains a challenge. This is mainly due to the large sensitivity of the complex methodology to key inputs, such as flame transfer functions, which can be only predicted in the burner design phase. In the present Section we discuss an example where an effort was made to apply the thermoacoustic approach in predictive mode. The example refers to the retrofit upgrade of a first generation diffusion burner with a partially premix burner to achieve low emissions. A particular challenge of this development program was that no test rig was available.

In the ALSTOM Single Diffusion Burner (SDB) shown in Fig. 6.8, reactions start in a zone of stoichiometric air fuel mixture thus ensuring good flame stability. The mixing achieved by injecting dilution air after the reaction zone reduces the temperature to the turbine inlet limit. However, the high temperatures in the reaction zone give NO_x dry emissions close to $200vppm$ in gas operation (reduced to $25-42vppm$ with H_2O-injection). In order to reduce burner emissions, a single burner retrofit project was launched in ALSTOM. The approach was to transfer the EV burner concept (see Section 3.3.3) into a single burner configuration with moderate changes of combustor hardware. The goal of the single burner retrofit project was to develop a premix flame diffusion stabilized burner (LEV Single Burner) able to achieve NO_x dry emissions lower than $80vppm$ ($25-42vppm$ with reduced H_2O-injection with respect to SDB). Neither water tunnel nor combustion rig experiments were performed because of the large burner size. On the contrary, Computational Fluid Dynamic (CFD) tools were extensively used to optimize the burner flow, combustor flow and gas hole pattern (including backflow margin of premix gas). The CFD simulations were performed with the commercial software Fluent using finite rate and eddy

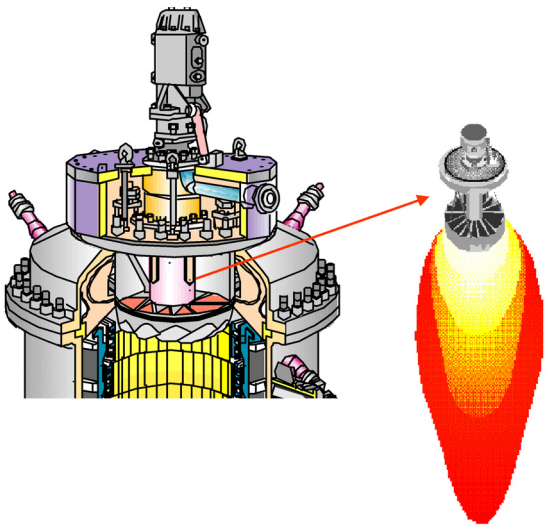

Figure 6.8: Single Diffusion Burner.

dissipation model with parameters optimized by means of genetic algorithms [89]. The resulting LEV burner is illustrated in Fig. 6.9. An EV-like conical swirl generator replaced the original outer swirler. The gas fuel was premixed with the combustion air along eight air inlet slots. The SDB gas injection lance was kept to generate a pilot diffusion flame used to stabilize the premix flame (see Fig. 6.10). Concerning the fuel distribution system, the existing gas pipe single branch was replaced by two split pipe branches (pilot and premix) equipped with control valves.

In parallel with the CFD study, the thermoacoustic analysis of a real silo combustion chamber type of engine in the field equipped with LEV burner was performed using the *TA3* network shown in Fig. 6.11. Since burner tests were not available, the thermoacoustic analysis was performed by modeling the acoustic flame response by means of pulsation data of engines equipped with the existing diffusion burner, CFD and data from thermoacoustic modeling of other engines. The SDB and LEV hood models used for the FEM modal analysis are presented in Fig. 6.12. The three-dimensional speed of sound distribution obtained from CFD was used in computing hood and combustor acoustic modes. Two modes obtained from the FEM models of SDB and LEV combustors are shown in Fig. 6.13. In Fig. 6.13, the modal frequencies are normalized with the reference frequency corresponding to the LEV pulsation peak (see next Section). The burner pressure loss coefficient of the $L-\zeta$ model was obtained from steady CFD simulations.

In order to validate the thermoacoustic model, *TA3* simulations of an existing engine equipped with SDB burner were performed. The analysis of the SDB pulsation data showed a resonance behavior, i.e. pulsation peaks mainly excited by combustion noise. Therefore, in the thermoacoustic analysis of the SDB combustor, no flame transfer matrix was applied (i.e. $\widehat{Q}_{A,I}/\overline{Q}_A = 0$). The combustion noise source term was approximated with the source term measured in an EV burner under conditions close to the SDB operating point. Fig. 6.14 shows the capability of the model to predict the resonance peaks of the engine in the low-frequency region of interest. Note that the *TA3* spectra were computed immediately downstream of the flame front, whereas the engine pulsation probe was located in the middle of the combustion chamber. For higher frequencies this could have been a cause of disagreement between computed and measured pulsation amplitudes, because acoustic modes become less uniform in space with increasing frequency.

EV flame transfer matrix measurements have been successfully approximated by using the only fuel concentration contribution (4.32) to heat release fluctuations [90]. Therefore, in the thermoacoustic LEV model we used Eq. (4.32) to represent the total heat release fluctuation term [i.e. $\widehat{Q}_{A,I}/\overline{Q}_A \simeq (\widehat{Q}/\overline{Q})_Y$]. In particular, the time-lag average value τ_Y and its variance σ_Y were computed from steady CFD results using the approach described in Ref. [91]. Pulsation spectra were calculated by varying the fuel saturation parameter u'_{lim} of Eq. (6.6) between a minimum and maximum value. The choice of the minimum and maximum values of u'_{lim} was made according the experience acquired from thermoacoustic simulations of EV burners installed on different ALSTOM heavy-duty engines.

Fig. 6.15 presents pulsation spectra predicted in the LEV combustor using both the minimum and maximum saturation values. In the first LEV analysis, the pilot lance axial position L (see Fig. 6.10) was kept equal to the fuel lance position L_1 of the SDB. For the case $L = L_1$, Fig. 6.15 shows that the pulsation peak was largely affected by the saturation value (lower pulsation amplitudes were obtained when further limiting the magnitude of heat release fluctuations using a smaller saturation). This indicates that such a pulsation peak was generated by a combustion instability that was then identified as

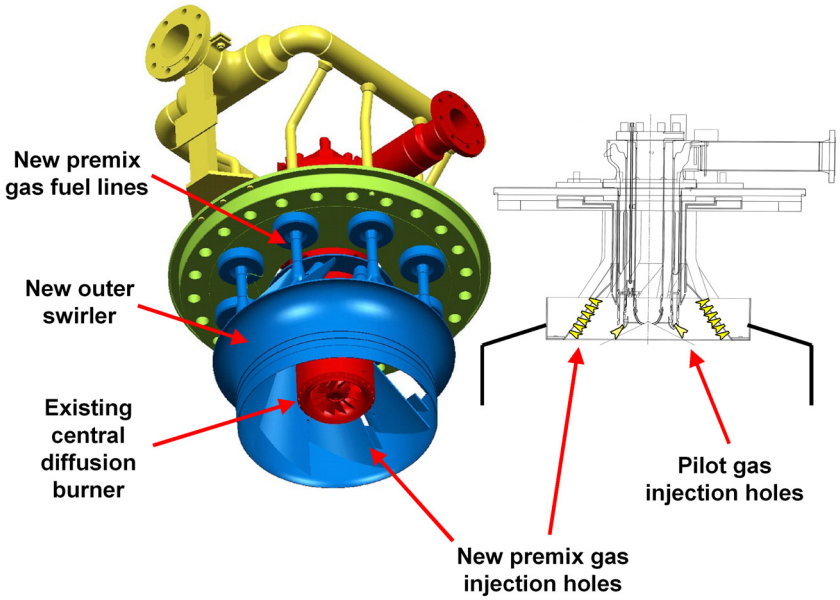

Figure 6.9: LEV single burner.

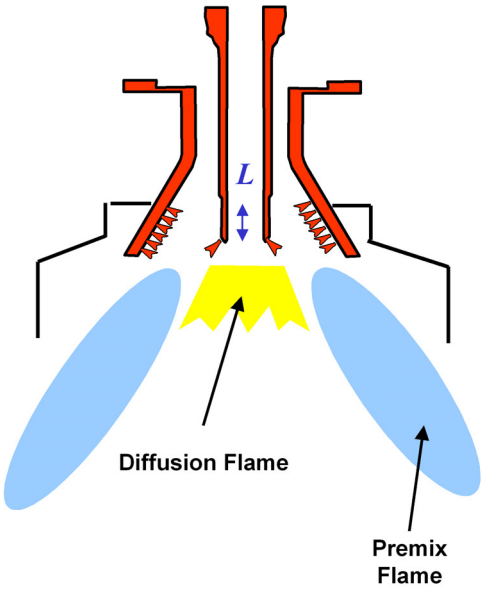

Figure 6.10: LEV burner concept.

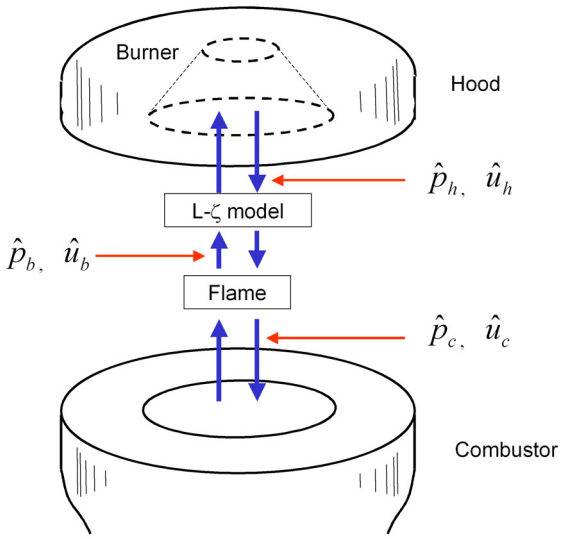

Figure 6.11: Thermoacoustic network.

a limiting factor for combustor operation. In order to suppress pulsation amplitudes, the thermoacoustic effect related to a different axial position of the fuel lance was investigated. In fact, an axial shift of the lance modifies the burner flow and then the position of the vortex breakdown, the flame front location and finally the time-lag. Therefore, a CFD steady analysis was performed using a lance position $L_2 > L_1$. The analysis gave a lower time-lag, in agreement with a more flat flame front (this effect being stronger than the time-lag increase related to the downstream displacement of the vortex breakdown bubble). The thermoacoustic simulation corresponding to the axial lance position L_2 is also reported in Fig. 6.15, showing the suppression of the pulsation peak of the case L_1 and the excitation of a pulsation peak at a larger frequency. Thus, simulations were performed for lance positions between L_1 and L_2 by interpolating linearly both time-lag average and variance. An optimum lance position L_{opt} was found corresponding to minimum pressure amplitudes. The spectrum for the case L_{opt} is also reported in

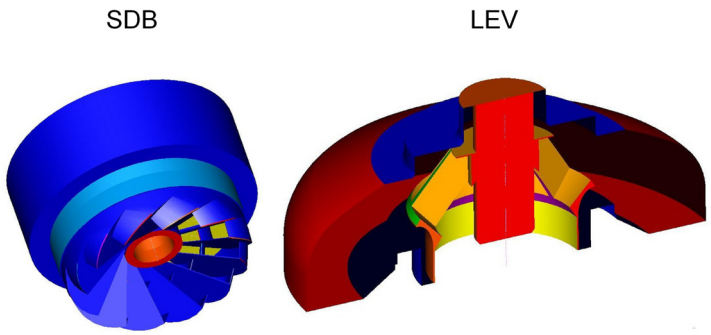

Figure 6.12: FEM models of engine hood with SDB and LEV burner.

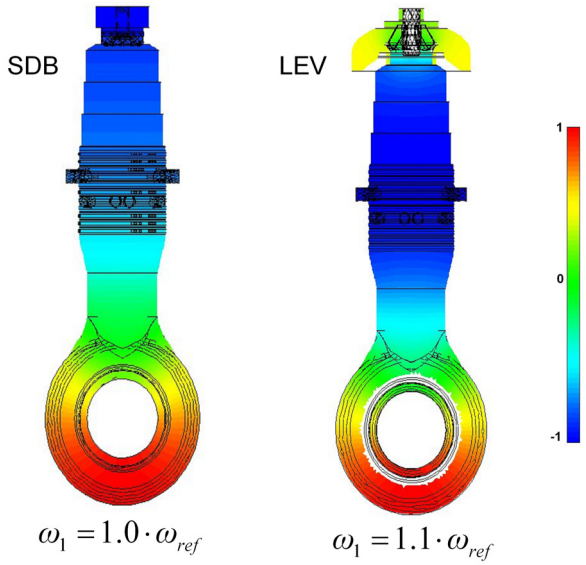

Figure 6.13: Acoustic modes of SDB and LEV combustor.

Fig. 6.15 (note that for this lance position the saturation value does not affect the amplitude, i.e. the system is stable). Hence, based on the input from the thermoacoustic analysis, the first LEV burner was designed with the capability of shifting the lance position between L_1 and L_{opt}. Moreover, a pulsation probe in the LEV combustor was located close to flame front, where the thermoacoustic analysis predicted a maximum of the acoustic modes excited in the pulsation spectra.

Fig. 6.16 shows two spectra measured in a silo combustion chamber of a field engine equipped with a LEV burner. First, tests with the L_1 lance position were performed. These tests confirmed the pulsation

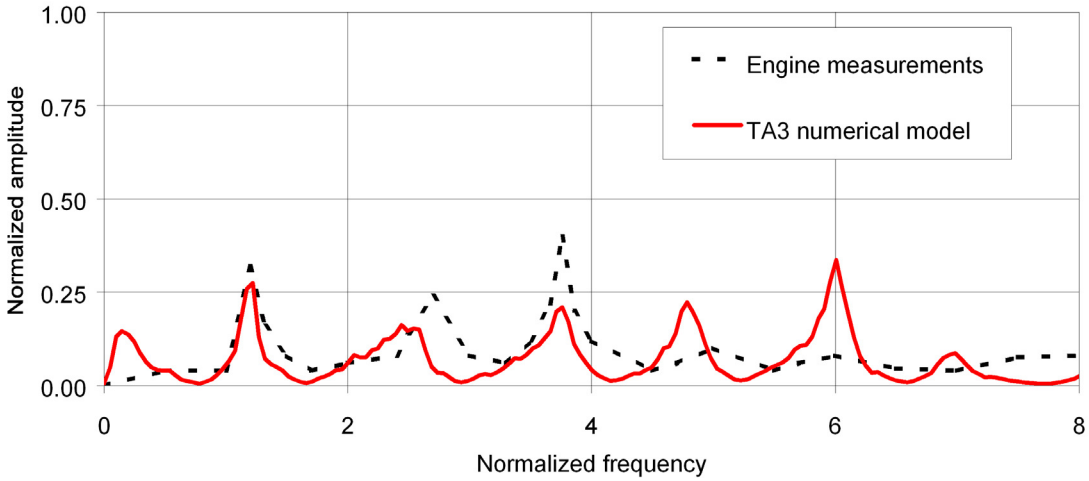

Figure 6.14: Pressure pulsations in SDB combustor: engine measurements vs. TA3 network simulations.

problem predicted by *TA3* for the case L_1. However, as predicted by our thermoacoustic analysis, when the lance was shifted to the L_{opt} position then thermoacoustic pulsations were no longer a limiting factor for combustor operation. For the two cases $L = L_1$ and $L = L_{opt}$, emissions at baseload without water injection were very similar and fulfilled the project target (see Fig. 6.17).

The engine spectrum for the case L_1 of Fig. 6.16 was also used to calibrate the value of the heat release saturation. The *TA3* results obtained with the calibrated saturation value for the cases L_1 and L_{opt} are reported in Fig. 6.18. Fig. 6.18 shows that the prediction of the low-frequency peak is very accurate, whereas the simulated amplitude of the second peak is overestimated for the L_1 case and underestimated for the L_{opt} case. However, simulations show that the first peak is unstable (the amplitude being mainly determined by the flame transfer function) whereas the second peak is stable, i.e. its amplitude is mainly related to the combustion noise term that generates resonance at that frequency. Therefore, the use of the same EV combustion noise source term for all the LEV simulations is probably responsible for the inaccurate pulsation trend of the second peak.

The above results show that the presented burner design engineering methodology has been able to provide good coincidence between predictions and actual field behavior. The predicted combustion instability represented a real limiting factor for combustor operation and engine tests fully confirmed the validity of the suggested pulsation mitigation strategy based on the thermoacoustic combustor tuning, that was achieved by varying the axial position of the pilot fuel lance.

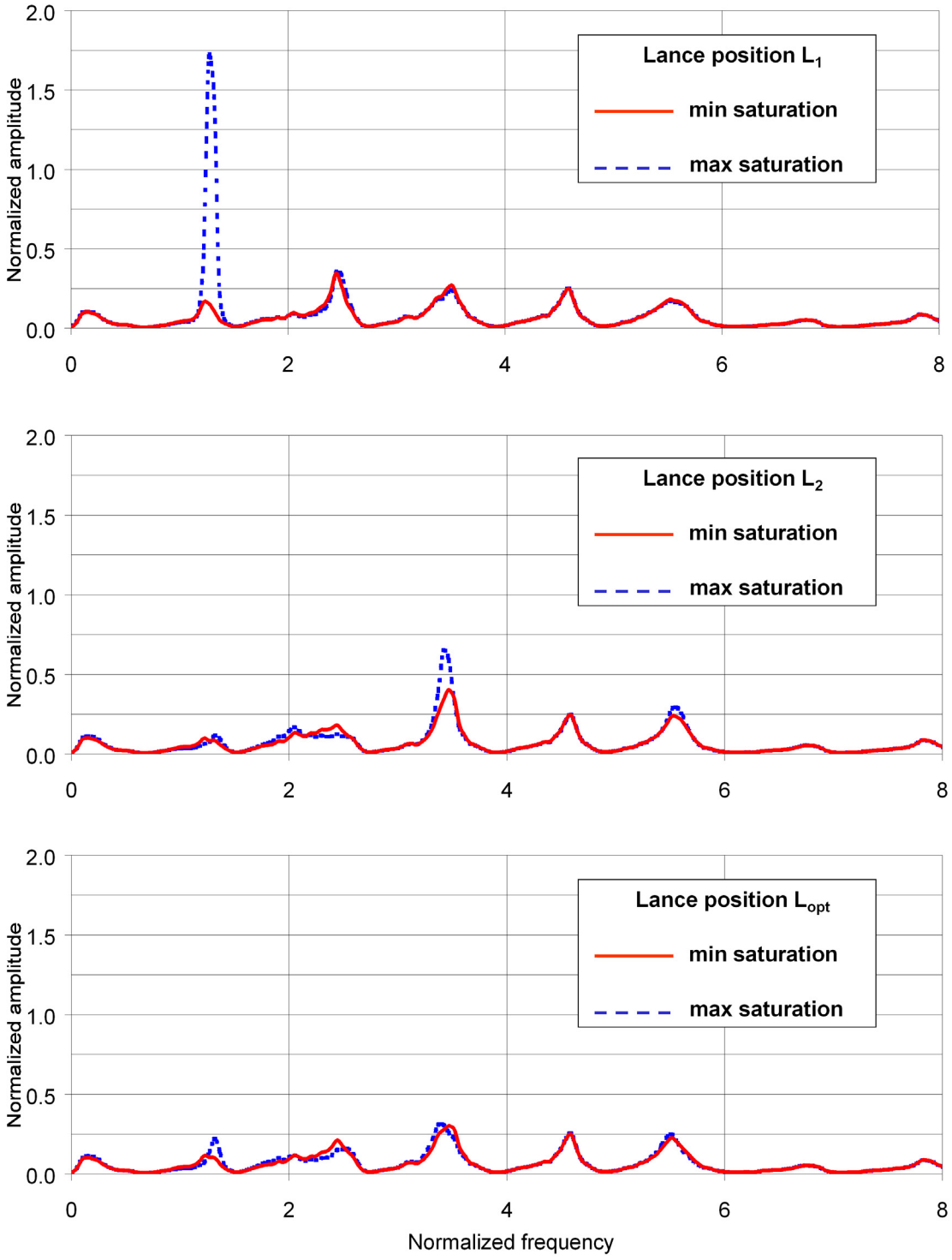

Figure 6.15: Pressure pulsations in LEV combustor: TA3 network simulations with minimum and maximum heat release saturation for the three axial lance positions L_1, L_2 and L_{opt} ($L_1 < L_{opt} < L_2$).

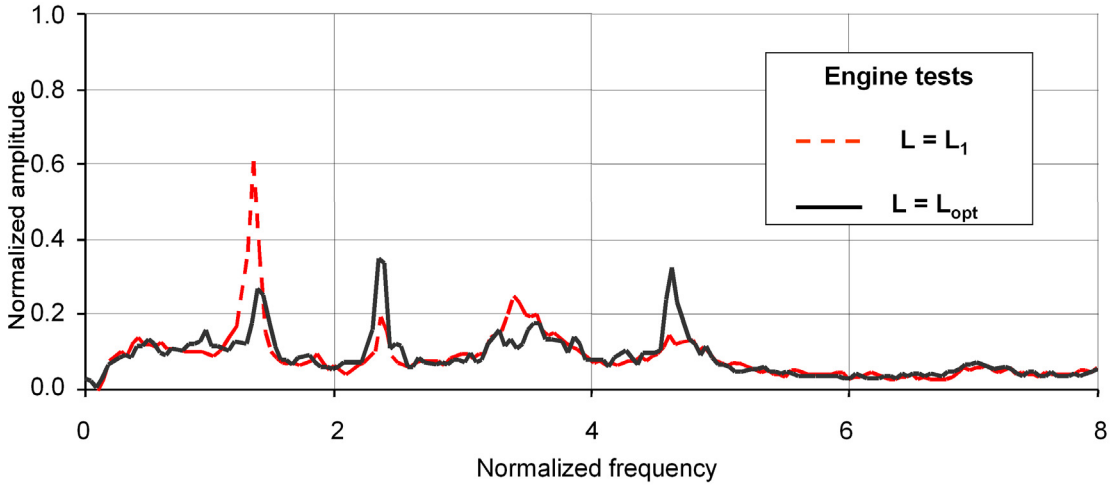

Figure 6.16: Pressure pulsations in LEV combustor: engine tests for axial lance positions L_1 and L_{opt}.

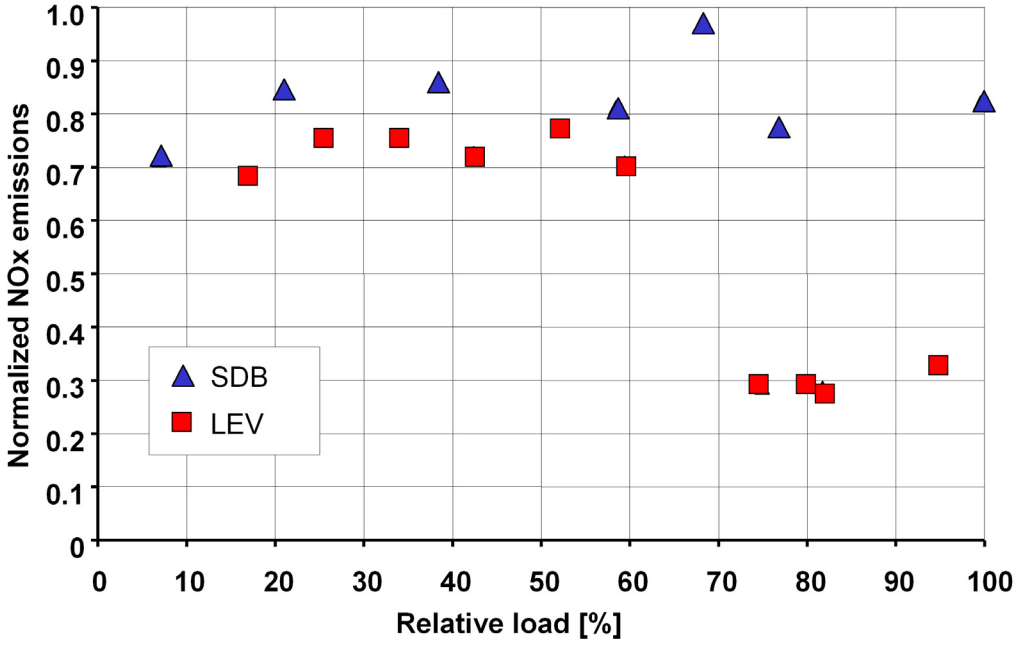

Figure 6.17: $\mathbf{NO_x}$ emissions from engine tests (no water injection): SDB vs. LEV with axial lance position L_{opt}.

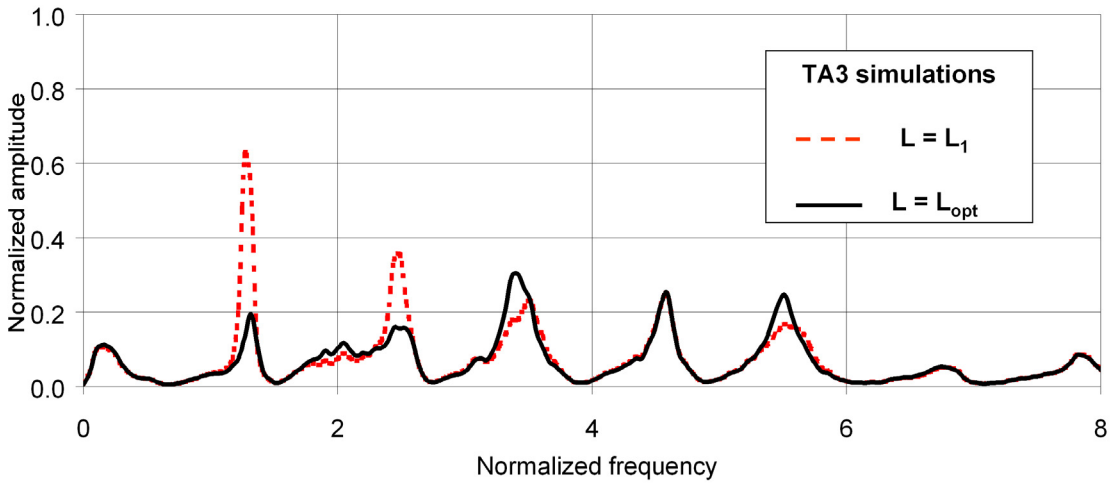

Figure 6.18: Pressure pulsations in LEV combustor: TA3 network simulations for axial lance positions L_1 and L_{opt}.

Bibliography

[1] Putnam, A. A., *Combustion Driven Oscillations in Industry*, American Elsevier Publishers, New York, 1971.

[2] Colonius, T., Basu, A. J., and Rowley, C. W., "Computation of Sound Generation and Flow/Acoustic Instabilities in the Flow Past an Open Cavity," *3rd ASME/JSME Joint Fluids Engineering Conference*, San Francisco, CA, July 18-23 1999.

[3] Tam, C. K. W., "Computational Aeroacoustics: Issues and Methods," *AIAA Journal*, Vol. 180, 1995, pp. 557–581.

[4] Monin, A. S. and Yaglom, A. M., *Statistical Fluid Mechanics: Mechanics of Turbulence*, The MIT Press, Cambridge, 1987.

[5] Wang, S. W. and Yang, V., "Unsteady Flow Evolution in Swirl Injectors, Part II: External Excitations," *Physics of Fluids*, Vol. 17, 2005, pp. 045107.

[6] Schmitt, P., Schuermans, B., Geigle, K. P., and Poinsot, T., "Large-eddy simulation and experimental study of heat transfer, nitric oxide emissions and combustion instability in a swirled turbulent high pressure burner," *Journal of Fluid Mechanics*, Vol. 507, 2007, pp. 17–46.

[7] Hardin, J. C. and Pope, D. S., "An Acoustic/Viscous Splitting Technique for Computational Aeroacoustics," *Theoretical and Computational Fluid Dynamics*, Vol. 6, 1994, pp. 323–340.

[8] Ewert, R. and Schröder, W., "Acoustic Perturbation Equations Based on Flow Decomposition via Source Filtering," *Journal of Computational Physics*, Vol. 188, 2003, pp. 365–398.

[9] Seo, J. H. and Moon, Y. J., "Linearized Perturbed Compressible Equations for low Mach Number Aeroacoustics," *Journal of Computational Physics*, Vol. 218, 2006, pp. 702–719.

[10] Chu, B. T. and Kovásznay, L. S. G., "Non-Linear Interactions in a Viscous Heat-Conducting Compressible Gas," *Journal of Fluid Mechanics*, Vol. 3, 1958, pp. 494–514.

[11] Paschereit, C. O., Flohr, P., and Schuermans, B., "Prediction of Combustion Oscillations in Gas Turbine Combustors," *39th Aerospace Sciences Meeting and Exhibit*, No. AIAA 2001-484, Reno, NV, Jan 8-11 2001.

[12] Akamatsu, S. and Dowling, A. P., "Three-Dimensional Thermoacoustic Oscillations in a Premix Combustor," *ASME Turbo Expo*, No. ASME 2001-GT-0034, New Orleans, LA, Jun 8-11 2001.

[13] Dowling, A. P. and Stow, S. R., "Modal Analysis of Gas Turbine Combustor Acoustics," *Journal of Propulsion and Power*, Vol. 19, 2003, pp. 751–764.

[14] Pankiewitz, C. and Sattelmayer, T., "Time Domain Simulation of Combustion Instabilities in Annular Combustors," *ASME Turbo Expo*, No. ASME GT-2002-30063, Amsterdam, The Netherlands, Jun 3-6 2002.

[15] Evesque, S. and Polifke, W., "Low-Order Acoustic Modelling for Annular Combustors: Validation and Inclusion of Modal Coupling," *ASME Turbo Expo*, No. ASME GT-2002-30064, Amsterdam, The Netherlands, Jun 3-6 2002.

[16] Schuermans, B., Polifke, W., and Paschereit, C. O., "Modeling Transfer Matrices of Premixed Flames and Comparison with Experimental Results," *ASME Turbo Expo*, No. ASME 1999-GT-0132, Indianapolis, IN, June 7-10 1999.

[17] Dowling, A. P., "Non-linear Self-Excited Oscillations of a Ducted Flame," *Journal of Fluid Mechanics*, Vol. 346, 1997, pp. 271–290.

[18] Ni, A., Polifke, W., and Joos, F., "Ignition Delay Time Modulation as a Contribution to Thermo-Acoustic Instability in Sequential Combustion," *ASME Turbo Expo*, No. ASME 2000-GT-0103, Munich, Germany, May 8-11 2000.

[19] Chu, B. T., "On the Generation of Pressure Waves at a Plane Flame Front," *Fourth Symposium (International) on Combustion*, Vol. 4, 1953, pp. 603–612.

[20] Crocco, L. and Cheng, S. L., *Theory of Combustion Instability in Liquid Propellant Rocket Motors*, Butterworths Scientific Publications, 1956.

[21] Harrje, D. T., "Liquid Propellant Rocket Combustion Instability," Tech. Rep. SP-194, NASA, 1972.

[22] Keller, J. J., "Thermoacoustic Oscillations in Combustion Chambers of Gas Turbines," *AIAA Journal*, Vol. 33, 1995, pp. 2280–2287.

[23] Lieuwen, T. C. and Zinn, B. T., "Theoretical Investigation of Combustion Instability Mechanisms in Lean Premixed Gas Turbines," *36th Aerospace Sciences Meeting and Exhibit*, No. AIAA 1998-641, Reno, NV, Jan 12-15 1998.

[24] Hubbard, S. and Dowling, A. P., "Acoustic Resonances of an Industrial Gas Turbine Combustion System," *ASME Turbo Expo*, No. ASME 2000-GT-0094, Munich, Germany, May 8-11 2000.

[25] Flohr, P., Paschereit, C. O., Van Roon, B., and Schuermans, B., "Using CFD for Time-Delay Modeling of Premixed Flames," *ASME Turbo Expo*, No. ASME 2001-GT-0376, New Orleans, LA, Jun 8-11 2001.

[26] Fleifil, M., Annaswamy, A. M., Ghoneim, A., and Ghoniem, A. F., "Response of a Laminar Premixed Flame to Flow Oscillations: A Kinematic Model and Thermoacoustic Instability Results," *Combustion and Flame*, Vol. 106, 1996, pp. 487–510.

[27] Dowling, A. P., "A Kinematic Model of a Ducted Flame," *Journal of Fluid Mechanics*, Vol. 394, 1999, pp. 51–72.

[28] Schuller, T., Durox, D., and Candel, S., "A unified model for the prediction of laminar transfer functions: comparison between conical and V-flame dynamics," *Combustion and Flame*, Vol. 134, 2003, pp. 21–34.

[29] Morse, P. M. and Ingard, K., *Theoretical Acoustics*, McGraw-Hill, New York, 1968.

[30] von Helmholtz, H., *Theorie der Luftschwingungen in Rohren mit Offenen Enden*, Crelle, 1860.

[31] Chanaud, R. C., "Effect of Geometry on the Resonance Frequency of Helmholtz Resonators," *Journal of Sound and Vibration*, Vol. 178, 1994, pp. 337–348.

[32] Panton, R. L. and Miller, J. M., "Resonant Frequencies of Cylindrical Helmholtz Resonator," *Journal of the Acoustical Society of America*, Vol. 57, 1975, pp. 1533–1535.

[33] Zinn, B. T., "A Theoretical Study of Non-Linear Damping by Helmholtz Resonators," *Journal of Sound and Vibration*, Vol. 13, 1970, pp. 69–78.

[34] Ingard, U. and Ising, H., "Acoustic Nonlinearities of an Orifice," *Journal of the Acoustical Society of America*, Vol. 42, 1967, pp. 6–17.

[35] Hersh, A. S. and Rogers, T., "Fluid Mechanical Model for the Acoustic Impedance of Small Orifices," *2nd Aero-Acoustics Conference*, No. AIAA 1975-495, Hampton, VA, Mar 24-26 1975.

[36] Disselhorst, J. H. M. and Van Wijngaarden, L., "Flow in the Exit of Open Pipes During Acoustic Resonance," *Journal of Fluid Mechanics*, Vol. 99, 1980, pp. 293–319.

[37] Cummings, A. and Eversman, W., "High Amplitude Acoustic Transmission Through Duct Terminations: Theory," *Journal of Sound and Vibration*, Vol. 91, 1983, pp. 503–518.

[38] Bechert, D. W., "Sound Absorption Caused by Vorticity Shedding Demonstrated With a Jet Flow," *JSV*, Vol. 70, 1980, pp. 389–405.

[39] Dean, P. D. and Tester, B. J., "Duct Wall Impedance Control as an Advanced Concept for Acoustic Suppression," Tech. Rep. CR-134998, NASA, 1975.

[40] Melling, T. H., "The Acoustic Impedance of Perforates at Medium and High Sound Pressure Levels," *Journal of Sound and Vibration*, Vol. 29, 1973, pp. 1–65.

[41] Fahy, F. J. and Schofield, C., "A Note on the Interaction Between a Helmholtz Resonator and an Acoustic Mode of an Enclosure," *Journal of Sound and Vibration*, Vol. 72, 1980, pp. 365–378.

[42] Cummings, A., "The Effects of a Resonator Array on the Sound Field in a Cavity," *Journal of Sound and Vibration*, Vol. 154, 1992, pp. 25–44.

[43] Gysling, D. L., Copeland, G. S., McCormick, D. C., and Proscia, W. M., "Combustion System Damping Augmentation With Helmholtz Resonators," *Journal of Engineering for Gas Turbines and Power*, Vol. 122, 2000, pp. 269–274.

[44] Gupta, A. K., Lilley, D. G., and Syred, N., *Swirl Flows*, Abacus Press, Tunbridge Wells, Kent, England, 1984.

[45] Batchelor, G. K., *An Introduction to Fluid Dynamics*, Cambridge University Press, Cambridge, 1967.

[46] Vincenti, W. G. and Kruger, C. H., *Introduction to Physical Gas Dynamics*, John Wiley and Sons, Inc., Malabar, Florida, 1965.

[47] Williams, F. A., *Combustion Theory*, Addison-Wesley Publishing Company, 1964.

[48] Lamb, H., *Hydrodynamics*, Cambridge, 1932.

[49] Quartapelle, L., *Numerical Solution of the Incompressible Navier-Stokes Equations*, ISNM 113, Birkhauser, Basel, 1993.

[50] Saffman, P. G., *Vortex Dynamics*, Cambridge University Press, Cambridge, 1992.

[51] Temkin, S., *Elements of acoustics*, John Wiley & Sons, 1981.

[52] Culick, F. E. C., "Nonlinear Behavior of Acoustic Waves in Combustion Chambers," *Acta Astronautica*, Vol. 3, 1976, pp. 714–757.

[53] Tijdeman, H., "On the Propagation of Sound Waves in Cylindrical Tubes," *Journal of Sound and Vibration*, Vol. 39, 1975, pp. 1–33.

[54] Lighthill, M. J., "On Sound Generated Aerodynamically I," *Proceedings of the Royal Society of London*, Vol. 211, 1953, pp. 564–587.

[55] Lighthill, M. J., "On Sound Generated Aerodynamically II," *Proceedings of the Royal Society of London*, Vol. 222, 1954, pp. 1–32.

[56] Marble, F. E. and Candel, S. M., "Acoustic Disturbance From Gas Non-Uniformities Convected Through a Nozzle," *Journal of Sound and Vibration*, Vol. 55, 1977, pp. 225–243.

[57] Paschereit, C. O., Gutmark, E., and Weisenstein, W., "Role of Coherent Structures in Acoustic Combustion Control," *29th Fluid Dynamics Conference*, No. AIAA 1998-2433, Albuquerque, NM, June 15-18 1998.

[58] Hinch, E. J., *Perturbation Methods*, Cambridge University Press, Cambridge, 1991.

[59] Kreiss, H. O., "Problems With Different Time Scales for Partial Differential Equations," *Communications On Pure and Applied Mathematics*, Vol. 33, 1980, pp. 399–438.

[60] Majda, A., *Compressible Fluid Flow and Systems of Conservation Laws in Several Space Variables*, Springer-Verlag, New York, 1984.

[61] Klein, R., Mikusky, E., and Owinoh, A., "Multiple Scales Asymptotics for Atmospheric Flows," *4th European Congress of Mathematics*, Stockholm, Sweden, Jun 27-Jul 2 2004.

[62] Meister, A., "Asymptotic Single and Multiple Scale Expansions in the Low Mach Number Limit," *SIAM Journal on Applied Mathematics*, Vol. 60, 1999, pp. 256–271.

[63] Matthaeus, W. H. and Brown, M. R., "Nearly Incompressible Magnetohydrodynamics at Low Mach Number," *Physics of Fluids*, Vol. 31, 1988, pp. 3634.

[64] Zank, G. P. and Matthaeus, W. H., "The Equations of Nearly Incompressible Fluids. I. Hydrodynamics, Turbulence, and Waves," *Physics of Fluids A*, Vol. 3, 1991, pp. 69.

[65] Klein, R., "Semi-Implicit Extension of a Godunov-Type Scheme Based on Low Mach Number Asymptotics I: One-Dimensional Flow," *Journal of Computational Physics*, Vol. 33, 1995, pp. 1788–1795.

[66] Morse, P. M. and Feshbach, H., *Methods of Theoretical Physics*, McGraw-Hill, New York, 1953.

[67] Culick, F. E. C., "Some Recent Results for Nonlinear Acoustics in Combustion Chambers," *AIAA Journal*, Vol. 32, 1994, pp. 146–169.

[68] Rayleigh, J. W. S., *The Theory of Sound*, New York, 1945.

[69] Howe, M. S., "On the Theory of Unsteady High Reynolds Number Flow Through a Circular Aperture," *Proceedings of the Royal Society of London A*, Vol. 366, 1979, pp. 205–223.

[70] Blevins, R. D., *Applied Fluid Dynamics Handbook*, Van Nostrand Reinhold Company Inc., 1984.

[71] Idelchik, I. E., *Handbook of Hydraulic Resistance*, Begell House Publishers, 1996.

[72] Keller, J. J. and Sattelmayer, T., "Double-Cone Burners for Gas Turbine Type 9 Retrofit Application," *19th International Congress on Combustion Engines CIMAC 1991*, Florence, Italy, 1991.

[73] *SYSNOISE 5.4 Documentation*, Brussels, Belgium, 1999.

[74] Dowling, A. P., "The Calculation of Thermoacoustic Oscillations," *Journal of Sound and Vibration*, Vol. 121, 1995, pp. 213–237.

[75] Landau, L. D. and M., L. E., *Fluid Mechanics*, Pergamon Press, Oxford, 1987.

[76] Schuermans, B., Bellucci, V., Nowak, D., and Paschereit, C. O., "Modelling of Complex Thermoacoustic Systems: A State-Space Approach," *9th International Congress on Sound and Vibration*, Orlando, FL, 2002.

[77] Clavin, P., Pelcé, P., and He, L., "One-Dimensional Vibratory Instability of Planar Flames Propagating in Tubes," *Journal of Fluid Mechanics*, Vol. 216, 1990, pp. 299–322.

[78] Scarinci, T. and Freeman, C., "The Propagation of a Fuel-Air Ratio Disturbance in a Simple Premixer and its Influence on Pressure Wave Amplification," *ASME Turbo Expo*, No. ASME 2000-GT-0106, Munich, Germany, May 8-11 2000.

[79] Lieuwen, T. C. and Zinn, B. T., "Theoretical Investigation of Unsteady Flow Interactions with a Planar Flame," *37th Aerospace Sciences Meeting and Exhibit*, No. AIAA 1999-324, Reno, NV, Jan 11-14 1999.

[80] Abu-Off, G. M. and Cant, R. S., "Reaction Rate Modeling for Premixed Turbulent Methane-Air Flames," *Joint Meeting of Spanish, Portuguese, Swedish and British Sections of the Combustion Institute*, Madeira, 1996.

[81] Markstein, G. H., *Nonsteady Combustion Propagation*, The Macmillan Company, Pergamon Press, Oxford, 1964.

[82] Norris, A. N. and Sheng, C., "Acoustic Radiation From a Circular Pipe With an Infinite Flange," *Journal of Sound and Vibration*, Vol. 135, 1989, pp. 85–93.

[83] Rschevkin, S. N., *A Course of Lectures on the Theory of Sound*, Pergamon Press, Oxford, 1963.

[84] Jing, X. and Sun, X., "Effect of Plate Thickness on Impedance of Perforated Plates with Bias Flow," *AIAA Journal*, Vol. 38, 2000, pp. 1573–1578.

[85] Peters, M. C. A. M., Hirschberg, A., Reijnen, A. J., and Wijnands, A. P. J., "Damping and Reflection Coefficient Measurements for an Open Pipe at Low Mach and Low Helmholtz Numbers," *Journal of Fluid Mechanics*, Vol. 256, 1993, pp. 499–534.

[86] Rienstra, S. W., "A Small Strouhal Number Analysis for Acoustic Wave-Jet Flow-Pipe Interaction," *Journal of Sound and Vibration*, Vol. 86, 1983, pp. 539–556.

[87] Nowak, D. and Bellucci, V., "On the Modeling of Helmholtz Resonators for Damping Acoustic Pulsations in Industrial Gas Turbines," *12th International Congress on Sound and Vibration*, Lisbon, Portugal, Jul 11-14 2005.

[88] *Using MATLAB Version 6*, Natick, MA, 1999.

[89] Polifke, W., Geng, W., and Döbbeling, K., "Optimization of Rate Coefficients for Simplified Reaction Mechanisms with Genetic Algorithms," *Combustion and Flame*, Vol. 113, 1998, pp. 119–134.

[90] Bellucci, V., Schuermans, B., Paschereit, C. O., and Flohr, P., "Thermoacoustic Simulation of Lean Premixed Flames Using an Enhanced Time-Lag Model," *31st AIAA Fluid Dynamics Conference and Exhibit*, No. AIAA 2001-2794, Anaheim, CA, Jun 11-14 2001.

[91] Flohr, P., Paschereit, C. O., and Bellucci, V., "Steady CFD Analysis for Gas Turbine Burner Transfer Functions," *41st Aerospace Sciences Meeting and Exhibit*, No. AIAA 2003-1346, Reno, NV, Jan 6-9 2003.